

# Millimeter-Wave Beam Scattering by Edge Turbulence in Magnetically-Confined Plasmas

Thèse N° 9092

Présentée le 1<sup>er</sup> mars 2019

à la Faculté des sciences de base  
SPC - Physique des Plasmas de Base  
Programme doctoral en physique

pour l'obtention du grade de Docteur ès Sciences

par

**Oulfa CHELLAÏ**

Acceptée sur proposition du jury

Prof. S. Manley, présidente du jury  
Prof. I. Furno, Dr T. Goodman, directeurs de thèse  
Dr O. Maj, rapporteur  
Dr P. Hennequin, rapporteuse  
Prof. A. Fasoli, rapporteur

2019



«Comme autant d'étoiles, ensemble nous brillerons.»

À vous qui m'avez offert des étoiles qui savent rire.



# Remerciements

*Lausanne, le 12 février 2019*

Quatre années sont passées et il est temps pour moi de vous remercier. J'espère ne commettre aucune maladresse et réussir à vous exprimer mon immense gratitude.

La première personne que je souhaite remercier c'est toi, Stefano. C'est le hasard de notre rencontre qui m'a menée ici aujourd'hui. Ceux qui te connaissent connaissent aussi ta qualité de pédagogue et comprendront sans peine que tu aies réussi à me transmettre ton intérêt pour la physique et la fusion thermonucléaire. Tu as toujours eu pour moi une grande bienveillance. J'ai eu l'honneur immense de travailler avec Ivo, Tim et toi ces dernières années. A vous trois, vous êtes un exemple d'intégrité scientifique. Vous m'avez appris l'importance de la collaboration et de l'esprit critique, deux notions essentielles à un scientifique. Ivo, je me souviens du temps que tu as passé avec moi dans la salle de contrôle de TORPEX à m'apprendre à mesurer des signaux, à les questionner, à les comprendre. Tu as su quand m'épauler et plus tard me faire confiance. Je te remercie de m'avoir donné absolument tous les moyens pour réussir. Tim, ton énergie est contagieuse, tu as l'esprit qui fuse. Je te remercie de me l'avoir transmise, de m'avoir toujours aidée à résoudre des problèmes complexes avec ta bonne humeur naturelle.

Lorsque j'ai commencé mon doctorat sur TORPEX, Marcelo, tu as été mon mentor. Un mentor pédagogue, avenant et disponible. Je vous remercie Fabian et toi pour votre aide précieuse. Ceux d'entre nous qui ont eu la chance de vous côtoyer Gennady, Remy et Riccardo savent que votre esprit protecteur et chaleureux transforme notre groupe en petite famille. Je te remercie en particulier toi Gennady pour avoir mis à ma disposition tes talents d'inventeur fou.

Au cours de ma thèse, j'ai également eu le plaisir de travailler avec toi, Omar Maj. Ton approche mathématique a véritablement enrichi ma vision d'un problème dont je n'ai fait qu'effleurer la complexité. Je te remercie pour ta générosité et ta modestie, d'avoir eu le temps et la patience de travailler avec moi et de m'apprendre tellement. Je remercie également Fabio et Paolo de m'avoir permis de travailler avec les simulations GBS et d'avoir été à l'écoute.

En parallèle de mon doctorat, j'ai découvert l'enseignement avec Quang, Jean-Philippe et Christian. Humbles, volontaires et dévoués, vous savez tous les trois montrer ce que

## Acknowledgements

---

l'enseignement a de plus beau : la volonté de transmettre un savoir, de passer le flambeau, sans orgueil et en toute humilité. Je vous remercie de me l'avoir rappelé et de m'avoir fait confiance.

Edith, je te remercie sincèrement, tu as été pour nous tous, étudiants fraîchement débarqués, un réconfort. Je te remercie et je remercie Roxane aussi. Je vous remercie Damien, Steve, Thierry, et en particulier toi Ugo pour toutes ces heures, ces jours passés à nous creuser la tête sur les sources de ce bruit invisible, sans jamais baisser les bras! Merci à vous Régis, Nelson, Christian et William, sans qui notre travail n'aurait pas beaucoup de sens. Merci à Xavier, Joan, Miguel, Pierre, Olivier et Laurent. Merci à Basil et Stefano de m'avoir soutenue. Merci à Ambrogio et à la direction du Swiss Plasma Center pour cette belle opportunité que vous m'avez donnée.

Un immense *grazie* Fed, Francesco et Lorenzo, *danke* Fabian et Mirko, *gracias* Pedro et en particulier 谢谢梦迪! Merci pour votre joie de vivre et pour ces milliers de petites attentions au quotidien. Merci à toi Arsène pour la chaleur que tu as apportée.

Camoulette, Amélie, Christoph, Colin, Guillaume, Hamish, Hugo, Jérémy et Umar, ces quelques lignes ne suffiront pas à rendre honneur à votre curiosité, votre folie, votre esprit d'aventure, à vos moqueries et à vos rires. Mais notre aventure ne fait que commencer!

A présent, ce n'est pas une tâche aisée de trouver les mots justes. Mon papou, mamati, je vous dois ce que je suis aujourd'hui. Vous avez mis dans mes yeux les étoiles de la curiosité, du respect et de l'Amour avec un grand A. Vous m'avez servi les frontières du possible sur un plateau. Vous, Yasmine, Denys et Cocotte, vous êtes ma source d'inspiration, mon leitmotiv et ma fierté.

Ainuti, Dida, Doudi et Simo, je vous remercie d'avoir toujours pardonné mes absences durant ces longues années. Khtiti Saïda, Abba, je finis avec vous, vous que je n'ai pas eu l'occasion de remercier, merci.

O. C.

# Résumé

Les ondes millimétriques haute puissance, dans la gamme de fréquence électron-cyclotron, sont abondamment utilisées dans les machines à fusion. Elles sont devenues essentielles pour un bon nombre d'applications qui s'étendent du chauffage plasma à la préservation du confinement du cœur. 24 MW de puissance électron-cyclotron seront installées sur ITER. Cette puissance sera répartie entre le lanceur équatorial qui aura pour fonction principale de chauffer le cœur du plasma et d'induire du courant plasma, et le lanceur supérieur qui lui aura pour fonction principale de stabiliser les modes néo-classiques et ainsi prévenir les disruptions. L'é étroitesse du profil de déposition de puissance est fondamentale pour pouvoir stabiliser les modes néo-classiques. On comprend ainsi qu'elle soit une contrainte pour le faisceau du lanceur supérieur. De récentes estimations ont prédit que la turbulence du bord du plasma qui est associée à de fortes fluctuations de la densité électronique pourrait être responsable d'un élargissement du faisceau d'un facteur deux. Cet élargissement pourrait, lui, être responsable d'une diminution de l'efficacité de la stabilisation des modes néo-classiques sur ITER.

Dans la première partie de cette thèse, la diffusion des ondes millimétriques par la turbulence plasma est étudiée dans la configuration SMT (pour « Simple Magnetized Torus »). Cette configuration aux lignes de champs hélicoïdales (et ouvertes) a pour particularité de générer une turbulence qui a des propriétés similaires à celle présente dans le bord des tokamaks. Des expériences menées sur la machine TORPEX et sur le Tokamak à Configuration Variable (TCV) montrent que des structures alignées le long des lignes de champs et associées à une augmentation locale de la densité électronique (que l'on nomme « blob ») sont responsables d'une fluctuation de la puissance transmise. En utilisant la méthode dite de l'échantillonnage conditionné (« conditional sampling » en anglais), appliquée à des mesures provenant de sondes Langmuir, nous montrons que les « blobs » peuvent induire soit une augmentation soit une diminution de la puissance mesurée. L'effet dépendant de la position du « blob ». Nous montrons également que l'effet des « blobs » est plus prononcé pour les « blobs » de grande densité électronique. Dans le cas de TORPEX, l'imagerie 2-D de la densité électronique provenant du réseau de sondes Langmuir HEX TIP-U est utilisée pour faire tourner des simulations « full-wave » de la propagation du faisceau. Les simulations révèlent que le « blob » défocalise le faisceau, entraînant des variations de la puissance millimétrique.

Dans la seconde partie de cette thèse, la diffusion est étudiée dans les plasmas de TCV en mode L. Un diagnostic mesurant la puissance millimétrique transmise après propagation dans le plasma est installé sur TCV. Un jeu de sonde Langmuir, installé sur la paroi interne

## Acknowledgements

---

de TCV, est utilisé pour faire de l'échantillonnage conditionné sur le signal de la puissance détectée et identifier ainsi l'effet des blobs présents dans le bord du plasma sur la transmission. Des résultats similaires à ceux observés sur TORPEX sont obtenus : les « blobs » présents dans la partie supérieur du bord du plasma sont responsables de variations dans la puissance transmise de l'ordre de 10 %. Ces variations peuvent être positives ou négatives en fonction de la position du « blob ». La direction et la norme de la vitesse quasi-poloïdale du « blob » est estimée depuis les mesures millimétriques. Les deux grandeurs sont en accord avec des mesures faites par la sonde rapide. L'effet d'un « blob » sur la transmission est étudiée numériquement. L'échantillonnage conditionné appliqué aux données du code de turbulences GBS est utilisé pour reconstituer l'évolution spatio-temporelle de la densité électronique associée à la propagation du « blob » dans TCV. L'évolution temporelle de la puissance détectée associée à la propagation du « blob » obtenue grâce aux simulations « full-wave » est en accord avec les expériences. Les simulations numériques montrent que les fluctuations négatives de densité électronique précédant le « blob » focalisent le faisceau tandis que le « blob » lui-même défocalise le faisceau. Cette focalisation-défocalisation entraîne des variations de la puissance détectée.

Finalement, une combinaison des simulations tournées sur le code WKBeam et des mesures expérimentales montre que la largeur du faisceau est 50% plus grande que la largeur prédite dans le cas d'une propagation dans un plasma non-turbulent.



# Abstract

High-power millimeter-waves (mmw) in the electron cyclotron range of frequencies are extensively used in fusion devices. They have become essential for a number of applications ranging from plasma heating and current drive to core confinement preservation. In ITER, 24 MW of power are planned to be injected through the equatorial launcher to perform bulk plasma heating and current drive; and through the upper-launcher, mainly to stabilize neo-classical tearing mode (NTM), and this way prevent plasma disruption. The narrowness of the power deposition is a key feature of NTM stabilization and thus a key requirement for the upper-launcher beam in ITER. Recent calculations have estimated that, because of the long path of the upper-launcher beam in ITER, electron density fluctuations associated with the turbulence in the edge of the plasma could be responsible for a broadening of the mmw-beam, possibly deteriorating NTM stabilization efficiency. In this thesis we investigate mmw-scattering by plasma turbulence experimentally and numerically.

In the first part of this thesis, millimeter-wave scattering by plasma turbulence is investigated in the simple magnetized toroidal configuration, which turbulence is known to exhibit universal properties of the turbulence present at the edge of tokamaks. Scattering experiments run on both the TORPEX device and the Tokamak à Configuration variable (TCV) reveal that field-aligned elongated structures of enhanced electron density (blobs) are responsible for fluctuations of the transmitted mmw-power. Using conditional sampling on Langmuir probe measurements, we show that blobs can either increase the locally measured mmw-power or decrease it, depending on their location. We also show that the effect of blobs on the mmw-transmission increases for blobs of higher electron density. In the case of the TORPEX experiments, experimental 2D-time imaging of the electron density from the HEX TIP-U array of Langmuir probes is used to run full-wave simulations of the mmw-beam propagation. The full-wave simulations are found in agreement with the experiments and reveal that blobs have a defocusing effect on the mmw-beam in the wake of the blob structure, leading to local changes in the mmw-power.

In the second part of this thesis, mmw-wave scattering is investigated in L-mode confined TCV plasmas. A transmission diagnostic is installed to measure the mmw-power from the X3 beam reaching the floor of the vessel after propagation in the plasma. A set of wall-embedded Langmuir probes located in the inner-wall of the TCV vessel is used to perform conditional sampling on the detected mmw-power signal and identify the effect of blobs present in the scrape-off layer on the mmw-transmission. Similar results to those found in TORPEX are observed: Blobs located in the upper-part of the scrape-off layer are responsible for changes

## Acknowledgements

---

in the transmitted power ( $\sim 10\%$ ) which can be either positive or negative depending on the blob location. The direction and norm of the quasi-poloidal velocity of the blob are inferred from the mmw-measurements and are found in agreement with measurements from the fast reciprocating probe. The effect of a blob on the mmw-transmission is investigated numerically. Conditional sampling is performed on the turbulence data from GBS to reconstruct the time-resolved 2D evolution of the electron density in the scrape-off layer associated with the propagation of a blob in TCV. The time-evolution of the detected mmw-power associated with the blob propagation from the full-wave simulations is successfully compared to the experiment. The numerical simulations show that negative fluctuations of the electron density preceding the blob focus the mmw-beam and the blob defocuses the mmw-beam, resulting in partial variations of the mmw-power.

Finally, a combination of simulations run with WKBeam and experimental measurements demonstrate that the mmw-beam is 50% broader in TCV due to the edge turbulence than the predicted mmw-beam after propagation in a non-turbulent plasma.

# Contents

<b>Remerciements</b>	<b>v</b>
<b>Abstract (Français/English)</b>	<b>vii</b>
<b>1 Motivation</b>	<b>1</b>
1.1 High-power electron cyclotron waves in tokamaks . . . . .	2
1.2 Electron cyclotron waves in ITER . . . . .	6
1.3 The case of neoclassical tearing mode stabilisation in ITER . . . . .	7
1.4 Effect of edge density fluctuations on the NTM stabilization in ITER . . . . .	10
1.5 Outline of the thesis . . . . .	13
<b>2 Tokamak à Configuration Variable</b>	<b>15</b>
2.1 Third harmonic heating system on TCV . . . . .	16
2.1.1 Third harmonic setup on TCV . . . . .	17
2.1.2 X3 transmission diagnostic . . . . .	20
2.2 Diagnostics for the plasma core . . . . .	25
2.2.1 Thomson scattering . . . . .	26
2.2.2 Far infrared interferometer . . . . .	28
2.2.3 Soft X-ray diagnostics . . . . .	29
2.3 Langmuir probes for diagnosing the plasma edge . . . . .	34
2.3.1 Theory of a single-tip probe . . . . .	34
2.3.2 Wall-embedded Langmuir probes on TCV . . . . .	35
2.3.3 Fast reciprocating probe . . . . .	36
<b>3 The TORPEX device</b>	<b>39</b>
3.1 Presentation of the device . . . . .	39
3.2 Millimeter-wave injection/detection system . . . . .	41
3.3 HEXTIP array . . . . .	45
3.4 Conditional averaged sampling . . . . .	46
<b>4 Numerical tools</b>	<b>49</b>
4.1 The turbulence code Global Braginskii Solver (GBS) . . . . .	49
4.2 Numerical tools for millimeter-wave propagation . . . . .	54
4.2.1 WKBeam . . . . .	55

## Contents

---

4.2.2	Full-wave model . . . . .	57
<b>5</b>	<b>Mmw-beam scattering by turbulent structures and blobs in simple magnetized toroidal plasmas</b>	<b>67</b>
5.1	Simple magnetized torus configurations in TCV . . . . .	68
5.2	Scattering experiments in TCV SMT plasmas . . . . .	70
5.3	Simple magnetized plasmas in TORPEX . . . . .	73
5.4	Influence of the plasma on the mmw-propagation . . . . .	77
5.5	Numerical investigation of mmw-scattering in TORPEX . . . . .	80
<b>6</b>	<b>Effect of MHD modes on the high power mmw-beam in TCV</b>	<b>85</b>
6.1	Description of the plasma mode $m=1, n=1$ . . . . .	85
6.2	Experimental observations on X3TD . . . . .	89
6.3	A test case for comparing full-wave and WKBeam simulations . . . . .	92
<b>7</b>	<b>Effect of edge turbulence on the high-power mmw-beam on TCV</b>	<b>95</b>
7.1	Plasma scenario . . . . .	95
7.1.1	Description of the plasma equilibrium . . . . .	95
7.1.2	Sawtooth activity in discharge <i>60612</i> . . . . .	97
7.2	A note on the effect of sawteeth on the propagation of mmw-beams . . . . .	98
7.3	Experimental evidence of mmw-scattering from turbulence in the scrape-off layer . . . . .	103
7.4	Investigating the effect of a single ‘average’ blobs on the mmw-transmission . . . . .	109
7.5	Numerical investigation of the effect of the edge turbulence on the mmw-beam . . . . .	112
7.5.1	Effect of a single blob on the mmw-beam power . . . . .	112
7.5.2	Effect of edge turbulence on the time-averaged mmw-beam power . . . . .	114
<b>8</b>	<b>Summary &amp; Conclusions</b>	<b>119</b>
<b>A</b>	<b>Notations</b>	<b>123</b>
A.1	List of frequently used symbols . . . . .	123
A.2	List of acronyms . . . . .	125
<b>B</b>	<b>Gaussian beams</b>	<b>127</b>
<b>C</b>	<b>X3 mirror</b>	<b>129</b>
C.1	Mirror surface parametrization . . . . .	129
C.2	Intersection of incoming beams with mirror . . . . .	130
C.3	Orientations of outgoing beams . . . . .	131
C.4	Focal lengths . . . . .	134
<b>D</b>	<b>Estimation of uncertainty in <math>n_e</math> measured by HEX TIP</b>	<b>137</b>
	<b>Bibliography</b>	<b>146</b>
	<b>Curriculum Vitae</b>	<b>147</b>

# 1 Motivation

Electron cyclotron resonant heating (ECRH) and electron cyclotron current drive (ECCD) are well-established millimeter-wave (mmw) techniques used in tokamaks and stellarators to perform plasma heating, non-inductive current drive and the stabilization of magnetohydrodynamic (MHD) modes, avoiding core confinement degradation and plasma disruption [1, 2, 3]. They are based on the use of mmws in the electron cyclotron (EC) range of frequency and its harmonics. Compared to other heating or current drive techniques, ECRH and ECCD provide the advantages of a "highly localized and a robustly controllable" power and current deposition [4]. The highly-localized driven-current profile is a key feature of an EC-wave utility. At EC-frequencies, compact, well collimated, coherent Gaussian-beams can be formed that couple efficiently to the plasma at its boundary. The EC-beams can be transported from the outside of the vessel and injected via the launchers placed far away from the plasma. The small wavelength of the EC-wave, compared to other electromagnetic waves used for magnetized plasma heating (see table 1.1)), enables the use of relatively small launching antennas. Since small-angle steering of an EC-beam can be performed by moving elements located far from the vessel [5], the vacuum vessel might benefit from the small size of the aperture dedicated to the EC-antenna. This could provide an important technical advantage for the use of ECCD and ECRH in a fusion reactor environment like DEMO where plasma-facing component could be at risk of damage. At present, however, the International Thermonuclear Experiment Reactor (ITER) uses a more common front-steer launcher where the mirror nearest the plasma moves. This allows the larger steering range required for an experimental machine. The Tokamak à Configuration Variable (TCV) and other present day machines also use this type of launcher. In this section, we set the basis to understand how small inhomogeneities in the plasma, far from the region where EC-power is deposited and in the path of the mmw-beam, can degrade the efficiency of their use in ITER.

## Chapter 1. Motivation

Machine	$R_0$ (m)	a (m)	$\lambda_{EC}$ (mm)	$\lambda_{LH}$ (m)	$\lambda_{ICRH}$ (m)
TCV	0.88	0.25	2.5		
ASDEX Upgrade	1.65	0.5	2.1	0.23	2.5-10
DIII-D	1.67	0.67	2.7	0.06 (in design)	
W7-X	5.5	0.53	2.1		10.0 (planned)
ITER	6.2	2.0	1.7	0.06 (proposed)	6.0

Table 1.1 – Examples of toroidal devices with their sizes and wavelength of the millimeter-wave heating systems

Device	Power (MW)	Frequency (GHz)	Mode	Nominal toroidal field (T)
TCV	1.5	82.7	X2	1.4
	1.5	117.8	X3	
	2.0	84	X2*	
	2.0	126	X3*	
ASDEX Upgrade	2.0	140	X2	3.1
DIII-D	5.0	110	X2	2.2
Wendelstein 7-X	10.0	140	X2	3.0
ITER	20.0	170	O1	5.3

Table 1.2 – Examples of toroidal devices with their high power EC-systems and injection modes. \* EC-system upgrade operational in 2019.

### 1.1 High-power electron cyclotron waves in tokamaks

To understand the propagation of EC-waves in tokamaks, a basic review of their properties is required. EC-waves are electromagnetic waves in the electron cyclotron range of frequency and its harmonics ( $l=1,2,3,\dots$ ). The EC frequency  $f_{ec}$  depends on local the magnetic field  $B_0$  as  $f_{ec} = \frac{\Omega_e}{2\pi} = \frac{eB_0}{2\pi\gamma m_e}$ , where  $m_e$  is the electron rest mass and  $e$  the elementary charge and  $\gamma$  the relativistic factor. We will see that the harmonics are commonly used in the naming of the modes excited in the plasma (e.g. O1, X2, etc.).

Most of the interesting features of the EC-wave propagation in plasmas can be understood from the cold plasma model. Following the treatment made by Stix in [6] and used by Prater in [4], the dispersion relation for EC-waves in a magnetized cold plasma can be written as

$$D(n, \frac{\omega_p^2}{\omega^2}, \frac{\Omega_e}{\omega}, \theta) = \tan^2 \theta + \frac{P(n^2 - R)(n^2 - L)}{(Sn^2 - RL)(n^2 - P)} = 0 \quad (1.1)$$

where  $n$  is the refraction index,  $\omega$  the angular frequency of the wave,  $\omega_p = \sqrt{\frac{n_e e^2}{\epsilon_0 m_e}}$  the plasma frequency<sup>1</sup>, where  $n_e$  is the electron density, and  $\theta$  the angle between the wave vector  $\mathbf{k}$  and the magnetic field  $\mathbf{B}$ . Knowing that the ion mass is much greater than the electron mass

<sup>1</sup> $\omega_p$  is commonly referred to as plasma frequency although it is an angular frequency.

## 1.1. High-power electron cyclotron waves in tokamaks

$\frac{\omega_{pi}}{\omega}, \frac{\Omega_i}{\omega} \ll 1$ , we can expand the different terms in eq. 1.1 as follow:

$$\begin{aligned} P &= 1 - (\omega_p/\omega)^2, & S &= (R + L)/2, \\ R &= (P - \Omega_e/\omega)/(1 - \Omega_e/\omega), & D &= (R - L)/2, \\ L &= (P + \Omega_e/\omega)/(1 + \Omega_e/\omega). \end{aligned}$$

For perpendicular propagation, i.e. when  $\theta \rightarrow \pi/2$ , the two solutions of the dispersion relation are:

$$n^2 = P \text{ and } n^2 = \frac{RL}{S}. \quad (1.2)$$

For parallel propagation, i.e. when  $\theta \rightarrow 0$ , the two solutions of the dispersion relation are:

$$n^2 = L \text{ and } n^2 = R. \quad (1.3)$$

These two solutions are referred to as the normal modes of of EC-waves in a magnetized plasma [4]. The O-mode is the mode associated with the solution  $n^2 = P$  for perpendicular propagation. The mode associated with the solution  $n^2 = \frac{RL}{S}$  for perpendicular propagation is called the X-mode. Harmonics of the EC-frequency are commonly used in the naming of the modes excited in the plasma (e.g. O1, X2, X3, etc.).

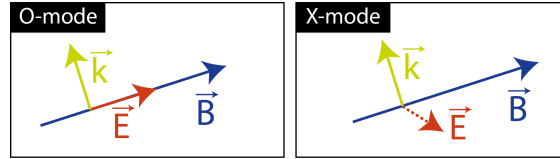


Figure 1.1 – Injection configuration for O-mode (left) and X-mode (right) for perpendicular propagation.

To identify the cut-offs ( $n^2 = 0$ ) and the resonances ( $n^2 \rightarrow \infty$ ), the dispersion relation is written in the form [6, 4]:

$$An^4 + Bn^2 + PRL = 0, \quad (1.4)$$

where  $A$  and  $B$  are functions of  $P, R, L$  and  $\theta$ . Cut-offs occur when  $PRL = 0$ .

## Chapter 1. Motivation

A convenient way of visualizing the cut-offs and resonances in the path of a mmw injected in a tokamak plasma is the Clemmow-Mullaly-Allis (CMA) diagram. The x-axis of the CMA diagram is  $\omega_p^2/\omega^2$ , which is proportional to the electron density and the y-axis is  $\Omega_e^2/\omega^2$ , which is proportional to  $B_0^2$ . The CMA diagrams for the O-mode and X-mode are shown in fig. 1.2.

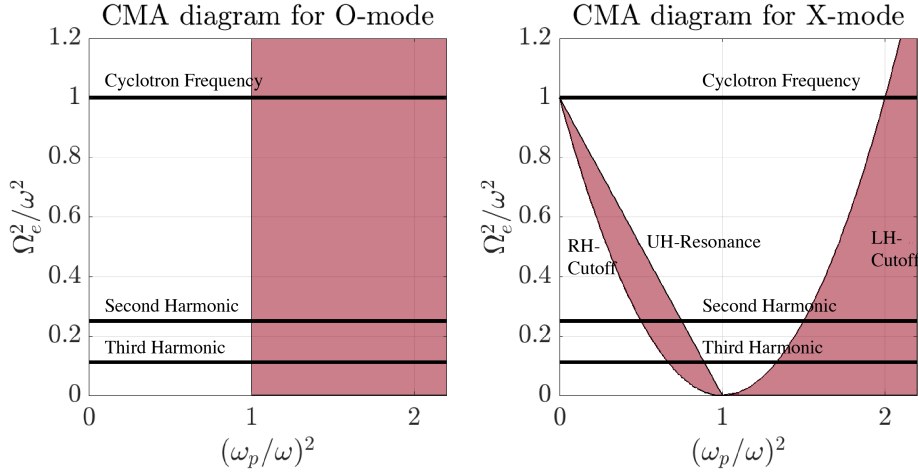


Figure 1.2 – CMA diagram for O-mode (left) and X-mode (right). The red shaded areas represent the regions of evanescence of the wave. The regions of interest for the propagation of the wave are the regions in white.

The cut-off of the O-mode occurs when  $P = 0$ , i.e. when  $\omega^2 = \omega_p^2$ . When the frequency of the mmw is the harmonic  $l$  of the electron cyclotron frequency, the cut-off density for the O-mode  $n_{c,O}$  is  $n_{c,O} = \frac{l^2 B^2}{10.3} [\times 10^{20} m^{-3}]$ , where  $B$  is the magnetic field given in Tesla. The O-mode resonance can be reached either from the high field side (HFS) or the low field side (LFS) of the vessel, provided that the high density region of the plasma ( $\omega_p^2 > \omega^2$ ) is not reached. Here, it is important to note that externally injected waves always begin their propagation from 0 on the x-axis and initially propagate towards the right. Similarly, in a tokamak, LFS injection starts near the zero of the y-axis and initially propagates upwards.

The CMA diagram for the X-mode (fig. 1.2 right) shows that the injection in the X-mode has to be performed carefully. The X-mode experiences the right-hand (RH) cut-off ( $R = 0$ ), the left-hand (LH) cut-off ( $L = 0$ ) and the upper-hybrid resonance ( $\tan\theta = P/S$ ). The red areas correspond to regions of evanescence for the X-mode wave. The regions of interest for the propagation for the X-mode are the regions in white. The CMA diagram shows that the fundamental resonance of the electron cyclotron wave cannot be accessed with an injection from the low-field side ( $\Omega_e^2/\omega^2 < 1$  and  $\omega_p^2/\omega^2 < 1$ ) because of the RH-cutoff. The injection of the wave must therefore be performed from the HFS, this enables access to the widest range of electron densities but suffers from technical constraints due to the limited space available at the HFS of tokamaks as well as the need for the power to cross the EC-resonance in the waveguides on the way to the antenna, albeit outside the plasma. The latter requires careful attention to breakdown along the beam path at high power and field strength. The second harmonic (X2) resonance is accessible by an injection from the LFS, in regions of the



## 1.1. High-power electron cyclotron waves in tokamaks

plasma where the electron density is twice higher than the one accessible for the X1-mode. The third harmonic launch in the X-mode (X3) enables to access regions of the plasma with a higher density<sup>2</sup>, justifying its use despite lower intrinsic optical depth, and a pioneer use of the X3 wave for plasma heating was achieved in the Tokamak à Configuration Variable (TCV) at the Swiss Plasma Center (SPC) [8] following earlier low-power X3 transmission experiments carried out at the Tore Supra tokamak [9] to investigate the optical thickness (defined in the next paragraph) for the novel vertical injection configuration proposed by SPC.

The electron cyclotron wave and its harmonics can be absorbed by electrons having a velocity parallel to the magnetic field  $v_{\parallel}$  satisfying:

$$\omega = \frac{l\Omega_e}{\gamma} + k_{\parallel} v_{\parallel}, \quad (1.5)$$

where  $v_{\parallel}$  and  $k_{\parallel}$  are the components of the velocity of the electron, the wave vector parallel to the magnetic field,  $\gamma$  is the relativistic factor respectively. To quantify the absorption of the EC-waves by the plasma, the optical thickness is introduced [10]. The optical thickness  $\Lambda$  is defined by

$$\Lambda_l^{(j)} = \int_L \alpha_l^{(j)} ds, \quad (1.6)$$

where  $\alpha$  is the absorption coefficient defined as  $\alpha \equiv 2\mathbf{k}'' \cdot \frac{\mathbf{S}}{|\mathbf{S}|}$ , with  $\mathbf{k} = \mathbf{k}' + i\mathbf{k}''$  the wave vector and  $\mathbf{S}$  the total power flux density.  $j = O$  for the O-mode and  $j = X$  for the X-mode. The integral is performed along the beam path of length  $L$ . The optical thickness accounts not only for the absorption coefficient of the EC-wave in a given mode but also for the trajectory of the beam. For typical plasma parameters, one finds  $\Lambda_1^{(O)} \approx \Lambda_2^{(X)} \geq 1$ , meaning that the first harmonic of the O-mode and the second harmonic of the X-mode are optically thick and are well absorbed by the plasma. On the other hand,  $\Lambda_1^{(X)} \approx \Lambda_3^{(X)} \approx \Lambda_2^{(O)} \ll 1$ . The first and third harmonic of the X-mode as well as the second harmonic for the O-mode are optically thin, which means that the 1<sup>st</sup> pass absorption of the associated waves is poor. To overcome this low absorption of the third harmonic, the injection of the X3 beam in TCV is performed vertically, maximizing the path of the beam along the resonance.

---

<sup>2</sup>One can note here that to overcome the density limit, another approach exists and consists of using Electron Bernstein Waves (EBW) which propagate without a density limit [7].

## 1.2 Electron cyclotron waves in ITER

In ITER, 24 gyrotrons located in the RF building will provide 24 MW of EC-power (20 MW injected) at 170 GHz ( $\lambda = 1.76$  mm). EC-power (O1 for the full-field operation phase and X2 for the half field operation phase) will be used for plasma breakdown, heating, current drive and control of MHD activity. The EC-system will be commissioned in four stages [11]. In the first stage, 8 gyrotrons, are needed for the plasma breakdown and burnthrough of the first plasma in ITER with an injected power of up to 6.7 MW for  $\leq 100$  ms. The complete 24 MW system will be installed in ITER for the second stage (first and second campaign) and will be capable of pulse lengths up to 3600 s. In the stages 3 and 4, two upgrades of the system are planned, increasing the installed (injected) power to 28.8 MW (24 MW) and 48 MW (40 MW), respectively. The power from the gyrotrons in the RF building will be transported to the launchers using  $HE_{11}$  corrugated waveguides on a distance of  $\sim 160$  m. Although the initial design for the diameter of the waveguides was 63.5 mm, the diameter was reduced to 50 mm, which provides a better mode purity in the waveguides. The EC-power from the gyrotrons will be redistributed to either the equatorial launcher (EL) or any of the four upper launchers (UL) using switches in the transmission lines (fig 1.3a). The heating and current drive (H&

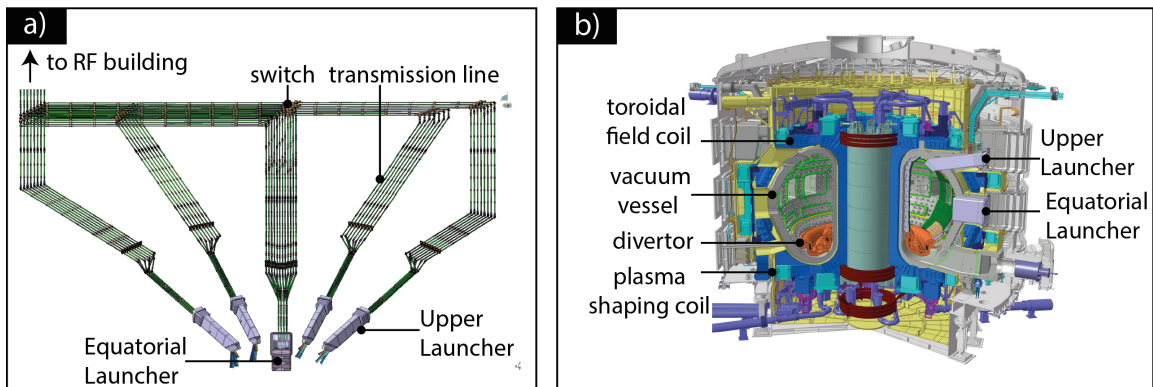


Figure 1.3 – a) Distribution of the EC-power in ITER between the four upper launchers (UL) and the equatorial launcher (EL). Note that the power can be re-distributed between the launchers depending on specific needs using a set of switches. b) 3D view of ITER with the location of the EL and UL ports identified.

CD) applications has been divided between those requiring a ‘narrow and peaked co ECCD deposition’ (UL) and those requiring a ‘broad deposition profile with either co ECCD, counter ECCD, or pure heating (no net driven current)’ (EL) [11]. The UL will provide a narrow co ECCD deposition in the region  $0.4 < \rho < 0.88$  and the EL will provide a broad deposition (1/3 counter ECCD and 2/3 co ECCD) in the region  $0.0 < \rho < 0.6$ . Figure 1.4 summarizes the access range and allocated power for each launcher and the associated H& CD applications. A brief summary of the H& CD applications is given below, more details can be found in [11].

During the plasma initiation, 6.7 MW of EC power (8 gyrotrons, pulse length  $\leq 5$  s) will be used

### 1.3. The case of neoclassical tearing mode stabilisation in ITER

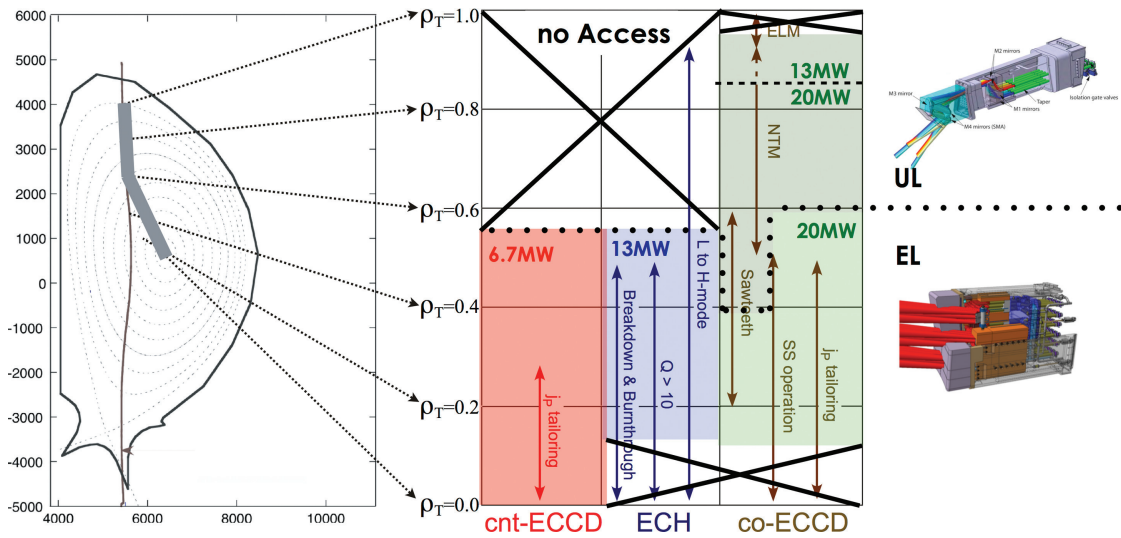


Figure 1.4 – From [11]: ‘The deposition access of the EL [equatorial launcher] and UL [upper launcher] across the plasma cross section and categorized based on driving counter (cnt) ECCD (shaded red), co ECCD (shaded green) or pure heating (shaded blue)’

for plasma breakdown and burnthrough over the range from half (2.65 T, X2) to full (5.3 T, O1) field. To balance the low O1 absorption in the full-field case, a higher second pass absorption will rely on the conversion from the O1 to the X1 mode after reflexion on the central column. This imposes a toroidal injection angle  $< 25^\circ$ . During the ramp-up and the flattop phase the 20 MW of injected power will be distributed over the EL and the UL to perform the following tasks. The EL will provide central heating and bulk current drive ( $\rho < 0.5$ ), as well as plasma current profile tailoring ( $\rho < 0.6$ ) and L to H-mode transition (in combination with other auxiliary heating system). The UL will be responsible for the control of MHD activity such as sawteeth ( $0.2 < \rho < 0.6$ ) and neoclassical tearing modes ( $0.4 < \rho < 0.88$ ).

### 1.3 The case of neoclassical tearing mode stabilisation in ITER

Neoclassical tearing modes (NTMs) are expected to be a major limitation of the performance of ITER in the standard scenario [12, 13]. NTMs are magnetic islands that affect the plasma performance by increasing locally the radial transport [14], limiting the maximum achievable plasma pressure [12]. A local flattening of the pressure profile inside the island causes a perturbation in the bootstrap current (see fig. 1.5). The associated degradation of the energy confinement time  $\tau_E$  can be estimated from the belt model<sup>3</sup> [15] as :

$$\frac{\Delta\tau_E}{\tau_E} = \Delta\tau \frac{w_{sat}}{a}, \quad \text{with } \Delta\tau = 4 \frac{R_s^3}{a^3}, \quad (1.7)$$

<sup>3</sup>The belt model "ignores the helical structure of the magnetic island and replaces it by a belt of uniformly flattened temperature" [15] to estimate the confinement degradation caused by the island.

## Chapter 1. Motivation

where  $w_{sat}$  is the width of the saturated island,  $a$  the minor radius of the plasma,  $R_s$  the radius of the resonant surface. The width of the saturated island can easily reach  $0.1a$  [14]. With such a width, when the mode is located near the mid-radius of the plasma, it induces a  $\Delta\tau_E/\tau_E \sim 5\%$ . A mode located in the outer part of the plasma, at  $R_s/a = 0.8$ , induces a  $\Delta\tau_E/\tau_E \sim 20\%$ . For this reason, NTMs with a poloidal mode number  $m=2$  and  $n=1$  ( $m/n = 2/1$ ) and  $m = 3$ ,  $n = 2$  ( $m/n = 3/2$ ) have to be avoided in ITER, being the most detrimental for the energy confinement. NTMs with higher  $m$  and higher  $n$  are located closer to the center of the plasma and have smaller effect on the energy confinement time [14]. Since the NTMs results from a missing bootstrap current, they can be stabilized by driving current inside the island using ECCD [14].

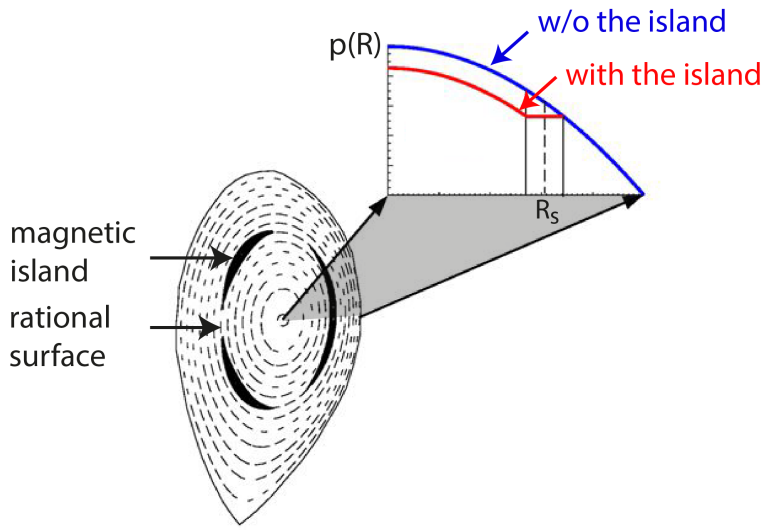


Figure 1.5 – Adapted from [16]: Poloidal cross-section of a diverted plasma illustrating the 3/2 NTM. The dotted lines show the contour of the flux surfaces and the black shaded area the island associated with the NTM. The unperturbed (w/o the island) and the perturbed (with the island) radial profile of the plasma pressure  $p$  on the plasma axis is schematically shown.

The upper-launchers (UL) in ITER were initially designed to be fully dedicated to the suppression of NTMs. A simple stabilization criterion for NTMs was derived by Zohm in [17] from the simplified Rutherford equation to guide the design of the UL as :

$$\eta_{NTM} \equiv \frac{j_{CD}}{j_{bs}} > 1.2, \quad (1.8)$$

with  $j_{CD}$  and  $j_{bs}$  the peak ECCD density and the bootstrap current density, respectively. This criterion is valid when the full-width at  $1/e$  of the ECCD profile  $w_{CD}$  is larger than the marginal width of the island  $w_{marg}$  ( $w_{CD} > w_{marg}$ ) at which the island will stabilize itself and disappear. Another criterion has been proposed by Sauter in [14], for cases where  $w_{CD} \leq w_{marg}$  and

### 1.3. The case of neoclassical tearing mode stabilisation in ITER

was written in [18] as:

$$\frac{w_{CD}j_{CD}}{j_{BS}} > \frac{w_{sat}}{8} \quad (1.9)$$

In order to guarantee the NTM stabilization, the UL will have to provide  $j_{CD}/j_{bs}$  over the entire scanning range determined by the location of the flux surfaces  $q = 2/1, 3/2$  for the ITER scenarios. The UL is also designed to focus the mmw-beam to ensure that the NTM stabilization is still achievable in the case that some gyrotrons are not available or that  $j_{bs}$  is greater than expected [19]. The launcher optics (fig. 1.6) therefore should ensure a focusing of the incident beam to a waist of  $w \approx 20$  mm (the waist here is defined by  $E = E_0 e^{-2(X-X_{beam\ axis})^2/w^2}$ , where  $X$  is the distance transverse to the beam axis) after  $\sim 2$  m propagation from the focusing unit.

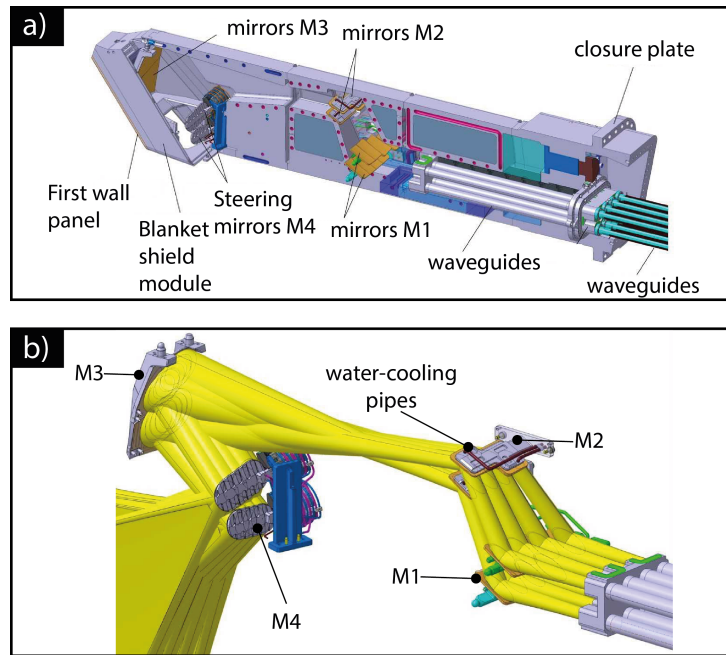


Figure 1.6 – Pictures from A. Sanchez [20]: a) Side view of the ITER upper launcher and its main components. b) Visualization of the paths of the beams (in yellow) launched through the eight waveguides. At the output of mirror 4 (M4), the yellow volume shows the range that the beams can sweep (not the actual beams themselves).

Four UL [21, 20] will be available in ITER (see fig. 1.3a)). Each one of the UL will have 8 beam entries split in two sets of four beams (fig. 1.6a)). The beams are carried from the outside of the vessel through eight 50 mm ex-vessel waveguides isolated thermally from the in-vessel waveguides. The in-vessel optical components of the optical unit consist of a set of water-cooled waveguides and 4 mirrors. Mirror 1 (M1) and 3 (M3) are focusing and mirror 2 (M2) and 4 (M4) are flat surfaces. The  $HE_{11}$  mode of the waveguides couples to Gaussian beams

in vacuum. The beams from the lower row of waveguides are focused by the lower M1 (see fig. 1.6), reflect on the lower M2 on the upper part of M3 where they are focused towards the upper steering M4 mirror (USM). The beams from the upper row of waveguides are focused by the upper M1, reflect on the upper M2 on the lower part of M3 where they are focused towards the lower steering M4 mirror (LSM). The output beam from the USM will access the region of the plasma between  $0.4 \leq \rho \leq 0.8$ . The output beam from the LSM will access the region of the plasma between  $0.6 \leq \rho \leq 0.88$ . Each one of the steering mirror is capable of injecting 3.35 MW of power into the plasma.

### 1.4 Effect of edge density fluctuations on the NTM stabilization in ITER

In the 1980s, it was already estimated that small fluctuations of the plasma electron density associated with the turbulence present at the edge of ITER (and thus of the refractive index of the plasma) could scatter the mmw-beam, leading to changes in the beam power profile [22, 23]. Compared to present days tokamak experiments, in ITER, the long path length of the beam from the focusing mirror to the deposition region in the plasma is expected to accentuate small perturbations of the beam profile occurring at the edge of the plasma. More recently, it was estimated [24] that a turbulent layer (with a width  $\Delta l = 10$  cm) located in the edge of the ITER device, with density fluctuations  $\delta n_e / n_e = 0.1$  and a typical scale length of the turbulent structures  $L_{\perp} = 1$  cm (in the direction transverse to the magnetic field) could broaden the collimated mmw-beam by a factor of two after a 2 m propagation, possibly affecting the NTM stabilization efficiency. Recently, the design of the UL triggered a renewed attention to the detrimental effect of edge density fluctuations on the mmw-beam propagation. The impact of such a broadening on the stabilization of the NTMs in ITER was studied in [3]. It was found that depending on the beam broadening caused by the edge turbulence, the NTM stabilization might not be guaranteed at the present designed use of the EC-power. Figure 1.7 (from [3]) illustrates the latter and shows the power requirement for a complete NTM stabilization (and also for a reduction of the island width to 5 cm) as a function of the deposition profile broadening  $w_{CD} / w_{CD,0}$ , where  $w_{CD}$  ( $w_{CD,0}$ ) is the deposition profile width (nominal deposition profile width), and the deposition misalignment  $x_{mis}$  for the USM and the LSM in ITER.

In the case of no misalignment, a small broadening of the beam (i.e. in the range  $w_{CD} / w_{CD,0} \leq 1.15$  for the USM and  $w_{CD} / w_{CD,0} \leq 1.5$  for the LSM) does not impact the power required for the NTM stabilisation. The power requirement increases for larger beam broadening, since a considerable fraction of the power in this case is misused to drive current outside the island. For instance, a doubling of the width of the deposition profile in the case of the USM leads to a power requirement ( $\approx 17$  MW), which is above the 13.3 MW maximum available power from a given set of mirrors. A further analysis detailed in the same reference shows that the impact of the beam broadening can be considerably reduced by depositing the power using a modulated injection instead of a continuous wave injection.

## 1.4. Effect of edge density fluctuations on the NTM stabilization in ITER

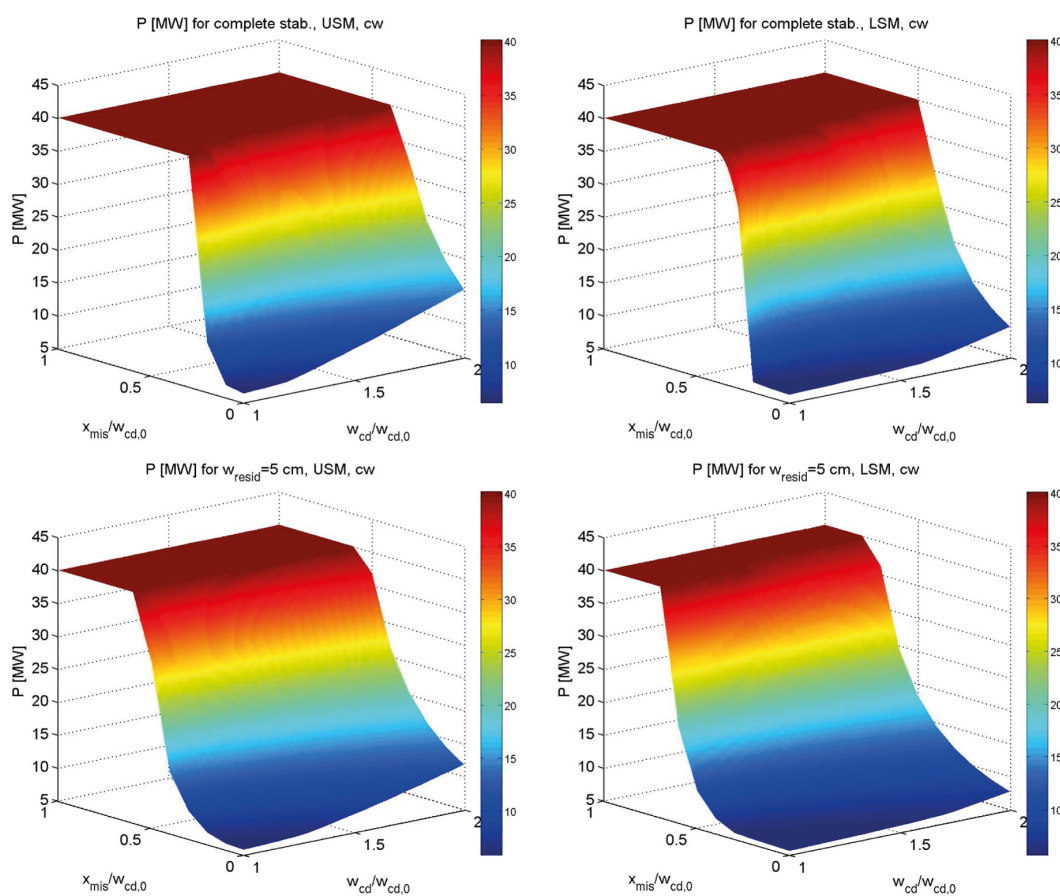


Figure 1.7 – From [3]: ‘Power requirements for complete NTM stabilization (upper row) or reduction of the island width to 5 cm (lower row) as a function of the profile broadening and of the misalignment for the  $q = 2$  surface. The left column refers to the USM, the right one to the LSM. CW [continuous-wave] injection is considered, with  $w_{margin} = 2$  cm [ $w_{margin}$  is the typical island width at which stabilization occurs].’

These recent results show that a reliable estimate of the UL-beam broadening by edge density fluctuations is necessary to verify whether a full stabilization of the NTMs will be possible with the present power availability and injection configuration. A large theoretical effort, based on numerical [25, 26, 27, 28] and analytical studies [29, 30, 31], is ongoing to predict the UL-beam width and guide the use of the launcher.

Three parameters of the edge turbulence are generally identified as the most relevant for estimating the mmw-beam broadening:

- the fluctuation level  $\delta n_e / n_e$
- the width of the turbulent layer  $\Delta l$
- the typical size of the turbulent structures  $L_{\perp}$  transverse to the magnetic field.

## Chapter 1. Motivation

A full-wave study performed by Köhn et al. [27] shows that the beam broadening increases linearly with  $\Delta l$  and quadratically with  $\delta n_e/n_e$  for  $L_\perp = 0.52\lambda$ ,  $\lambda$  being the wavelength of the wave in vacuum.

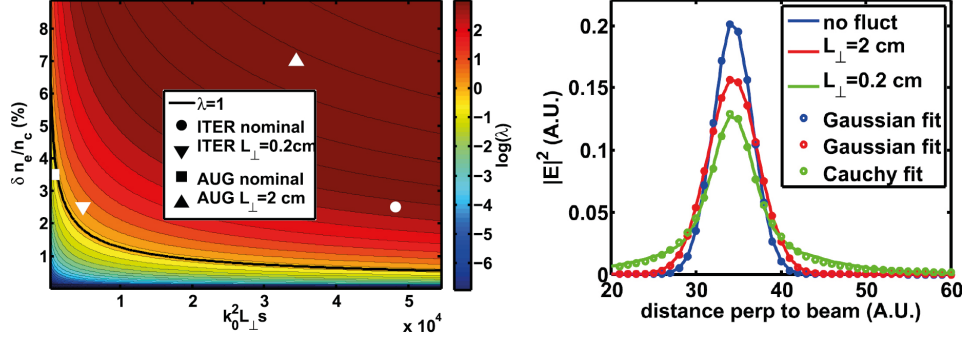


Figure 1.8 – From [25]. Left: ‘Transport regimes in AUG and ITER. Everything below  $\lambda = 1$ , like AUG nominal parameters, is superdiffusive and above, like ITER and AUG modified parameters, is diffusive.’ Right: ‘Shape of the EC beam after the fluctuation layer in ITER with diffusive (red line,  $\delta n_e/n_e = 10\%$ ,  $L_\perp = 2$  cm) and superdiffusive (green line,  $\delta n_e/n_e = 10\%$ ,  $L_\perp = 0.1$  cm) parameters. Gaussian fit is very accurately modeling the diffusive and quiescent beam shape, while Cauchy fit is necessary for super-diffusive parameters with elevated tails.’ [Note that here, unlike in the rest of the thesis,  $\lambda$  is not the wavelength of the beam but a scattering parameter used to determine the diffusion regime. Also,  $s = \Delta l$ ]

An interesting study performed by Snicker et al. in [25] shows that the radiative transport of EC-beams due to scattering from turbulence can be either *diffusive* or *super-diffusive*. The study indicates that a combination of the three parameters mentioned above can lead to either one of the diffusion regimes (diffusive and super-diffusive) for the mmw-beam; each resulting in a particular effect on the mmw-beam profile (see fig. 1.8). In a *diffusive* regime (the one likely to be representative of the case of ITER), the profile of the launched Gaussian beam after scattering by the edge turbulent structures is broadened but remains Gaussian. In the case of a *super-diffusive* regime, the beam profile after the turbulent layer is better fit by a Cauchy distribution. In this case, the beam broadening, measured by the full-width at half-maximum, is smaller, with more power then distributed to the wings of the mmw-beam. The two diffusion regimes are illustrated in fig. 1.8.  $L_\perp$  has been identified as a key parameter for the transition between the two diffusion regimes. Clearly, the characterization of edge fluctuations in ITER will be essential to predict the associated UL-beam broadening.

The predictions for the beam broadening in ITER are still missing experimental validation and a prediction of the turbulence characteristics<sup>4</sup>. The experimental measurements of mmw scattering by blobs in fusion plasmas are, to date, limited to attempts to compare indirectly inferred heating power deposition profiles with predictions of the same using the ray-tracing code TORAY-GA [32]. Direct experimental evidence of scattering and the induced broadening, which is of fundamental importance for the validation of codes and quantitative predictions,

<sup>4</sup>This point will be discussed at the end of this thesis



is still missing.

## 1.5 Outline of the thesis

The aim of this thesis is to investigate the mmw-beam scattering by turbulent structures present at the edge of tokamaks, to show experimental evidence of mmw-scattering by plasma turbulence and provide an experimentally validated numerical tool for the prediction of the EC-beam profile in ITER after propagation through the edge-turbulence.

An introduction to the importance of understanding the mmw-scattering by the edge turbulence in tokamaks and its implications for the design and use of the ITER upper launcher was given in this chapter.

**Chapter 1** introduces the Tokamak à Configuration Variable (TCV) where some of the experiments of this thesis were performed. First, the EC-system in TCV (more precisely the third harmonic system) is described together with the X3 Transmission Diagnostic (X3TD). This latter was installed in the frame of this thesis to measure the high-power mmw-power reaching the floor of the vessel after the propagation through the plasma. Next, we present the main diagnostics used in TCV to characterize both the core and the edge of the plasma.

In **Chapter 2**, we present the TORPEX device, a simple magnetized torus used for the scattering experiments. After describing the device and the HEX TIP-U diagnostic, an array of Langmuir probes used to characterize the time-evolution of the electron density in TORPEX, we present the millimeter-wave injection/detection system [33] installed in the frame of this thesis .

Numerical tools are described in **chapter 3**. The full-wave model for the beam propagation developed in the frame of this thesis is described. A complementary code, WKBeam from Max-Planck-Institut für Plasmaphysik in Garching, is also described. The limitations of the full-wave model are also discussed in this chapter. Finally, we describe the turbulence code GBS used to characterize the scrape-off layer (SOL) in TCV.

In **chapter 4**, we present the first scattering experiments performed in a simple-magnetized toroidal configuration [34], a magnetic configuration characterized by a plasma turbulence similar to the one present at the edge of tokamaks. The typical size of the turbulent structures  $L_{\perp}$  verify  $\lambda/L_{\perp} \sim 1$ . Combining experimental measurements and full-wave simulations based on the experimental electron density profiles, we show that single blobs (elongated filaments of enhanced electron density) have a defocusing effect on the mmw-beam in their wake. We also show that the changes in the detected mmw-power, induced by the propagation of the blob, depend on the position of the blob and that of the detection antenna. Finally, we show that the effect of the blob on the mmw-beam propagation is increased for blobs of higher electron density [35].

Before discussing the scattering experiments in the L-mode configuration in TCV in chapter 6, we show in **chapter 5** that mode activity (here a mode  $m = 1, n = 1$ ) present in the plasma

## Chapter 1. Motivation

---

core can considerably affect the mmw-transmission by deviating the mmw-beam. Here  $L_{\perp}$  associated with the mode rotation is much greater than the wavelength of the wave ( $L_{\perp}/\lambda \gg 1$ ). Using tomographic reconstruction of 2D electron density profile and also its time-evolution in TCV, simulations of the mmw-beam transmission from the full-wave model is compared to the WKBeam code and results from the two codes are found to be in good agreement.

Finally in **chapter 6**, we give experimental evidence that blobs present in the turbulent scrape-off layer of TCV L-mode plasmas scatter the mmw-beam [36]. We show the universality of the observations made in the simple magnetized toroidal configuration. Using the turbulence code GBS and the full-wave model, we successfully reconstruct the effect of a single blob passing through the mmw-beam, benchmarking the full-wave model against the experiment. Combining numerical simulations from the WKBeam and the GBS codes with experimental measurement, we find that the mmw-beam (at the  $z$ -location of X3TD) is 50% broader than the predicted mmw-beam in a non turbulent plasma due to the effect of the edge turbulence.

For better clarity, a list of the symbols and acronyms frequently used in this thesis is given in annex A.

## 2 Tokamak à Configuration Variable

The Tokamak à Configuration Variable (TCV) [37, 38, 39], located at the Swiss Plasma Center is one of the three European facilities which are part of the medium-size tokamak work package (MST-WP) of the EUROfusion Consortium aiming at ‘complementing the work at JET to provide a step-ladder approach for extrapolations to ITER and DEMO [...] covering areas and regimes, where MSTs have unique experimental capabilities and flexibility’ [40]. The TCV tokamak was built to investigate the effect of plasma shaping on tokamak physics, plasma confinement and stability [41]. To host plasmas with extremely high elongation, the vessel is built with a quasi-rectangular poloidal cross section with a ratio height/width $\approx 3$ . We will see later that this extremely elongated rectangular poloidal cross-section enables a long path length for the high power mmw-beam (from the SOL to the detector), similar to the one expected for the upper-launcher beam in ITER (from the SOL to the deposition region). The toroidal field in TCV is produced by 16 toroidal field coil connected in series. They allow for a maximum toroidal field of 1.54 T on axis. The unique shaping capability of TCV is provided by an active feedback system controlling 16 independently-powered shaping coils and 2 in-vessel fast coils; the latter facilitates the stabilization of vertical instabilities with growth rate of  $\sim 10^3 \text{ s}^{-1}$  [41]. Auxiliary plasma heating on TCV can be achieved by neutral beam injection (up to 1 MW) or electron cyclotron heating at the 2<sup>nd</sup> (up to 2.79 MW at 82.7 GHz) and 3<sup>rd</sup> harmonic frequency (up to 1.44 MW at 117.8 GHz). A schematic of TCV is shown in fig.2.1. The main tokamak parameters are given in table 2.1.

Machine parameters		
Major radius	$R_0$	0.88 m
Minor radius	$a_0$	0.25 m
Nominal aspect ratio	$R_0/a_0$	3.5
Magnetic field on axis	$B_0$	$\leq 1.54$ T
Discharge duration		$\leq 2$ s
Plasma parameters		
Core electron density	$n_{e0}$	$1 - 20 \times 10^{19} \text{m}^{-3}$
Core electron temperature	$T_{e0}$	$\leq 1$ keV (Ohmic) $\leq 15$ keV (EC)
Maximum plasma current	$I_p$	1.2 MA
Plasma elongation	$\kappa$	0.9 – 2.8
Plasma triangularity	$\delta$	-0.8 – +0.9
Main ion component		D,H or $\text{H}_e$

Table 2.1 – Plasma and machine parameters in TCV

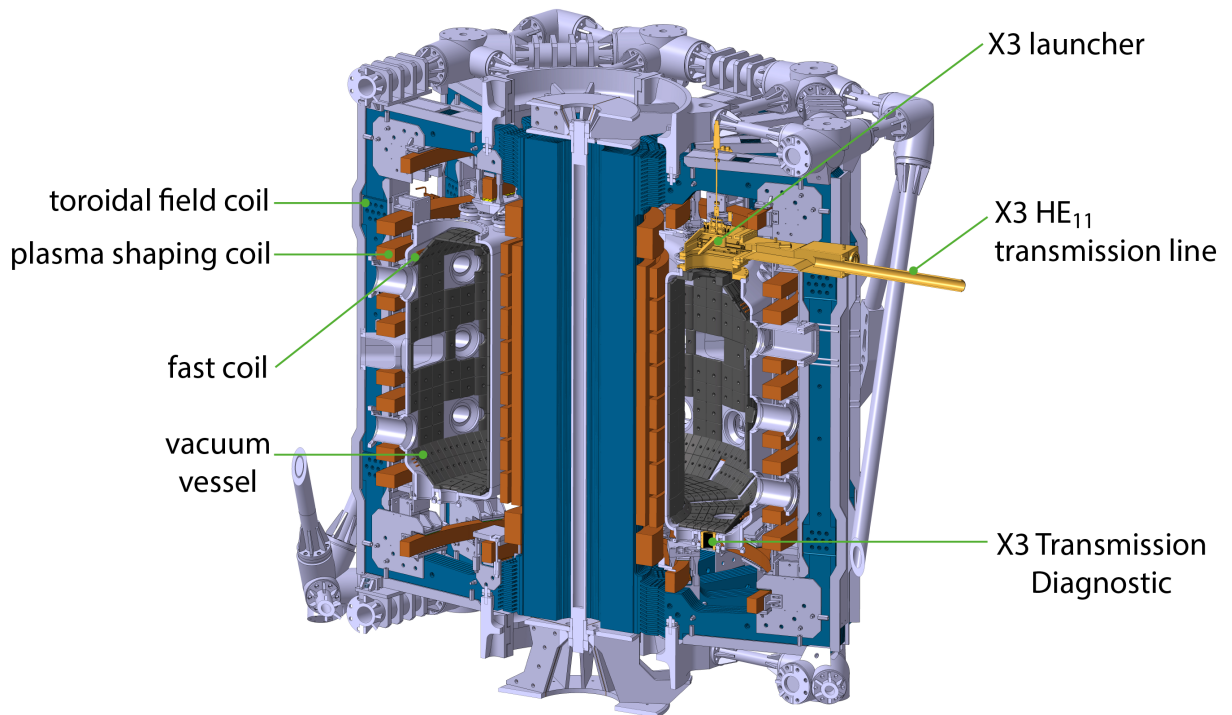


Figure 2.1 – 3D cutaway view of the TCV tokamak

## 2.1 Third harmonic heating system on TCV

The electron cyclotron heating system (ECRH) on TCV is composed of 9 mmw-sources; 6 at the second ( $f = 82.7$  GHz,  $\lambda = 3.63$  mm) and 3 at the third ( $f = 117.8$  GHz,  $\lambda = 2.55$  mm) harmonic of the EC-frequency.

2.1.1 Third harmonic setup on TCV

The third harmonic heating system (generally referred to as the X3 system on TCV, although O-mode polarization can also be generated and will be used in this thesis) consists of 3 gyrotrons operating at 117.8 GHz (gyrotrons 7, 8 and 9) with a nominal power of  $\approx 0.5$  MW each. Pulse lengths of up to 2 s are used in this thesis. The propagation of the mmw-wave from the gyrotron to the TCV vessel is done in an evacuated, 63.5 mm diameter transmission line (TL) made of corrugated waveguides supporting the  $HE_{11}$  mode during an EC-RF pulse. There are no windows separating the torus and the TLs (a gate valve insures the separation between the TL and the torus vacuum outside the EC-RF pulse). A detailed view of the X3 heating system from the gyrotron to the torus is shown in fig. 2.2. The output of the gyrotron

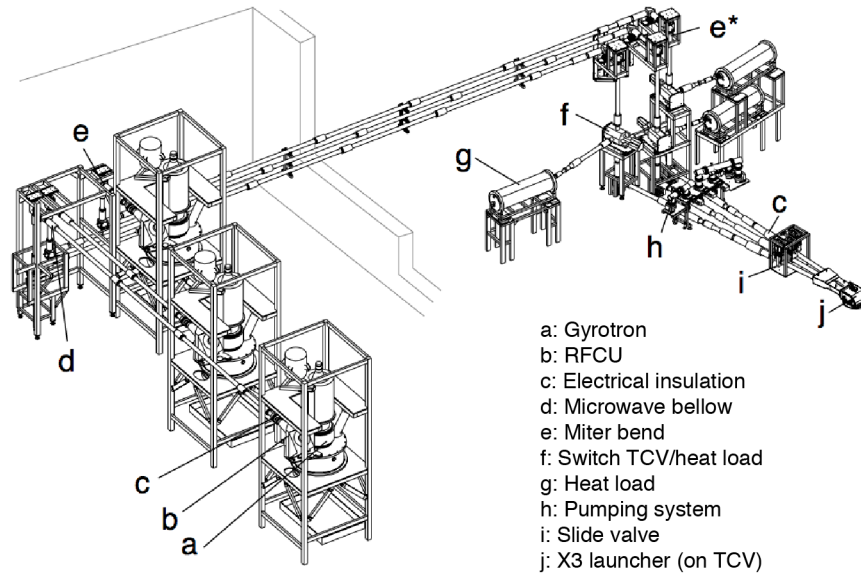


Figure 2.2 – From [42]: Detailed view of the X3 heating system from the gyrotrons to the TCV vacuum vessel.

(a) is connected to the optical conditioning unit RFCU (b). The RFCU is used to control the polarization of the wave electric field and to optimally couple the mmw-beam to the waveguide. The RFCU is composed of two universal polarizers followed by an ellipsoidal mirror. The two polarizers are corrugated mirrors which can rotate around their axis. The polarization of the output electric field used throughout this thesis is linear and its orientation is controlled by the angle formed between the corrugation of the first polarizing mirrors and the linearly polarized gyrotron radiated field [43]. The ellipsoidal mirror focuses the beam at the entrance of the circular waveguide with a focal spot at the waveguide entrance  $w = 0.6435 \cdot d/2$  to maximize the coupling with the  $HE_{11}$  fundamental mode, where  $d = 63.5$  mm is the diameter of the waveguide. The waveguides transmit the mmw-power from the RFCU to the TCV vessel, over a distance of  $\approx 30$  m on average. For this reason, the inner surface of

the waveguides is corrugated to reduce the surface currents, and thus reduce the associated ohmic losses. Along its path, the mmw-wave is reflected by right-angled bends, called Miter bends (e). Besides changing the orientation of the mmw-wave, one of the Miter bends allows the measurements of both the transmitted and reflected mmw-wave in the waveguides (e\*) via multihole directional couplers. At the end of the waveguide, the  $HE_{11}$  mode is coupled to the fundamental  $TEM_{00}$  mode (Gaussian beam) and injected in the TCV vessel using the launching mirror. A more extensive description of the X3 heating system on TCV can be found in [42].

In this thesis, we will focus on measurements performed with gyrotron number 8. The reason for this choice is that its mmw-power is injected inside the vessel using the central transmission line (fig. 2.2) and offers the best radial alignment in vacuum with the X3 transmission diagnostic X3TD (see section 2.1.2) when injected at  $R_m = 0.88$  m, defined below.

### X3 launcher

A downtaper (diameter 63.5 – 59.2 mm) is placed at the end of the TL shown in fig. 2.3. After exiting the downtaper, the mmw-beam is best approximated by a circular cross-section Gaussian beam with a waist of  $w_0 = 19.05$  mm. The distance between the waveguide end and the mirror, when the mirror is located at  $R_m = 880$  mm, is  $d_1 = 727.5$  mm. For an arbitrary position  $R_m$  of the mirror,  $d_1 = 727.5 + (880 - R_m)$  mm.

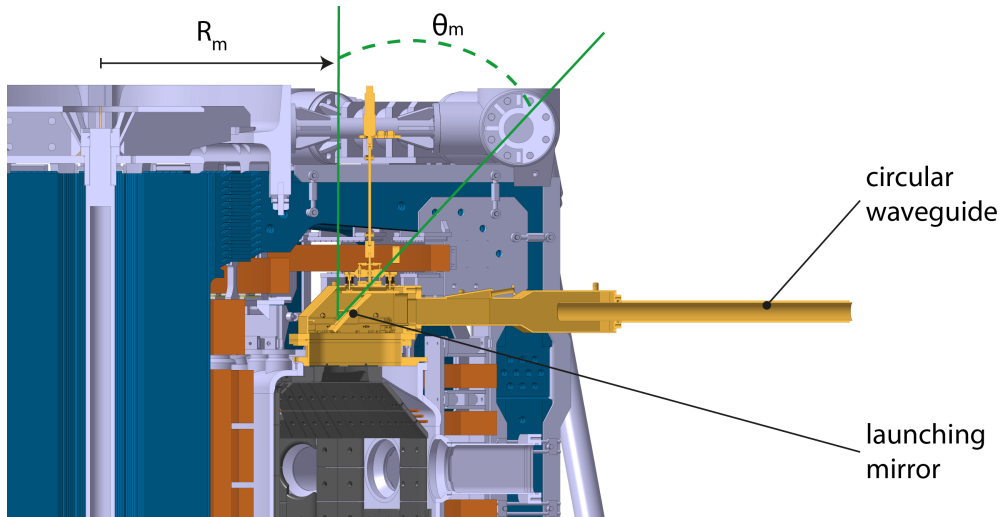


Figure 2.3 – Schematics of the X3 launcher.

The mirror is a rectangular-shaped toroidal mirror (radius of curvature:  $R_{pol} = 1342$  mm and  $R_{tor} = \infty$ , in the poloidal and toroidal direction respectively) made of Oxygen-Free High Conductivity (OFHC) copper. After reflection on the mirror, the mmw-beam is astigmatic and has an ellipsoidal cross-section. It is focused in the poloidal direction but continues expanding in the toroidal direction. A schematic of a cross-section of the mmw-beam together with the

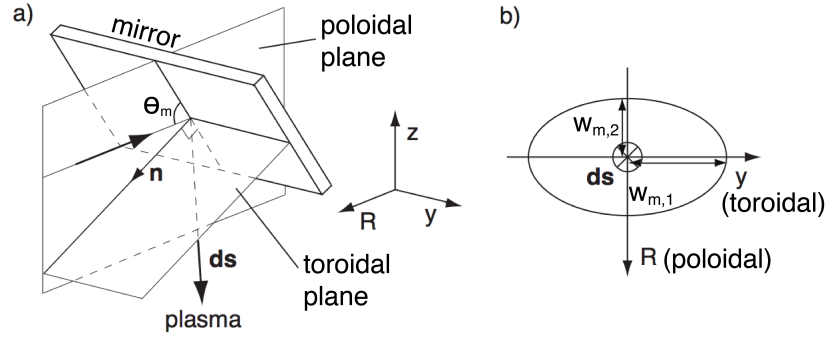


Figure 2.4 – From [42]: a) Schematic of the injection configuration of the X3 beam with the definition of the toroidal and poloidal plane. b) Schematic of the mmw-beam in a plan perpendicular to its direction of propagation  $d\mathbf{s}$ .

injection configuration is shown in fig. 2.4. The original launcher mirror was redesigned and replaced in 2012. The focal length  $f_i$  of the new mirror in the quasi-poloidal ( $i = 1$ ) and quasi-toroidal ( $i = 2$ ) direction has been recomputed and documented by S. Coda in an internal report in 2012 given in Appendix C:

From the knowledge of  $f_i$  we can deduce the waist at the mirror  $w_{m,i}$  together with the focal distance  $d_{m,i}$  between the mirror and the output beam waist in the two directions.

$$w_{m,i} = \sqrt{\frac{w_0^2 f_i^2}{(d_1 - f_i)^2 + \pi^2 w_0^4 / \lambda^2}} \quad (2.1)$$

$$d_{m,i} = f_i + f_i^2 \frac{d_1 - f_i}{\pi^2 w_0^4 / \lambda^2 + (d_1 - f_i)^2}. \quad (2.2)$$

Defining the Rayleigh length  $Z_R = \frac{\pi w_0^2}{\lambda}$ , the curvature radius  $R_{c,i}$  of the wavefronts of the beam in the quasi-toroidal and poloidal planes ('quasi' because the beam direction,  $d\mathbf{s}$ , is slightly out of the usual toroidal and poloidal planes of the tokamak ( $< 5^\circ$ )) as:

$$R_{c,i} = d_{m,i} \left( 1 + \frac{Z_R^2}{d_{m,i}^2} \right). \quad (2.3)$$

The beam parameters are always defined in the direction perpendicular to the direction of propagation  $d\mathbf{s}$ . Numerically, the beam parameters projected onto the radial and  $y$ -direction are negligibly different from those described here. The poloidal launching angle of the mirror  $\theta_m$  (see fig. 2.3 for its definition) can be swept during the shot over any region between  $40^\circ$

and  $50^\circ$ ; the radial position  $R_m$  of the mirror is set before the shot to a value ranging between 0.82 and 0.96 m. Figure 2.5 shows the position of the mirror inside the TCV vessel at three radial positions  $R_m = 0.83, 0.88$  and 0.96 m (looking upwards from the midplane).

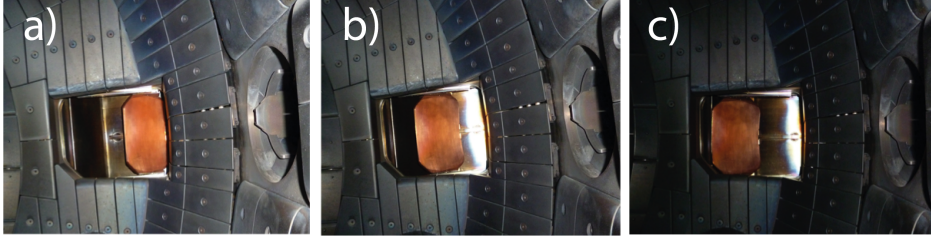


Figure 2.5 – Pictures of the X3 mirror from the bottom of the TCV vessel for  $R_m = 0.96$  m (a),  $R_m = 0.88$  m (b) and  $R_m = 0.83$  m. (c)

### 2.1.2 X3 transmission diagnostic

The X3 transmission diagnostic (X3TD) is the key diagnostic which was developed during this thesis to measure the transmitted power profile on the vacuum vessel floor injected via the X3 launcher at 117.8 GHz. The main initial objectives of X3TD were to perform characterization of the beams from the 3 gyrotrons in vacuum, as well as to carry out direct absorption and scattering measurements. In this thesis, as previously mentioned, only one gyrotron ( $n^o$  8) is used and the studies are focused on scattering measurements. X3TD is installed in TCV in port B01A 2 (TCV vacuum vessel floor) in sector 1. The port is centered at  $R = 0.88$  m and has a diameter of 100 mm. The location of the diagnostic is shown in fig. 2.1 and fig. 2.6 (bottom of the vessel). X3TD takes advantage of the good coupling of a Gaussian beam in the far field to an  $HE_{11}$  waveguide. The receiving antenna (X3TD) is not movable but the launching antenna (the launching mirror) allows sweeping of the mmw-beam across X3TD. In this section, we describe the main components of the X3TD diagnostic, in-vessel and ex-vessel. We also discuss the in-vessel alignment of the mirror as well as the *in-situ* calibration-transmission measurements performed in vacuum on the mmw-beam from gyrotron 8.

#### In-vessel components

The in-vessel components of X3TD are shown in fig. 2.6. They consist of an  $HE_{11}$  corrugated graphite waveguide, topped with an attenuating cap ( $\approx -57$  dB), placed between the bottom of the tiles and a vacuum tight sapphire window. The  $HE_{11}$  waveguide and attenuating cap were designed to handle the heat flux from the three 500 kW heating beams (3 gyrotrons for 2 s) while protecting the vacuum window and insuring an optimum coupling between the high-power mmw-beams and the fundamental  $HE_{11}$  mode of the waveguide. As mentioned earlier, in our experiments we use only the central beam, but the diagnostic must survive during all possible TCV experiments. In order to handle the high heat-flux associated with the incident mmw-beam, the front end of the X3TD detector is made in graphite. In an internal



## 2.1. Third harmonic heating system on TCV

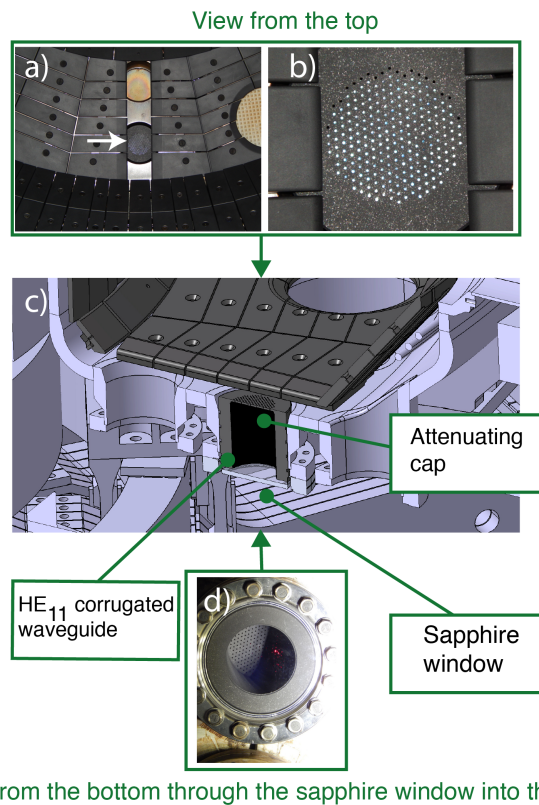


Figure 2.6 – In vessel components of the X3 transmission diagnostic. A corrugated  $HE_{11}$  waveguide with an attenuating cap is placed behind the tiles to protect the vacuum-sapphire window. a) Picture of the floor of the TCV vessel viewed from above. The X3TD is placed behind the tiles and is identified by the white arrow. b) Zoom on the attenuating cap of X3TD. The cap is made of 241 holes of diameter 1.2 mm. c) 3D cutaway view of the in-vessel components of X3TD integrated in the TCV vessel. d) Picture of the X3TD in-vessel waveguide from the bottom through the vacuum sealing sapphire window.

design work, a COMSOL-based simulation run by B. Sudki showed that, assuming no thermal losses, the maximum temperature of the carbon surface heated by the high-power mmw-beam after 2s is  $\approx 713^\circ$ . Although this temperature is far below the sublimation point of carbon, such a long high-power exposition to high mmw-power could result in stresses on the attenuating cap close to the elastic limit. For this reason, long vacuum pulses should be avoided. The outer diameter of the waveguide is set to 98.1 mm to fit within the 100 mm diameter port and to allow the alignment with the port using circular aligning springs fitting into the groves on the outer waveguide diameter. This also prevents mmw-power from reaching the window.

The attenuating cap of the waveguide is made of 241 circular holes with diameter  $d = 1.2$  mm (fig. 2.6). The incoming mmw-beam reformes after attenuation by diffraction from the holes into the waveguide. The spacing between the holes is 3.6 mm, value chosen to avoid the weakening of the cap when submitted to heat stresses. Ideally, a spacing smaller than  $\lambda = 2.55$  mm (wavelength of the beam) should be used to ensure a better excitation of the

$HE_{11}$  waveguide in the waveguide. Each circular hole act as a cylindrical waveguide with a cut-off frequency for the fundamental  $TE_{11}$  mode of  $f_c = 146.4$  GHz. The incoming wave at 117.8 GHz is therefore evanescent in the attenuating cap and the level of attenuation is tuned by the machining thickness of the cap. The thickness of the cap is set to 2.5 mm which results in an attenuation level of  $\approx -57$  dB. The measurements of the transmission ( $S_{21}$ ) and reflection ( $S_{11}$ ) parameters of the waveguide were made (and are shown in fig.2.7), using an Agilent N5224A network analyser (PNA), Virginia Diodes WR 6.5 extension heads and and a Thomas Keating optical table with appropriate coupling mirrors. The transmission parameter  $S_{21}$  for a 2.5 mm thickness of the cap in the range 110 – 140 GHz is 6.26 dB higher than calculated, but will sufficiently attenuate the power to protect the window while at the same time provide good signal to noise ratio. The transmission parameter is found to be independent of the orientation of the waveguide. The cross-polarization of the measured field after coupling to the graphite waveguide is  $-35$  dB, the limit of the sensitivity of the system; therefore, the input polarization is preserved.

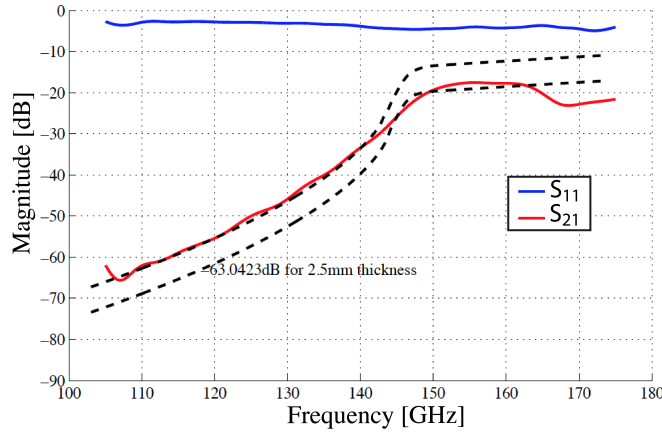


Figure 2.7 – S-parameters of the front-end graphite waveguide.  $S_{11}$  and  $S_{21}$  are the reflection and transmission coefficient respectively. At 117.8 GHz, the attenuation is  $\approx -56$  dB. The lower black-dotted line corresponds the calculated attenuation of the X3TD waveguide. It is shifted by 6.26 dB upwards (upper black dotted line) to match the experimental measurements.

The vacuum window (thickness  $d = 4.16 \pm 0.03$  mm) is made of sapphire, which is transparent to incoming mmw-waves at 117.8 GHz. The  $S_{11}$  (reflection) and  $S_{21}$  (transmission) parameters of the window in the frequency range 110 – 170 GHz are shown in fig. 2.8. One of the transmission maximum occurs around 117.8 GHz and has an attenuation level of 0.27 dB. A minimum in the reflexion occurs every  $\Delta f = 11.8$  GHz (see fig. 2.7). From these measurements, we can deduce the relative permittivity  $\epsilon_r$  of the window

$$\epsilon_r = \left( \frac{c}{2\Delta f d} \right)^2 = 9.3, \quad (2.4)$$

from which we confirm the sapphire composition of the window.

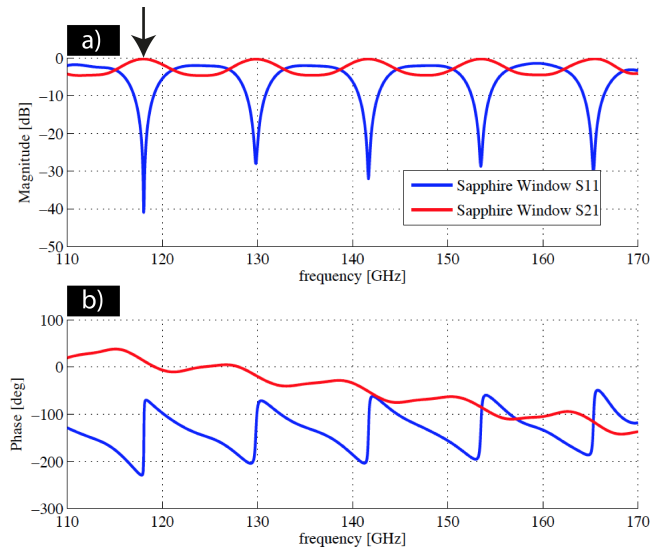


Figure 2.8 – Magnitude (a) and phase (b) of the S-parameters of the sapphire window. The 117.8 GHz of the X3 gyrotrons in TCV is indicated by the black arrow. The window has a maximum of transmission at 117.8 GHz.

### Ex-vessel receiver

The ex-vessel part of the X3TD (fig. 2.9) consists of an aluminum corrugated  $HE_{11}$  waveguide of diameter 63.5 mm (insulated from the TCV vessel using a DC-break), a horn-lens antenna focusing the mmw-power to a circular-to-rectangular transition and a WR6 (110 – 170 GHz) Schottky diode detector (SDD) from Farran LTD (reference FTL1665B until 02/2018 and then FTL1692B from *discharge* 60045). To avoid the creation of a stationary wave inside the  $HE_{11}$  waveguide, between the rectangular fundamental  $TE_{10}$  waveguide and the attenuator cap, an absorbing foam ( $\approx -20$  dB attenuation) is placed across the waveguide at one of the joints between components. The orientation of the detector relative to the magnetic field (O-mode or X-mode) is achieved by rotating the circular waveguide such that the  $TE_{10}$  fundamental mode of the rectangular WR6 waveguide (cross-section  $\approx 1.6 \times 0.8$  mm, placed before the SDD) is oriented in either one of the two directions.

### Mmw-beam measurements in vacuum

The mmw-beam from gyrotron 8 is swept across the detector to calibrate the beam in vacuum. To avoid damaging TCV diagnostics, the mmw-beam is pulsed using 2.5 ms pulses. The transmitted power is shown in fig. 2.10a). The normalized power can be fit by a Gaussian

profile  $e^{-2 \frac{(\theta_m - \theta_0)^2}{w_\theta^2}}$  with  $\theta_0 = 45.39^\circ$  and  $w_\theta = 0.89^\circ$ .

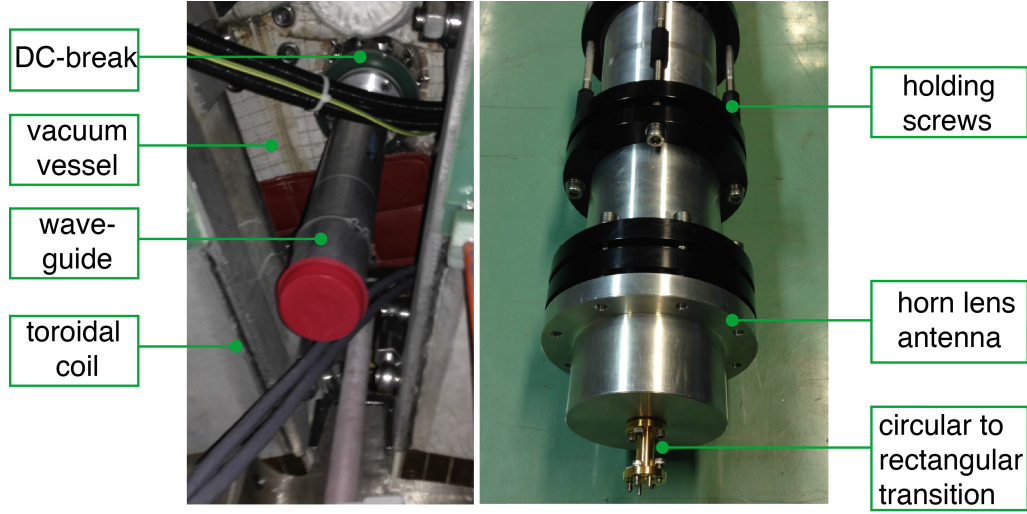


Figure 2.9 – Ex-vessel part of the X3TD receiver. On the left, a circular waveguide is aligned with the sapphire window and connected to the vessel using a DC break. The red plastic cover was temporarily placed during the installation and is at the joint location where the absorbing foam is. On the right, the horn lens antenna is used to focus the mmw-power from a diameter of 63.5 mm down to the WG 5.9 waveguide (with a measured cut-off frequency of 117.6 GHz). A circular-to-rectangular transition couples the  $TE_{11}$  mode of the small mono-mode circular waveguide to the  $TE_{10}$  mode of the rectangular waveguide connected to the SDD.

Around 45.2 deg (shaded area in fig. 2.10b), the experimentally measured transmitted power significantly deviates from a Gaussian. At these injection angles, a fraction of the injected power is reflected back into the transmission lines of the gyrotron and disturbs its operation. The distortion of the pulse measured by X3TD caused by the perturbed operation of the gyrotron is shown in fig. 2.10a).

The measurements are compared to full-wave simulations (described in chapter 4). We define a synthetic diagnostic for the power measurement of X3TD (see [36]) by

$$P_{syn} \propto \frac{1}{d_{diag}} \int_{X3TD} |E|^2 G(R) dR, \quad (2.5)$$

where  $G(R)$  is the transfer function of X3TD (defined in the following) and  $d_{diag}$  the diameter of the  $HE_{11}$  waveguide along the major radius  $R$ . We suppose that all the power going through the  $HE_{11}$  waveguide is measured by the SDD and therefore we consider that X3TD can be modeled by an attenuating cap placed on top of an  $HE_{11}$  waveguide of diameter  $d_{diag} = 63.5\text{mm}$ . The best-fit gaussian profile for the  $HE_{11}$  mode of the waveguide, which has a diameter  $d_{diag} = 63.5\text{ mm}$ , is  $e^{-2\frac{(R-R_0)^2}{0.02^2}}$  where  $R$  and  $R_0$  are measured in m. We thus use  $G(R) = Ae^{-2\frac{(R-R_0)^2}{0.02^2}}$ , where A is a coefficient of attenuation. The beam waist and curvature

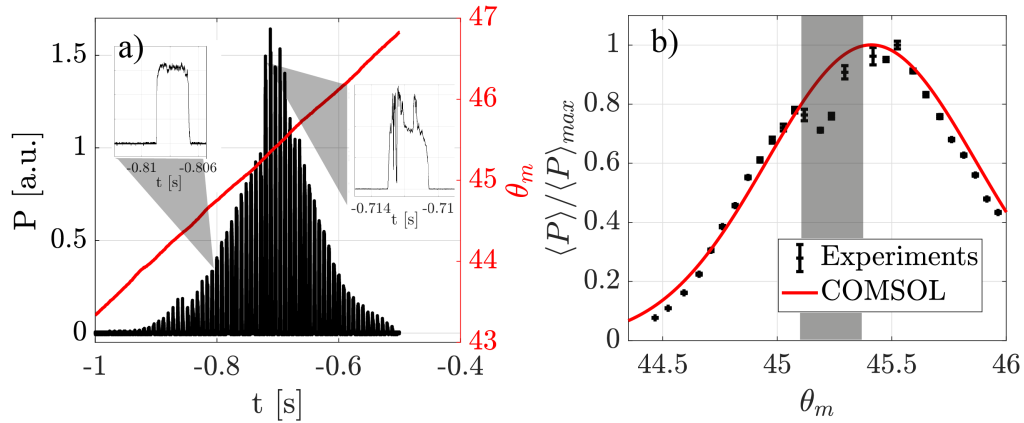


Figure 2.10 – a) Detected mmw-power during a scan of the poloidal angle  $\theta_m$  of the injection mirror ( $R_m = 0.88$  m) and zoom on two pulses. The zoomed pulse located at the left of the figure is a pulsed measured during the normal operation of the gyrotron. The zoomed pulse on the right shows a perturbed operation of the gyrotron caused by partial reflection of the mmw-power back to the gyrotron. b) The experiments are compared to full-wave numerical simulations (see chapter 4). For the angles in the shaded areas, a fraction of the injected power is reflected back to the gyrotron, significantly deviating the correspondent measurements from the Gaussian profile.

radius of the wavefronts of the wave are computed using the formulas described previously (eq. 2.2 and 2.3). The comparison for the scan of  $\theta_m$  in vacuum from both the full-wave simulations and the experiments are shown in fig. 2.10. Despite many efforts to calibrate the X3 mirror both in free space and via plasma absorption – with comparison to beam tracing codes – an offset of  $0.39^\circ$  in the experimental  $\theta_m$  has been taken into account to provide the good match between the experimental and numerical profiles shown in fig. 2.10.

In this section we have presented the “Tokamak à configuration variable” together with the X3 high power mmw-system used in the scattering experiments in this thesis. We then presented and characterized the X3 transmission diagnostic which is used to measure the transmitted power reaching the floor of the vessel and coupling to a 63.5 mm diameter  $HE_{11}$  cylindrical waveguide. A synthetic diagnostic was also implemented in the full wave model (see chapter 4). Free-space numerical simulations compare well to the experiments.

## 2.2 Diagnostics for the plasma core

In this section, we will present the main TCV-diagnostics used in this thesis to characterize the confined plasma region ( $0 < \rho < 1$ ).

### 2.2.1 Thomson scattering

The Thomson Scattering (TS) [44] diagnostic is an essential diagnostic in the TCV operation. It is the main diagnostic used in the machine to reconstruct electron density and temperature profiles in the plasma. The TS consists of three Nd:YAG lasers emitting 1.5 J of energy at  $\lambda_0 = 1.064 \mu\text{m}$  with a repetition rate of 20 Hz and a pulse length of 10 – 12 ns. The vertical spatial resolution varies between 6 – 12 mm. For high density, high temperature plasmas, the three lasers are used with an independent triggering, increasing the repetition rate to 60 Hz. The lasers are injected vertically at a radial position of  $R = 0.9 \text{ m}$ .

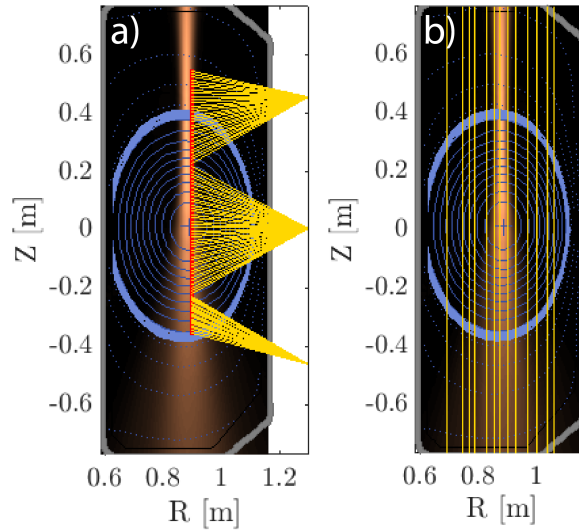


Figure 2.11 – Viewlines of the Thomson Scattering diagnostic (left) and the Far Infrared Interferometer (right) diagnostic. The copper-shaded area represents the electric field norm of the high-power mmw-beam as computed using full-wave simulations. The contours represent the flux surfaces and the blue shaded area covers the region of the SOL between the LCFS and the location where the density has dropped to half the value that it has at the LCFS.

The principle of the TS is the following: electrons are accelerated in the laser electric field and re-emit radiation. The light from the lasers is thus scattered by the free electrons in the plasma and is collected by 3 wide-angle camera lenses installed on three horizontal ports on which are installed 96 spectrometers (the lines of sight are shown in fig. 2.11a). If the wavelength of the laser is small compared to the Debye length, we speak of incoherent TS since the light emitted is not coherent.

Because of the thermal distribution of the electrons, the measured light emission has a broader spectrum than the lasers. The spectrum is increasingly shifted to lower wavelength as the electron temperature increases due to the Doppler shift associated with the electron speed. Assuming a Maxwellian velocity distribution of electrons  $f_k(v)$  with thermal velocity  $v_t = \sqrt{2T_e/m_e}$ ,  $T_e$  being the electron temperature:

$$f_k(v) = n_e \frac{1}{\sqrt{\pi}} \sqrt{\frac{m_e}{2T_e}} e^{-\frac{m_e v^2}{2T_e}},$$

and its spectral form factor

$$S(\mathbf{k}, \omega) d\omega = \frac{1}{\sqrt{\pi}} \frac{1}{k v_t} e^{-\left(\frac{\omega}{k v_t}\right)^2} d\omega,$$

The scattered power  $P_s$  within a solid angle  $d\Omega$  and spectral bandwidth  $d\omega$  can be written as:

$$\frac{d^2 P_s}{d\omega d\Omega} = r_e n_e P_i L |\Pi \cdot \mathbf{e}_i|^2 S(\mathbf{k}, \omega)$$

$n_e$  is the electron density,  $r_e = \frac{e^2}{4\pi\epsilon_0 m_e c^2}$ ,  $P_i$  is the incident power of the laser,  $\mathbf{e}_i$  is the unit vector associated with the electric field and  $P_i$  is an operator defined as  $\Pi = \mathbf{s} \times (\mathbf{s} \times \dots)$  with  $\mathbf{s}$  the direction of observation.  $T_e$  is obtained from the width of the spectrum (at 1/e)  $\Delta\omega_{1/e} = k \sqrt{\frac{2T_e}{m_e}}$  and  $n_e$  from the total scattered power  $\int P(k, \omega) d\omega$  which is proportional to  $n_e$ . In practice, the electron density measured profiles are calibrated against the far infrared interferometer measurements described in section 2.2.2.

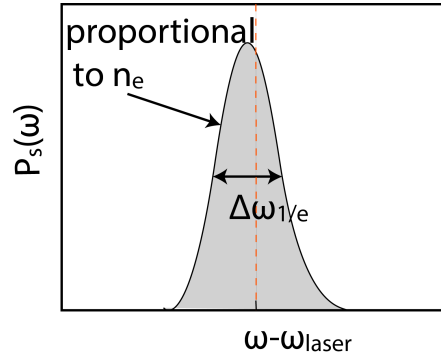


Figure 2.12 – Schematic spectrum of the scattered power and relevant quantities for the determination of  $T_e$  (from  $\Delta\omega_{1/e}$ ) and  $n_e$  (from the surface black shaded area)

Spectral filters are installed to crudely reconstruct the spectrum of the emitted light. An example of TS scattering spectrum (here,  $T_e = 2$  keV) is shown in fig. 2.13 and compared to the spectral bandwidths of the spectrometer filters.

A comparison of the measured response of the spectrometer is compared to a database of pre-calculated spectra. The electron  $T_e$  is then attributed by solving a maximum likelihood problem. More details on the hardware and data analysis techniques can be found in [45].

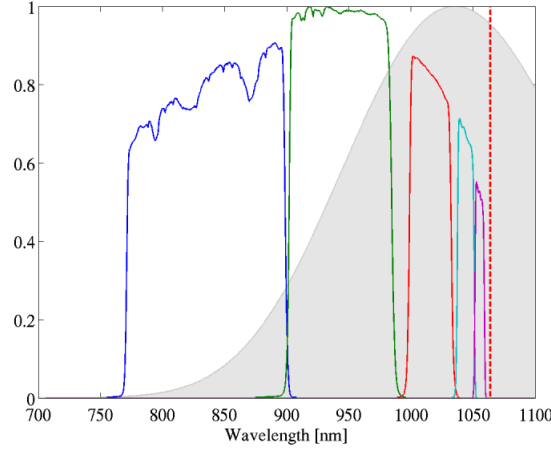


Figure 2.13 – [From P. Blanchard]: normalized Thomson scattering spectra for  $T_e = 2$  keV (grey surface) with the 5 spectral filter sensitivity (blue, green, red, cyan and magenta curves) of a typical 5-channel spectrometer. The dashed red line indicates the 1064 nm YAG laser.

### 2.2.2 Far infrared interferometer

Interferometry is a wide-spread measurement technique used in tokamaks. This is due to the fact that interferometry provides an absolute-calibration of electron density by measuring the path-length differences between a reference beam and a beam subjected to a varying refractive index  $N$ . In TCV, the Far Infrared Interferometer (FIR) uses the principles of the Mach-Zehnder interferometer and consists of a continuous laser emitting at  $184.3 \mu\text{m}$  and a multi-element detector unit using InSB hot-electron bolometers in a helium cryostat. The beam is split into 14 chords and injected into the vessel with the polarization parallel to the magnetic field. The FIR chords have a diameter of  $\approx 20$  mm at the radial locations shown in fig. 2.11.

In these O-mode conditions, the refractive index of the plasma is a simple function of the electron density :

$$N = \sqrt{1 - \frac{\omega_p^2}{\omega^2}}, \quad (2.6)$$

The net phase shift between the reference beam and the beam passing through the plasma is given by:

$$\Delta\Phi = \Phi_{ref} - \Phi_p = \frac{\omega}{c}(L_{ref} - L) - \frac{1}{\omega^2} \int_{\Delta_z} \omega_p^2(z) dz, \quad (2.7)$$



where  $\phi$  ( $\phi_{ref}$ ) is the phase of the probing (reference) beam,  $L$  ( $L_{ref}$ ) the distance covered by the (reference) beam and  $\Delta z$  is the path of the beam in the plasma. If the two distances are equal then the difference in the phase between the two signals is only due to the refractive index of the plasma. In this case, the net phase shift is given by:

$$\Delta\Phi = \int_{\Delta z} k dz = \int_{\Delta z} N \frac{\omega}{c} dz, \quad (2.8)$$

where  $\omega$  is the angular frequency of the wave. Introducing eq. 2.6 in eq. 2.8, the phase shift can be written as:

$$\Delta\Phi = \frac{\omega}{c} \int_{\Delta z} \left[ \left( 1 - \frac{n_e}{n_c} \right)^{\frac{1}{2}} - 1 \right] dz. \quad (2.9)$$

Here we have introduced the cutoff density  $n_c = m_e \epsilon_0 \omega^2 / e^2$ . If the electron density in the plasma is small compared to the cutoff density ( $\frac{n_e}{n_c} \ll 1$ ), we can re-write:

$$N \approx 1 - \frac{1}{2} \frac{n_e}{n_c}, \quad (2.10)$$

and the beam path is essentially unaffected by refraction so the geometrical path is a straight line. With these assumptions, the phase shift is :

$$\Delta\Phi = \frac{\omega}{c 2 n_c} \int_{\Delta z} n_e dz, \quad (2.11)$$

which is directly proportional to the line integrated-electron density along the beam path.

Signals from the FIR are acquired with a sampling frequency of 100 kHz, lower than the maximum frequency response of the detector (750 kHz). The electron density is measured with an accuracy of  $\sim 5 \times 10^{-17} \text{ m}^{-3}$ .

### 2.2.3 Soft X-ray diagnostics

Soft X-ray diagnostics in tokamaks measure soft X-ray emission from the plasma. A brief recall of the basics of radiation emission observed in plasmas is given. Radiation emission from the plasma originates from the following processes:

## Chapter 2. Tokamak à Configuration Variable

---

- Bremsstrahlung radiation is dominated by small angle scattering of electrons in the electric field of the ions. It is a result of the deceleration of the electrons when they are scattered by the ions. The lost kinetic energy is emitted as a radiation. Bremsstrahlung is also called a free-free radiation since both the initial and final energy states of the electron is free. The Bremsstrahlung produces a continuum spectrum of radiation.
- Recombination radiation is another important contribution to the continuum spectrum of radiation. Recombination radiation occurs during the collision of an electron and an ion of the plasma in which the final state of the electron is bound.
- Line radiation is a discrete emission arising when a bound electron in an excited energy state  $E_{p1}$  drops to a lower energy state  $E_{p2}$ , emitting a photon of energy  $E = h\nu = E_{p1} - E_{p2}$ .
- The electron cyclotron radiation originates from the gyration of the electrons around the magnetic field. The emission occurs at harmonics of the electron cyclotron frequency  $f_{EC} = \frac{eB}{2\pi m_e}$ . In magnetically confined fusion devices, electron cyclotron emission occurs in the mmw range of frequencies.

In TCV low- $Z_{eff}$  (definition given below) hot plasmas, the main contribution to the measured soft X-ray spectrum comes from the Bremsstrahlung and the recombination radiation. The line radiation is strongest at the ultra-soft X-ray energies and can be detected by spectrometry techniques, but is essentially eliminated by the filters used in the diagnostics described below. The intensity  $I(\omega)$  of the soft-X ray in the plasma emission resulting from Bremsstrahlung and recombination radiation depends upon  $n_e$  and  $T_e$  in the following way [46]:

$$I(\omega) = 1.5 \times 10^{-38} \times n_e^2 Z_{eff} \frac{e^{-\frac{h\omega}{T_e}}}{\sqrt{T_e}} \quad [W \cdot m^{-3} \cdot eV^{-1}], \quad (2.12)$$

where:

$$Z_{eff} = \frac{\sum_i n_i Z_i^2}{\sum_i n_i Z_i}; \quad (2.13)$$

the sum being performed over the ion species of the plasma.

In TCV, the two main diagnostics for the soft X-ray emission are the multi-camera soft X-ray tomographic system (XTOMO) and the single-camera Duplex Multiwire Proportional X-ray counter (DMPX).

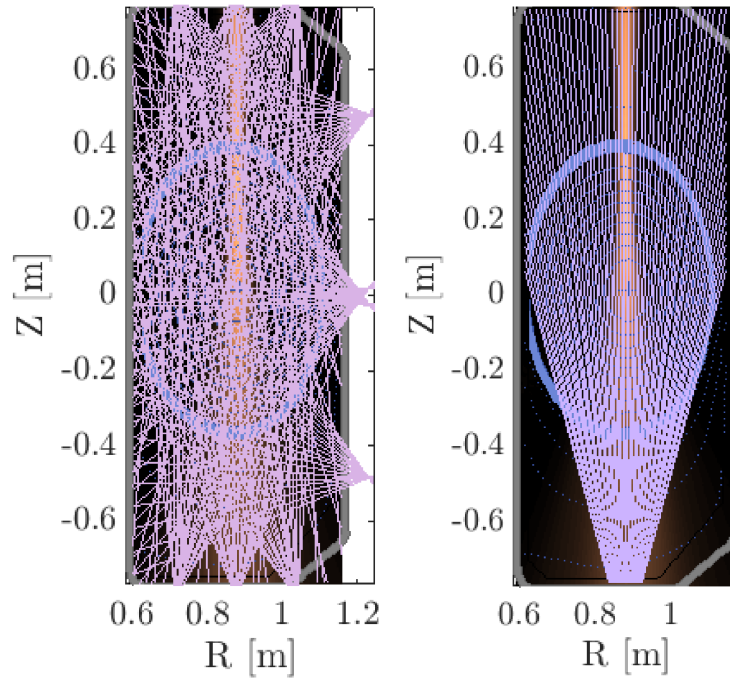


Figure 2.14 – Viewlines of the XTOMO diagnostic (a) and the DMPX detector (b). The copper-shaded area represents the electric field norm of the high-power mmw-beam. The contours represent the flux surfaces and the blue shaded area covers the region of the SOL between the LCFS and the location where the density has dropped to half the value that it has at the LCFS.

### Soft X-ray tomographic system (XTOMO)

The XTOMO diagnostic on TCV is a soft X-ray tomographic system. Its spectral sensitivity ranges from 1 – 10 keV and the signals are acquired with a sampling frequency of 100 kHz. The XTOMO diagnostic consists of 10 pinhole cameras, located in the same toroidal location and offering a full coverage of the TCV vessel. Each camera is equipped with a linear array of 20 silicon p-n junction photodiodes. Since their sensitivity extends to the visible region, a Beryllium filter (filtering the photons with an energy lower than  $\approx 1$  keV), is placed at the entrance of each camera. The viewlines of the photodiodes are shown in 2.14a).

The tomographic reconstruction analysis of the XTOMO data on TCV is based on the pixel method. In the following, we aim at giving a basic overview of the pixel method. More details on the mathematical challenges arising from the finite number of viewlines and implementation of tomographic analysis on TCV can be found in [47, 46].

The pixel method consists of dividing the region of the plasma responsible for the emission into a number of finite elements, also called ‘pixels’ (see 2.15). The emissivity of the plasma is supposed to be homogeneous inside a finite element. We consider a rectangular grid of  $n_x$  horizontal and  $n_y$  vertical elements for a total of  $N = n_x n_y$  elements. The heart of the pixel

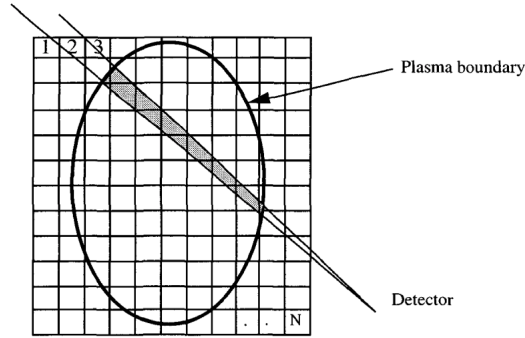


Figure 2.15 – Picture from [46] ‘Finite element techniques divide the cross section into pixels which can have arbitrarily complicated shapes. The transfer matrix T of the problem is calculated by adding the contribution of each pixel to each detector.’

method lies in the approximation of the line-integrated emission measured by each detector as a summation. Since each detector views a number of pixels, we can write the power  $P_i$  collected by the detector  $i$  as:

$$P_i = T_{i1}g_1 + T_{i2}g_2 + \dots + T_{iN}g_N, \quad (2.14)$$

where  $g_j$  is the emissivity of the plasma (that we are trying to determine) contained in the  $j$  pixel and  $T_{i,j}$  the fraction of the radiation emitted by the pixel  $j$  ( $j = 1..N$ ) incident on the detector  $i$  ( $i = 1..n_i$ ). The chord brightness  $f_i$  can be written as:

$$f_i = \frac{P_i}{(A\Omega)_i/(4\pi)}, \quad (2.15)$$

where  $A_i$  is the area of the detector and  $\Omega_i$  the solid angle of detection. The set of  $n_i$  linear equations from 2.14 can be rearranged in matrix form:

$$\mathbf{f} = \mathbf{T} \cdot \mathbf{g} \quad (2.16)$$

where  $\cdot$  is the usual matrix multiplication. When the number of detector  $n_i$  is larger than the number of pixels  $N$  ( $n_i > N$ ), the solution to the problem is unique and can be found by

minimising the functional :

$$\chi^2 = (\tilde{\mathbf{T}} \cdot \mathbf{g} - \mathbf{f})^t \cdot (\tilde{\mathbf{T}} \cdot \mathbf{g} - \mathbf{f}) \quad (2.17)$$

Here, we use the abbreviation  $\tilde{\mathbf{T}}_{li} = \mathbf{T}_{li}/\sigma_l$  with  $\sigma_l$  the error in the brightness measurement from the chord  $f_i$ .

In the case where  $N > n_i$  (representative of the TCV setup), the solution is no longer unique and the problem is solved using the minimum Fisher information method. This case is addressed in [47, 46].

### Duplex multiwire proportional X-ray counter (DMPX)

The DMPX diagnostic [48] consists of two superimposed multi-wire chambers (separated by a 10 mm thickness of air) and provides measurements of soft X-ray intensity along 64 lines of sight (fig. 2.14). Soft X-rays mostly interact with matter via photo-electric absorption. When the incident photon is absorbed by an atom, the atom becomes ionized. The free charges resulting from this process are used to detect the incident soft X-rays in a wire-chamber. A wire-chamber is composed of an array of wires acting as anodes and two plane electrodes placed on each side of the wire array. The wire-chamber is filled with a detection gas. When an incident soft X-ray photon interacts with an atom of the detection gas, it creates an electron/ion pair. The electron and the ion are accelerated by the electric field created between the anode and the cathode. While moving towards the closest wire-anode, the primary electron excites another detection gas atom which in turn liberates free electrons creating an avalanche reaction. This avalanche reaction results in a change in the voltage of the wires.

The DMPX detectors are sensitive to X-rays in the range 3 – 40 keV and have a frequency bandwidth of 50 kHz. They are made of an air-tight aluminium box containing 64 gold-plated tungsten wires, aligned in the toroidal direction, each separated from its neighbors by 2 mm. The chambers of the detectors are separated from the TCV vacuum using a beryllium window (again filtering out the low energy soft X-rays) and are filled with a mixture of 90% krypton (the detection gas) and 10% methane, at atmospheric pressure. Each wire collects the electrons arising from photonization (from a given line of sight) in a gas volume of  $2 \times 8 \times 40$  mm. The DMPX diagnostic consists of 64 channels covering most of the TCV poloidal cross-section [48, 49]. The viewlines of the channels are shown in fig. 2.14.

In practice, the soft X-rays diagnostics are used to monitor MHD activity (such as sawtooth and modes) which is associated with periodic changes in  $n_e$ ,  $T_e$  and  $Z_{eff}$  (see chapter 6 and 7).

## 2.3 Langmuir probes for diagnosing the plasma edge

A Langmuir probe (LP) is a diagnostic used to measure plasma electron density, temperature and potential in low temperature plasmas. It is made of one or more electrodes (depending on the type of measurement we want to achieve) placed in the plasma and biased to a constant or varying voltage. In this section, after a brief introduction to a simple probe theory, we describe the two Langmuir probe-based diagnostics on TCV: the wall-mounted probes system and the fast-reciprocating probe.

### 2.3.1 Theory of a single-tip probe

In both TORPEX and TCV, the current  $I_{pr}$  collected by a Langmuir probes biased at a voltage  $V_{pr}$  is interpreted using the following four-parameter model [50]:

$$I_{pr}(V_{pr}) = I_{sat} \left[ 1 - \alpha(V_{pr} - V_{fl}) - \exp \frac{V_{pr} - V_{fl}}{T_e} \right]. \quad (2.18)$$

Here,  $V_{fl}$  is the floating potential of the probe measured when  $I_{pr} = 0$  and  $I_{sat}$  the ion saturation current. The  $\alpha$  parameter accounts for the sheath expansion that occurs at large negative voltages, increasing the collection area and preventing the current from saturating. In the following, we neglect the contribution from the sheath expansion and assume  $\alpha = 0$ . This assumption is not valid in TCV but is used here for simplicity. The I-V characteristic of the LP can be reconstructed by biasing the probe with a sawtooth-like voltage. Figure 2.16 shows an example of I-V characteristic of a LP. Here, we represent  $J_{pr}(V_{pr}) = I_{pr}(V_{pr})/A$ .

Following the Bohm relation, we can re-write  $I_{sat}$  as:

$$I_{sat} = \frac{n_e}{2} \sqrt{\frac{T_e}{m_i}} eA \quad (2.19)$$

where  $A$  is the effective surface of the probe.

When the applied negative voltage is large enough, the probe is in the ion saturation regime with  $j_{pr} = j_{sat}$  directly proportional to  $n_e$  at a constant electron temperature.

In practice, in this thesis, we are interested in measuring the variations of the electron density. For this reason, we make sure that the probes are used in the ion saturation regime and we get  $n_e$  from eq. 2.19.

### 2.3. Langmuir probes for diagnosing the plasma edge

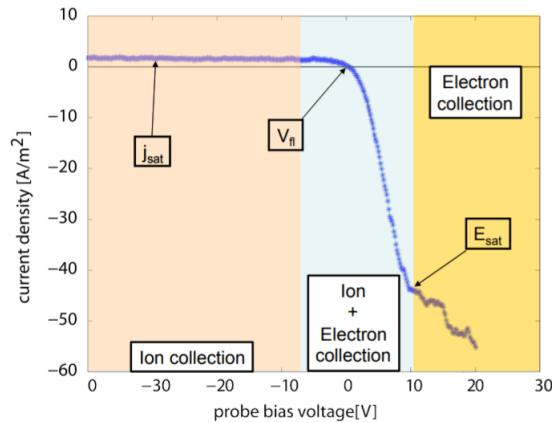


Figure 2.16 – Example of a current density collected by a Langmuir probe as a function of the bias voltage.

#### 2.3.2 Wall-embedded Langmuir probes on TCV

The wall-embedded Langmuir probe system on TCV consists of 114 LPs [51]. The probes are made of graphite and have a diameter of 4 mm. Most of the probes are flush embedded into the tiles except for a few rooftop and dome-shaped probes. A picture of the three different LP heads installed on TCV is shown in fig. 2.17. The location of the probes on the poloidal plane of TCV is shown in fig. 2.18 with their different labels.

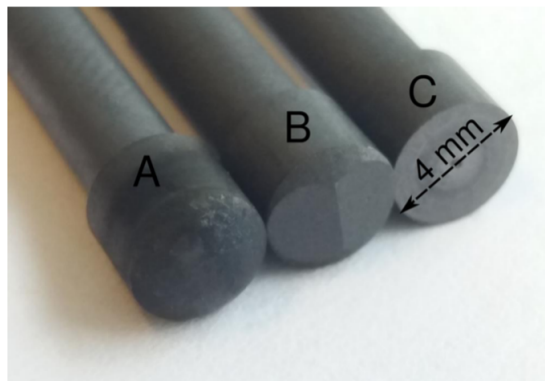


Figure 2.17 – Picture of the different probe heads installed in TCV. A: dome-shaped head. B: rooftop. C: flush (fig. 1 in [51]).

The data from each probe is acquired with a frequency of 200 kHz and two operating modes are possible. In the first one, no biasing voltage is applied to the probe. Charges accumulate on the probe such that the current is zero. The measured voltage is  $V_{fl}$ . In the second operating mode, the probes can be biased at an arbitrary potential in the range  $\pm 120$  V or swept using a sawtooth voltage in this range. In the frame of this thesis, the voltage of the probe is set to  $-100$  V, ensuring the functioning of the probe in the ion saturation regime for the considered plasmas. This allows local measurements (at the locations of the probes shown in fig. 2.18)

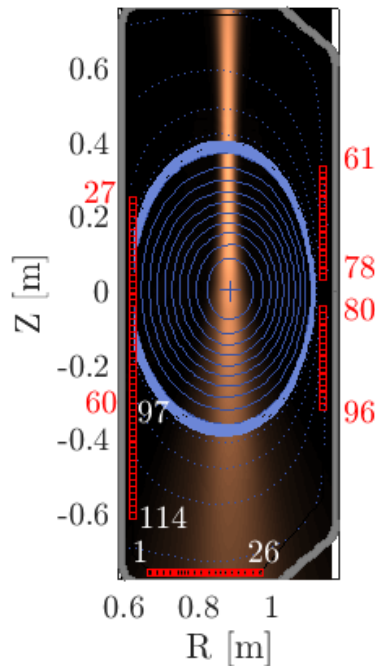


Figure 2.18 – Position and numbering of the wall-mounted Langmuir probes in the poloidal plane. The copper-shaded area represents the electric field norm of the high-power mmw-beam. The contours represent the flux surfaces and the blue shaded area covers the region of the SOL between the LCFS and the location where the density has dropped to half the value that it has at the LCFS.

proportional to the electron density at the edge of the plasma, and provides information on the time-dependent fluctuations of the electron density. Examples of LP measurements in ion saturation regime are shown in chapter 7.

### 2.3.3 Fast reciprocating probe

A fast reciprocating probe (FRP) [52] is installed on the equatorial mid-plane of TCV [53] and is used to perform local measurements of  $n_e$ ,  $T_e$ , plasma potential and correlation length of the turbulence at the edge of the plasma ( $\rho \sim 1 - 1.1$ ). The probe can span a distance of 20 cm in  $\sim 100$  ms. The probe has interchangeable boron-nitride heads adapted to different magnetic configurations. An adapted head allows using two pins to lying on the same flux surface to compute the poloidal electric field or the correlation lengths. A drawing of the FRP is shown in fig. 2.19.

The probe has 10 pins, allowing the measurement of the electron temperature, density and electric potential across the SOL. In particular, pin 4 is used to measure the ion saturation current  $I_{sat}$  and its fluctuations. A double probe (pin 5 and 6) is used to determine the electron temperature and density. Compared to a single probe, a double probe has the advantage



### 2.3. Langmuir probes for diagnosing the plasma edge

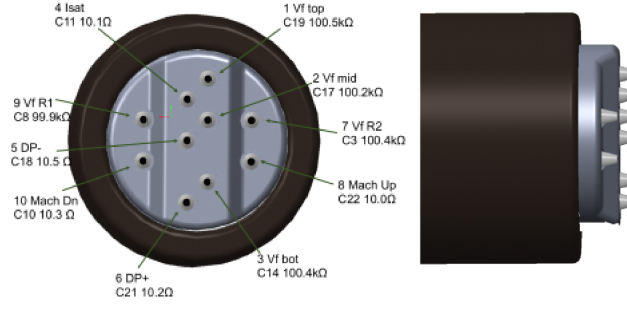


Figure 2.19 – *Picture from [53].* The reciprocating probe head electrode layout. Two  $V_{fl}$  [here noted  $V_f$ ] electrodes (number 1 and 2) are bracketing the  $I_{sat}$  electrode (number 4), allowing for the determination of  $E$  for events centered over the three electrodes.

of an  $I_{sat}$  current saturating at positive and negative voltages, avoiding risks of damage on the probe caused by a large  $I_{sat}$ . The current collected by the double probe is given by  $I_{pr}(V_{pr}) = I_{sat} \tan(\frac{V_{pr}}{T_e})$ . 6 floating pins, separated radially (pin 2,7 and 9) and poloidally (pin 1,2 and 3) are used to measure the floating potential and its fluctuations, measuring simultaneously the poloidal and radial component of the electric field. The data is acquired at 250 kHz. FRP data is used in chapter 7 to provide the poloidal rotation velocity of the background plasma. We will make an important comparison to this data using a novel method developed in this thesis.

#### Summary of the TCV diagnostics used in this thesis

In this chapter we have described the TCV tokamak, third harmonic high-power system and the TCV diagnostics used in this thesis. Table 2.2 summarizes the diagnostics presented in this chapter, their main measured quantities and uses in this thesis.

Diagnostic	quantity	use
X3TD	mmw-power	mmw-transmission measurements
TS	$n_e, T_e$	local measurements ( $R = 0.9$ )
FIR	$\int n_e dl$	TS $n_e$ calibration, and $\int n_e dl$ in TCV SMT
XTOMO, DMPX	$n_e^2 Z_{eff} / \sqrt{T_e}$	monitoring MHD activity
LP	$n_e$	at the edge, SOL
FRP	$n_e$ and blob speed	at the edge, SOL

Table 2.2 – Summary of the diagnostics presented in this chapter, the main measured quantities and use in this thesis.



## 3 The TORPEX device

The TORoidal Plasma EXperiment (TORPEX) is a toroidal device in operation at the Swiss Plasma Center since march 2003. TORPEX device was designed to be a flexible basic plasma physics device for the study of plasma instabilities, wave-particle interaction and their impact on particle and heat transport. To generate plasma instabilities and transport phenomena of relevance for magnetically-confined fusion-plasmas, a toroidal shape was selected, bringing magnetic field gradient and curvature. In drift-turbulence regime in TORPEX, elongated structures of enhanced electron density (blobs) are generated and convected away from the main plasma by  $\mathbf{E} \times \mathbf{B}$  drift. The nature of the turbulence observed is similar to the one observed in the SOL of tokamaks, of relevance for this thesis [54]. The universality of the properties of TORPEX turbulence together with the extensive diagnostic accessibility makes it an invaluable tool for the study of the mmw-scattering by plasma turbulence addressed here. The low  $n_e$  ( $\sim 5 \times 10^{16} \text{ m}^{-3}$ ) and  $T_e$  ( $\sim 5 \text{ eV}$ ) compared to TCV ( $n_e$  up to  $10^{20} \text{ m}^{-3}$  and  $T_e$  up to 15 keV), enables an easy in-situ access for the diagnostics and thus in-situ measurements with no risk of damaging the diagnostics.

In this section, the TORPEX device is described together with its main parameters and diagnostics. An emphasis is put on the mmw-injection/detection system installed for the purposes of this thesis. The physical properties of the plasmas in TORPEX are discussed later in chapter 5.

### 3.1 Presentation of the device

TORPEX (fig. 3.1) is a toroidal device of major radius  $R_0 = 1 \text{ m}$  and minor radius  $a_0 = 0.2 \text{ m}$ . The vacuum vessel is made of twelve  $30^\circ$  sectors made of stainless steel. Amongst these sectors, four are retractable, providing good modularity and access to the vacuum vessel. The plasma is accessible through 48 ports located all around the vacuum vessel. As in TCV, the vessel grounding is made to a common ground through a copper surface covering the surface below the TORPEX vessel. The vacuum vessel is divided into four quadrants (of three sectors each), electrically insulated from each other. The plasma can be produced in steady-state.

### Chapter 3. The TORPEX device

---

However, typically a shot duration is 2 s with a repetition rate of  $\approx 3$  min. The signals from the diagnostics are acquired using DTACQ cards [55] with an acquisition frequency up to 250 kHz; they are stored in an MDSplus [56] database as is done at TCV. The acquisition frequency can be adapted to cover longer discharges.

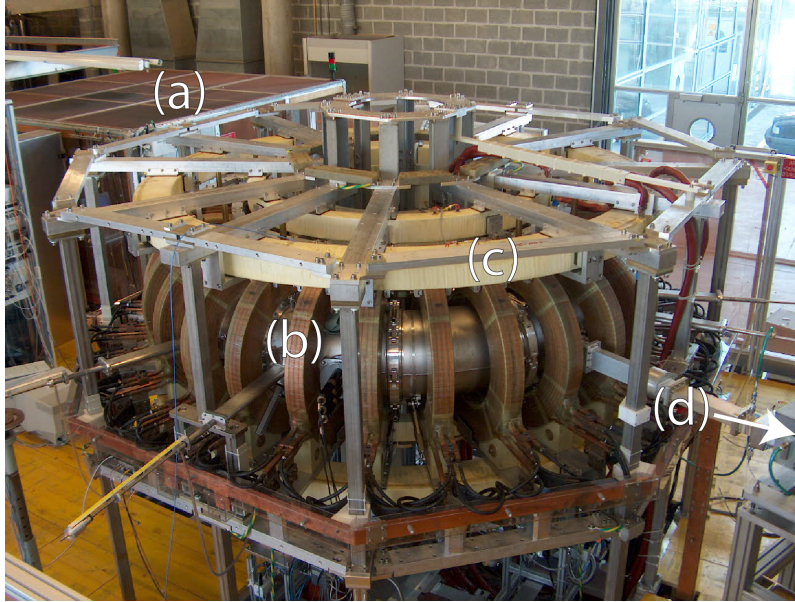


Figure 3.1 – The TORPEX device with its main elements. (a) Control room. (b) Toroidal-field coil. (c) Vertical-field coil. (d) High-power magnetron.

#### Magnetic field

The magnetic field in TORPEX is produced by the superimposition of a toroidal field  $B_T$  and a vertical field  $B_z$  generating an open helical field line configuration; unlike TCV since there are no ohmic coils to drive current in the plasma itself. Recently, closed field-line configurations, with and without the presence of X-points, were accessed in TORPEX after the installation of an in-vessel toroidal conductor (TC) [57, 58, 59]. The toroidal field ( $B_T$ ) of  $\sim 0.76$  mT on axis is generated by 28 toroidal coils placed around the torus. The vertical field is generated by four horizontal coils and is  $\approx 5$  mT on axis.

#### Plasma production

The plasma is produced by the injection of microwaves at 2.45 GHz ( $\lambda = 12.2$  cm) in O-mode; two 2.45 GHz-mmw magnetron sources of different power are installed on TORPEX. The higher-power magnetron delivers mmw-power  $P_{RF}$  in the range  $\approx 0.2 - 20$  kW. The power is injected from the low-field side of the TORPEX vessel and can be modulated (at a maximum frequency of 10 kHz).

The lower-power magnetron injects power from the bottom of the vessel in the range  $P_{RF} \approx$

### 3.2. Millimeter-wave injection/detection system

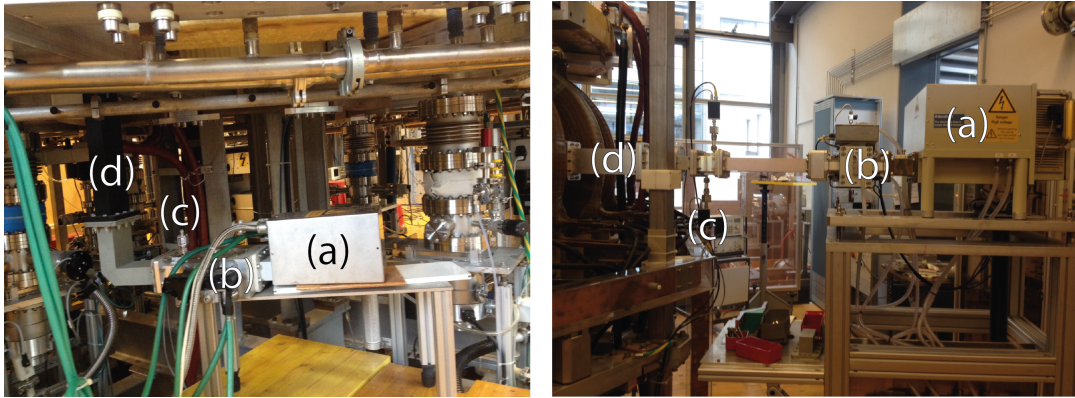


Figure 3.2 – Left: lower-power magnetron injection setup below. Right: higher-power magnetron setup from the LFS. Both injections are performed in O-mode. (a) Lower-power magnetron. (b) mmw-isolator. (c) Mmw-detector. (d) Injection-waveguide.

0.2 – 1.2 kW. The injection setups of the two magnetrons are similar (fig. 3.2). The wave from the magnetron is carried to the vessel using fundamental rectangular waveguides. An mmw-isolator is used to prevent the mmw from reflecting back into the magnetron. The transmitted and reflected powers are measured using mmw-detectors connected on directional couplers. It was observed that the higher-power magnetron is a strong source of electrical noise in the 30 GHz detection system used in the scattering experiments (see below). Hence, all the experiments are performed using the low-power magnetron.

The physical processes of the plasma production and the properties of the TORPEX plasmas are discussed in section 5.3. The main TORPEX plasma and machine parameters are summarized in table 3.1.

Machine parameters		
Major radius	$R_0$	1 m
Minor radius	$a_0$	0.2 m
Nominal aspect ratio	$R_0/a_0$	5
Magnetic field on axis	$B_0$	$\sim 0.07$ T
Discharge duration		$\leq 4$ s
Plasma parameters		
Maximum electron density	$n_{e0}$	$1 - 10 \times 10^{16} \text{m}^{-3}$
Maximum electron temperature	$T_{e0}$	$\sim 5$ eV
Main ion component		H, He, Ar, Ne

Table 3.1 – Plasma and machine parameters in TORPEX

### 3.2 Millimeter-wave injection/detection system

To perform scattering experiments on TORPEX, a low-power mmw-injection/detection system was developed and installed in the frame of this thesis. The mmw-system is located  $90^\circ$  toroidally from a HEX TIP array (see fig. 3.3).

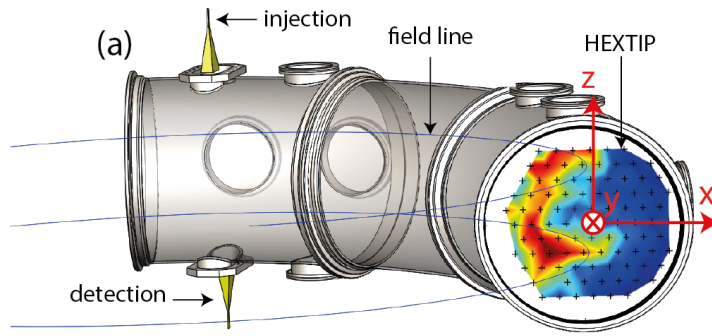


Figure 3.3 – From [35]: Illustration of the experimental setup in TORPEX with a helical magnetic field line (in blue) in a simple magnetized torus configuration. A mmw-beam is injected in X mode from the top of the vessel and detected at the bottom through dielectric windows. In situ 2D measurements of density fluctuations associated with blobs are obtained from the HEXTIP array of 95 Langmuir probes at the positions indicated in black.

A low-power (7 mW) mmw-beam at  $f = 29.7$  GHz (wavelength  $\lambda \approx 12.2$  mm in vacuum; vessel diameter = 400 mm) is launched in the X-mode from the top of the device through a Plexiglass window using a pyramidal horn antenna at  $[x = 5 \text{ cm}, z = 23 \text{ cm}]$  outside of the vacuum. The X-mode component of the mmw transmitted power is detected at the bottom of TORPEX using a pyramidal horn antenna (also outside of the vacuum) and WR22 waveguide of length  $\approx 22$  cm leading to an optically-isolated mmw-detector (OIMD) [33]. The dimension of the horn is 4.2 cm in the radial direction and 5.5 cm in the toroidal direction. The signal is digitized at 250 kHz. The detector can be moved radially to probe the mmw-beam in the range  $x \in [-3, 12]$  cm. This is done to reconstruct the time-averaged radial profile of detected power as well the corresponding fluctuations. The set-up is shown in fig. 3.3 and 3.4. The OIMD was designed to improve the signal to noise ratio of the transmitted power measurements in TORPEX. The plexiglass-opening in the TORPEX vessel makes it possible for some of the mmw-power at 2.45 GHz, used for the plasma production, to leak out. The WR22 waveguide placed after the receiving antenna has a cut-off frequency of 26.53 GHz and stops the propagation of the 2.45 GHz. Nonetheless, the 2.45 GHz mmw may couple to the measurement system through the surrounding environment (e.g. cables). In TORPEX, the spurious 2.45 GHz mmw may couple to any metallic element with a size  $\sim \lambda = 10.1$  mm. Figure 3.5 shows the OIMD and its components. The detection antenna is connected to a Schottky Diode Detector (SDD) using a series of WR22 bends with a total length of  $\approx 22$  cm to ensure the correct orientation of the antenna. The SDD provides a voltage signal proportional to the power of the mmw received after the bends. The SDD is placed inside a sealed-stainless steel box which has a thickness of 3.5 mm. No open hole is present on the box that could provide a path for the spurious 2.45 GHz mmws. The voltage signal from the SDD is carried to the acquisition using an optical emitter/receiver system power using two 12V batteries. The metallic box is placed on a plastic support, isolating it electrically from the TORPEX vessel.

A series of tests was performed with different values of  $P_{RF}$  varying between 0.3 – 0.6 kW to

### 3.2. Millimeter-wave injection/detection system

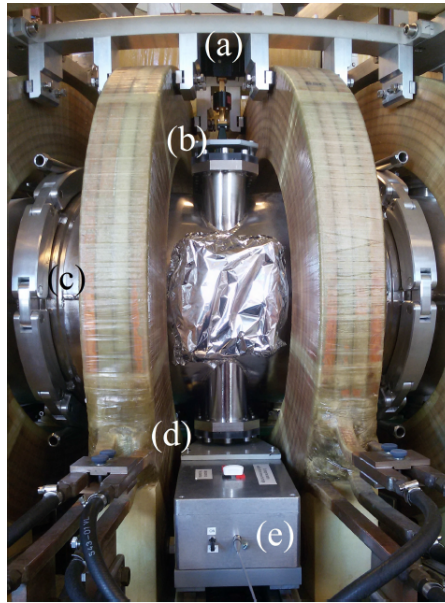


Figure 3.4 – *From [33]:* ‘Millimeter-wave system installed in TORPEX. (a) mmw source. (b) mmws are injected on top through a Plexiglas window using a pyramidal horn. (c) TORPEX vessel and toroidal B-field coils. (d) Second Plexiglas port, receiving pyramidal horn and waveguide. The last two items are hidden from view by the plastic support that fixes the orientation of the antenna directly in front of the transmission horn. (e) Detection system of mmws. There is no direct contact between the system and any metallic surfaces, as the detector rests on an insulating stand. Notice the fiber-optics cable connected in front.’

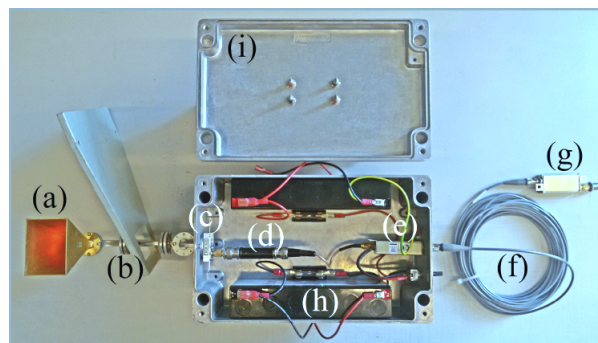


Figure 3.5 – *From [33]:* ‘Optically-isolated mmw detector (OIMD). (a) Pyramidal horn antenna. (b) WR22 waveguide. The plastic support around it is used to fix the orientation of the antenna during operations (see Fig. 3.4). (c) Zero-bias SDD. (d) Resistive load (RL). (e) Optical link transmitter. (f) Fiber optics. (g) Optical link receiver. The output of this unit can be connected directly to the data-acquisition system. (h) Two 12V batteries are used to power the analog-to-optical unit and keep the circuitry isolated. They are shown disconnected only to avoid cable clutter in the image. The optical receiver unit (g) is powered with separate supplies or batteries (not shown). All components in the metallic box are sealed off using the lid (i) during operations (see fig. 3.4).’

confirm to noise-reducing capabilities of the OIMD. The experiments aim at comparison the measurements taken with the OIMD and a bare SDD and showing that the OIMD improves the signal-to-noise ratio. In the experiments, a Hydrogen plasma is produced, with a simple magnetized torus magnetic field configuration  $B_T = 71$  mT and  $B_\nu = 2$  mT. The fluctuations  $\delta P(t)$  of the power  $P(t)$  measured with the OIMD are compared to the measurements performed with the diode directly connected to the acquisition using a coaxial cable in the presence of  $P_{RF} = 400$  W with and without plasma. The traces are compared in fig.3.6a) and b), respectively. In the absence of a plasma,  $\delta P(t)$  measured using the bare SDD has a step-like modulation noise with an amplitude  $< 50 \mu\text{W}$  (see fig. 3.6). The use of the OIMD reduces the noise level to the least significant bit level. The measurement of the standard deviation  $\sigma(P)$  of the four signals as a function of  $P_{RF}$  is shown in fig. 3.6c). The lower  $\sigma(P)$  obtained for traces measured with the OIMD (in particular the red dots, without plasma) show its noise reducing effect. In particular, fig. 3.6c) shows that for  $P_{RF} = 0.3 - 0.6$  kW, the use of the OIMD is necessary to distinguish variations of the signal associated with the plasma activity from the background noise. For example at  $P_{RF} = 400$  kW, the use of the OIMD improves the signal-to-noise ratio by a factor  $\sim 5$  by using the OIMD.

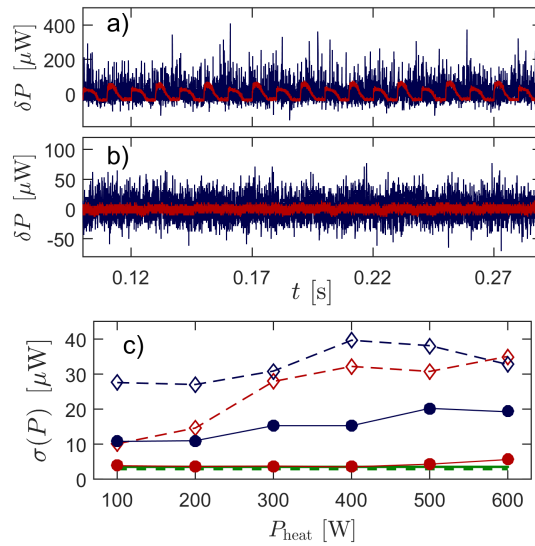


Figure 3.6 – From [33]: Experimental observations. (a) mmw-power fluctuations  $s(t)$  recorded with  $P_{RF} = 400$  W and a bare SDD in the cases with plasma (blue) and without plasma (red). (b) OIMD time trace with (blue) and without plasma (red) for the same value of  $P_{RF}$ . Notice the different vertical-axis scale. (c) Standard deviation  $\sigma(P)$  for the cases: SDD with (hollow blue diamonds) and without plasma (hollow red diamonds), and OIMD with (solid blue circles) and without (solid red circles). The lines are not fits and are present only to guide the eye. The baseline values of (s) acquired with no HWS [magnetron power] are shown in green for OIMD (solid line) and the bare SDD (dashed line). The markers of  $P_{RF} = 400$  W correspond to the data shown in (a) and (b).



### 3.3 HEXTIP array

The main diagnostic in TORPEX used in this thesis is the HEXagonal Turbulence Imaging Probe Upgrade (HEXTIP-U) [60]. The HEXTIP-U is used to provide 2D time-resolved images of  $n_e$  covering the entire poloidal cross-section of TORPEX, necessary for blob detection and full-wave beam propagation simulations. The HEXTIP-U is made of two identical arrays of 95 LP each, located  $180^\circ$  toroidally from each other (see fig. 3.7). The LPs are made of stainless steel, they have a cylindrical shape with a radius of 3.1 mm and a length of 2 mm. The probes are on ceramic arms placed 35 mm from each other. Each of the two LP arrays of HEXTIP-U (95 probes each) is made of a set of Low Field Side (LFS) probes installed on movable ceramic arms and a set of fixed High Field Side (HFS) probes (fig. 3.7b). The 11 arms located on the HFS of the vessel are mounted on two rings and are held in place inside the vessel using screws. These fixed arms cover the region of the plasma  $x < -35$  mm. The low field side region of the plasma is covered by 59 probes, installed on 11 arms. The arms are fixed to two movable stainless arcs connected to a linear actuator which enables their translation as a group in the  $x$ -direction. The arcs can be moved by  $\Delta \leq 20$  mm to the HFS and  $\Delta \leq 70$  mm to the LFS with a precision lower than 1 mm. When the linear actuator is in a neutral position ( $\Delta = 0$ ), the entire poloidal cross section of the vessel is covered with a uniform spatial resolution of 35 mm.

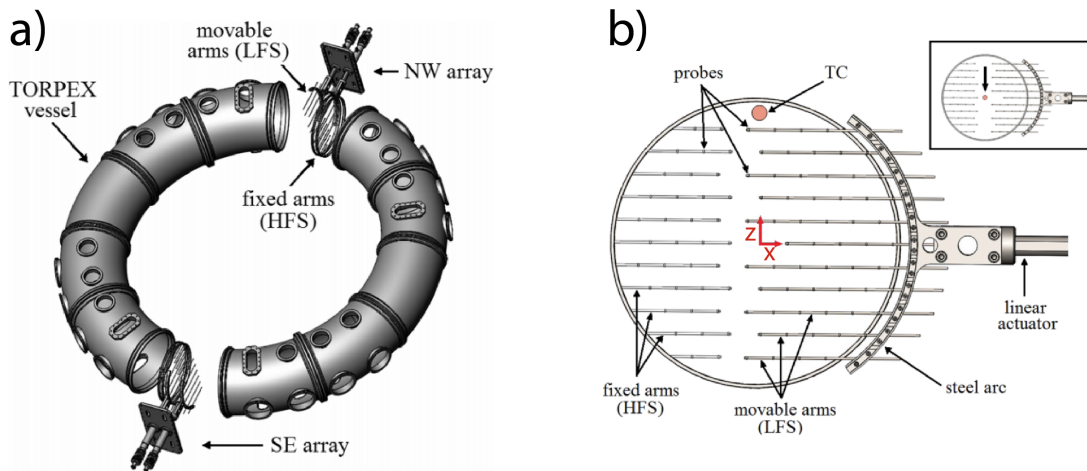


Figure 3.7 – From [60]: a) ‘Two complete LP arrays are installed on opposite toroidal locations in TORPEX, on the southeast (SE) and northwest (NW) areas. The movable LFS arms are installed separately from the fixed HFS arms and therefore have a small toroidal separation ( $\leq 10^\circ$ ) from the latter. Each array has its own independent front-end electronics and data acquisition system.’ b) ‘Each of the two LP arrays of HEXTIP-U is made of a set of Low Field Side (LFS) probes resting on movable ceramic arms and a complementary set of fixed High Field Side (HFS) probes. When the LFS arms are not displaced, the system forms an hexagonal grid which provides comprehensive LP coverage of the entire poloidal cross section. The LFS arms can be displaced radially (along  $x$ ) to allow the TC to move unobstructed.’ The movable arm is shown at the neutral position  $\Delta = 0$

Each of the two HEXTIP arrays has an electronic consisting of 12 independent boards gathering 8 probes each. Each group of 8 probes can be independently set to a voltage bias to measure the saturation current ( $-42 V$  in this thesis), or left floating. The data from the HEXTIP array is acquired using a D-tAcq ACQ196CPCI acquisition system which has a sampling frequency of 250 kHz.

### 3.4 Conditional averaged sampling

The conditional averaged sampling (CS) is a widely used technique in the investigation of coherent structures in turbulent media [61, 62, 63]. This technique allows evaluating the effect of the so-called average structure on a given quantity. In the frame of this thesis, only the SE array is used, but similar results are obtained using the NW array. An example of measurements performed with HEXTIP-U in the LFS is shown in fig. 3.8. To illustrate the principle of the CS, we use an example:

As described later in chapter 5, blobs are detected by LPs as intermittent spikes in the  $n_e$  signal. An example of  $n_e$  computed from the  $I_{sat}$  measured by a probe (see section. 2.3.1 for more details) located in the blob region is shown in fig. 3.8a). Events are defined as local maxima of the detected signal peaking above a given value that fulfill the condition  $n_e > \langle n_e \rangle_t + m\sigma$ , here  $m=3$ , with  $\sigma$  being the standard deviation of  $n_e$  calculated over the entire time trace. The events are identified here by the red crosses. The threshold  $\langle n_e \rangle_t + 3\sigma$  is shown in green. A time-window  $\Delta\tau$  (here  $\Delta\tau = 400\mu s$ ) is selected around each event (identified in orange in fig. 3.8a)) and highlighted on both the reference and also the signal of interest, here for example the measured power fluctuations  $\delta P$  (fig. 3.8b)). If two events are separated by less than the auto-correlation time of the signal, only the first one is selected. The  $\delta P$  signal is averaged on the selected time-windows to extract the coherent part of the signal  $\delta\tilde{P}$  as shown in fig.3.8c).  $\delta\tilde{P}$  can be written as

$$\delta\tilde{P}(\tau) = \frac{1}{N} \sum_{i=1}^{i=N} \delta P_i(\tau),$$

where  $N$  is the number of events, and  $\delta P_i(\tau)$  the measured  $\delta P$  occurring in the  $i^{th}$  time window at the instant  $\tau$  relative to the blob detection. All quantities obtained with CS are labeled with a tilde, except  $\tau$  which is the time relative to the blob event;  $\tau = 0 \mu s$  corresponding to the detection of the blob. Here, the average is performed on  $N \approx 1000$  events.

This technique can be applied to one signal to detect the local effect of an average coherent structure or to many signals (e.g. from the HEXTIP array) to identify the spatio-temporal evolution of a quantity. The technique presented here is also used in TCV with the same principles and using the  $I_{sat}$  current from the wall-embedded LPs as a reference.

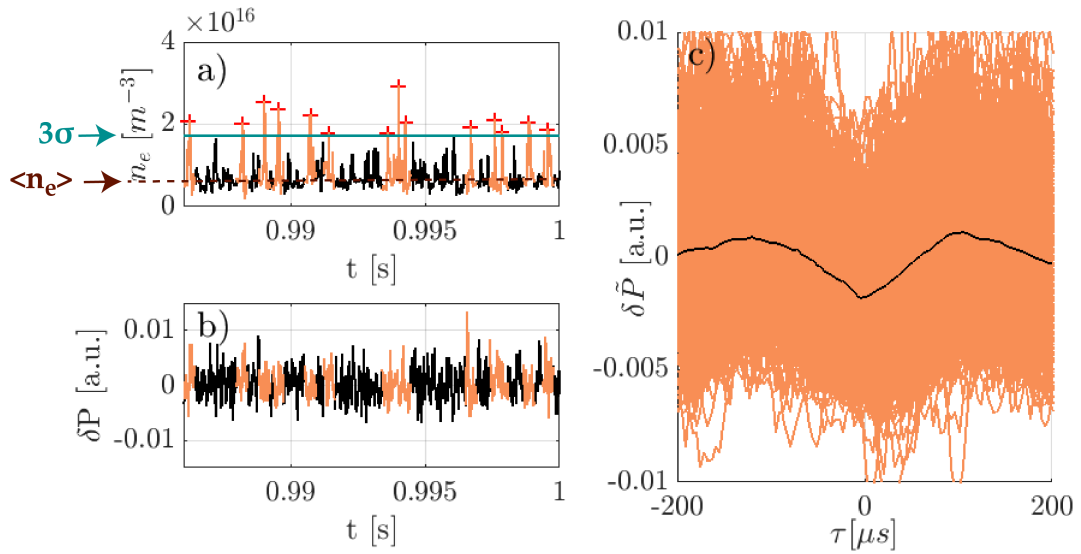


Figure 3.8 – Conditional averaged sampling: a) Blobs are detected as local maxima (red crosses) in the  $n_e$  signal occurring above a threshold (in green). Time-windows are identified around the blob detection (in orange) and reported on the measured power signal  $\delta P$  in b). c) The  $\delta P$  signal is averaged on the selected time-windows to extract the coherent part of the signal (in black). The signals from all the selected time-windows are shown in orange.

In this chapter, we have introduced the simple magnetized toroidal device TORPEX on which some scattering experiments were performed. We described the mmw injection/detection system as well as HEX TIP-U array of LPs, used for time-resolved 2D-imaging of the plasma electron density. Finally, we described the conditional sampling technique which is often used in this thesis.



## 4 Numerical tools

In chapter 1 & 2, we have introduced the experimental tools used in this thesis. This chapter is dedicated to the numerical tools. First the Global Braginskii Solver (GBS), a turbulence code used to model the plasma in the SOL, is presented. Then, in the second part of the chapter, the numerical models used for beam propagation in tokamaks are discussed together with their domain of validity. An emphasis is made on the WKBeam code, run by O. Maj at the Institute of Plasma Physics (IPP) in Garching and the full-wave model implemented in the frame of this thesis.

### 4.1 The turbulence code Global Braginskii Solver (GBS)

In TCV, the electron density  $n_e(\mathbf{x}, t)$  cannot be measured experimentally in the entire poloidal cross-section of the vessel and it is necessary to compute the dielectric tensor of the plasma used in mmw-beam propagation simulations. Non-linear, 3D, numerical simulations of the plasma are used to describe the spatio-temporal evolution of the electron density  $n_e(\mathbf{x}, t)$  in the scrape-off layer of TCV. The simulations are based on the GBS code developed at the Swiss Plasma Center to simulate plasma turbulence in the open field line regions of tokamaks [64, 65] and in basic plasma physics devices [66].

At the edge of the tokamak, the plasma temperature is typically lower than 100 eV and both the electron and ion mean-free paths  $\lambda^{mfp}$  between Coulomb collisions are much shorter than the parallel connexion length  $L_{\parallel}$  (typically in the TCV SOL,  $L_{\parallel}/\lambda^{mfp} \sim 50$  [67]). The SOL is therefore characterized by high collisionality, which enable a local thermodynamic equilibrium to be reached quickly. Under these conditions, it is justified to describe the SOL with the three lowest fluid moments of the  $\alpha$  species distribution function  $f_{\alpha}$ , where  $\alpha$  denotes the species; these are: the plasma density  $n_{\alpha}$ , the fluid velocity  $\mathbf{v}_{\alpha}$  and temperature  $T_{\alpha}$ . These

moments are defined as follows:

$$n_\alpha(\mathbf{x}, t) = \int_{\mathbb{R}^3} f_\alpha(\mathbf{x}, \mathbf{v}, t) d\mathbf{v}, \quad (4.1a)$$

$$\mathbf{v}_\alpha(\mathbf{x}, t) = \frac{1}{n_\alpha} \int_{\mathbb{R}^3} \mathbf{v} f_\alpha(\mathbf{x}, \mathbf{v}, t) d\mathbf{v}, \quad (4.1b)$$

$$T_\alpha(\mathbf{x}, t) = \frac{1}{n_\alpha} \int_{\mathbb{R}^3} \frac{m_\alpha}{3} (\mathbf{v} - \mathbf{v}_\alpha)^2 f_\alpha(\mathbf{x}, \mathbf{v}, t) d\mathbf{v}. \quad (4.1c)$$

The time evolution of  $f_\alpha$  is derived from the Boltzmann equation:

$$\frac{\partial f_\alpha}{\partial t} + \mathbf{v} \cdot \frac{\partial f_\alpha}{\partial \mathbf{x}} + \frac{q_\alpha}{m_\alpha} (\mathbf{E} + \mathbf{v} \times \mathbf{B}) \cdot \frac{\partial f_\alpha}{\partial \mathbf{v}} = S_\alpha + \sum_\beta C(f_\alpha, f_\beta), \quad (4.2)$$

where  $S_\alpha$  is a source term for the particles and  $C(f_\alpha, f_\beta)$  the collisional operator describing the Coulomb collisions between the  $\alpha$  and  $\beta$  species. Braginskii introduced in 1965 [68] a two-fluid model assuming a quasi-Maxwellian distribution function for the ions and electrons to obtain a closed set of equations. This assumption is valid for highly-collisional plasmas. A set of equations used to describe collisional plasmas in the SOL was derived by Braginskii in [68].

In the SOL, a wide range of spatio-temporal scales are involved and assumptions such as small-amplitude fluctuations and the separation of turbulent and equilibrium scale length are not valid. The numerical simulations are thus extremely challenging and a number of approximations are introduced to make the set of equations more tractable. Since turbulence time scales in the SOL are much slower than the ion cyclotron time and the scale lengths perpendicular to the magnetic field are longer than the ion Larmor radius, Braginskii's equations are typically simplified by using a drift approximation. The drift approximation allows splitting the particle dynamics into parallel and perpendicular motions with respect to the magnetic field and expresses the ion and electron velocities as :

$$\mathbf{v}_e = v_{\parallel e} \mathbf{b} + \mathbf{v}_{\perp e}, \quad (4.3a)$$

$$\mathbf{v}_i = v_{\parallel i} \mathbf{b} + \mathbf{v}_{\perp i}, \quad (4.3b)$$

where  $\mathbf{b} = \frac{1}{|\mathbf{B}|} \mathbf{B}$ .

Two operators were introduced in GBS to simplify implementation of the drift-reduced Bra-

ginskii equations. The curvature operator  $C(-)$ :

$$C(A) = \frac{B}{2} \left( \nabla \times \frac{\mathbf{b}_0}{B} \right) \cdot \nabla A, \quad (4.4)$$

where  $A$  is a scalar field,  $\mathbf{b}_0$  is the unit vector parallel to the unperturbed magnetic field,  $C$  accounts for the  $\nabla B$  and curvature drift as well as plasma compressibility, and the Poisson's brackets operator

$$\{\phi, A\} = \mathbf{b}_0 \cdot (\nabla \phi \times \nabla A), \quad (4.5)$$

where the  $\mathbf{E} \times \mathbf{B}$  convection is introduced.

The drift-reduced Braginskii equations, in normalized units, as solved by GBS [69], are:

$$\frac{\partial n}{\partial t} = -\frac{R_0}{B} \{\phi, n\} - \nabla \cdot (n v_{\parallel e} \mathbf{b}_0) + \frac{2}{B} [C(p_e) - nC(\phi)] + D_n(n) + S_n, \quad (4.6a)$$

$$\begin{aligned} \frac{\partial \Omega}{\partial t} = & -\frac{R_0}{B} \nabla \cdot \{\phi, \omega\} - \nabla \cdot [\nabla_{\parallel} (v_{\parallel i} \omega)] + \frac{B}{3} C(G_i) \\ & + B^2 \nabla \cdot (j_{\parallel} \mathbf{b}_0) + 2BC(p_e + \tau p_i) + D_{\Omega}(\Omega), \end{aligned} \quad (4.6b)$$

$$\begin{aligned} \frac{\partial U_{\parallel e}}{\partial t} = & -\frac{R_0}{B} \{\phi, v_{\parallel e}\} - v_{\parallel e} \nabla_{\parallel} v_{\parallel e} \\ & + \frac{m_i}{m_e} \left[ \frac{v j_{\parallel}}{n} + \nabla_{\parallel} \phi - \frac{\nabla_{\parallel} p_e}{n} - 0.71 \nabla_{\parallel} T_e - \frac{2}{3n} \nabla_{\parallel} G_e \right] + D_{v_{\parallel e}}(v_{\parallel e}), \end{aligned} \quad (4.6c)$$

$$\frac{\partial v_{\parallel i}}{\partial t} = \frac{R_0}{B} \{\phi, v_{\parallel i}\} - v_{\parallel i} \nabla_{\parallel} v_{\parallel i} - \frac{2}{3n} \nabla_{\parallel} G_i - \frac{1}{n} \nabla_{\parallel} (p_e + \tau p_i) + D_{v_{\parallel i}}(v_{\parallel i}), \quad (4.6d)$$

$$\begin{aligned} \frac{\partial T_e}{\partial t} = & -\frac{R_0}{B} \{\phi, T_e\} - v_{\parallel e} \nabla_{\parallel} T_e + \frac{4T_e}{3B} \left[ \frac{C(p_e)}{n} + \frac{5}{2} C(T_e) - C(\phi) \right] \\ & + \frac{2T_e}{3} \left[ 0.71 \frac{\nabla \cdot (j_{\parallel} \mathbf{b}_0)}{n} - \nabla \cdot (v_{\parallel e} \mathbf{b}_0) \right] + \nabla_{\parallel} (\chi_{\parallel e} \nabla_{\parallel} T_e) + D_{T_e}(T_e) + S_{T_e}, \end{aligned} \quad (4.6e)$$

$$\begin{aligned} \frac{\partial T_i}{\partial t} = & -\frac{R_0}{B} \{\phi, T_i\} - v_{\parallel i} \nabla_{\parallel} T_i + \frac{4T_i}{3B} \left[ \frac{C(p_e)}{n} + \frac{5\tau}{2} C(T_i) - C(\phi) \right] \\ & + \frac{2T_i}{3} \left[ \frac{\nabla \cdot (j_{\parallel} \mathbf{b}_0)}{n} - \nabla \cdot (v_{\parallel i} \mathbf{b}_0) \right] + \nabla_{\parallel} (\chi_{\parallel i} \nabla_{\parallel} T_i) + D_{T_i}(T_i) + S_{T_i}. \end{aligned} \quad (4.6f)$$

Here,  $j_{\parallel} = n(v_{\parallel i} - v_{\parallel e})$ ,  $D_{T_e}$  and  $D_{T_i}$  are perpendicular diffusion terms,  $\Omega = \nabla \cdot \omega$  is the scalar vorticity,  $\omega = n \nabla_{\perp} \phi + \tau \nabla_{\perp} p_i$ ,  $U_{\parallel e} = v_{\parallel e} + \beta_{e0} m_i \psi / (2m_e)$ ,  $v$  the normalized resistivity and  $\tau = T_{i0} / T_{e0}$  ( $T_{i0}$  and  $T_{e0}$  are respectively the ion and electron temperature on axis given in physical

units). The source terms  $S_n$ ,  $S_{T_e}$  and  $S_{T_i}$  mimic the hot plasma outflow from the closed flux surface region into the SOL. The sources are assumed to be constant in the poloidal and toroidal direction with a Gaussian shape in the radial direction.  $G_i$  and  $G_e$  the gyroviscous terms written as

$$G_i = -\eta_{0i} \left[ 2\nabla_{\parallel} v_{\parallel i} + \frac{1}{B} C(\phi) + \frac{\tau}{nB} C(p_i) \right], \quad (4.7a)$$

$$G_e = -\eta_{0e} \left[ 2\nabla_{\parallel} v_{\parallel e} + \frac{1}{B} C(\phi) + \frac{1}{nB} C(p_e) \right]. \quad (4.7b)$$

Here,  $\eta_{0i}$  and  $\eta_{0e}$  are the ion and electron viscosity coefficients defined as  $\eta_{0i} = 0.96 T_{i0} \tau_i \rho_{s0} / (m_i R c_{s0})$  and  $\eta_{0e} = 0.73 T_{e0} \tau_e \rho_{s0} / (m_e R c_{s0})$ .  $\rho_{s0}$  is the ion Larmor radius,  $c_{s0}$  the ion sound speed,  $R$  the plasma major radius and  $\tau_e$  and  $\tau_i$  the electron and ion collision times, respectively.

The equations are integrated in time using a 4<sup>th</sup> order Range-Kutta algorithm. More details on the derivation of the drift-reduced Braginskii equations and their implementation in GBS can be found in [65, 69].

The GBS simulations for the TCV plasmas used in this thesis were performed by F. Riva in [69]. The simulations were run for the case of a TCV L-mode limited plasma with an elongation of 1.52 and no triangularity. They were run with a temporal resolution of  $\Delta t = 1.95 \mu\text{s}$  for 0.22 ms in total. The spatial resolution in a spherical coordinate system  $[R, \theta, \phi]$  is  $[0.5 \text{ mm } 5 \times 10^{-3} \text{ rad } 0.03 \text{ rad}]$ . For comparison, the perpendicular size of blobs  $L_{\perp}$  is  $\approx 1 \text{ cm}$ .

A snapshot of  $n_e$  as computed by GBS is shown in fig. 4.1. Blobs are recognizable as field-aligned elongated structures of locally enhanced electron density relative to the background plasma. The associated  $T_e$  is shown in fig. 4.2. The computed normalized level of fluctuations (r.m.s)  $\delta n_e / n_e$  at the LCFS is 0.15. A systematic underestimation of a factor two of  $\delta n_e / n_e$  in GBS compared to the experiments is taken into account in the mmw-simulations.

A rigorous validation of the GBS results against the experimental measurements was performed by F. Riva in [69]. Validations observables are defined as physical relevant quantities common to both the experiments and the simulations, independent from each other and with a resolution sufficient to describe their variation in both time and space. Here, the observables of interest are  $n_e$ ,  $T_e$ ,  $j_{sat}$ ,  $V_{f1}$  and  $E_{\theta}$  the poloidal component of the electric field. We note  $e_{j,i}$  and  $s_{j,i}$  the value of the  $j^{th}$  observable at the point  $i = 1, 2, \dots, N_j$  of the spatio-temporal evaluation grid, respectively from the experiments and the simulations. The distance  $d_j$  between experiments and simulations is normalized with respect to the uncertainties  $\Delta e_{j,i}$  and  $\Delta s_{j,i}$  as :

$$d_j = \sqrt{\frac{1}{N_j} \sum_{i=1}^{N_j} \frac{(e_{j,i} - s_{j,i})^2}{\Delta e_{j,i}^2 + \Delta s_{j,i}^2}},$$



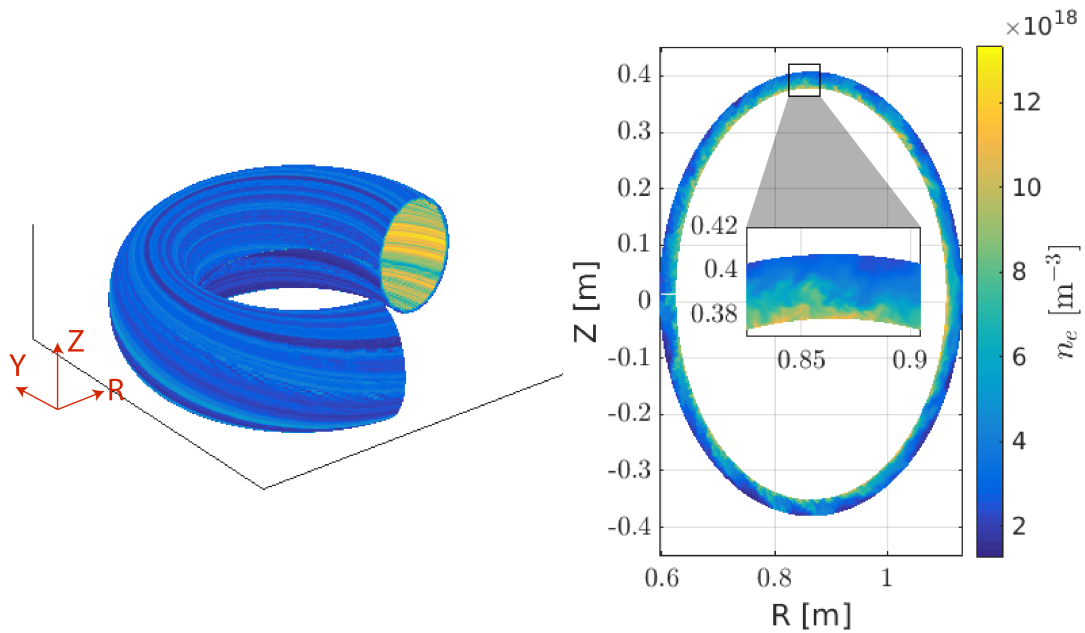


Figure 4.1 – Snapshot of GBS simulation results for a TCV case. On the left: 3D view of  $n_e$ . On the right: Poloidal cross section representing  $n_e$  in the SOL. Field-aligned Local enhancement of the electron density relative to the background plasma are blobs. Their elongated toroidal (parallel) structure is clearly seen in the left image; this leads to the name “filaments” that is often used in this thesis.

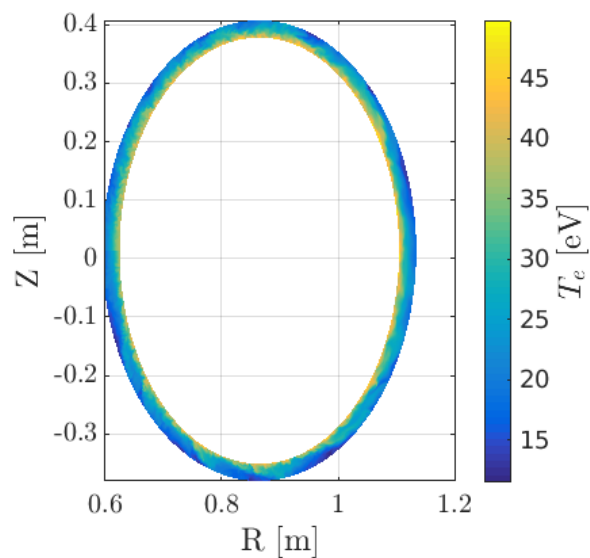


Figure 4.2 – Snapshot of the electron temperature in the SOL as computed by GBS and corresponding to the snapshot in fig. 4.1.

where  $\Delta e_{j,i}$  and  $\Delta s_{j,i}$  are uncertainties affecting  $e_{j,i}$  and  $s_{e,j}$  respectively. The level of agreement between experiments and simulations for the observable  $j$  is defined as

$$R_j = \frac{\tanh[(d_j - 1)/(d_j - d_0)/\Lambda] + 1}{2}$$

The specific choice of the parameters  $d_0$  and  $\Lambda$  was found not to affect the conclusion of the validation exercise.  $R_j \leq 0.5$  corresponds to an agreement (relative to the observable  $j$ ) between the experiments and the simulations within uncertainties and  $R_j \geq 0.5$  to a disagreement.

Finally, the metric

$$\chi = \frac{\sum_j R_j H_j S_j}{\sum_j H_j S_j}$$

and the index  $Q = \sum_j H_j S_j$  are defined to estimate the overall agreement between the experiments and the simulations as well as the quality of the comparison. A perfect agreement is observed for  $\chi = 0$  and the complete disagreement is observed for  $\chi = 1$ . Here,  $H_j$  accounts for the hierarchy primacy level that takes into account the number of assumptions used in evaluating  $e_{j,i}$  and  $s_{j,i}$  ( $H_j = 1$  for no assumption and  $H_j = 1/2, 1/3, \dots$  for 1, 2, ... assumptions). The quantity  $S_j$  is a decreasing function of the experimental and simulation uncertainty defined as:

$$S_j = \exp\left(-\frac{\sum_i \Delta e_{j,i} + \sum_i \Delta s_{j,i}}{\sum_i |e_{j,i}| + \sum_i |s_{j,i}|}\right),$$

$S_j = 1$  for no uncertainty.

For the discharge of interest in this thesis, it was found  $\chi = 0.34$  and  $Q = 2.46$ , denoting a good overall agreement between the experiments and a good quality of comparison.

## 4.2 Numerical tools for millimeter-wave propagation

Millimeter-wave codes are used in tokamaks to calculate the propagation of EC-waves from the antenna to the deposition regions in the plasma [4], the power absorbed by the plasma and the current driven by the wave for diagnostic, heating and current drive applications [70]. The mmw-codes can be classified in groups depending on their propagation models, which can be categorized as ray tracing, Gaussian beam (or beam tracing) or full-wave [71]. While the ray tracing approximation - where the Gaussian beam is approximated by a number of independent rays with a ray distribution mimicking that of the Gaussian power distribution over a given propagation range - can treat the refraction of mmw-beams in a non-turbulent plasma, it cannot account for diffraction and fails in the presence of turbulent structures with a typical size  $a$  such that  $\lambda/a \sim 1$  (where  $\lambda$  is the wavelength of the beam) [25]. This limitation also applies the other methods based on the semiclassical assumption providing approximate solutions of the wave electric field equation [71]; examples are the paraxial Wentzel-Kramers-Brillouin (WKB) method [72] or the quasi-optical ray tracing[73], based

on the complex eikonal method. Under conditions where  $\lambda/a \sim 1$ , a statistical description of the mmw-propagation in random media or a full-wave model is needed. In this section, we will present the two models used in this thesis to treat the propagation of mmw-beams in the presence of plasma turbulence with  $\lambda/a \sim 1$ . The first one is based on a statistical description of wave propagation in random media, first developed by Mc Donald in 1991 [74] and implemented in the WKBeam code [75] at the Max Planck Institute for Plasma Physics. The second one is based on a full-wave model implemented in COMSOL Multiphysics [76]. A successful comparison between the two codes in the case of a non-turbulent plasma is performed in the chapter 6. The results of the codes in the presence of turbulence are discussed in chapter 7.

### 4.2.1 WKBeam

The following is given as a brief description of the mathematical model of the WKBeam code. The WKBeam simulations referred to in this thesis were run by O. Maj. WKBeam is a Monte Carlo code which describes the propagation of an EC-wave beam in fully realistic tokamak geometry including diffraction and absorption. It is based on a statistical treatment of the propagation through random media in the frame of the semiclassical approach. McDonald has shown [74] that the semi-classical approach can still be applied to determine the average effect of a distribution of turbulent structures on the mmw-beam propagation. Under this approach, the range of validity becomes  $\lambda/L \ll 1$ , where the limiting scale length  $L$  is now the scale length of the *equilibrium*, allowing for turbulent structures of arbitrary size to be taken into account. The plasma is treated as the sum of the equilibrium  $\langle n_e(\mathbf{x}) \rangle$ ,  $\mathbf{x}$  being the position vector, and an ensemble of independent stochastic perturbations of the plasma equilibrium  $\delta n_e$  such that  $n_{e,j}(\mathbf{x}) = \langle n_e(\mathbf{x}) \rangle + \delta n_{e,j}(\mathbf{x})$  and:

$$\delta n_{e,j}(\mathbf{x}) = \frac{1}{\sqrt{\kappa}} \mu_j(\mathbf{x}) \quad (4.8)$$

where  $\mu_j(\mathbf{x})$  is the  $j^{th}$  realization of the random field  $\mu(\mathbf{x})$  with a zero average and  $\kappa = k_0 L$ ,  $k_0$  being the wave vector in vacuum.

Knowing the electric field  $\mathbf{E}(\omega, \mathbf{x})$ , in order to compute the time-average electric field associated with the mmw-beam, we can extract samples  $E_j(\omega, x) = E(t_j, \omega, \mathbf{x})$ , corresponding to the observation times  $t = t_j$ , and compute the ensemble average over the samples. Two consecutive observation at times  $t_j$  and  $t_{j+1}$  are defined such that  $\Delta t = t_{j+1} - t_j \gg \tau_i$ ;  $\tau_i$  is the auto-correlation time of the turbulence. When the typical time scale of the turbulence is much larger than the propagation time of the mmw-beam, the turbulence can be seen as frozen; i.e. not changing in time. This approximation is called the ‘frozen-turbulence’ (or ‘frozen-blob’) approximation.  $E_j(\omega, x)$  can therefore be well approximated by the solution of the equation 4.9 of the wave electric field in the frequency domain, with  $\delta n_e$  frozen to the

value of  $\delta n_{e,j}(\mathbf{x})$ .

$$\nabla \times (\nabla \times \mathbf{E}(\omega, \mathbf{x})) - \kappa^2 \hat{\epsilon} \mathbf{E}(\omega, \mathbf{x}) = 0. \quad (4.9)$$

Here, the Hermitian part of the dielectric tensor  $\hat{\epsilon}$  is obtained from the cold plasma model (more details in the next section) and accounts for propagation, whereas the anti-Hermitian part of the dielectric tensor describes mmw-absorption. Under the ‘frozen turbulence’ assumption, averaging over the time slices  $t_j$  is equivalent to the ensemble average over independent realizations of the random field  $\mu(x)$  and  $\mathbf{E}(\omega, \mathbf{x})$  becomes a random field. If  $\mathbf{E}$  is square integrable, the trace of the point-to-point correlation matrix  $C$

$$C(\omega, \mathbf{x}, \mathbf{x}') = \mathbb{E}(\mathbf{E}(\omega, \mathbf{x})\mathbf{E}^*(\omega, \mathbf{x}')), \quad (4.10)$$

$\mathbb{E}$  being the mathematical expectancy, is proportional to the averaged energy carried by the wave electric field,

$$\int_{\Omega} \mathbb{E}(|\mathbf{E}(\omega, \mathbf{x})|^2) d\mathbf{x} = \int_{\Omega} \text{Tr}C(\omega, \mathbf{x}, \mathbf{x}) d\mathbf{x}. \quad (4.11)$$

Here,  $\Omega$  is an arbitrary spatial domain and  $\text{Tr}C$  is the trace of  $C$ . In practice, in WKBeam, the main quantity computed is the ensemble average of the electric field energy density  $\xi$  in the  $(\mathbf{x}, \mathbf{N})$  phase space, where  $\mathbf{N}$  is the refractive index vector of the wave, namely:

$$\xi(\omega) = \frac{1}{16\pi|\Omega|} \left(\frac{\kappa}{2\pi}\right)^3 \int_{\Omega \times \mathbb{R}^3} \text{Tr}W(\omega, \mathbf{x}, N) d\mathbf{x} dN, \quad (4.12)$$

where  $|\Omega|$  is the volume of the domain  $\Omega$ .  $W(\omega, \mathbf{x}, N)$  is referred to as the average Wigner matrix of the field  $\mathbf{E}(\omega, \mathbf{x})$  and is defined by:

$$W(\omega, \mathbf{x}, N) = \int e^{i\kappa N} \mathbb{E}(E(\omega, \mathbf{x} + \frac{\mathbf{s}}{2})E^*(\omega, \mathbf{x} - \frac{\mathbf{s}}{2})) d\mathbf{s}, \quad (4.13)$$

such that :

$$\int_{\Omega} \text{Tr}C(\omega, \mathbf{x}, \mathbf{x}) d\mathbf{x} = \left(\frac{\kappa}{2\pi}\right)^3 \int_{\Omega \times \mathbb{R}^3} \text{Tr}W(\omega, \mathbf{x}, N) d\mathbf{x} dN. \quad (4.14)$$

The relevant equation for  $W$ , solved in WKBeam, has the form of a constrained wave kinetic equation:

$$\begin{cases} \{\mathcal{H}_\alpha, w_\alpha\} &= -2\gamma_\alpha w_\alpha + \sum_{\beta=O,X} S_{\alpha,\beta}(\Gamma, w_\alpha, w_\beta), \\ \mathcal{H}_\alpha w_\alpha &= 0 \end{cases}$$

$w_\alpha$  being the scalar Wigner function for the O or X-mode ( $\alpha = O$  or  $\alpha = X$  respectively),  $\mathcal{H}_\alpha$  the geometrical optics Hamiltonian,  $\Gamma$  the Wigner function of the density correlation defined as

$$\Gamma(\omega, \mathbf{x}, N) = \int e^{-i\kappa N \cdot \mathbf{s}} \mathbb{E}(\delta n_e(\mathbf{x} + \frac{\mathbf{s}}{2}) \delta n_e(\mathbf{x} - \frac{\mathbf{s}}{2})) ds, \quad (4.15)$$

and  $S_{\alpha,\beta}(\Gamma, w_\alpha, w_\beta)$  the scattering operator which ‘expresses the normalized rate of change of the energy  $w_\alpha(\omega, \mathbf{x}, N) d\mathbf{x} dN$  contained in an infinitesimal phase space volume centered on  $(\mathbf{x}, N)$ ’ as a result of cumulative energy gain via scattering  $N' \rightarrow N$ , from any  $N'$  and cumulative energy loss via scattering  $N \rightarrow N'$ , to any  $N'$  [75]. The scattering term is obtained through an iterative solution of the wave equation (Born approximation), based on the assumption that the random density fluctuations can be treated as a perturbation, consistently with the ordering (4.8). For a discussion of the validity of the Born approximation see [77]. This equation is solved in WKBeam by a Monte Carlo method. More details on the derivation and formalism can be found in [75, 74].

### 4.2.2 Full-wave model

In the frame of this thesis, a 2D full-wave model was implemented in the COMSOL Multiphysics finite element solver [76]. We have seen previously that under the ‘frozen-blob’ approximation,  $E_j(\omega, \mathbf{x})$  can be well approximated by the solution of the equation of the wave electric field in the frequency domain, with  $n_e$  frozen to the value of  $n_{e,j}(\mathbf{x}) = \langle n_e(\mathbf{x}) \rangle + \delta n_{e,j}(\mathbf{x})$ , namely:

$$\nabla \times (\nabla \times \mathbf{E}(\mathbf{x}, \omega)) - \frac{\omega^2}{c^2} \hat{\epsilon}_r(\mathbf{x}, \omega) \mathbf{E}(\mathbf{x}, \omega) = \mathbf{S}(\mathbf{x}, \omega), \quad (4.16)$$

where  $c$  is the speed of light in free space, and  $\hat{\epsilon}_r(\mathbf{x}, \omega)$  is the cold plasma dielectric tensor computed with the equilibrium magnetic field and with density  $n_{e,j}(\mathbf{x})$  frozen at time  $t_j$ . In this thesis, a particular care was taken to avoid absorption of the mmw-beam by the plasma in the experiments, making the cold plasma model suitable for the numerical study of the propagation of the mmw-beam. The source  $\mathbf{S}$  accounts for the excitation of the beam at the launching antenna, with a polarization that can be either X or O-mode.

### Cold plasma tensor in arbitrary Cartesian coordinates

The standard derivation of the cold plasma tensor in the cold plasma model is performed in a local reference system  $(\mathbf{e}_1, \mathbf{e}_2, \mathbf{e}_3)$ , where  $\mathbf{e}_3$  is the unity vector  $\mathbf{e}_3 = \frac{\mathbf{B}_0}{|\mathbf{B}_0|}$  parallel to the magnetic field, and  $\mathbf{e}_1, \mathbf{e}_2$  are chosen such that  $(\mathbf{e}_1, \mathbf{e}_2, \mathbf{e}_3)$  is orthonormal. To avoid the local use of rotation matrices, thereby lightening the numerical calculations, the cold plasma dielectric tensor is derived in an arbitrary Cartesian frame. The derivation was performed by O. Maj in an internal report and is summarized here.

From the equation of motion in the cold plasma model, the current  $\mathbf{J} = \mathbf{J}(t, \mathbf{x})$  induced by the electric field  $\mathbf{E} = \mathbf{E}(t, \mathbf{x})$  is

$$\frac{\partial \mathbf{J}(t, \mathbf{x})}{\partial t} = \frac{\omega_p^2(\mathbf{x})}{4\pi} \mathbf{E}(t, \mathbf{x}) - \omega_c(\mathbf{x}) \mathbf{J}(t, \mathbf{x}) \times \mathbf{b}(\mathbf{x}). \quad (4.17)$$

Here,

$$\omega_p^2(\mathbf{x}) = \frac{4\pi e^2 n_e(\mathbf{x})}{m_e}, \quad \text{and} \quad \omega_c = \frac{e|\mathbf{B}_0(\mathbf{x})|}{m_e c}$$

are the electron plasma frequency and electron cyclotron frequency respectively,  $n_e(\mathbf{x})$  the electron density and  $\mathbf{b}(\mathbf{x}) = (b_1, b_2, b_3) = \frac{\mathbf{B}_0}{|\mathbf{B}_0|}$  the unity vector aligned with the magnetic field  $\mathbf{B}_0$ . The equation and quantities are given in the CGS units for better simplicity of the equations.

In the frequency domain, assuming

$$\mathbf{J}(t, \mathbf{x}) = e^{-i\omega t} \tilde{\mathbf{J}}(\omega, \mathbf{x}), \quad \mathbf{E}(t, \mathbf{x}) = e^{-i\omega t} \tilde{\mathbf{E}}(\omega, \mathbf{x}),$$

we can rewrite equation 4.17 as

$$\tilde{\mathbf{J}} - i \frac{\omega_c}{\omega} \mathbf{b} \times \tilde{\mathbf{J}} = -\frac{\omega_p^2}{4\pi i \omega} \tilde{\mathbf{E}}. \quad (4.18)$$

To find a linear algebraic relation between  $\tilde{\mathbf{J}}$  and  $\tilde{\mathbf{E}}$ , we separate the parallel and perpendicular components of equation 4.18 as follows

$$\tilde{J}_{\parallel} = -\frac{\omega_p^2}{4\pi i \omega} \tilde{E}_{\parallel}, \quad (4.19)$$

$$\tilde{\mathbf{J}}_{\perp} - i \frac{\omega_c}{\omega} \mathbf{b} \times \tilde{\mathbf{J}}_{\perp} = -\frac{\omega_p^2}{4\pi i \omega} \tilde{\mathbf{E}}_{\perp}. \quad (4.20)$$

The parallel component provides a direct relation between  $\tilde{J}_{\parallel}$  and  $\tilde{E}_{\parallel}$ . It can be demonstrated that equation 4.20 is equivalent to

$$\tilde{\mathbf{J}}_{\perp} = -\frac{\omega_p^2}{4\pi i \omega} \frac{\omega^2}{\omega^2 - \omega_c^2} \left[ \tilde{\mathbf{E}}_{\perp} + i \frac{\omega_c}{\omega} \mathbf{b} \times \tilde{\mathbf{E}} \right] \quad (4.21)$$

By adding the two components of  $\tilde{\mathbf{J}}$ , we find

$$\tilde{\mathbf{J}} = \tilde{\mathbf{J}}_{\perp} + \tilde{J}_{\parallel} \mathbf{b} \quad (4.22)$$

$$= -\frac{\omega_p^2}{4\pi i \omega} \left[ \left( 1 - \frac{\omega^2}{\omega^2 - \omega_c^2} \right) (\mathbf{b} \cdot \tilde{\mathbf{E}}) \mathbf{b} + \frac{\omega^2}{\omega^2 - \omega_c^2} \tilde{\mathbf{E}} + i \frac{\omega_c \omega}{\omega^2 - \omega_c^2} \mathbf{b} \times \tilde{\mathbf{E}} \right]. \quad (4.23)$$

From the Maxwell equation, we can write

$$\begin{aligned} \nabla \times (\nabla \times \tilde{\mathbf{E}}) &= \frac{\omega^2}{c^2} \left[ \tilde{\mathbf{E}} + \frac{4\pi i}{\omega} \tilde{\mathbf{J}} \right] \\ &= \frac{\omega^2}{c^2} \hat{\epsilon} \tilde{\mathbf{E}} \end{aligned} \quad (4.24)$$

From the expression of  $\tilde{\mathbf{J}}$  in 4.23, we obtain

$$\hat{\epsilon}\tilde{\mathbf{E}} = \tilde{\mathbf{E}} + \frac{4\pi i}{\omega} \tilde{\mathbf{J}} \quad (4.25)$$

$$= \left(1 - \frac{\omega_p^2}{\omega^2 - \omega_c^2}\right) \tilde{\mathbf{E}} + \left(\frac{\omega_p^2}{\omega^2 - \omega_c^2} - \frac{\omega_p^2}{\omega^2}\right) \mathbf{b}(\mathbf{b} \cdot \tilde{\mathbf{E}}) - i \frac{\omega_c}{\omega} \frac{\omega_p^2}{\omega^2 - \omega_c^2} \mathbf{b} \times \tilde{\mathbf{E}}. \quad (4.26)$$

With the standard Stix parameters [6],

$$S = 1 - \frac{\omega_p^2}{\omega^2 - \omega_c^2}, \quad D = \frac{\omega_c}{\omega} \frac{\omega_p^2}{\omega^2 - \omega_c^2}, \quad P = 1 - \frac{\omega_p^2}{\omega^2}, \quad (4.27)$$

we can write equation 4.26 as

$$\epsilon\tilde{\mathbf{E}} = S\tilde{\mathbf{E}} - iD\mathbf{b} \times \tilde{\mathbf{E}} + (P - S)\mathbf{b} \cdot (\mathbf{b} \cdot \tilde{\mathbf{E}}). \quad (4.28)$$

Introducing  $Q = P - S$ , the matrix form of the cold plasma dielectric tensor in an arbitrary Cartesian coordinate system is therefore

$$\epsilon = \begin{pmatrix} S(1 - b_1^2) + Pb_1^2 & +iDb_3 + Qb_1b_2 & -iDb_2 + Qb_1b_3 \\ -iDb_3 + Qb_2b_1 & S(1 - b_2^2) + Pb_2^2 & iDb_1 + Qb_2b_3 \\ +iDb_2 + Qb_3b_1 & -iDb_1 + Qb_3b_2 & S(1 - b_3^2) + Pb_3^2 \end{pmatrix}.$$

This cold plasma dielectric tensor is implemented in COMSOL with no assumption on the Cartesian coordinate system. One can notice that the tensor is Hermitian and therefore does not account for dissipation.

### Computational domain and boundary conditions

In this section and the following, we discuss the choice of the computational domain, the boundary conditions and the mesh elements together with their influence on the results of the full-wave simulations. For clarity, we define a simple but relevant test case. A 170 GHz ( $\lambda = 1.8$  mm) Gaussian beam, with a waist  $w_0 = 20$  mm is launched in the O-mode and traverses a blob with a Gaussian density distribution with a maximum  $\delta n_e = 1 \times 10^{19} \text{ m}^{-3}$ , which represents a fluctuation of electron density  $\delta n_e / n_e = 0.33$ . The situation is represented in fig. 4.3a). Figure 4.3b) shows a profile of  $|E|$  after propagation of the beam through the blob,



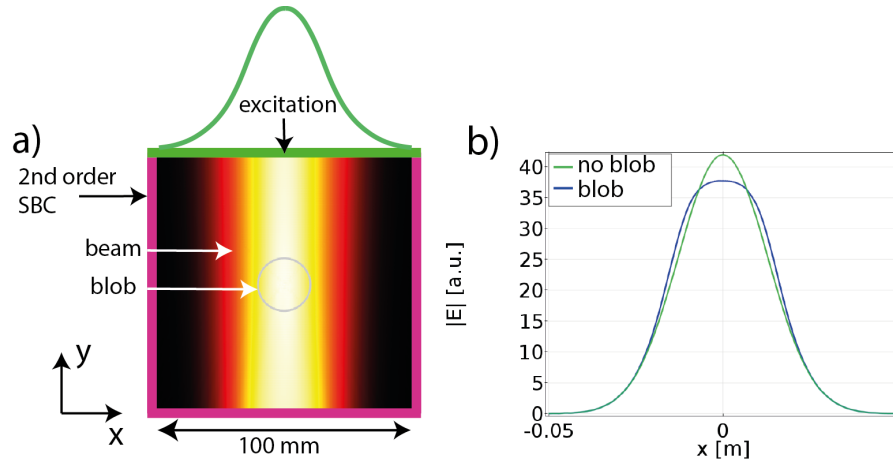


Figure 4.3 – Test case for the discussion of the computational domain, boundary conditions and mesh elements. a)  $|E|$  of an mmw-beam with  $w_0 = 20$  mm. The beam traverses a blob with a Gaussian distribution and a FWHM of 20 mm. The contour shows the blob at  $\delta n_{e,max}/2$ . Here, the size of the computational domain is  $0.1 \times 0.1$  m. b) Electric field profile at  $y = -0.05$  m in the presence (blue) and in the absence (green) of the blob.

at  $y = -0.05$  m in the absence and in the presence of the blob. The blob introduces a small broadening of the mmw-beam accompanied by a drop of  $|E|_{max}$  of about 12%.

Absorbing boundary conditions are used in this thesis. Perfectly reflecting boundary conditions were also investigated on a larger domain approximating the vacuum chamber cross section, but they did not provide satisfactory results. One reasonable explanation is that mmw's reflecting off of metallic surfaces can, in the real toroidal three-dimensional case, propagate away from the region near the beam and thus dissipate the mmw power.

In COMSOL, three absorbing boundary conditions are implemented, the first and second order Scattering Boundary Conditions (SBC) and the Perfectly Matched Layer (PML) [78, 76]. The SBCs are based on the Sommerfeld radiation condition, which can be written for a wave polarized in the  $z$ -direction as:

$$\lim_{r \rightarrow \infty} \sqrt{r} \left( \frac{\partial E_z}{\partial r} + i k_0 E_z \right) = 0. \quad (4.29)$$

Here  $r$  is the radial axis in cylindrical coordinates centered at the location of the mmw-source. The Sommerfeld radiation condition is exactly non-reflecting if the edges of the domain are infinitely far from the mmw-source. In practice, the SBC implemented in COMSOL is similar

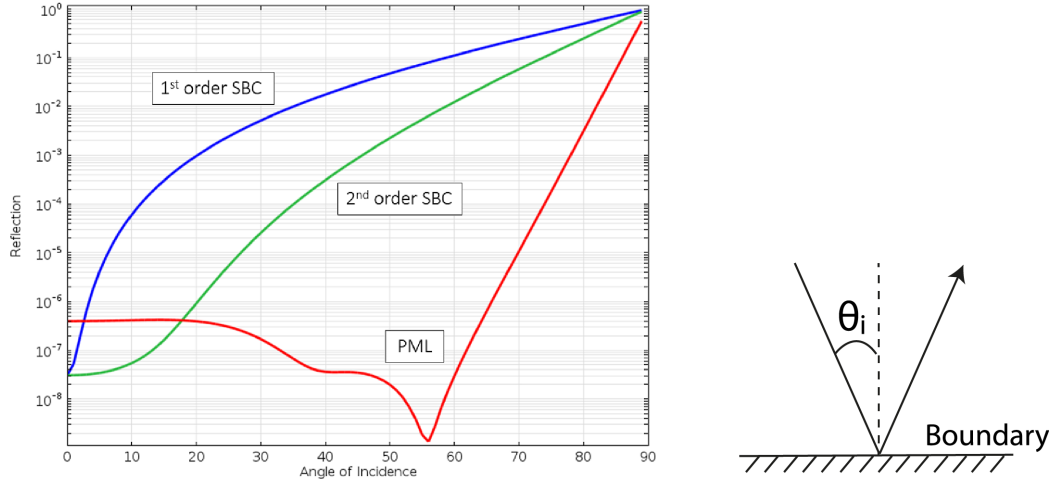


Figure 4.4 – From [76]: Reflection coefficient of an incoming mmw as a function of the incidence angle of the wave for three types of absorbing boundary conditions in COMSOL.

to the Sommerfeld radiation condition and can be written as:

$$\mathbf{n} \cdot (\nabla E_z) + i k_0 E_z + \frac{i}{2k_0} \nabla^2 E_z = 0, \tag{4.30}$$

where the second order term  $-\frac{i}{2k_0} \nabla^2 E_z$  is only taken into account in the second order SBC. The PML mimics a damped wave in a layer of thickness  $s$  defined by the user. The interested reader can find more details on the implementation of the PML in [79]. Figure 4.4 shows the reflection coefficient  $\Gamma = E_i/E_r$ ,  $E_i$  being the incident electric field amplitude and  $E_r$  the reflected electric field amplitude, associated with each absorbing boundary condition as a function of the incidence angle of the mmw on the boundary. Here, a grazing incidence angle is equal to  $90^\circ$  and a wave propagating perpendicular to the boundary has an incidence angle of  $0^\circ$ . Figure 4.4 shows that waves propagating parallel to the boundary are entirely reflected and that the absorption of the wave at the boundary is better when the propagation is closer to perpendicular. While PMLs exhibit the smallest reflexion coefficient over the largest range, they are not used in this thesis because they require either a circular or rectangular computational domain. Instead, we use  $2^{nd}$  order SBCs. They are also used in the following. Figure 4.5 illustrates the dependence of the reflection of the incident mmw-beam at the boundary on the incident angle. The bottom boundary is tilted to generate an incidence angle of  $0^\circ, 25^\circ, 75^\circ$  (fig. 4.5a-c) respectively. While the reflection is negligible for an incidence angle of  $0^\circ$  and  $25^\circ$ , it becomes visible for an incidence angle of  $75^\circ$ . At this angle, the reflected wave generates an interference pattern, indicated by the white arrow in fig. 4.5c). In practice, in both TORPEX and TCV simulations, the shape of the computational domain is designed to avoid grazing incidence angles, either by tilting the boundary or (is the computational

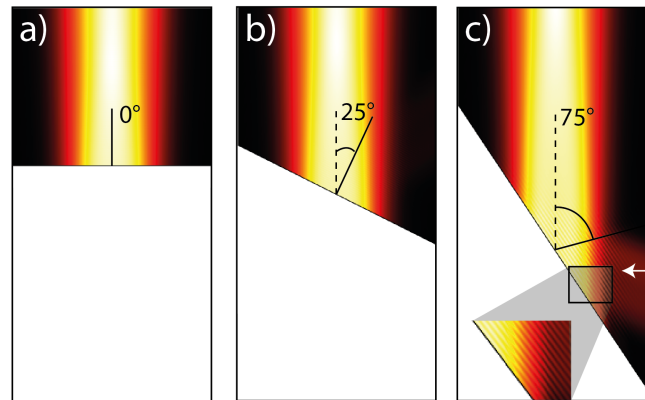


Figure 4.5 – a-c) Electric field norm associated with the mmw-beam propagation for three incidence angles on the bottom boundary,  $0^\circ$ ,  $25^\circ$ ,  $75^\circ$  respectively. The white arrow in c) points out to the wave reflected at the boundary, an interference pattern.

resources allows it) by enlarging the computational domain.

We will see later that for cases where the propagation length of the beam  $h$  is considerably larger than the wavelength of the beam  $\lambda$  (e.g. in TCV,  $h \sim 1.7m$  and  $\lambda = 2.5\text{ mm}$ ), the computational domain must be adapted to the geometry of the problem to avoid running out of memory during the computation. In fig. 4.6 and fig. 4.7, we study the influence of a shortening

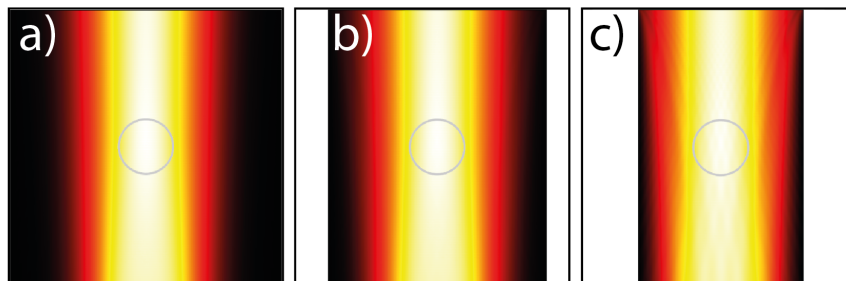


Figure 4.6 – a-c) Electric field norm associated with the mmw-beam propagation for three width of the computational domain, 0.1, 0.08, 0.06 m respectively. The black squares are equal and cover an area of  $0.1 \times 0.1\text{ m}$ . The waist of the Gaussian beam is 20 mm

of the computational domain in the direction transverse to that of the mmw-beam  $\mathbf{k}$  vector. Three widths of the computational domain are considered 0.1, 0.08, 0.06 m. Their size relative to the beam width can be seen in fig. 4.6. The results obtained for a width of 0.08 m and 0.1 m are similar although a small difference can already be observed in the edges, or ‘wings’ of the beam. For a width of the computational domain of 0.06 m, oscillations appear on the  $|E|$  profile and are associated with numerical diffraction. Numerical diffraction occurs when the non-physical edges of the computational domain act as diffracting edges such that non-physical (to the problem at hand) diffraction patterns appear in results elsewhere in

the physically relevant domain. In practice, we found that the effect numerical diffraction meaningful is negligible when the truncation of the computational domain occurs where  $|E| < 0.01|E|_{max}$ .

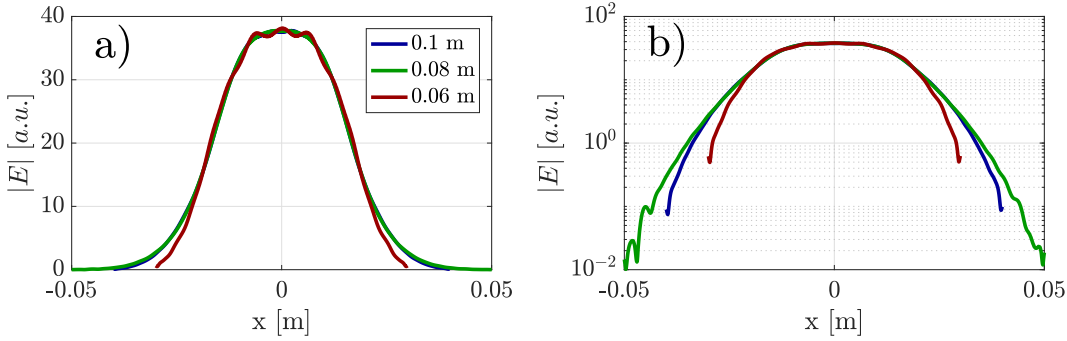


Figure 4.7 – Electric field norm profile after propagation at  $y = -5$  m for three width (in m) of the computational domain, in linear scale in a) and logarithmic scale in b). The results obtained for a width of 0.08 m and 0.1 m are similar although a small difference can already be observed in the edges, or ‘wings’ of the beam. For a width of the computational domain of 0.06 m, oscillations appear on the  $|E|$  profile and are associated with numerical diffraction.

**Mesh elements**

The mesh used in COMSOL is an unstructured triangular grid. The mesh is automatically generated by COMSOL and adapts to the geometry of the problem. Based on convergence studies, the maximum size of the mesh elements is set to  $\lambda/5$ . To illustrate the numerical aberrations occurring when coarse meshes are used, we solve our test case using three maximum sizes of the mesh elements,  $\lambda/5, \lambda/3$  and  $\lambda/2$ . A zoom on the mesh elements for the three cases is shown in fig. 4.8.

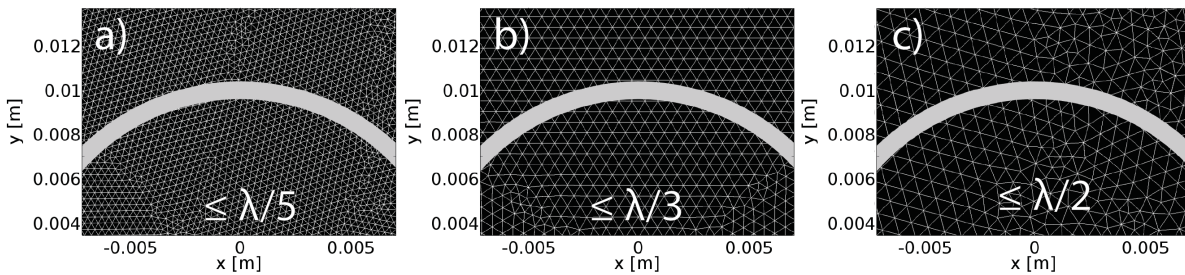


Figure 4.8 – a-c) Zoom on the mesh elements with a size of  $\lambda/5, \lambda/3$  and  $\lambda/2$  respectively. The contour represents the blob at  $\delta n_{e,max}/2$  as shown in fig. 4.3a) and 4.7.

The 2D map of  $|E|$  corresponding to the three cases is shown in fig. 4.9. For a coarse mesh, corresponding to a maximum size of the mesh elements of  $\lambda/2$ , the calculated  $|E|$  exhibits many structures and is considerably different than the other two cases. Figure 4.10 shows a profile of  $|E|$  at  $y = -0.05$  m for the three cases. It shows that the profile at  $\lambda/2$  exhibits

## 4.2. Numerical tools for millimeter-wave propagation

structures, that in our case could be mistaken by fluctuations of  $|E|$  induced by the plasma turbulence (see Chapter 7). The profiles at  $\lambda/3$  do not exhibit such structures and is similar to the one computed with  $\lambda/5$  on the outer part of the mmw-beam, but is more peaked at the center ( $x \in [-0.01 \ 0.01]$  m).

We have seen in this section that mesh elements with sizes larger than  $\lambda/5$  are not suitable for our study. It is important to note here that this is indeed the limiting size since the structures encountered in the turbulences of both TORPEX and TCV have typical sizes of  $a \geq \lambda$ .

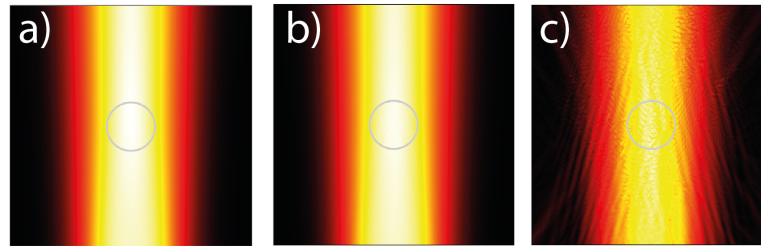


Figure 4.9 – a-c) Electric field norm for three sizes of the mesh elements,  $\lambda/5, \lambda/3$  and  $\lambda/2$  respectively

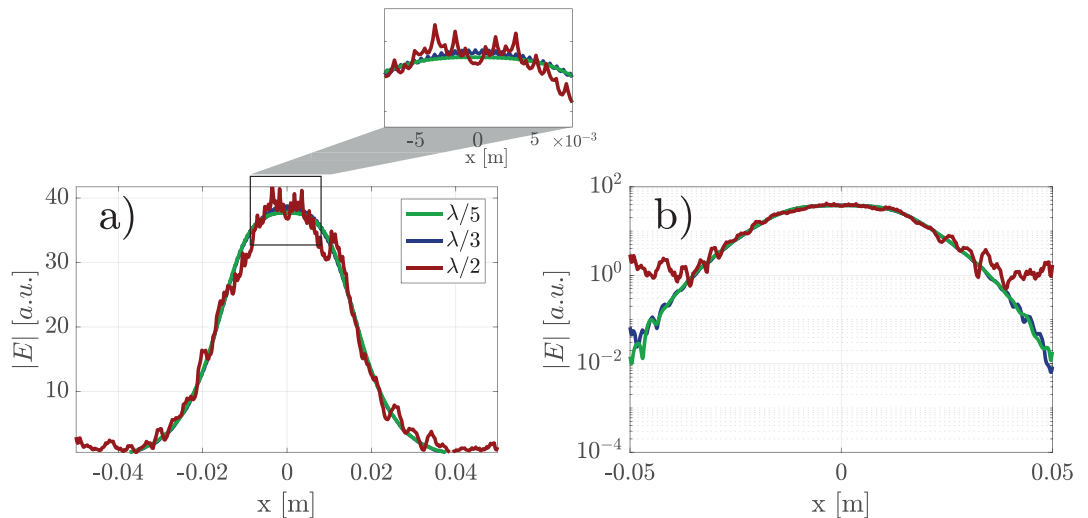


Figure 4.10 – a) Electric field norm profile after propagation at  $y = -5$  m for three sizes of the mesh elements,  $\lambda/5, \lambda/3$  and  $\lambda/2$  respectively b) Same in logarithmic scale.

### A note on the computational resources

Because we must calculate all three components of both the electric and magnetic field at each mesh point, full-wave simulations are voracious in terms of computational resources. Memory and time resources are often the limiting factor when considering a full-wave prob-

lem. To illustrate the situation<sup>1</sup>, we consider a 2D computational domain of size  $20\lambda \times 36\lambda$ . The computations were performed on a computer with 4 GB of RAM and 2 CPUs. Figure 4.11-right shows the evolution of the computational resources (computational time -left- and memory) with the size of the mesh elements (defined as a function of  $S$  the surface of a triangular element of side  $\lambda$ ) and therefore the number of grid elements. It shows that that the

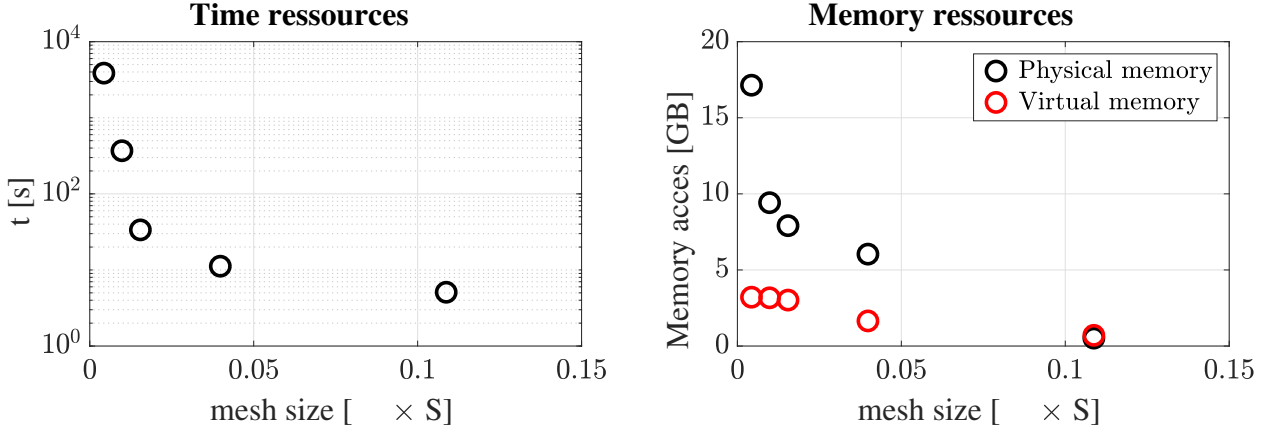


Figure 4.11 – Computational resources for the full-wave model as a function of the size of the mesh elements  $S$ . Note, left plot (time) has a logarithmic scale.

calculation time grows as the size of the mesh elements is decreased. The memory access is multiplied by ten when the mesh size is multiplied by ten (when the size of the mesh element is varied from  $0.11S$  to  $0.01S$ ). The computational time is multiplied by more than 70. The same is also true for increasing the size of the computational domain.

To be able to run TCV simulations, a server with 196 GB of RAM and 16 CPUs was installed at the SPC. With this configuration, the computational domain covering the mmw-beam propagation has to be divided in 3 sections:  $Z = 0.99 \text{ m} \rightarrow 0.5 \text{ m}$ ,  $Z = 0.5 \text{ m} \rightarrow -0.1 \text{ m}$  and  $Z = -0.1 \text{ m} \rightarrow -0.77 \text{ m}$  with a transverse dimension between 0.2 m (at the beam injection) and 1 m (at the floor of the vessel) in order not to run out of memory. The complex electric field computed at each output boundary line is taken as an input for the following section. Each run takes approximately 50 min to be completed using the 16 CPUs.

In this chapter we have presented the numerical tools used in this thesis. The turbulence code GBS, used to provide a 2-D time-resolved imaging of the electron density in the SOL, was described together with the validation procedure. We introduced the physical model of the WKBeam code run by O. Maj at the Institute of Plasma Physics in Garching. Finally, we presented the full-wave model implemented in the frame of this thesis. We discussed the boundary conditions, the size of the computational domain and the size of the mesh elements.

<sup>1</sup>The study of the computational resources was performed in the frame of my master project at the Swiss Plasma Center in 2014

## 5 Mmw-beam scattering by turbulent structures and blobs in simple magnetized toroidal plasmas

The simple magnetized torus (SMT) is a magnetic configuration characterized by helical open magnetic field lines (see fig. 3.3 in chapter 3). In this magnetic configuration where the SOL extends over typical distances of a few centimeters, in SMTs, plasma turbulence exhibits universal properties similar to those observed in the SOL of tokamaks [54]: blobs and filaments are also present in this configuration. Unlike in a confined magnetic configuration, a similar turbulence state exists over a long path length for the mmw-beam (here up to  $\sim 1.7$  m in the TCV case). Hence, we can expect its effect on the mmw-beam to be enhanced. The experiments are run in both TCV and TORPEX. In the two cases, a mmw-beam is injected from the top of the vessel and the transmitted power is measured at the bottom of the vessel after propagation in the plasma.

This chapter is organized as follows: In section 5.1 and 5.2<sup>1</sup>, we present TCV SMT plasmas together with experimental observations during the TCV SMT campaign. We report on preliminary indications of an effect of positive electron density structures on the mmw-beam transmission. Better diagnostic accessibility and device simplicity motivate to pursue the experiments on the TORPEX device. In section 5.3, we present the SMT plasmas and associated turbulence in TORPEX together with a reliable methodology to measure the electron density  $n_e(\mathbf{x}, t)$ . In section 5.4, we investigate experimentally the influence of blobs on the mmw-propagation and show that the presence of blobs in the path of the mmw-beam is responsible for fluctuations of the locally-measured mmw-power. Depending on the location of a blob, we demonstrate that it can have an opposite effect on the detected mmw-power, and blobs associated with larger densities have a stronger effect on the mmw-propagation. Finally, using full-wave numerical simulations, we show in section 5.5 that a defocusing of the mmw-beam occurs in the wake of the blob, resulting in a decrease in power density behind the structure and an increase in power density at the edges of the structure, explaining the observed fluctuations of the detected mmw-power.

---

<sup>1</sup>The work presented in this section was published in [34]

## 5.1 Simple magnetized torus configurations in TCV

Scattering experiments on TCV in the SMT configuration prior to L-mode limited plasmas were motivated by the following: while using the same experimental setup as in the L-mode TCV scattering experiments, the well characterized turbulence and blob dynamics of SMT plasmas in TORPEX [80, 81, 82] (see section 5.3) suggest that turbulent structures are present along the entire beam path in TCV SMT experiments. This would result in an enhanced effect of the turbulence on the mmw-beam.

The simple magnetized torus (SMT) is not a standard plasma configuration in TCV. It was first developed for the EC-wall cleaning (ECWC) TCV campaign to help preparing the operation of the JT-60SA tokamak [83]. ECWC represents an alternative to DC-glow discharges for machines using superconducting toroidal field coils, in which the toroidal field is always present. ECWC between discharges helps reducing hydrogen recycling at plasma facing walls, which can affect plasma confinement. During the TCV SMT campaign, successful plasma breakdown

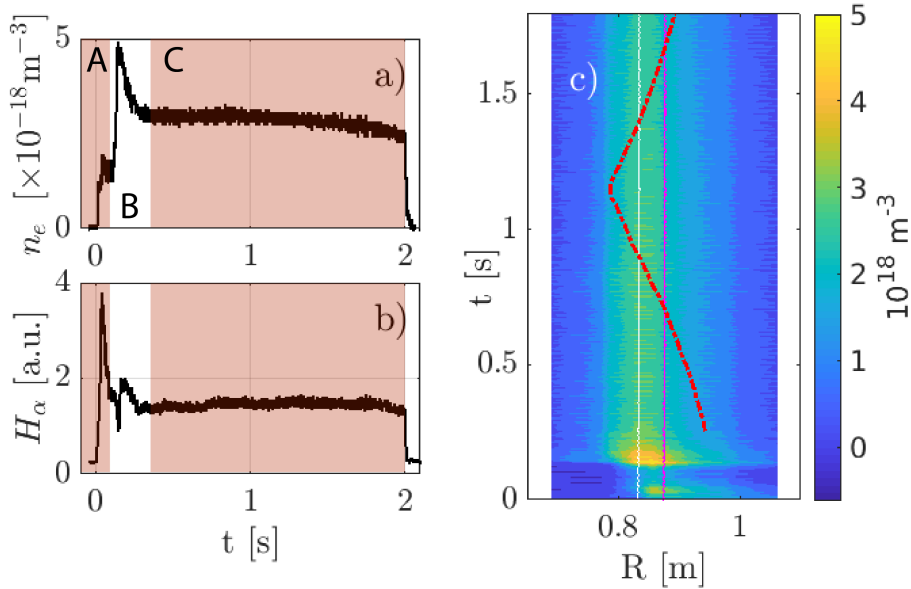


Figure 5.1 – Discharge 55790: a) Line integrated electron density measured by the Far InfraRed interferometer (FIR) chord located at the radial position of the cold X2 resonance (in white in c). b)  $D_\alpha$  emission measured by a photodiode with a vertical line of sight. The breakdown phase (or ionization phase) is identified by the red shaded area A. During the second phase (identified by the white-shaded area B), the plasma is spread throughout the vessel. The red shaded area C is the stationary phase of the plasma. c) Time-evolution of the radial electron density profile measured by the FIR. The red line is the geometric footprint of the center of the mmw-beam in vacuum associated with the scan of the  $\theta_m$  angle. The white line shows the radial position of the cold X2 resonance and the magenta line the cold X3 resonance.

was achieved by injecting 450 kW of X2-power in deuterium  $D_2$  gas. The EC-power is evenly injected via gyrotron 4 (equatorial) and 6 (upper lateral). The magnetic field components are



## 5.1. Simple magnetized torus configurations in TCV

$B_T = 1.4$  T and  $B_v \sim 0.6\% B_T$ , resulting in a helical field line configuration with  $N \approx 93$  turns;  $N = 2\pi R_0 B_v / (B_T h_0)$ ,  $h_0$  being the height of the vacuum vessel. Since all the field lines are open, there is no confined region in SMT plasmas and the EC-power is necessary to sustain the discharge. Figure. 5.1 shows the evolution of the line integrated electron density and the  $D_\alpha$  emission during an SMT discharge in TCV.

The plasma breakdown phase lasts for  $\sim 100$  ms (A in fig. 5.1a,b) and corresponds to the ionization of the plasma. During this phase, the plasma is locally formed around the X2 launcher and is associated with strong  $D_\alpha$  emission. In the second phase (B,  $\sim 100 - 200$  ms), the plasma spreads throughout the vessel. It is associated with a rapid increase of the electron density. Finally, the plasma reaches a stationary phase (C), for which typical electron densities of  $0.7 - 4 \times 10^{18} \text{m}^{-3}$  and electron temperatures of  $30 - 50$  eV are achieved as indicated by TS measurements (not shown here). Since  $n_e$  and  $T_e$  are low in the TCV SMT plasmas, absorption is negligible for the third harmonic beam. The length of the plasma is in principle only limited by the pulse length of the gyrotrons and could be extended to 4 s. During the stationary phase, the electron density can be kept constant within a range of  $\sim 10\%$ .

The time-evolution of the line-integrated  $n_e$  profile measured by the Far InfraRed interferometer (FIR) is shown in fig.5.1c) and its time-average  $\langle n_e \rangle$ , computed on the stationary phase C, is shown in fig. 5.2a). The maximum of  $\langle n_e \rangle$  is located at the position of the cold  $X_2$ -resonance (in white in fig.5.1c), i.e.  $R = 0.83$  m. The  $n_e$  profile is steeper on the HFS and flatter in the LFS. Fig. 5.2b) shows the time averaged  $\langle I_{sat} \rangle$  profile (black) and the standard deviation  $\sigma_{I_{sat}}$  (red) of the ion saturation current measured by the Langmuir probes located at the floor of the TCV vessel.  $\langle I_{sat} \rangle$  is maximum at  $R = 0.83$  m, consistently with  $\langle n_e \rangle$  within the spatial accuracy of FIR measurements. The  $\sigma_{I_{sat}}$  profile shows the level of fluctuations in the  $I_{sat}$  signal measured by the probes. The maximum of  $\sigma_{I_{sat}}$  occurs a few centimeters more to the LFS at  $R = 0.85$  m indicating a region of larger  $n_e$  fluctuations. To determine the radial extent of the electron density structures around  $R = 0.85$  m, we compute the cross-correlation of the  $I_{sat}$  signal of the probe located at  $R = 0.85$  cm with the other probes located on the floor of the vessel. The cross-correlation coefficient at zero time-lag  $C_0(0)$  is shown in fig.5.2c). It indicates the presence of electron density structures with typical scale lengths of the order of  $\sim 2$  cm.

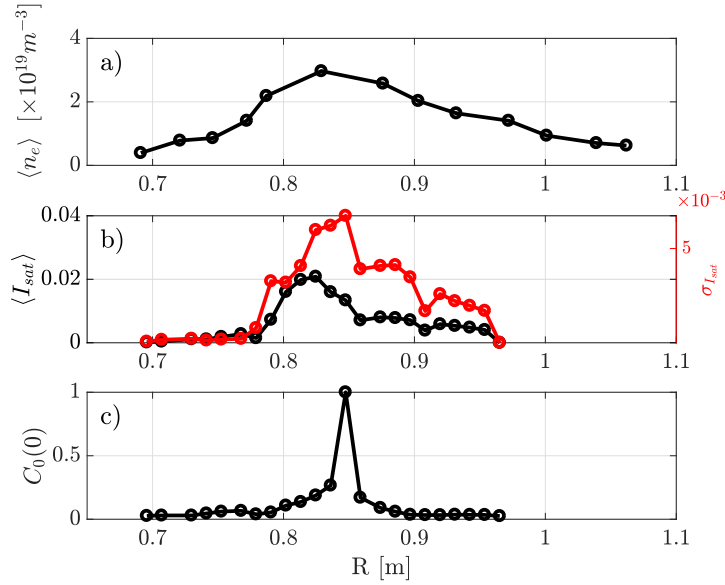


Figure 5.2 – Discharge 55790: a) Time-averaged radial profile of  $n_e$  measured by the FIR. b) In black: time-averaged ion saturation current profile measured by the Langmuir probes (LPs) located at the floor of the vessel. In red: standard deviation associated with the probes' measurements. c) Cross-correlation coefficient at zero time-lag between the LPs  $I_{sat}$  signals and the  $I_{sat}$  signal from the probe located at  $R = 0.85$  cm.

## 5.2 Scattering experiments in TCV SMT plasmas

For the scattering experiments, 200 kW of X3 power are injected at  $R = 0.88$  m. The mmw-power  $P$  measured by X3TD is shown in fig. 5.3a), for two values of the electron density  $n_e = 2.3 \times 10^{18} \text{ m}^{-3}$  (discharge 55776) and  $n_e = 3.4 \times 10^{18} \text{ m}^{-3}$  (discharge 55790). The geometrical center of the beam footprint on the floor of the vessel (as computed in vacuum) during the discharge is shown in fig. 5.1c). A double scan in angle is performed. The poloidal angle  $\theta_m$  of the injection mirror is swept from  $43.5^\circ$  to  $48^\circ$  (LFS to HFS) and back again (HFS to LFS), see fig. 5.3b). The first half of the sweep is performed during the non-stationary phase of the gyrotron pulse (the frequency is changing as the cavity heats) and is not used in this study (and not shown in fig. 5.3). Figure 5.3a) shows that the transmission is maximum around  $\theta_m = 45.5^\circ - 46^\circ$  and drops to zero for angles smaller than  $44^\circ$  and larger than  $47^\circ$ .  $P$  is characterized by the presence of fluctuations. Note that although the mmw-power  $P$  is represented as a function of  $\theta_m$ , the fluctuations are a temporal feature.

The first four moments of  $P(t)$ , are shown in fig.5.4a-d) as a function of  $\theta_m$  for the two discharges. The moments are computed on time-windows of 32 ms, during which the poloidal angle of the mirror varies by  $0.2^\circ$ . On each time-window, the moments are computed on  $N \sim 600$  independent values of  $P$  separated by a time step longer than the auto-correlation time of  $P$  ( $\sim 30 \mu_s$ ). Figure 5.4a) (red curve) shows that the maximum of  $\langle P \rangle$  occurs at a smaller  $\theta_m$  in discharge 55776 ( $\langle n_e \rangle = 2.3 \times 10^{18} \text{ m}^{-3}$ ) and reaches a higher value  $\langle P \rangle_{max}$ . This

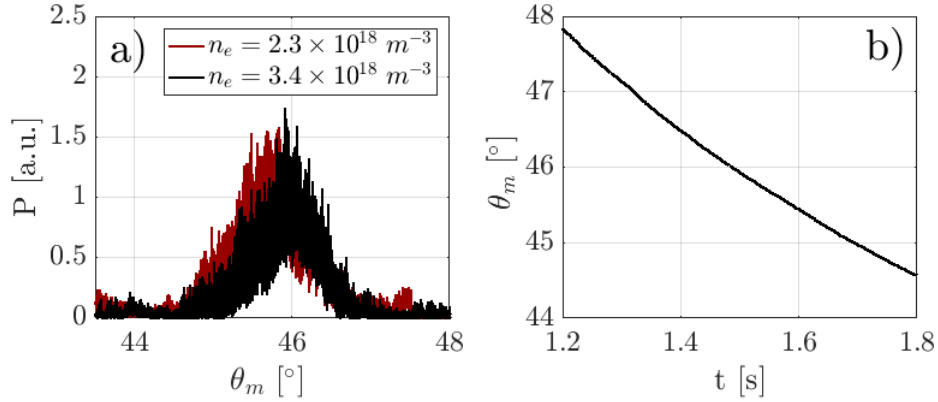


Figure 5.3 – a) Mmw-power measured by X3TD as a function of the poloidal angle of the launching mirror for discharge 55776 and 55790, corresponding to a maximum electron density of respectively  $2.3 \times 10^{18} \text{ m}^{-3}$  and  $3.4 \times 10^{18} \text{ m}^{-3}$ . b) Poloidal angle of the mirror as a function of time.

is consistent with a weaker refraction of the mmw-beam occurring at lower densities. The normalized level of fluctuations  $\Sigma = \frac{\sigma(P)}{\langle P \rangle}$ , where  $\sigma(P)$  is the standard deviation of  $P$  and  $\langle P \rangle$  the time-averaged value of  $P$  respectively, is shown in fig.5.4b).  $\Sigma \approx 0.1$  at the maximum of  $\langle P \rangle$  for both cases and reaches  $\sim 0.7$  at the minimum of detection for  $\langle n_e \rangle = 3.4 \times 10^{18} \text{ m}^{-3}$ . The small value of skewness (fig. 5.4c) and the value of the kurtosis  $\sim 3$  (fig.5.4d) around the maximum of transmission indicate that the probability distribution function (PDF) of  $P$  fluctuations is rather Gaussian around  $\langle P \rangle$ . For  $\langle n_e \rangle = 3.4 \times 10^{18} \text{ m}^{-3}$ , both the skewness and the kurtosis are larger for  $\theta_m$  around the minima of  $\langle P \rangle$  (the wings of the distribution), indicating that at these angles ( $\theta_m \leq 45^\circ$  and  $\theta_m \geq 46.8^\circ$ ), the fluctuations are caused by infrequent extreme increases of  $P$  (bursty events).

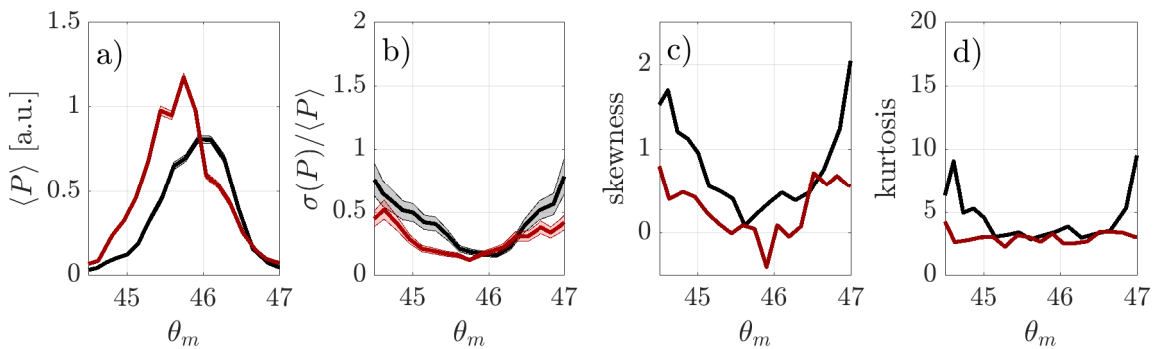


Figure 5.4 – The first four statistical moments of the transmitted mmw-power signal as a function of the poloidal angle of the injection mirror computed on time windows of 32 ms, in red for discharge 55776 and in black for discharge 55790. b) The standard deviation is normalized to the time-averaged value of the detected mmw-power. The errors in a) and b) are given by the statistical uncertainties in the estimates [84, 85].

## Chapter 5. Mmw-beam scattering by turbulent structures and blobs in simple magnetized toroidal plasmas

A continuous injection of mmw-power at  $\theta_m = 45.5^\circ$  is performed in discharge 56455. In this discharge  $\langle n_e \rangle \approx 10^{18} \text{m}^{-3}$ . The cross-correlation function  $C_0$  between the  $P$  signal and the  $I_{sat}$  signal measured by the Langmuir probes is computed to investigate the possible effect of electron density fluctuations on the mmw-transmission. Probes located on the floor of the vessel between  $R = 0.87 \text{ m}$  and  $R = 0.88 \text{ m}$ , where the aperture of the X3TD waveguide is located ( $R \in [0.848, 0.912] \text{ m}$ ), show a significant level of cross-correlation (see fig. 5.5). As shown in fig. 5.5, the maximum level of correlation is found for the probe located at  $R = 0.87 \text{ m}$  located at the same radial position as the X3TD aperture. Its positive value indicates that structures associated with positive electron density fluctuations detected by the probe at this location are correlated with an increase of the detected mmw-power. The probe located at  $R = 0.88 \text{ m}$  have a similar maximum level of cross-correlation, occurring with a time-delay of  $20 \mu\text{s}$ , suggesting that the same structure is causing a positive  $\delta P$  but is detected later by the probe on the LFS. For the probe located at  $R = 0.89 \text{ m}$   $|C_0|_{max} \approx 0.05$ , the correlation is shown in fig.5.5)c) and is no longer significant.

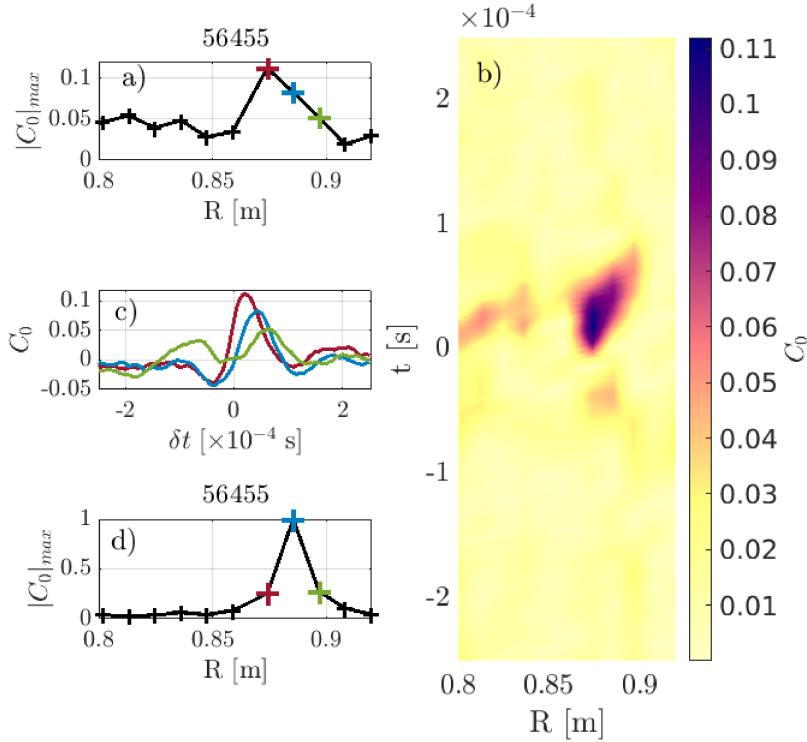


Figure 5.5 – a) Maximum of the cross-correlation function  $C_0$  between the  $I_{sat}$  signal from the LPs at the floor of the vessel and the measured mmw-power  $P$ . b) Map of the cross-correlation function as a function of the position of the LPs in a). c) Cross-correlation function between the  $I_{sat}$  signal, measured between the three LPs indicated by the colored crosses in a), and the  $P$  signal. d) Maximum of the cross-correlation function between the  $I_{sat}$  signal from the LPs at the floor of the vessel and the  $I_{sat}$  signal of the probe identified in blue in a).

The probes located at  $R = 0.87 - 0.89 \text{ m}$  are selected as a reference to perform Conditional

Sampling (CS) on the  $P$  signal. We detect positive bursts in  $I_{sat}$  satisfying the following condition:  $I_{sat} > \langle I_{sat} \rangle + 2\sigma$ , where  $\langle I_{sat} \rangle$  is the time-average of  $I_{sat}$  performed over the time trace,  $\sigma$  the standard deviation of  $I_{sat}$ . We find  $N \sim 1000$  events. The results of the CS are shown in fig.5.6. An increase of power  $\frac{\delta \tilde{P}}{\langle P \rangle} \approx 5\%$  (defined in section 3.4) is clearly visible after a smaller amplitude drop. This increase is maximum for the reference probe located at  $R = 0.87$  m and is less pronounced for the probe located at  $R = 0.89$  m. This analysis suggests that positive density structures can be responsible for fluctuations in the mmw-transmission.

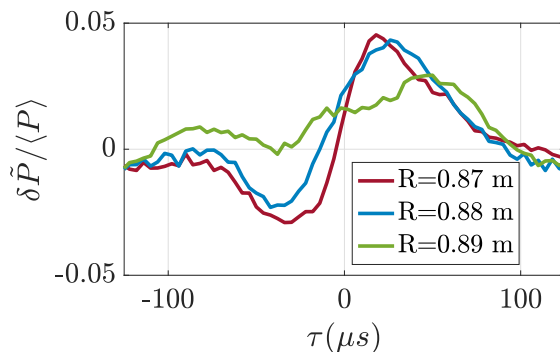


Figure 5.6 – Normalized fluctuations of the detected mmw-power obtained by CS using three different LPs (identified in fig. 5.5a) as a reference as a function of the CS time  $\tau$  centered around the event detection. The definition of the CS time  $\tau$  is given in section 3.4.

Advancing the physics understanding is hampered by both the difficulty of performing SMT discharges on TCV and the limited diagnostic accessibility on TCV at these values of  $n_e$  and  $T_e$ . For this reason, in the next sections of this chapter, investigations are carried out in the TORPEX device. We will show that TORPEX is a very powerful device providing a well-diagnosed environment to study mmw-scattering in an SMT configuration.

### 5.3 Simple magnetized plasmas in TORPEX

In this section<sup>2</sup>, we describe the SMT scenarios in TORPEX. After discussing the plasma production in TORPEX, we present the main characteristics of the plasma and the associated turbulence. Finally, a description of the blobs occurring in TORPEX together with their generation mechanisms are presented.

In TORPEX, the SMT configuration is produced by the superimposition of a vertical magnetic field  $B_z = 2.1$  mT on a toroidal magnetic field  $B_y = 74$  mT (see fig.3.3 in chapter 3). A hydrogen plasma is produced by injecting 300 W of microwave power at  $f_{RF} = 2.45$  GHz. Power is injected in the O-mode from the bottom of the vessel. A small fraction of the power is absorbed directly at the EC-layer (first-pass absorption). The remaining fraction is reflected-off the metallic walls of the vacuum chamber back into the plasma exciting both O1- and X1-mode waves.

<sup>2</sup>The work presented in section 5.3-5.5 of this chapter was published in [35]. The content of the article is freely adapted to match the format of this thesis.

## Chapter 5. Mmw-beam scattering by turbulent structures and blobs in simple magnetized toroidal plasmas

The X-mode polarization of the wave encounters the upper-hybrid (UH) resonant layer, where  $f_{RF} \approx \sqrt{f_{ec}^2 + f_p^2}$ , where  $f_{ec} = 2\pi \frac{eB_0}{m_e}$  is the electron cyclotron frequency and  $f_p = 2\pi \sqrt{\frac{e^2 n_e}{m_e \epsilon_0}}$  the plasma frequency.

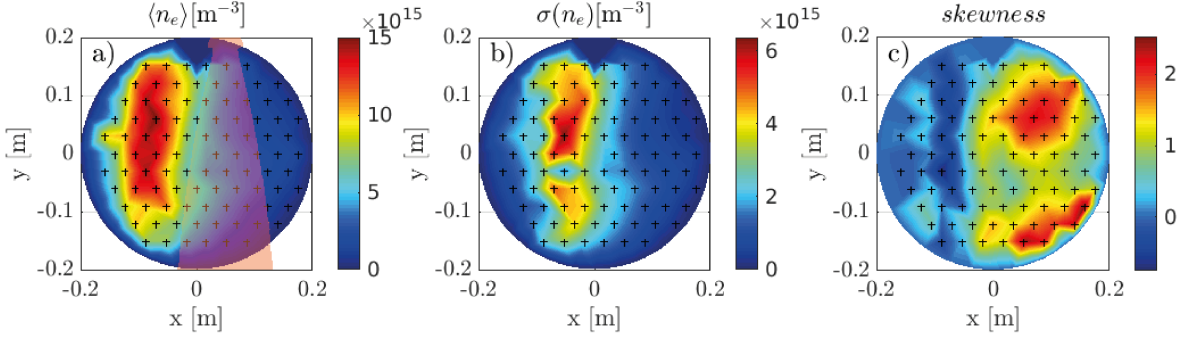


Figure 5.7 – *Discharge 69184*: a) Time-averaged electron density profile. The orange area represents the electric field contour at 1/e of the maximum associated with the 29 GHz mmw-beam. b) Standard deviation of the  $n_e$  time-traces measured by the HEX TIP-U probes. c) Skewness of the  $n_e$  time-traces measured by the HEX TIP-U probes. The black crosses correspond to the position of the probes.

Most of the plasma is produced in the UH layer, which in the present experiments is located at  $x = -0.07$  m and typically has a width of  $\sim 1$  cm [86]. Absolute measurements of  $n_e$  are prone to errors (that can exceed 50%) due to the uncertainties in the estimate of the ion collection surface. The 2-D average electron density  $\langle n_e \rangle$ , standard deviation  $\sigma(n_e)$  and skewness profiles in a typical discharge used in this thesis is shown in fig. 5.7. To obtain the time-averaged electron density profile shown in figure 5.7a), the ion saturation current profile from HEX TIP-U (more details in chapter 3) is calibrated using the following methodology. The electron density profiles from HEX TIP-U are obtained from the ion saturation current  $I_{sat}$  through the Bohm relation:

$$I_{sat} = \frac{n_e}{2} \sqrt{\frac{T_e}{m_i}} eA \quad (5.1)$$

where  $A$  the effective surface of the probe. The effective surface  $A$  is not well determined, and needs therefore to be calibrated. Since most of the absorption in TORPEX occurs at the UH resonance, the electron density profile measured by HEX TIP-U (in yellow in fig. 5.8) is re-scaled to match  $n_{UH}$  at the position of the maximum absorption, taken to be the position of the maximum density. This is equivalent to adjusting the effective surface of the probe  $A$  (see below) to obtain a good match of the HEX TIP density and the  $n_{UH}$  density at the location

of the peak density. The electron density  $n_{UH}$  for which  $f_{RF} = f_{UH}(x)$  in TORPEX is:

$$n_{UH}(x)[10^{17} \text{m}^{-3}] \approx \frac{f_{RF}^2[\text{GHz}]}{8} \left[ 1 - \left( \frac{x_{EC}}{x} \right)^2 \right] \quad (5.2)$$

$n_{UH}(x)$  is represented in green in fig. 5.8a). The resulting profile is shown in light blue in fig. 5.1a). Here, the  $n_e$  profile is re-adjusted taking into account the variations of  $T_e$  in the  $x$ -direction. The  $T_e(x)$  profile is shown in fig.5.8b). For  $x \in [-0.11, 0.1]$  m it is obtained using triple probe measurements at the TORPEX midplane [87]. The profile is extrapolated linearly for  $x < -0.11$  m and  $x > 0.1$  m. The  $n_e$  profile is corrected to account for the variations in  $T_e(x)$  and the result is shown in dark blue in fig. 5.8a).

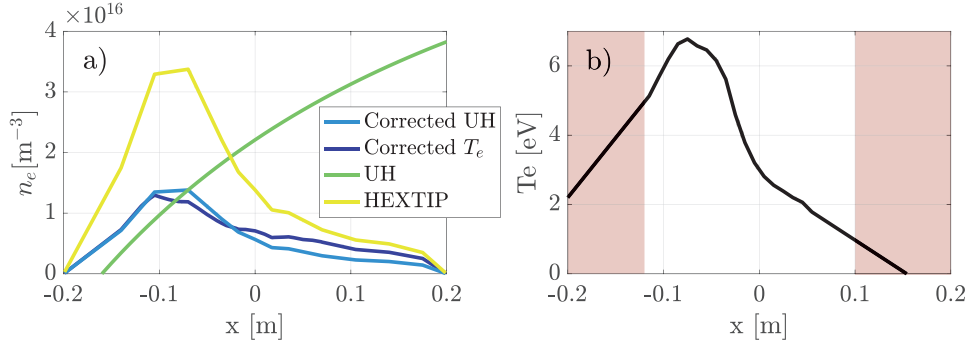


Figure 5.8 – a) The electron density profile measured by the HEXTIP robe (yellow) is adjusted to match the electron density at the UH resonance (light blue) and corrected (dark blue) using the  $T_e$  profile show in b). The electron density associated with the UH resonance is shown in green. b) Radial profile at  $z = 0$  m of the electron temperature. The electron temperature profile in the red-shaded area was extrapolated linearly from the profile in the white area.

The plasma in TORPEX is dominated by an ideal interchange wave located around  $x \approx -7$  cm [88, 89]. The parallel wave number is  $k_{\parallel} \approx 0$  and the perpendicular wave number is  $k_{\perp} = 2\pi/\Delta \approx 35 \text{m}^{-1}$ , where  $\Delta = 2\pi R_0 B_z / B_y \approx 17.8$  cm is the vertical displacement of a field line after one toroidal turn. The ideal interchange wave is associated with coherent oscillations of the electron density at the frequency  $f_m \approx 4.15$  kHz. The power spectral density coefficient  $\Gamma$  at  $f_m$  of the HEXTIP probes located at  $z = 0$  m is shown in fig. 5.9 and clearly identifies the radial location of the interchange wave.  $\Gamma$  is maximum at the location of the interchange wave and decreases with  $x$ . At  $x = 5$  cm,  $\Gamma \approx 0.1\Gamma_{max}$ .

Radially elongated density structures can form on the LFS of the positive cells of the interchange wave. An example is shown in fig. 5.10a). These structures are sheared off by the  $\mathbf{E} \times \mathbf{B}$  plasma flow in a corridor where the  $\mathbf{E} \times \mathbf{B}$  drift is directed radially outwards due to plasma convection. Once detached from the interchange wave, these structures form blobs. The

## Chapter 5. Mmw-beam scattering by turbulent structures and blobs in simple magnetized toroidal plasmas

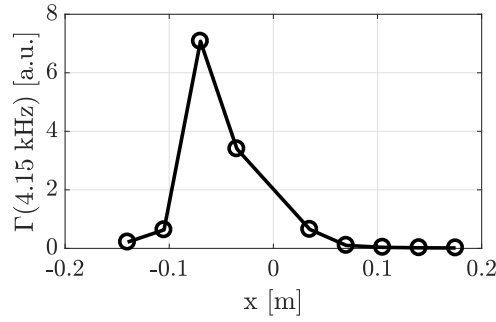


Figure 5.9 – Power spectral density coefficient at the frequency of the mode  $f_m$  of the  $I_{sat}$  signal measured by the HEXTIP probes located at  $z = 0$  m.

newly-formed blobs represent field-aligned structures of enhanced electron density relative to the background plasma. The  $\nabla B$  and curvature drifts are responsible for a vertical charge separation in the blob, which generates a vertical electric field. The resulting  $\mathbf{E}$  produces a radially outward  $\mathbf{E} \times \mathbf{B}$  drift, responsible for the radial motion of the blob in the LFS with a radial velocity typically of the order of  $v_x \approx 1$  km/s [82]. More details on blob formation mechanisms can be found in [80, 63, 81, 82, 90].

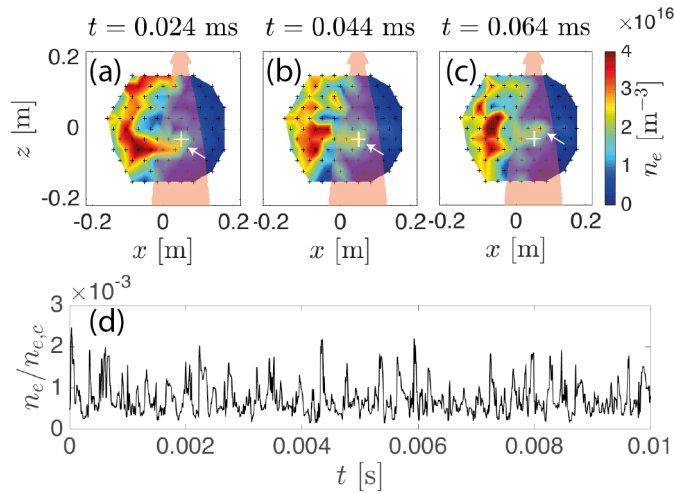


Figure 5.10 – a-c) Snapshots of density fluctuations showing a) blob (indicated by the white arrow) formation, b) detachment and c) radial propagation (in the vicinity of the white cross). The shaded area represents the mmw-beam at full-width-at-half-maximum of the mmw-power from COMSOL simulations in vacuum. d) Time evolution of the electron density normalized to the X-mode cut-off electron density as measured at the location in white in a-c).

An example of blob formation in TORPEX is shown in the snapshots of fig.5.10a-c). The radially elongated structures, which will generate the blob, is forming from the interchange wave (a). The blob is detaching (b) where it is detected by the probe at the position of the white cross and then propagates radially outwards (c). A typical blob in TORPEX has a half-width at half-maximum (HWHM) of  $a \sim 2.5$  cm and is associated with density fluctuations  $\delta n_e/n_e$  up



to 100% [82]. The time-trace of the electron density measured by the probe in white is shown in fig. 5.10d). The fast increases, or bursts, in  $n_e$  are associated with blobs passing by the probe.

## 5.4 Influence of the plasma on the mmw-propagation

A low-power (7 mW) mmw-beam at  $f = 29.7$  GHz (wavelength  $\lambda = 10.1$  mm in vacuum) is injected from the top of the TORPEX vessel at  $x = 5$  cm,  $z = 23$  cm. The contour of the electric field norm (at  $1/e$  of the maximum) associated with the mmw-beam is shown in fig. 5.10a) as a shaded orange area. This is obtained from full-wave simulations described later in section 5.5. From fig. 5.10d), we see that in the blob region,  $n_e/n_{e,c} \sim 10^{-3}$ , where  $n_{e,c}$  is the cut-off density of the X-mode. Hence, the mmw-beam frequency is far from cut-off. The wave is launched in the X-mode using a pyramidal horn antenna and is detected (X-mode polarization) after transmission through the plasma. The receiver is a radially-movable ( $x \in [-3, 12]$  cm) pyramidal horn that can, thus, be used to reconstruct the time-averaged beam profile as well as to measure mmw-power fluctuations at different radial positions. Technical details on the millimeter-wave injection/detection system are given in chapter 3. At these low electron densities and toroidal field, the O-mode and X-mode component of the mmw-wave have very similar behavior in the plasma. The measured beam profile is a convolution between the radiation patterns of the transmitter and the receiver.

Figure 5.11 summarizes the results of the experiment.

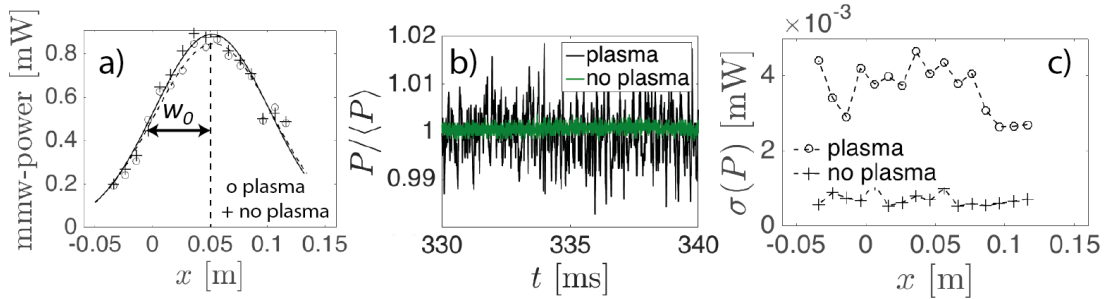


Figure 5.11 – Statistical properties of the detected mmw-power signal. (a) Time-averaged detected mmw-power with and without plasma as a function of the radial position of the receiver. (b) Comparison of the time evolution of the detected mmw power  $P$ , normalized to its mean value  $\langle P \rangle$ , with (black) and without (green) a plasma. (c) Standard deviation of the detected mmw-power signal as a function of the radial position of the receiver.

The profiles obtained in the presence and in the absence of a plasma are shown in fig. 5.11a). Both profiles can be approximated by a Gaussian profile with a HWHM of  $w_0 \approx 6$  cm, showing that the presence of the plasma does not affect (within the detection limit) the time-averaged profile of the mmw-beam. The time-trace associated with the detected mmw-power measured at  $x = 5$  cm (peak time-averaged power) is shown in figure 5.11b). Here, we observe that the presence of the plasma in the path of the beam introduces fluctuations in the detected

## Chapter 5. Mmw-beam scattering by turbulent structures and blobs in simple magnetized toroidal plasmas

mmw-power  $\delta P(x, t)$  of the order of a few percent of the time-averaged value  $\langle P \rangle$ ; these are not present in the absence of the plasma. The standard deviation of the time-traces  $\sigma(P)$  measured for  $x \in [-3, 12]$  cm in the presence and in the absence of a plasma is shown in fig 5.11c). In the presence of the plasma,  $\sigma(P)$  ranges between 3–5  $\mu\text{W}$ . In the absence of a plasma,  $\sigma(P)$  is lower than 1  $\mu\text{W}$ . Fluctuations of the detected mmw-power induced by the presence of the plasma occur over the entire range  $x \in [-3, 12]$  cm and are positive and negative - that is the power can either increase or decrease.

Figure 5.12a) shows the cross-correlation coefficient at zero time-lag  $C_0(0)$  between  $\delta P(x, t)$  (measured at  $x = 5$  cm) and  $\delta n_e(\mathbf{x}, t)$  measured with HEX TIP-U. Figure 5.12b) shows the same, except that the receiver is placed at  $x = 10$  cm.  $C_0(0)$  ranges approximately between -0.2 and 0.2:  $\delta n_e(\mathbf{x}, t)$  and  $P(x, t)$  are positively correlated in some regions and negatively correlated in others. When the cross-correlation is computed with a non-zero time-lag between  $\delta P(x = 5 \text{ cm}, t)$  and  $\delta n_e(\mathbf{x}, t)$ , the same structures are obtained but they are shifted vertically. When passing through the mmw-beam, blobs are still coherent with the ideal interchange wave located in the region  $x \leq -5$  cm (higher density plasma regions - source). This explains the finite-value of the cross-correlation coefficient measured outside the beam path.

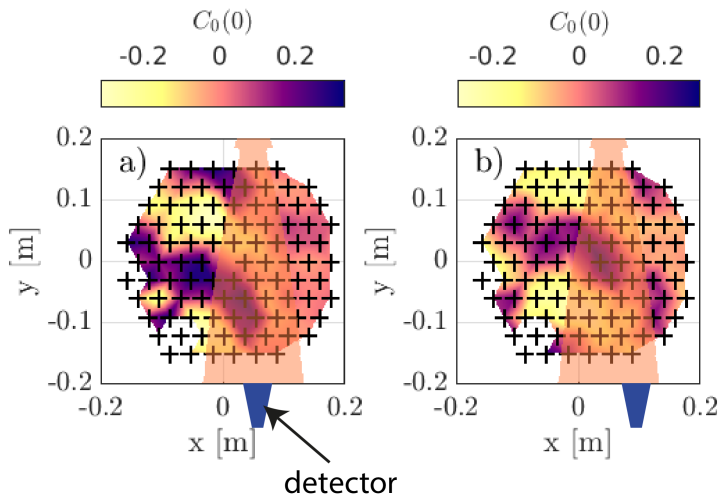


Figure 5.12 – a) Cross-correlation at zero time lag between  $\delta P(x = 5 \text{ cm}, t)$  and  $\delta n_e(\mathbf{x}, t)$ . b) Cross-correlation at zero time lag between  $\delta P(x = 10 \text{ cm}, t)$  and  $\delta n_e(\mathbf{x}, t)$ .

The cross-correlation coefficient  $C_0(0)$  between  $\delta P(x = 10 \text{ cm}, t)$  and  $\delta n_e(\mathbf{x}, t)$  has the same patterns as the one computed for  $\delta P(x = 5 \text{ cm}, t)$  but with opposite sign [the location  $x = 10$  cm has been chosen explicitly to illustrate this]. These figures show that, depending on its spatial location in the poloidal plane, a blob can reduce (negative correlation) or increase (positive correlation) the power detected at the location of the detection horn. Furthermore, while the same structure can increase (or decrease) the power detected at one specific location of the detection horn, it can decrease (or increase) the power detected at another location. This behaviour will be explained in more detail using full-wave simulations in the next section.

## 5.4. Influence of the plasma on the mmw-propagation

We focus here on the detection performed at  $x = 5$  cm, but the same analysis could be performed for the detection at  $x = 10$  cm. To investigate the effect of a typical blob on the mmw-beam transmission, we perform conditional sampling (CS)[63] of the mmw-power signal and the HEXTIP signals over many blob events within a time window centered around each blob events. Events are defined as local maxima, in the time-trace of a selected HEXTIP probe, that fulfill the condition  $n_e > \langle n_e \rangle_t + 3\sigma$ , with  $\sigma$  being the standard deviation of  $n_e$  calculated over the entire time trace. All quantities obtained with CS are labeled with a tilde, except  $\tau$  which is the time relative to the blob event;  $\tau = 0 \mu\text{s}$  corresponding to the detection of the blob. Either one of the two HEXTIP probes - shown in white in Fig. 5.13b,c) - are used for blob detection. Their location is chosen to correspond approximately to the positions of the maximum and minimum values of the cross-correlation in the blob region in Fig. 5.12a).

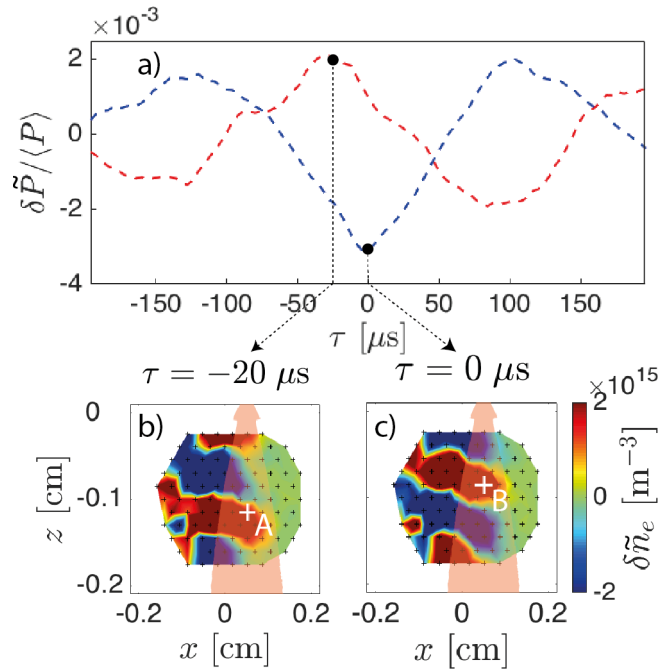


Figure 5.13 – Conditional sampling (CS) using two different probes to detect blobs ( $m=3$ , see text). Note that, since  $k_{\parallel} \approx 0$ , a single blob would appear twice within the poloidal cross-section of TORPEX. a) Red (probe A) and blue (probe B) dashed lines show the result of CS using the probes identified in white in b) and c). b,c) CS of electron density fluctuations snapshots at  $\tau = -20 \mu\text{s}$  and  $0 \mu\text{s}$ , respectively.

The results of CS of the detected mmw-power over  $N \approx 1000$  events are presented in Fig. 5.13a) as a function of time. Errors in the averaging process are proportional to  $1/\sqrt{N}$  and are of the order of  $10^{-4}$ . The blob detected by probe A (fig. 5.13b)) induces a positive  $\delta P(x = 5 \text{ cm}, \tau)$  at  $\tau = -20 \mu\text{s}$  which is preceded and followed by a negative  $\delta P(x = 5 \text{ cm}, \tau)$ . The blob detected by the probe B, which is located at the same  $x$  position as the probe A but vertically displaced (fig. 5.13b), has the opposite effect on  $P(x = 5 \text{ cm}, \tau)$ . In this case the blob induces a negative  $\delta P(x = 5 \text{ cm}, \tau)$  at  $\tau = 0$  which is preceded and followed by a positive  $\delta P(x = 5 \text{ cm}, \tau)$ . This example shows that blobs located at different  $z$  positions can have an opposite effect on the

## Chapter 5. Mmw-beam scattering by turbulent structures and blobs in simple magnetized toroidal plasmas

locally measured mmw-transmission.

Several classes of blobs are defined by the condition  $\langle n_e \rangle_t + m \cdot \sigma < n_e < \langle n_e \rangle_t + (m + 0.5)\sigma$  with  $m = 1, 2, 3$  to investigate the effect of the electron density associated with the blob on the mmw-transmission. In practice, defining these classes of blobs is equivalent to detecting blobs with different electron densities,  $n_e$  increasing with  $m$ . The dynamics revealed by the CS shown in fig. 5.13a) are preserved. The extrema occur in a time window of  $+/- 20 \mu s$  relative to the ones in Fig. 5.13(a). Figure 5.14 shows the evolution of the extrema identified in fig. 5.13 with  $n_e$ . It shows that blobs with larger density fluctuations have larger effects on the mmw-detected power.

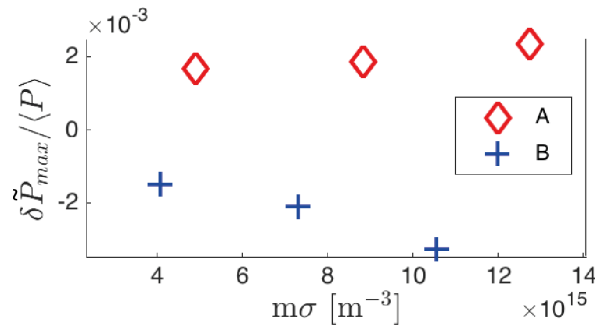


Figure 5.14 – Maximum amplitude of fluctuations of the normalized detected power  $\delta \hat{P}_{max} / \langle P \rangle$  as a function of the range of the CS threshold, taking probes A or B as a reference.

In this section, we have seen that the presence of blobs in the path of the mmw-beam introduces local fluctuations of the mmw-power. We have seen that these fluctuations can be either positive (increase of the mmw-power) or negative (decrease of the mmw-power), depending on the blob location. Finally, we have seen that blobs or larger density have a larger effect on the detect mmw-power. Since the mmw-detection is pointwise, full-wave numerical simulations are used in the next section to reconstruct the 2D fluctuations of the electric field  $\delta |\vec{E}(\mathbf{x}, \tau)|$  associated with the mmw-beam and propose a physical interpretation to the observations discussed in this section.

### 5.5 Numerical investigation of mmw-scattering in TORPEX

We investigate the effect of blobs on the propagation of the mmw-beam using numerical modelling. We have discussed in chapter 4 that in the presence of blobs with typical scale  $a$  such that  $\lambda/a \sim 1$  (as here), a full-wave model is needed to capture the underlying physics [91] and resolve the instantaneous profile of the mmw-beam. Here, the plasma is regarded as stationary -with blobs “frozen-in”- and the cold plasma model is reduced to a single equation for the electric field  $\mathbf{E}(\mathbf{x}, \omega)$  in frequency domain, namely,

$$\nabla \times (\nabla \times \mathbf{E}(\mathbf{x}, \omega)) - \frac{\omega^2}{c^2} \hat{\epsilon}_r(\mathbf{x}, \omega) \mathbf{E}(\mathbf{x}, \omega) = \mathbf{S}(\mathbf{x}, \omega), \quad (5.3)$$

where  $c$  is the speed of light in free space, and  $\hat{\epsilon}_r(\mathbf{x}, \omega)$  is the cold plasma dielectric tensor computed with the equilibrium magnetic field and with density  $n_e(\mathbf{x}, \tau)$  frozen at time  $\tau$  (see chapter 4).

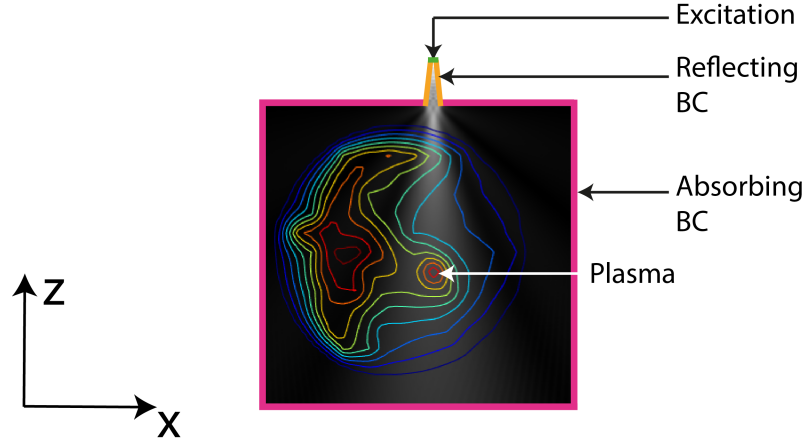


Figure 5.15 – Visualization of the computational domain and the boundary conditions (BC).

The source  $\mathbf{S}$  is defined for the  $TE_{10}$  mode of the antenna with polarization chosen in order to excite the X-mode. The radiation pattern of the antenna, and therefore the mmw-beam, is obtained by defining the boundary condition at the edges of the antenna in the 2D plane as perfectly reflecting and the electric field at the entrance of the antenna as  $\mathbf{E}_{inj}(x) = E_{inj}\mathbf{e}_x$  (see fig. 5.15). Equation(5.3) is solved using the COMSOL Multiphysics solver [76] over the entire 2D spatial computational domain for a sequence of snapshots at times  $\tau_i$  with  $\Delta\tau = \tau_{i+1} - \tau_i = 4\mu\text{s} \gg 2\pi/\omega$ , thus obtaining a sequence of beams  $\mathbf{E}_i(\mathbf{x}, \omega)$  corresponding to different density snapshots. The time-resolved 2D profiles of the electron density  $\tilde{n}_e(\mathbf{x}, \tau_i)$  are supplied as inputs by applying the CS procedure on the experimental density measurements (Fig. 5.17). These are used to compute  $\hat{\epsilon}_r$ . Given that blobs are field-aligned structures with  $k_{\parallel} \approx 0$  and that magnetic field lines are helical, the 2D electron density profile at the toroidal location of the mmw-system is similar to the one measured by HEX TIP-U (toroidally displaced by  $90^\circ$  from the mmw-system); but vertically shifted by  $\Delta/4 \approx 4.5\text{ cm}$  (see fig. 5.13),  $\Delta$  being the vertical displacement of a field line after one toroidal turn. In practice, we compute the 2D electron density profile using as a reference two probes vertically distant (i.e. from A and B, fig. 5.13(c-d)) by  $\Delta/4$ .

Absorbing boundary conditions [76] and perfectly reflecting BC were tested. While the former were used at the edge of the computational domain, resulting in numerical results in agreement with the experiments, perfectly reflecting boundary conditions were used on a larger domain approximating the vacuum chamber cross-section but did not provide satisfactory results. One reasonable explanation for this is that mmws reflecting off metallic surfaces can, in the real toroidal three-dimensional case, propagate away from the region near the beam and thus dissipate mmw-power; whereas the numerical model with perfectly reflecting walls does not. These three-dimensional effects cannot be captured by the two-dimensional model

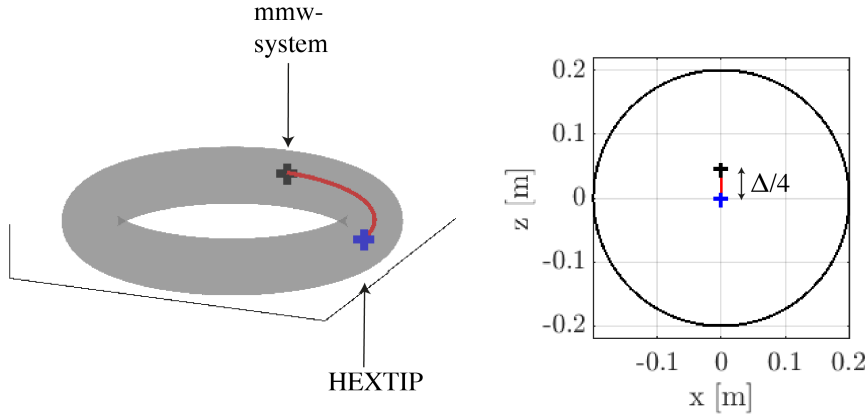


Figure 5.16 – On the left: A portion of a field line from the plane of HEX TIP (blue cross) to the mmw-system plane (black cross). On the right: projection of the field line in the TORPEX poloidal plane.

used here. Therefore, absorbing BCs will be used in the following.

Figure 5.17 shows four snapshots of the propagation of the blob detected by probe A and the associated fluctuations  $\delta\tilde{E}(\mathbf{x}, \tau)$  of the electric field. We can see that  $\delta\tilde{E}(\mathbf{x}, \tau)$  is the result of a complex interaction between  $\delta\tilde{n}_e(\mathbf{x}, \tau)$  and the mmw-beam.  $|\delta\tilde{n}_e|$  is of the order of  $\approx 4 \times 10^{15} m^{-3}$  ( $\approx 0.3\langle n_e \rangle_{max}$ ) and the associated  $|\delta\tilde{E}|$  of the order of  $10^{-4} E_{inj}$ . Figure 5.17 shows that the positive structures associated with the blob induce a negative  $\delta\tilde{E}(\mathbf{x}, \tau)$  in the wake of the structure (i.e. to the receiver side of the structure), resulting in local variations of  $\tilde{E}$ .

For each one of the  $\approx 100$  snapshots, corresponding to  $\tau \in [-200, 200] \mu s$ , we compute the mmw-power coupled to the detection horn at  $x = 5$  cm and  $x = 10$  cm. The numerically computed  $\delta\tilde{P}/\langle P \rangle$  is shown as shaded areas in figure 5.18c-d) and compared to the experimental measurement  $\delta\tilde{P}/\langle P \rangle$  shown as dashed lines. The uncertainty of the model are obtained by bounding the outcome with numerical results obtained using  $n_{e,min} = 0.5n_e$  and  $n_{e,max} = 2n_e$  (see appendix D for more details). The shaded areas in fig. 5.18c-d) indicate this variability. In general, we find a good agreement between the numerical simulations and the experiments. The agreement can be quantified by computing the coefficient of the cross-correlation between the numerically obtained and experimentally measured  $\delta\tilde{P}(x, t)$  at zero time-lag. We find that the coefficient ranges between 0.45 and 0.90, for the red and blue curves in Fig. 5.18(c), respectively. Figure 5.18a,b) show the fluctuation  $\delta|\tilde{E}_i(\mathbf{x}, \omega)|$  of the electric field of the mmw-beam associated with the two configurations of electron densities described above. In the two cases presented here, a blob defocuses the beam as detailed in Refs. [30] and [29, 31]. In Fig. 5.18 (a), the blob (white arrow) is at the center of the mmw-beam (i.e.  $x = 5$  cm). Defocusing of the mmw-beam occurs in the wake of the blob and causes a decrease of the detected power at the beam center, where the blue horn is (blue lines, Fig. 5.18(c)). The power is spread out, which results in an increase in power density and transmission at the beam

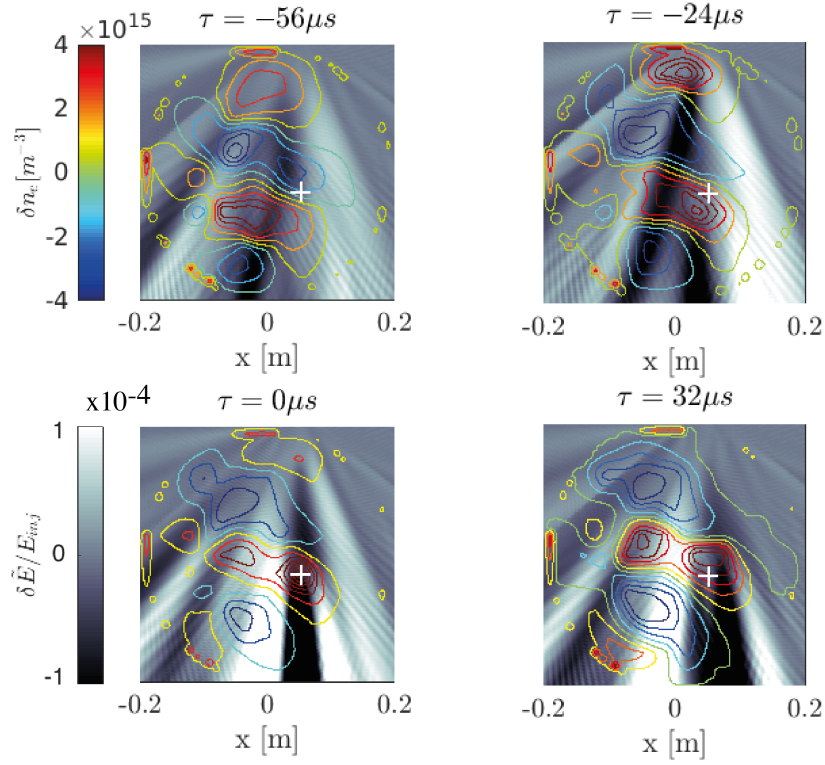


Figure 5.17 – Snapshots of the fluctuations of the electron density (contours) and electric field associated with the propagation of the blob detected by the probe A shown in 5.13 at indicated here by the white cross.

edges, where the red horn is, as shown in red, Fig. 5.18(c). Figure 5.18(b) presents another situation where the blob (white arrow) is located at the beam edge. Only part of the beam is defocused. The beam power at the edge is refracted to the center resulting in an increase of the power detected at the beam center as shown in blue, Fig. 5.18(d). Here, the structure with negative fluctuations of the electron density also contributes to the partial focusing of the beam.

In this section, combining experimental observations and full-wave simulations, we have shown that blobs are responsible for a defocusing of the mmw-beam in the wake of the blob structure. The defocusing of the mmw-beam is responsible for a redistribution of the mmw-power to the sides of the blob density structure, generating local fluctuations of the mmw-power, which can be either positive (increase of power) or negative (decrease of power), depending on the blob location relative to the receiver.

## Chapter 5. Mmw-beam scattering by turbulent structures and blobs in simple magnetized toroidal plasmas

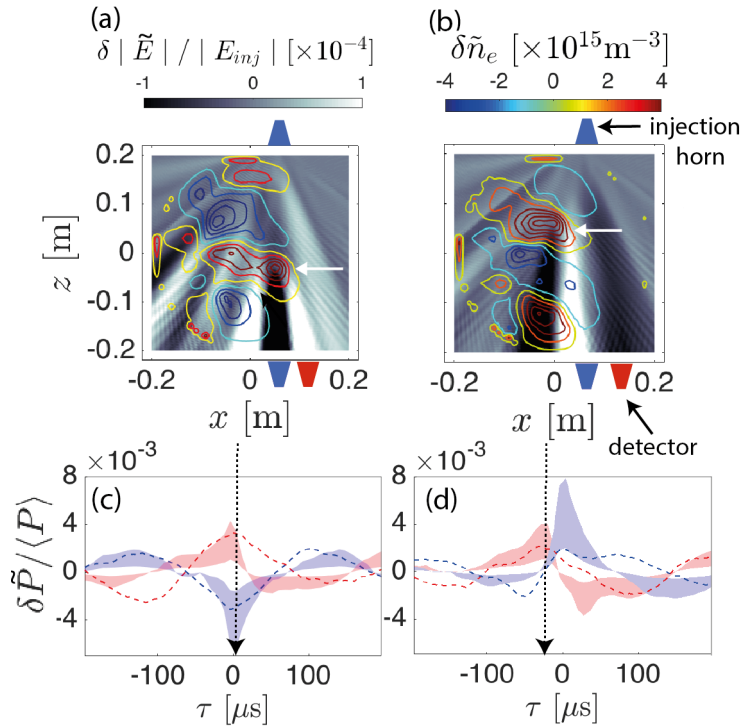


Figure 5.18 – Full-wave simulations results: (a,b) Fluctuations of the electric field amplitude associated with the blobs identified in Fig. 5.13(b,c) projected to the poloidal plane of the mmw-system. The detected electric field is normalized to the electric field maximum of the launching horn  $|E_{inj}|$ . (c,d) Comparison of the time evolution of the mmw-power at the two positions of detection identified by the blue and red horns in (a,b). The white arrows indicate a blob. The CS time evolution of the detected mmw power is obtained using probes A and B from Fig. 5.13(b) and (c) to detect blobs. Experimental results (dashed lines) are compared to numerical simulations (shaded areas).

### Conclusions of the scattering experiment in SMT configuration

In this chapter, we have shown that the presence of an SMT plasma in the path of the mmw-beam introduces fluctuations in the transmitted mmw-power. The scattering experiments in TCV SMT plasmas suggested that these fluctuations are caused by variations in the electron density of the plasma but the physical interpretation was hampered by the difficulty of performing reproducible SMT discharges on TCV and the limited diagnostic accessibility at the low electron densities and temperatures of the SMT. Further experiments were carried out in well diagnosed an accessible TORPEX SMT configurations. Here, we have shown experimental evidence of mmw-scattering by blobs. Combining experimental measurements and full-wave simulations, we have demonstrated that blobs have a defocusing effect on the mmw-beam in the wake of the blob structure, resulting in local increases or decrease of the mmw-power, depending on the position of the blob relative to the receiving antenna. We have also shown that the effect of blobs on the mmw-beam is stronger for blobs of higher density.



## 6 Effect of MHD modes on the high power mmw-beam in TCV

From the experimental setup presented in chapter 2, it is clear that before reaching the transmission diagnostic X3TD, the mmw-beam traverses not only the SOL (twice) but also the confined region of the plasma. In this chapter, we investigate the effect of core plasma dynamics on the mmw-propagation. Ideally, the expected scattering should have a different signature in the data making core and SOL effects separable and easily distinguishable. Here, we focus on the case of an MHD mode  $m = 1$ ,  $n = 1$ . Another dynamic of the core plasma, the sawtooth crash is discussed later in chapter 7. In this chapter, we show that the rotation of the plasma column associated with the mode oscillation is responsible for periodic deflections of the mmw-beam, resulting in a periodic drop of the transmitted power of up to 100%. Numerical simulations using the full-wave model and the WKBeam code are used to reconstruct the beam propagation during the mode oscillation and qualitatively explain the periodic deflection of the beam. The two codes are compared and found in good agreement.

This chapter is organized as follows: in section 6.1 the MHD mode is characterized. Experimental observations using the X3TD diagnostic associated with the rotation of the mode are shown in and discussed in section 6.2. Numerical calculations of the beam propagation during one period of the mode oscillation are presented in 6.3; results from the two codes are finally compared.

### 6.1 Description of the plasma mode $m=1$ , $n=1$

The internal  $m = 1$ ,  $n = 1$  kink mode [92, 93] results in a rigid helical displacement of the plasma inside the  $q = 1$  surface. In the poloidal plane, it results in a periodic rotation of the plasma profile. By affecting the  $n_e$  profile, and therefore the dielectric permittivity of the plasma, the kink mode can be responsible for a strong perturbation of the mmw-beam trajectory.

Discharge 60393 is an elongated limited plasma with the main parameters summarized in table 6.1. To identify the dominant mode in this discharge, we perform the fast Fourier transform

## Chapter 6. Effect of MHD modes on the high power mmw-beam in TCV

$q_{95}$	$\kappa$	$\delta$	$n_{e,0}$	$T_{e,0}$	$B_T$	$R_0$	$Z_0$
3	1.52	-0.02	$10.5 \times 10^{19} \text{ m}^{-3}$	0.74 keV	-1.41 T	0.89 m	0.0 m

Table 6.1 – Plasma parameters for the TCV discharge 60393: safety factor at 95% of the plasma minor radius, plasma elongation and triangularity, electron density and temperature, magnetic field on axis, and position of the plasma, respectively.

(fft) of the magnetic probe signals (details of the magnetic probe array diagnostics and example of use are given in [94, 95, 96]) on the poloidal array located in sector 3 and on the toroidal array located at the midplane of the vessel, on the low field side. We find a dominant mode at  $f_m = 5.88$  kHz. Figure 6.1 show the amplitude and the phase of the fft coefficient at  $f_m$  for each probe of the poloidal and toroidal array, respectively. The poloidal angle  $\theta$  is defined clockwise, it is equal to 0 at the HFS mid-plane and to  $\pi$  at the LFS mid-plane. From fig. 6.1a-b, we find that the amplitude of the fft at  $f_m$ , and therefore the mode signature, is stronger for  $\theta \in [0.75\pi; 1.25\pi]$  associated with the probes in the LFS of the vessel. From the slope of the phase in the region  $[0.75\pi; 1.25\pi]$ , we find  $m = \frac{\Delta\psi}{\Delta\theta} = 1$ , with  $\psi$  the phase of the fft coefficient at the frequency  $f_m$  from the magnetic probes in the poloidal array. Similarly, from the phase of the fft coefficient at the frequency  $f_m$  from the magnetic probes in the toroidal array (fig. 6.1c-d), we find  $n = 1$ .

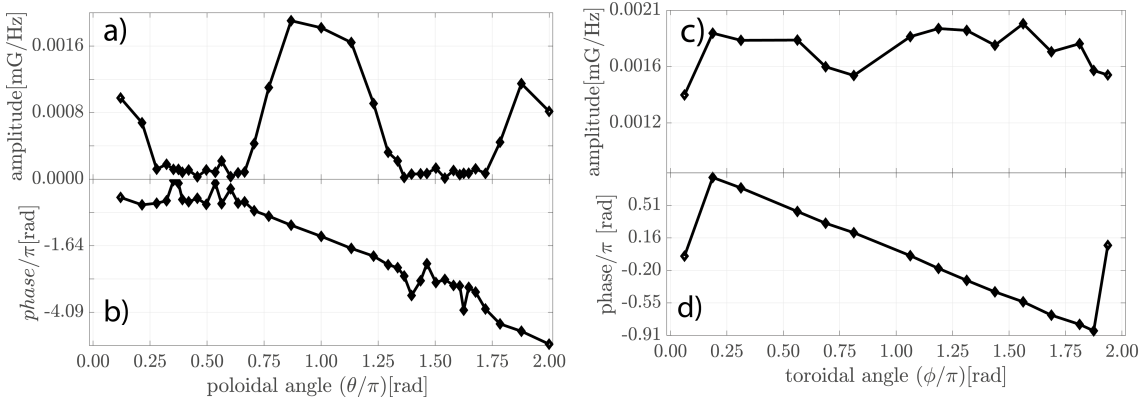


Figure 6.1 – a,b) Amplitude and phase of the fft of the poloidal array of magnetic probes in sector 3 at the frequency of the dominant mode  $f_m = 5.88$  kHz. c,d) Amplitude and phase of the fft of the toroidal array of magnetic probes in the LFS mid-plane at the frequency of the dominant mode  $f_m = 5.88$  kHz.

The rigid shift of the plasma core associated with the  $m = 1$ ,  $n = 1$  kink mode is displayed in fig. 6.2, which shows the time-evolution of the intensity of the soft X-ray emission measured by the DMPX detector. The lines of sight of the corresponding detectors are shown in fig.6.2c). The chord represented in red goes through the plasma axis and the one in black has a radial offset of a few centimeters to the low-field side with respect to the plasma axis. The radial position at  $z = 0$  cm of these chords is shown by matching-color dashed lines in fig. 6.2b). The intensity of the soft X-ray emission measured along the low-field side chord oscillates with

## 6.1. Description of the plasma mode $m=1, n=1$

a frequency  $f_m$  corresponding to the frequency of the kink mode. Since the plasma axis is aligned twice with the central chord during one rotation of the plasma associated with the mode, the soft X-ray intensity measured by the central chord (red traces and line in fig. 6.2)

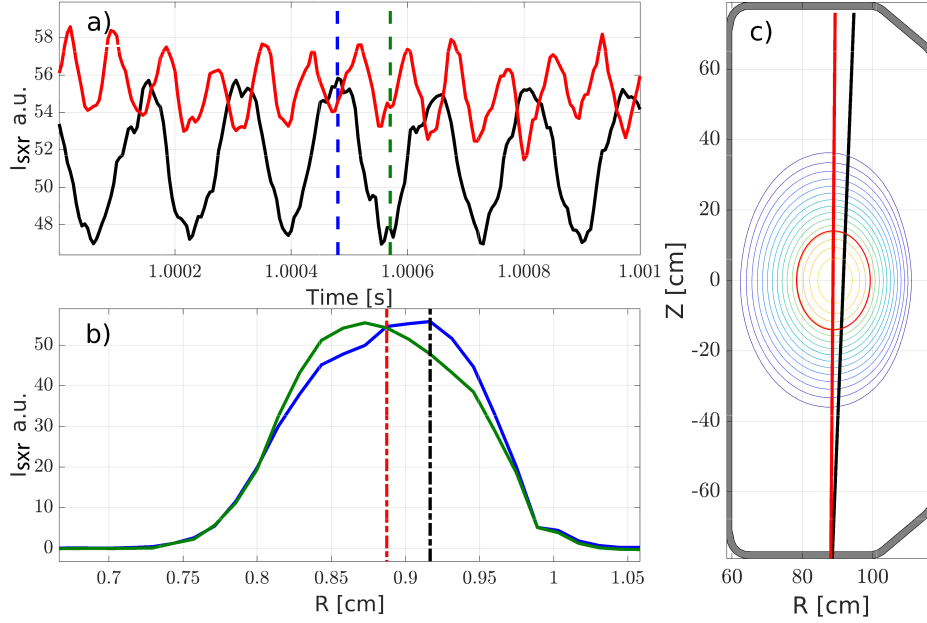


Figure 6.2 – Discharge 60393: a) Intensity of the soft X-ray emission measured along the matching-color MPX chords shown in black and red in c) Their radial position at the  $z$ -position of the plasma axis is reported in b). b) Soft X-ray emission profile at the two times identified in a) by the vertical dashed lines of the same color. c) Contours of the flux surfaces of the plasma and lines of sight of the MPX chords corresponding to the soft X-ray intensity traces in a). The  $q = 1$  flux surface is shown in red.

oscillates at a frequency  $2f_m$ . The reconstructed profile of soft X-ray intensity at  $z = 0$  cm is shown in fig. 6.2b) at two different times indicated by the matching-color dashed lines in fig. 6.2a). The blue curve corresponds to the maximum measured intensity along the LFS chord and the green one to the minimum measured intensity along the same chord during one rotation of the mode. The position of the maximum of the intensity profile (fig. 6.2b) shifts by  $\approx \Delta R = 5$  cm during one period of the mode.

As already discussed in chapter 2, the intensity  $\iota$  of the soft-X ray emission from the plasma depends upon  $n_e$  in the following way:

$$\iota = \int I(\omega) d\omega = 1.5 \times 10^{-38} \int n_e^2 Z_{eff} \frac{e^{-\frac{\hbar\omega}{T_e}}}{\sqrt{T_e}} d\omega \propto n_e^2 \sqrt{T_e} Z_{eff}, \quad (6.1)$$

the integral being performed over the soft X-ray range of frequencies. From the soft X-ray

tomographic system [46, 47, 97] installed on TCV, the time-evolution of the 2D soft X-ray intensity profile  $\iota(R, Z, t)$  is tomographically reconstructed with a time step of  $10 \mu\text{s}$ . Based on eq. 6.1, we extract  $n_e$  from  $\iota$  the following way: the proportionality factor between  $\iota$  and  $n_e$  is computed from the time-averaged  $\langle \iota(R, Z) \rangle$  and  $n_{e,TS}(R, Z)^2$  obtained from TS by remapping the TS measurements onto the flux surfaces using the LIUQE equilibrium code. The electron temperature  $T_{e,TS}(R, Z)$  is taken to be constant during one cycle of the mode; it is similarly obtained from TS measurements.

The time-evolution of the  $n_e$  profile during one period of the mode obtained using this procedure is shown in fig.6.3. As expected, the central plasma is observed to rotate around its axis. The obtained  $n_e$  profiles will be used as an input of the mmw-wave simulations in section 6.3. The time-traces  $n_e(R_i, Z_i, t)$  of the four points at the locations indicated by the colored circles in fig. 6.3a) are shown in fig. 6.3e). We find that the time traces associated with two points located on opposite sides of the plasma axis, on the same flux surface, (e.g. blue and black or red and green) are in quasi opposite phase; this confirms the rotation of the central plasma around its axis (from the sequence in time we see that the rotation is in the counterclockwise direction).

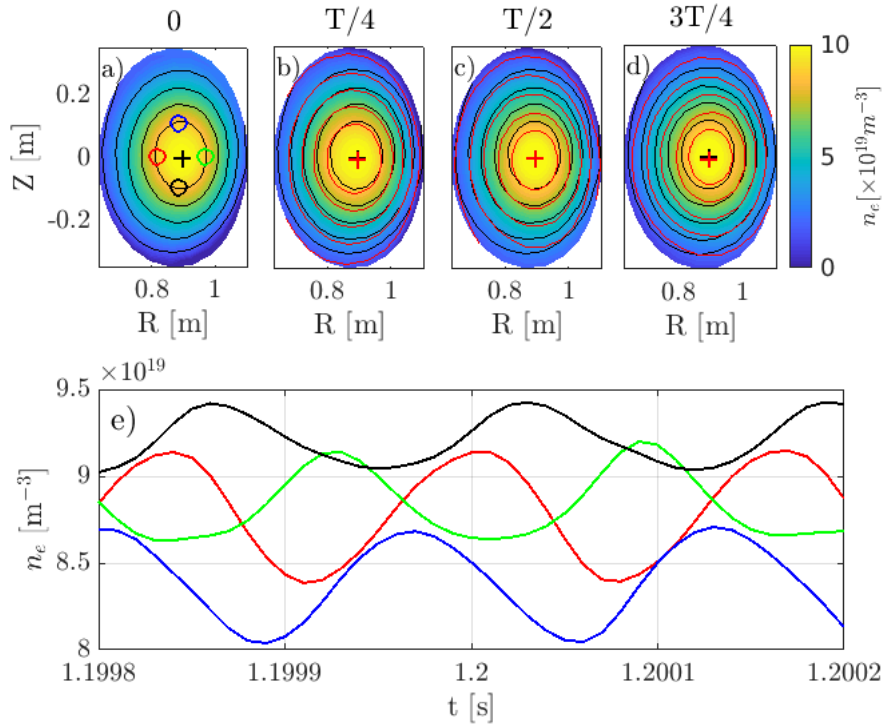


Figure 6.3 – Discharge 60393: a-d) Electron density profile evolution during one period  $T$  of the kink mode. The black lines are isocontours of  $n_e$  at  $t = 0$  and the red ones are the same isocontours at the corresponding times,  $T/4$ ,  $T/2$ ,  $3T/4$ , respectively. e) time evolution of  $n_e$  at the locations indicated by the matching-color circles in a).

## 6.2 Experimental observations on X3TD

In this section, we will describe the experimental observations on the mmw-transmitted power measured by X3TD during the kink mode activity. The mmw-beam is injected at  $R = 0.88$  m and the mmw-power is pulsed for  $\sim 2.2$  ms (see fig.6.5) during a poloidal angle sweep of the launching mirror (from  $46^\circ$  to  $44.5^\circ$ , more details in chapter 2) to reconstruct the mmw-beam profile while protecting diagnostics from excessive scattered radiation. The injection setup is shown in fig. 6.4 . The mmw-power transmitted through the plasma and detected by the

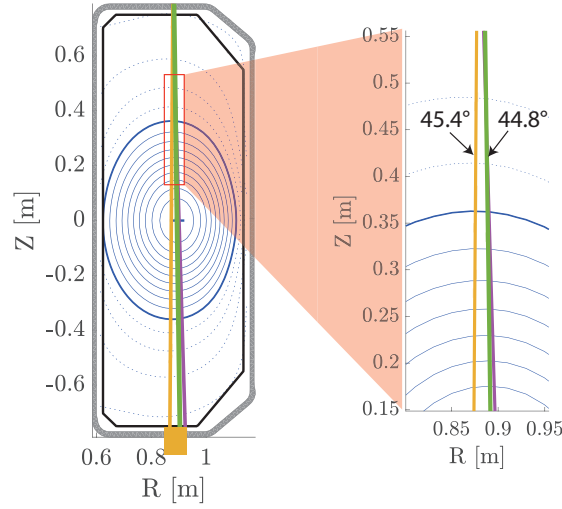


Figure 6.4 – Discharge 60393: Experimental setup. Contours of the flux surfaces. The yellow and green line represent the geometric center of the mmw-beam in vacuum at the injection poloidal angle of  $\theta_m = 45.4^\circ$  and  $44.8^\circ$ , respectively. The purple line (partially hidden behind the green line) is the line of sight of the XTOMO camera 1, channel 12. The yellow rectangle indicates the aperture of X3TD at the bottom of the vessel. On the right is a zoomed view of the lines at the entrance of the plasma.

X3TD diagnostic is shown in fig.6.5a). Figure 6.5b,c) shows the measured mmw-power during two pulses with an injection angle of  $45.4^\circ$  and  $44.8^\circ$ , respectively. The detected power measured during each pulse is fluctuating periodically, in synchronization with the rotation of the plasma. At  $\theta_m = 45.4^\circ$ , the periodic oscillation occurs at the frequency  $f_m$  of the mode. During one oscillation, the measured mmw-power drops to  $\approx 10\%$  of its maximum value. At  $\theta_m = 44.8^\circ$ , the periodic oscillation occurs at  $f = 2f_m$  and the measured power drops to  $\approx 30\%$  of its maximum value.

Since the mmw-detection is performed in one position in space, to understand the effect of the plasma rotation associated with the kink mode on the mmw-beam propagation, we identify the measured power ( $P_i(\theta_m)$ ) at different times during the mode rotation. We proceed as follows: the soft X-ray measurement  $S_x$  from the XTOMO chord 1, channel 12 (line of sight shown in fig. 6.4) of the camera installed at the top of the vessel is used as a reference for the

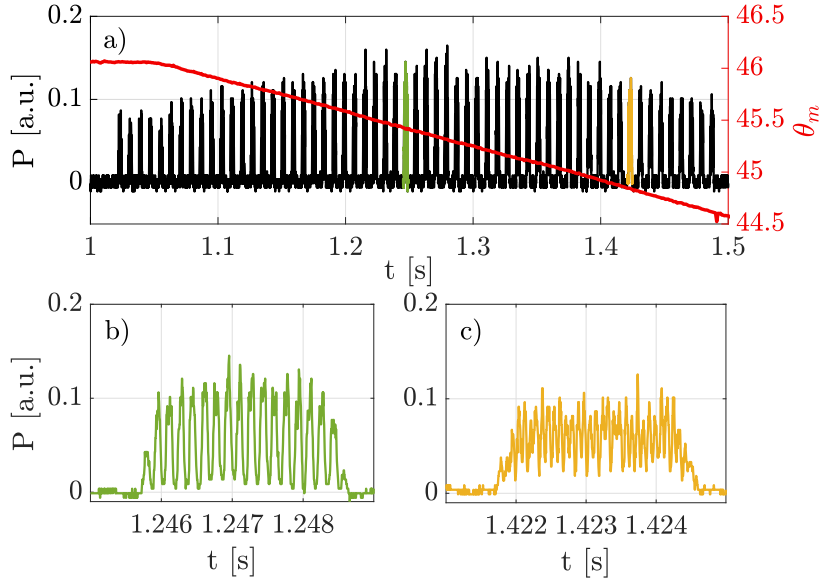


Figure 6.5 – a) Mmw-power measured by X3TD in discharge 60393. The poloidal angle of the launching mirror  $\theta_m$  (in red) is swept during the discharge. An expanded view of the yellow and green pulses is shown in b) and c), respectively. Note the frequency doubling ( $f_m$  to  $2f_m$ ) from b) to c).

identification of the different phases of the mode. The  $S_x$  signal is filtered around  $f_m$  and the four times along the period  $T$  of the mode ( $0$ ,  $T/4$ ,  $T/2$  and  $T$  in fig. 6.3) are identified in fig. 6.6a) (in yellow, purple, blue and orange, respectively). The times corresponding to each phase of the mode are highlighted using on the mmw-detected signal in fig.6.6b-e). We find that during one period of the mode, the maximum in the detected power  $P$  is shifted to lower  $\theta_m$  (recall that during the discharge, a scan in  $\theta_m$  was performed, from larger  $\theta_m$  at  $t \approx 1$  s to lower  $\theta_m$  at  $t \approx 1.5$  s, see fig. 6.5). The profile is later re-established at the end of the period. This suggests a periodic deflection of the mmw-beam during the plasma rotation associated with the kink mode.

The dependence of the measured mmw-power on both the phase of the mode and the mmw-injection angle is presented with more details in fig.6.7. The period of the mode (phase  $\in [0; T]$ ) is divided in twelve portions. The measured mmw-power corresponding to each phase of the mode is averaged on time-windows during which the variation of the injection angle of the beam is  $\sim 0.12^\circ$ . During one period of the mode, the mmw-power has one maximum for injection angles  $\theta_m \geq 45^\circ$ , and two maxima for  $\theta_m \leq 45^\circ$  (i.e. the frequency doubling is occurring, see fig. 6.5). While advancing from  $0^+$  to  $T/2$ , the maximum mmw-powered is slightly displaced to larger  $\theta_m$ . The maximum is then strongly deviated to lower  $\theta_m$  for a phase of the oscillations of the mode increasing from  $T/2$  to  $T^-$ . The cycle restarts at the end of the period.

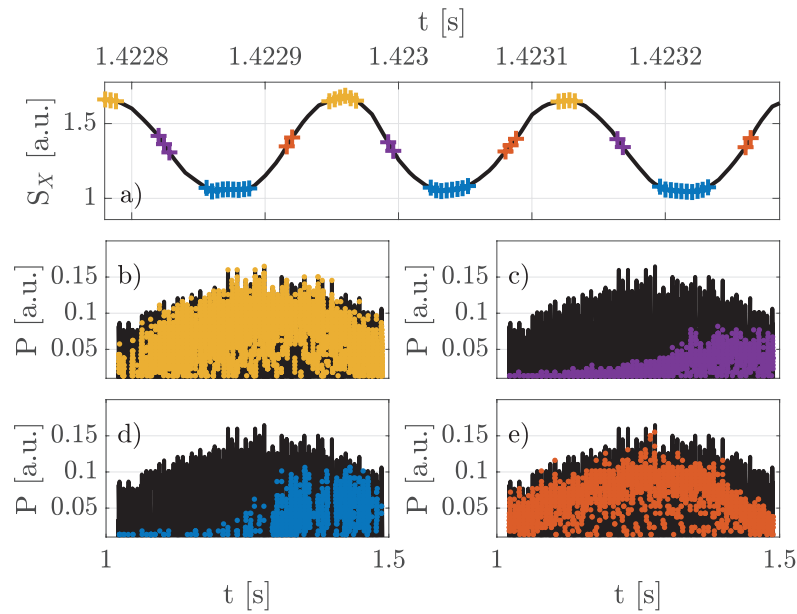


Figure 6.6 – a) Soft x-ray emission measured by XTOMO camera 1, channel 12 (line of sight shown in fig. 6.4). Mode oscillations at four different phases ( $0$ ,  $T/4$ ,  $T/2$  and  $T$ ) are identified by the colored crosses. The associated times are highlighted on the mmw-transmitted signal in b-e).

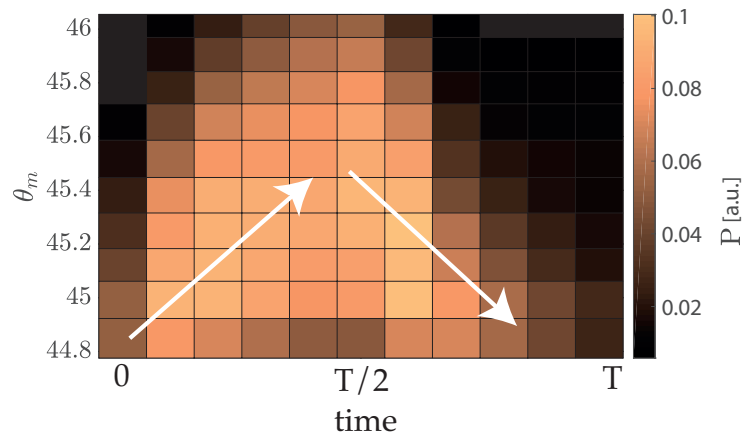


Figure 6.7 – Mmw-power measured by X3TD as a function of the phase of the mode oscillations and the mirror injection angle. The phase of the mode oscillation is set to zero at the maximum of detection of the soft X-ray emission measured by XTOMO camera 1, channel 12, shown in fig.6.6a).

In section 6.3, using numerical simulations, we will see that the plasma rotation associated with the kink mode is responsible for a deflection of the mmw-beam to the low-field side of the vessel, explaining the shift in the maximum in the detected power to lower  $\theta_m$  during one

oscillation of the mode.

### 6.3 A test case for comparing full-wave and WKBeam simulations

In this section, the effect of the kink mode on the propagation of the high-power mmw-beam is investigated numerically. In the previous section, the experimental observations from the X3TD diagnostic showed a periodic drop of the transmitted power associated with the rotation of the mode shown by fig. 6.5. The experimental observations suggested a periodic deflection of the mmw-beam. Here, we present a qualitative interpretation of the experimental observations based on full-wave numerical simulations as well as simulations from the WKBeam code. The two codes are compared and they are found in good agreement.

The mmw-beam is injected vertically at  $R = 0.88$  m. The magnetic equilibrium is taken to be unperturbed by the mode. This assumption is not correct for the plasma itself but is applied to the computation of the dielectric tensor for the mmw-propagation. The time-evolution of the plasma 2D electron density profiles is reconstructed by combining soft X-ray measurements and Thomson scattering measurements as detailed in section 6.1. Results of the full-wave simulations are shown in fig. 6.8, which presents four snapshots of  $|E|$  associated with the mmw-beam during one period  $T$  of the mode. In the same figure, contours of  $n_e$  at the same times demonstrate the displacement of the plasma column associated with the mode (taken respectively at  $t = 1.1998, 1.9985, 1.19989$  and  $1.19993$  s in discharge 60393). The presence of the plasma rotation causes a radial displacement of the beam in addition to its broadening. While the beam is still directed towards the detector at  $t = 0$ , the displacement of the plasma causes a deflection of the beam towards the low-field at later times. The deflection angle is maximum at  $t = T/2$  and starts decreasing on the second half of the mode oscillation.

The footprint of the beam at the floor of the vessel ( $z_0 = -0.77$  m) is shown in fig. 6.9. The square of the electric field amplitude  $E^2$  is normalized as:  $\frac{|E(R, z_0)|^2}{\int_{-\infty}^{+\infty} |E(R, z_0)|^2 dR}$  and is shown in fig. 6.9. At  $t = 0$ , the maximum of  $|E|^2$  is located at  $R = 1.0$  m. The large value of  $n_e$  causes the  $E^2$  profile to have a full-width-at-half maximum of 0.52 m. The largest displacement of the maximum of  $E^2$  occurs at  $t = T/2$  (fig. 6.9) and is of 0.5 m.

The  $E^2$  profiles (red) from the full-wave simulations are compared to the WKBeam results (black) in fig. 6.9. The agreement between the two profiles is quantified by the parameter  $\zeta$  defined as:

$$\zeta = \frac{|\int_{R_1}^{R_2} E_C(z_0, R) \cdot E_W(z_0, R) dR|}{\sqrt{\int_{R_1}^{R_2} |E_C|^2 dR \int_{R_1}^{R_2} |E_W|^2 dR}}, \quad (6.2)$$

where  $E_C$  (C for COMSOL) is the amplitude of electric field computed using the full-wave model and  $E_W$  the amplitude electric field computed by the WKBeam code.  $R_1$  and  $R_2$  are the



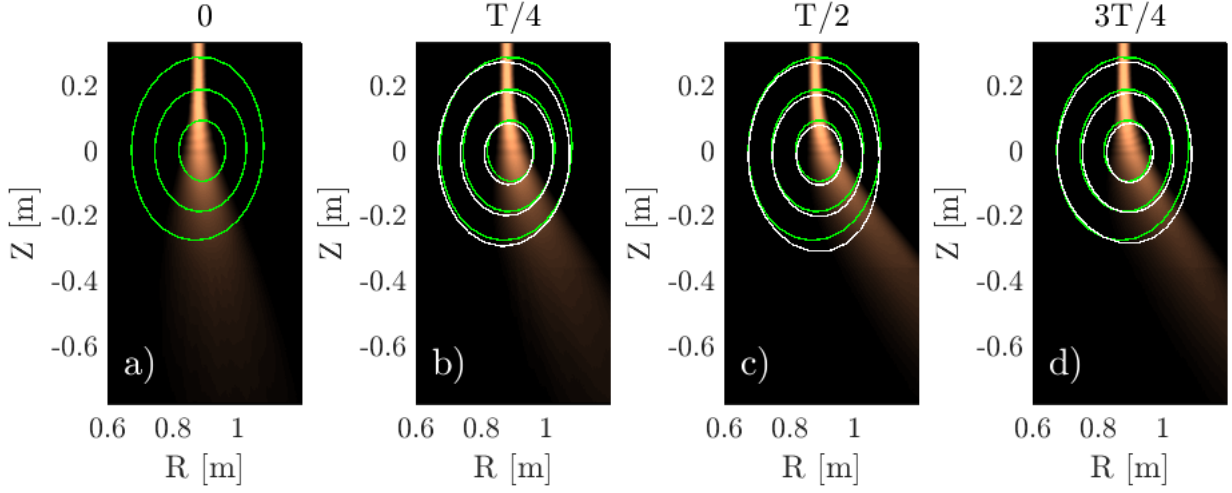


Figure 6.8 – a-d) Full-wave simulations. The electric field norm of the mmw-beam is shown for an injection at  $R = 0.88$  m and  $\theta_m = 45^\circ$  during one period  $T$  of the mode in TCV discharge 60393. The contours are isodensity lines ( $3, 6, 9 \times 10^{19} \text{ m}^{-3}$ ). The green contours are the isodensities at  $t = 0$  and the white contours are the isodensities at  $T/4, T/2$  and  $3T/4$ , respectively (taken respectively at  $t = 1.1998, 1.9985, 1.19989$  and  $1.19993$  s)

limits of the smaller computational domain (here, WKBeam) at  $Z = -0.77$  m position. The parameter  $\zeta$  is equal to 0 for two mmw-beam that have no overlap and it is equal to 1 for identical mmw-beam profiles. We find  $\zeta \geq 0.99$  for each snapshot, which shows a good agreement between the two models. The structures in  $E^2$  (clearly visible in the WKBeam profiles in fig. 6.9) do not seem to be linked to the size of the computational grid in WKBeam. We suspect that they are caused by the resolution the  $n_e$  profiles from the soft X-ray tomographic reconstruction.

## Conclusions

In this chapter, we have seen that the rotation of the plasma associated with the kink mode is responsible for a periodic modulation of the transmitted power with drops in the power up to 100%. Combining the experimental observations with numerical simulations using the full-wave model and the WKBeam code, we have seen that this can be explained by periodic deflections of the mmw-beam due to the radial displacement of the plasma associated with the rotation. Although the amplitude of the drop in the transmission caused by the rotation of the plasma is large and should be avoided for scattering experiments, its spectral signature (peaked at  $f_m$  or  $2f_m$ ) can easily be distinguished from that of a broadband turbulence. To investigate the frequency doubling feature as well as to perform a quantitative comparison with the numerical simulations would require running the simulations for different injection angles and could be matter for a following publication. A simple intuitive interpretation for

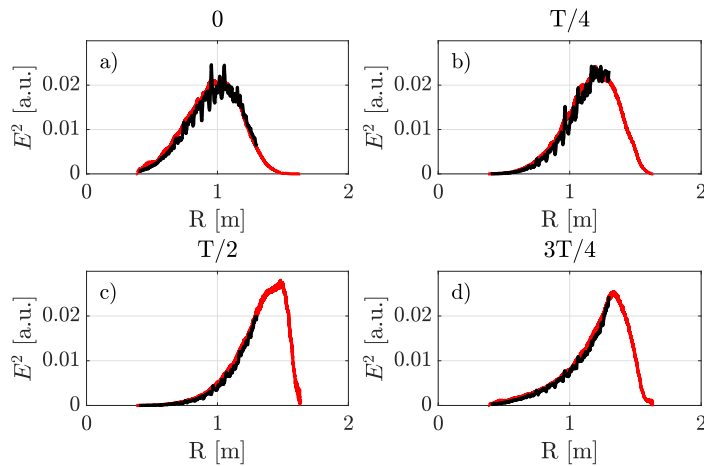


Figure 6.9 – Discharge 60393: a-d) Comparison of the profiles of  $|E|^2$  computed using full-wave (red) and WKBeam (black) simulations. The profiles are taken at  $z = -0.77$  m (X3TD position) during one period of the mode, each quarter of the period.

the frequency doubling is that, similarly to what is observed on the soft X-ray measurements (fig. 6.2), at the injection angles where the frequency doubling occurs, the mmw-beam goes through the central part of the plasma twice during the mode rotation. In the next section, we will see that the kink mode preceding the sawtooth crash is also responsible for periodic deflections of the mmw-beam.

# 7 Effect of edge turbulence on the high-power mmw-beam on TCV

In the previous chapters, we have investigated the effect of plasma turbulence on the propagation of low-power mmw-beams in simple magnetized plasmas. We have seen that plasma turbulence affects the instantaneous profile of the mmw-beam, introducing fluctuations in the locally-measured transmitted mmw-power. Conditional sampling analysis combined with full-wave simulations revealed that the mmw-beam is scattered in the wake of blob structures, resulting in a local decrease or increase of the mmw-power depending on its spatial location. The associated level of fluctuations of the detected mmw-power was found to increase with the electron density. In this chapter, using similar techniques, we will address the case of the scrape-off layer (SOL) in TCV confined plasmas and see that the previous results are also applicable to blobs in the SOL.

The chapter is organized as follows: the plasma scenario is described in section 7.1. Section 7.2 investigates the effect of plasma sawtooth activity on the mmw-beam propagation. Experimental evidence of mmw-scattering from SOL turbulence is provided in section 7.3. Finally, using SOL simulations from the GBS code together with wave propagation simulations, based on both the full-wave model and the WKBeam code (see chapter 4), the effect of edge turbulence upon the mmw-beam is investigated numerically in section 7.4.

## 7.1 Plasma scenario

In this section, we describe the L-mode limited plasma scenario used in the scattering experiments performed in TCV.

### 7.1.1 Description of the plasma equilibrium

The experiments are performed in an L-mode limited deuterium plasma. The duration of the plasma discharge is 2 s with a current flat-top starting at  $t = 0.37$  s and ending  $t = 1.87$  s. The main parameters of the plasma discharge are summarized in table 7.1

## Chapter 7. Effect of edge turbulence on the high-power mmw-beam on TCV

$q_{95}$	$\kappa$	$\delta$	$n_{e,0}$	$T_{e,0}$	$B_T$	$R_0$	$Z_0$
2.8	1.52	-0.02	$7.3 \times 10^{19} \text{ m}^{-3}$	0.8 keV	-1.41 T	0.89 m	0.01 m

Table 7.1 – Plasma parameters for the TCV discharges 60612, 60614, 60616, and 60617. safety factor at 95% of the plasma minor radius, plasma elongation and triangularity, electron density and temperature, magnetic field on axis, and position of the plasma, respectively

The plasma equilibrium is represented in fig. 7.1a). The plasma axis is located at  $(R_0, Z_0) = (0.89, 0.01)$  m. The inner wall of the vessel naturally limits the plasma around  $Z = 0.01$  m. The width of the SOL at  $n_{e,LCFS}/2$  [69] is shown in fig. 7.1. At the entrance of the mmw-beam in the plasma, this represents  $\approx 30$  mm. Figure 7.1b,c) show the electron density and temperature profiles as a function of the flux coordinates  $\rho_\psi$ . From the Thomson scattering profiles in fig. 7.1b,c), we find that the electron density at the last closed flux surface is (fig. 7.1b)  $n_{e,LCFS} \approx 6 \times 10^{18} \text{ m}^{-3}$  and the electron temperature is  $T_{e,LCFS} \approx 30$  eV (fig. 7.1c).

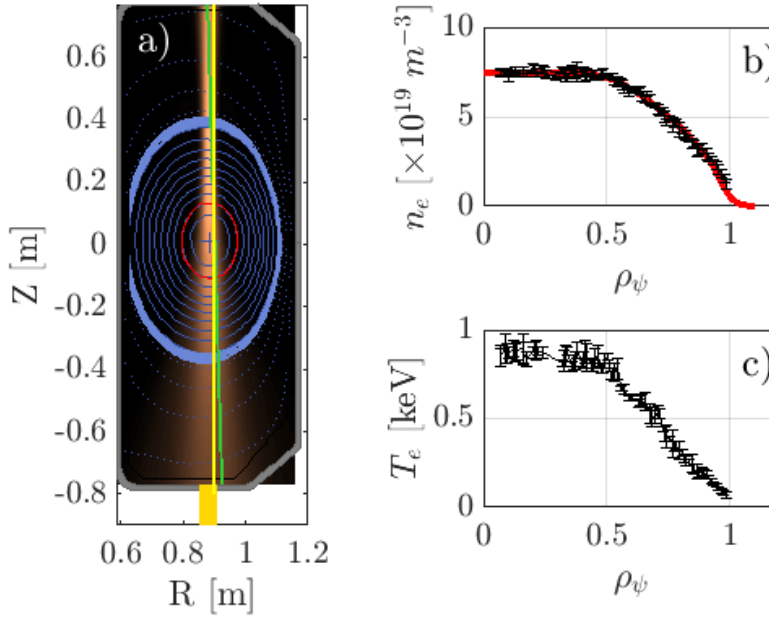


Figure 7.1 – Discharge 60612. a) Contours of the flux surfaces and mmw-beam. The mmw-beam is represented in the background. The electric field norm shown here is obtained from full-wave simulations. The solid (respectively dotted) lines represent closed (respectively open) flux surfaces. The blue surface identifies the SOL region and the blue cross the plasma axis. The red line represents the  $q = 1$  flux surface. The green line represents the line of sight of camera 2, channel 11 of the XTOMO X-ray tomographic diagnostic (described in Chapter 2). The yellow line is the line of sight of FIR located at  $R = 0.90$  m. The yellow rectangle at the bottom of the vessel represents the X3TD diagnostic. b) Average electron density and c) temperature profiles from the Thomson scattering diagnostic over the flattop of the plasma.  $\rho_\psi = 1$  corresponds to the last closed flux surface. The red curve in b) shows the fitted  $n_e$  profile that will be used later in this chapter for numerical simulations in section 7.5.

### 7.1.2 Sawtooth activity in discharge 60612

TCV ohmic discharges with a safety factor  $q_{edge}$  up to  $\approx 10$ , here  $q_{edge} = 3.2$ , exhibits sawtooth activity [46]. Sawtooth activity results in periodic relaxations of the core electron density and temperature that occurs when the safety factor at the axis  $q_0$  drops below unity. A ramp phase (sawtooth ramp) during which the electron density and temperature increase linearly in the central region of the plasma is followed by a fast drop of the two quantities (sawtooth crash), triggered by the instability of a kink mode developing at the  $q = 1$  surface with poloidal mode number  $m=1$  and toroidal mode number  $n=1$  [46]. Since the mmw-beam traverses the core of the plasma before reaching the X3TD diagnostic, it is essential to identify the effect of the sawtooth activity on the propagation of the mmw-beam and separate its contribution from that of the turbulence in the SOL.

Since soft X-ray emission from the plasma depends on both  $n_e$  and  $T_e$ , XTOMO is a natural diagnostic for sawtooth activity. Figure 7.2a) shows the soft X-ray emission intensity  $S_X$  measured by the central XTOMO channel (camera 2, channel 21). The line of sight is shown in fig. 7.1a) and follows the path of the mmw-beam with a vertical injection at  $R = 0.88$  m. The sawtooth activity is associated with a slow increase of  $S_X$  followed by a rapid drop with a frequency of  $\approx 300$  Hz. The duration of the sawtooth ramp is  $\approx 2.6$  ms and that of the sawtooth crash is  $\approx 0.6$  ms. The crash of the sawteeth is preceded by the growth of the kink mode, characterized by an oscillation of  $S_X$  with a frequency centered around  $\approx 5.8$  kHz associated with the kink mode.

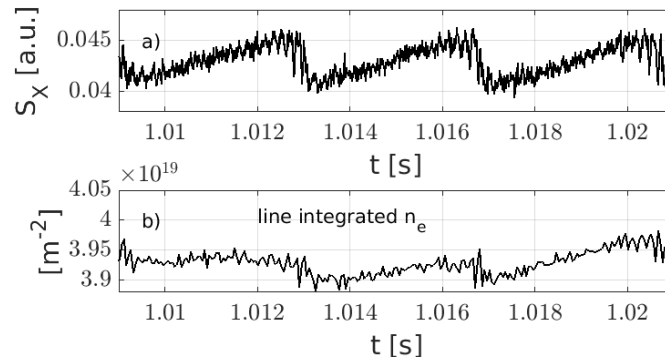


Figure 7.2 – a) Soft X-ray emission from XTOMO camera 2, detector 11. The crash of the sawtooth is preceded by periodic oscillations associated with a kink mode with a frequency of  $\approx 5.8$  kHz. b) Line integrated electron density from the central chord of the far infrared interferometer (FIR) located at  $R = 0.90$  m and shown in fig. 7.1.

The peak-to-peak amplitude of the fluctuations of the soft X-ray emission  $\frac{\Delta S_X}{\langle S_X \rangle}$  is about 20%. Figure 7.2b) shows the line integrated electron density from the central chord of the far infrared interferometer (FIR) which traverses the plasma vertically at  $R = 0.90$  m. The fluctuations of the line integrated density measured by the central chord of the FIR are small and of the order of 3%. This suggests that the larger fluctuations of  $S_X$  are instead associated with fluctuations of  $T_e$  and  $Z_{eff}$ . These two quantities do directly affect  $\epsilon_r$  but can affect the reconstructed

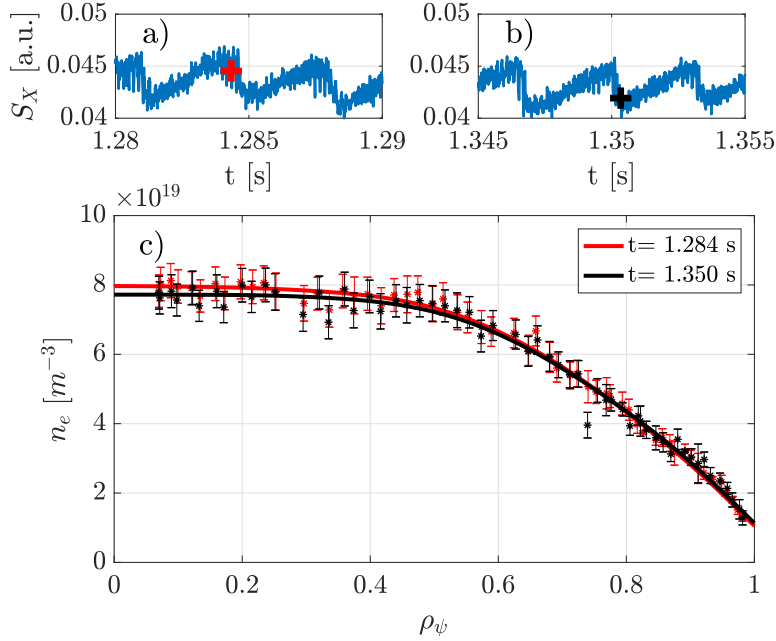


Figure 7.3 – a) and b) Soft X-ray emission from the XTOMO camera 2, detector 11 at two different time windows. The red cross and the black cross represent a pre-crash and a post-crash Thomson scattering time respectively. c) Electron density profiles associated with the pre (red) and post (black) crash of the sawtooth identified in a) and b) respectively.

$n_e$  profile. To reconstruct spatial changes of the electron density during the sawtooth crash, we select two Thomson scattering measurements performed before and after the sawtooth crash. Figure 7.3a,b) shows both Thomson scattering times identified on the soft X-ray signal. The corresponding electron density profiles are shown on fig. 7.3c). We can see that the difference in the electron density on the axis is also small and lies within the errorbars of the two measurements, which is consistent with the FIR measurements.

In the next section, we will see that, although small, these changes in the electron density during the sawtooth crash can explain an observed variation of the maximum detected power of the order of 13%.

## 7.2 A note on the effect of sawteeth on the propagation of mmw-beams

In the previous section, we have seen that sawtooth activity in the limited plasma under study is associated with a periodic oscillation of the electron density and temperature. Although small, we can expect changes in the  $n_e$  profile to affect the mmw-beam propagation since O-mode propagation is perturbed by density fluctuations. In this section, we will investigate the effect of the sawtooth activity on the mmw-power transmission in TCV. In discharge 60612, the mmw-beam is injected in the O-mode at  $R = 0.88$  m. The poloidal angle of the mirror is

## 7.2. A note on the effect of sawteeth on the propagation of mmw-beams

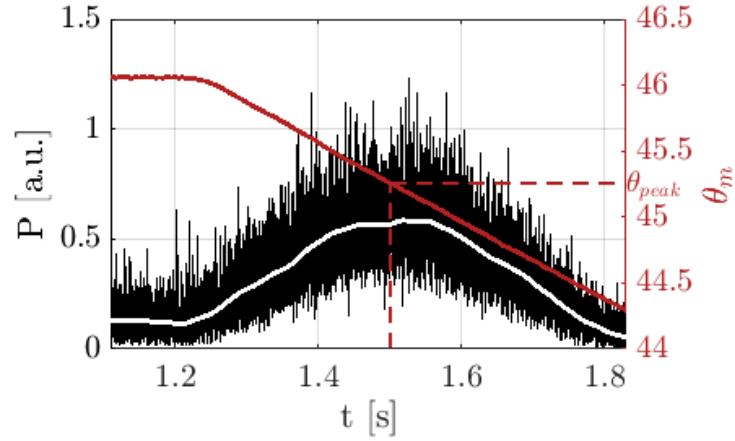


Figure 7.4 – Discharge 60612. The power measured by X3TD is shown in black. The angular position of the poloidal launching mirror is shown in red. Here, the beam is swept across the detector by varying  $\theta_m$ .

swept from a measured  $\theta_m = 46^\circ$  to  $\theta_m = 44.3^\circ$ . Figure 7.4 shows the evolution of the measured mmw-power together with  $\theta_m$  during the discharge. The maximum of transmission occurs at  $\theta_{peak} \approx 45.2^\circ$  and the power drops significantly at  $\theta_m = 46^\circ$  and  $\theta_m = 44.3^\circ$ . The transmitted signal is characterized by a level of fluctuations  $\Sigma = \sigma(P)/\langle P \rangle$  up to 0.5 (fig. 7.11), where  $\sigma(P)$  is the standard deviation of  $P$  and  $\langle P \rangle$  the time-average of  $P$  computed over a time-window of 20 ms. Over this time,  $\theta_m$  varies of  $\approx 0.5^\circ$ . The power spectral density (PSD) of the two

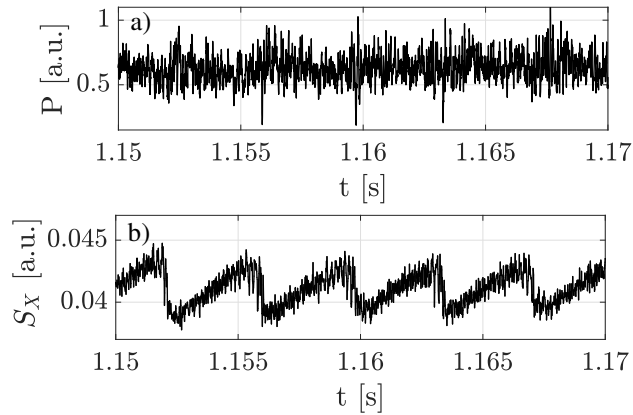


Figure 7.5 – Discharge 60614: a) transmitted power measured by X3TD. The injection is performed at  $\theta_{peak}$ . b) Soft X-ray emission from the XTOMO camera 2, detector 11.

signals ( $P$  and  $S_X$  in fig.7.5) shows that the spectra of both signals are characterized by a broad peak around  $f \sim 5$  kHz associated with the kink mode and a peak around  $f = 300$  Hz (and harmonics for the soft X-ray emission), which is the frequency of the sawtooth oscillations.

Figure 7.5a) shows the power measured by X3TD in the time window covering  $t = 1.15 - 1.17$  s

and is compared to the soft X-ray emission measured by XTOMO camera 2, channel 11. Some of the signal features are synchronized with the sawtooth crash. The largest variations of the mmw-power transmission occur at the crash of the sawtooth. The cross-correlation function between  $S_X$  and  $P$  is shown in fig. 7.6a) and exhibits the characteristic decaying oscillations of periodic signals with a significant level of correlation ( $\sim 0.2 - 0.3$ ). The power spectral density (PSD) of the two signals is shown in fig. 7.6b). The PSD is computed on the standardized signals (see section 7.3 for more details).

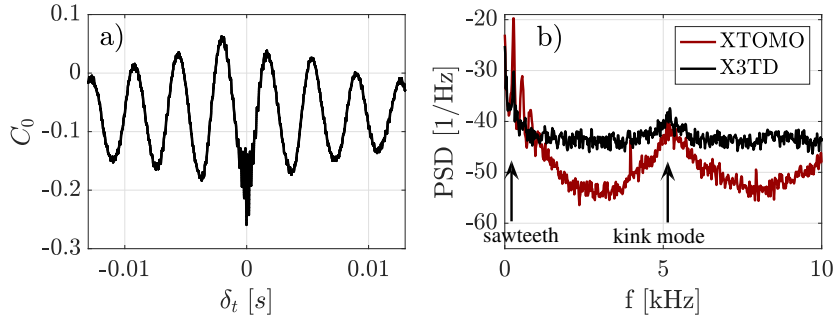


Figure 7.6 – Discharge 60614. a) Cross-correlation function between the X3TD signal and the soft X-ray signal shown in fig. 7.5. b) Power spectral density (PSD) of the X3TD signal (in black) and the soft X-ray emission from the XTOMO camera 2, detector 11 (in red). The PSD is computed in the time-window  $t = [1.1, 1.85]$ . In this discharge,  $\theta_m$  is constant and equal to  $\theta_{peak}$ . Both signals contain the mode signature  $f = 5$  kHz and the sawtooth signature around  $f = 300$  Hz and its harmonics.

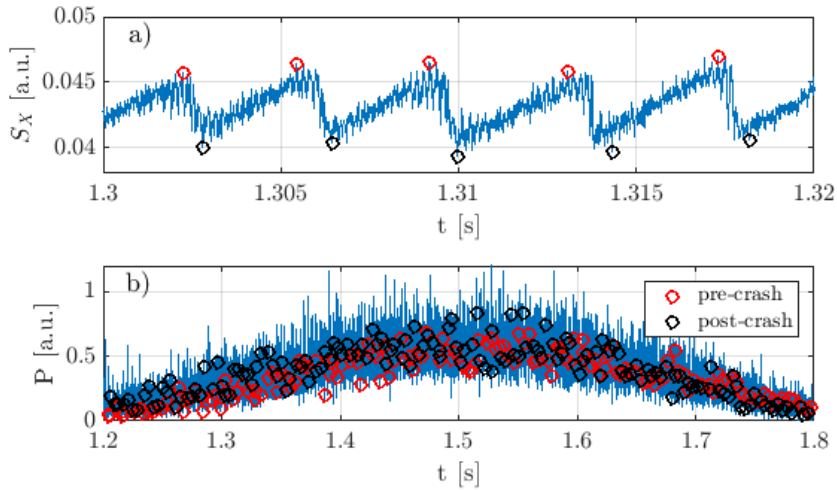


Figure 7.7 – a) Soft X-ray emission from the XTOMO camera 2, detector 11. Pre-sawtooth crash times are identified by the red circles and post-crash times are identified in black. b) Transmitted power measured by X3TD during discharge 60612 with the same times indicated.

We perform the conditional sampling (CS) on the soft X-ray signal to identify times associated



## 7.2. A note on the effect of sawteeth on the propagation of mmw-beams

with the pre- and post-crashes of the sawteeth. Pre- (post-) crashes times are identified as local maxima (minima) of the  $S_X$  signal, separated in time by more than 3 ms. The detection of the pre- (in red) and post- (in black) sawtooth crash times is shown in fig. 7.7a). The  $P$  signal measured by X3TD at the selected times is shown in fig. 7.7b). Figure 7.8 is a zoom on three different parts of the  $P$  signal. The larger power measured *after* the sawtooth crash for high  $\theta_m$

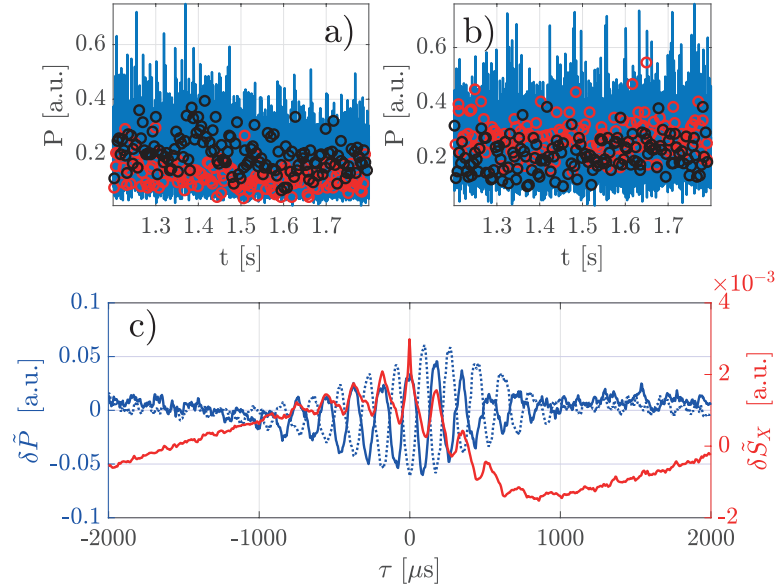


Figure 7.8 – Transmitted power measured by X3TD during discharge 60617 a), respectively 60616 b), with a constant injection angle  $\theta_m = 46^\circ$ , respectively  $\theta_m = 44.5^\circ$ . Pre-sawtooth crash times are identified by the red circles and post-crash times are identified in black. 60612. c) In red: CS performed on the soft X-ray signal from the XTOMO camera 2 detector 11. The time  $\tau = 0 \mu\text{s}$  corresponds to the sawtooth crash. In blue: CS performed on the  $P$  signal at  $\theta_m = 46^\circ$  (dotted line) and  $\theta_m = 44.5^\circ$  (solid lines).

(fig. 7.8a) and inversely, the larger power measured *before* the sawtooth crash from low  $\theta_m$  (fig. 7.8b), seem to indicate a small deflection of the mmw-beam during the sawtooth oscillation. Figure 7.8c) shows the CS of the soft X-ray emission and the detected power  $P$  at the minima of detection ( $\theta_m = 44.5^\circ$  and  $46^\circ$ ).  $\delta \tilde{S}_X$  (in red) increases slowly ( $\sim 3$  ms) during the sawtooth ramp and decreases rapidly ( $\sim 1$  ms) after the crash. The periodic oscillations at  $f_m = 5$  kHz are visible in  $\delta \tilde{S}_X$ . The same oscillations are even more visible on  $\delta \tilde{P}$  at the two  $\theta_m$  angles for  $\tau \in [-1, 1]$  ms and are synchronous with the oscillations of  $\delta \tilde{S}_X$ . We find that  $\delta \tilde{P}$  at the two angles are in phase opposition, meaning that when the detected power decreases at  $\theta_m = 46^\circ$ , it increases at  $\theta_m = 44^\circ$  and inversely. This confirms the deflections of the mmw-beam, which are caused by the kink mode associated with the sawtooth, similarly to the observations made in chapter 6.

To study the effect of the sawtooth crash on the average mmw-power profile and the normalized level of fluctuations (fig. 7.9a) and b), respectively, we identify the crash of the sawtooth

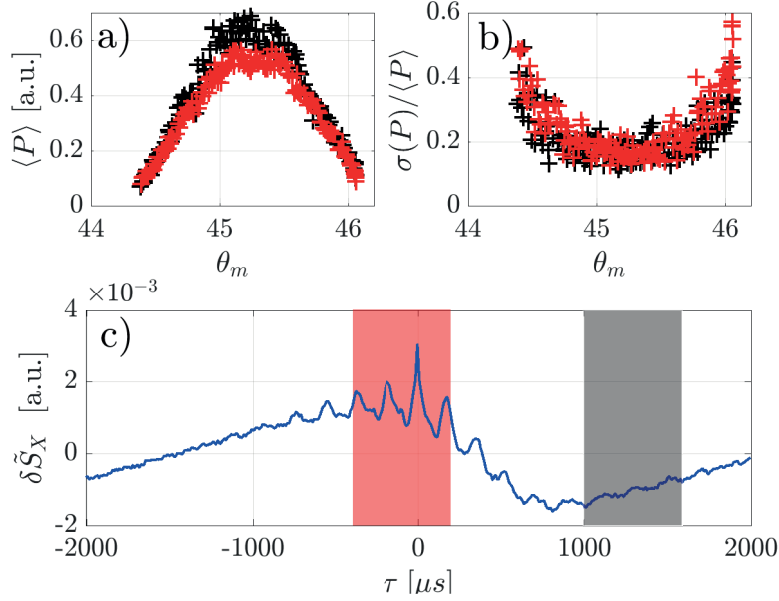


Figure 7.9 – a,b) Time-averaged  $\langle P \rangle$  and normalized level of fluctuation  $\sigma(P)/\langle P \rangle$ , respectively, computed at the sawtooth crash (time window in red in c) and after the sawtooth crash (in black in c)).

on the  $S_X$  signal (as shown in red in fig. 7.9) and a time window (in black) after the sawtooth crash. Each matching-color cross in fig. 7.9 a) and b) represents the time-averaged  $\langle P \rangle$  and normalized level of fluctuation  $\sigma(P)/\langle P \rangle$ , during and after the sawtooth crash. The full-width at half maximum of  $\langle P \rangle$  is not significantly affected by the sawtooth crash whereas  $\langle P \rangle_{max}$  drops of  $\sim 15\%$  with the crash of the sawtooth. The normalized level of fluctuations (which will be discussed in more details in section. 7.3) is not affected by the sawtooth activity. The sawtooth activity can therefore not explain all the fluctuations of  $P$ . We will see in section 7.3 that the turbulence in the SOL is responsible for part of the fluctuations of  $P$ . Full-wave simulations (more details in chapter 4) are performed for the pre- and post-crash plasma profiles ( $\delta n_{e,0}/n_{e,0} \approx 0.03$  between the two profiles) identified in red and black, respectively in fig. 7.3. The simulations are performed for five different injection angle between  $44^\circ$  and  $46^\circ$ . For each injection angle, we compute the power detected by X3TD using the synthetic diagnostic (more details in chapter 2). The results of the simulations are shown in fig. 7.10. At the sawtooth crash, the maximum detected power drops of 13%, which is in agreement with the experimental observations. The 3% variation in the electron density on axis is sufficient to explain the variation of detected power, associated with the sawtooth activity, around  $\theta_m = 45.2^\circ$

In this section, we have investigated the effect of the sawtooth activity in the core plasma on the propagation of the mmw-beam in the plasma of interest for the scattering studied on TCV. We have seen that the activity of the mode associated with the sawtooth is responsible for periodic deflections of the mmw-beam. We have also seen that, although the associated

### 7.3. Experimental evidence of mmw-scattering from turbulence in the scrape-off layer

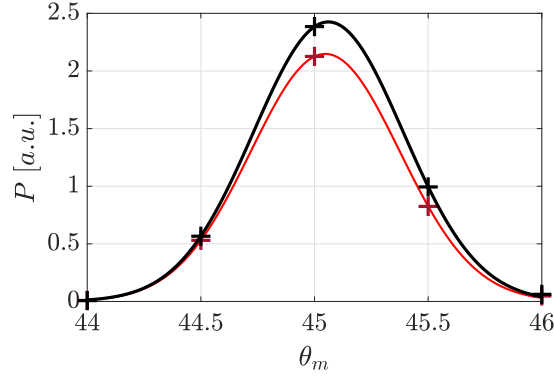


Figure 7.10 – Detected mmw-power during (red) and after (black) the crash of the sawtooth as a function of the injection angle  $\theta_m$  computed using full-wave simulations using the electron density profiles shown in fig. 7.3. The solid lines are a Gaussian fit to the data.

changes in the electron density are small ( $\delta n_e / n_e \approx 3\%$ ) during the crash of the sawtooth, they modulate the detected power signal and cause variations of the detected power of up to 15%. The normalized fluctuation  $\sigma(P) / \langle P \rangle$  level (fig. 7.9), however, is not influenced by the sawtooth activity. We will see in section 7.3 that the SOL is responsible in part for the observed fluctuations in the detected mmw-power.

### 7.3 Experimental evidence of mmw-scattering from turbulence in the scrape-off layer

In this section, we present experiments designed to study the effect of the turbulent structures in the SOL on the propagation of the high-power mmw-beam. We have seen in chapter 5 that field aligned structures, associated with an increase of electron density relative to the background density and referred to as blobs, are responsible for localized and time-dependent fluctuations of the mmw-power along the path of the beam. In this section, we will provide experimental evidence of scattering of the mmw-beam by the blobs present in the SOL of TCV L-mode limited plasmas.

Figure 7.4 shows the mmw-power measured by X3TD during a sweep of the poloidal angle of the launcher. The four moments of the PDF of the measured mmw-power  $P$  across the poloidal angle of the launcher  $\theta_m$  are shown in fig. 7.11. They are estimated from a set of  $N = 400$  independent measurements, i.e. separated by a time delay larger than the autocorrelation time of  $P$ , in this case  $\approx 50 \mu s$ .  $P$  is maximum at  $\theta_m \approx 45.2^\circ$ , when the center of the mmw-beam is aligned with the X3TD detector, and drops at the edges of the sweep of  $\theta_m$ . The normalized level of fluctuations  $\Sigma(\theta_m) = \sigma(P) / \langle P \rangle$  ranges from 0.2, around the maximum of mmw-power detection, up to 0.6 around the minimum of mmw-power detection.  $\Sigma(\theta_m)$  in the case with no plasma (vacuum) is also given as a reference in fig. 7.11 b) and is lower than 0.1; this measure accounts for the inherent changes in the injected power as well as electronic

noise during the pulse. As detailed in chapter 2 and for machine safety reasons, the power of the gyrotron is pulsed in vacuum. Here,  $\Sigma$  is computed on the last 2 ms of each 8 ms pulse to avoid artifacts from the non-linear response of the gyrotron to the pulse command. The errors in the calculation of  $\langle P \rangle$  and  $\Sigma(\theta_m)$  are shown in fig. 7.11a,b). They result from the statistical errors in the estimates [85, 84]. The positive skewness and the kurtosis ( $\geq 4$ ) around the minima of mmw-detection ( $\theta_m \approx 44.3^\circ$  and  $\theta_m \approx 46^\circ$ ) indicate that the PDF is not Gaussian and that most of the variance of the signal at these extreme angles is due to infrequent large deviations from the average value. This indicates that the mmw-beam at these angles reaches the detector mostly due to intermittent events.

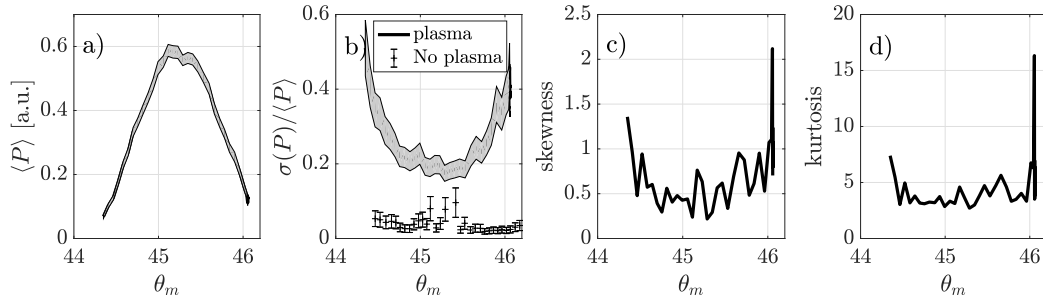


Figure 7.11 – Discharge 60612. The first four moments of the PDF of the measured mmw-signal as a function of the poloidal angle of the injection mirror computed on time windows of 8 ms. b) the standard deviation is normalized to the time-averaged value of the detected mmw-power. The black crosses in b) represent the case with no plasma. The errors in a) and b) are given by the statistical uncertainties in the estimates [84, 85].

In the following, to investigate the contribution of the SOL turbulence to the fluctuations in the transmitted mmw-power, we compute the cross-correlation between the measured mmw-power signal  $P$  and the  $I_{sat}$  signal from the wall-embedded Langmuir probes. We also show that these latter are not affected significantly by sawtooth crashes nor mode activity near the  $q = 1$  flux surface. An example of  $I_{sat}$  measured by LP 50, located in the inner-wall of the TCV vessel, is shown in fig.7.12b). The positive bursts in  $I_{sat}$  are associated with the detection of blobs [64, 98]. The cross-correlation function  $C_0$  is defined as follows

$$C_0(\delta t) = \frac{1}{T_2 - T_1} \int_{T_1}^{T_2} p(t) i_{sat}(t + \delta t) dt, \quad (7.1)$$

where  $p$  and  $i_{sat}$  are the standardized mmw-power signal and  $I_{sat}$  signal defined by  $p = \frac{P - \langle P \rangle}{\sigma(P)}$  and  $i_{sat} = \frac{I_{sat} - \langle I_{sat} \rangle}{\sigma(I_{sat})}$  respectively,  $\delta t$  is the time-lag and  $[T_1, T_2]$  is the selected time window.  $\delta t$  can be interpreted as following: when a feature occurs in  $P$  at  $t$ , it occurs in  $I_{sat}$  at  $t + \delta t$ . The  $I_{sat}$  signal from the three probes indicated in yellow is found to be correlated to the  $P$  signal. The location of the probes is shown in yellow in fig. 7.12a) and corresponds to the region where the SOL terminates on the inner-wall of the vessel. The cross-correlation function for the probe LP 50 (located at  $z = -14$  cm), corresponding to the maximum level of cross-correlation,

### 7.3. Experimental evidence of mmw-scattering from turbulence in the scrape-off layer

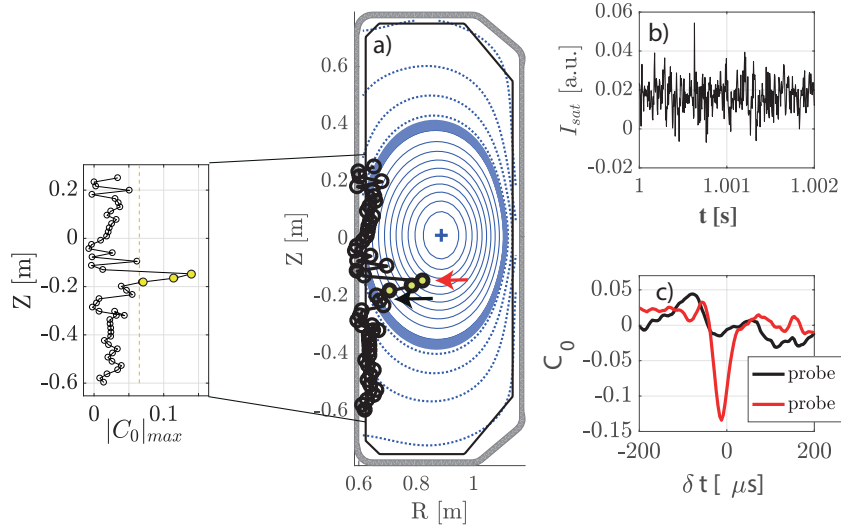


Figure 7.12 – a) Contours of the flux surfaces as detailed in fig. 7.1a). The black curve represents the amplitude of the cross-correlation function  $|C_0|_{max}$ , on a horizontal axis, of the X3TD signal and the  $I_{sat}$  signal of the Langmuir probes of the inner wall of the vessel as defined in eq. 7.1. The signal of the three probes, identified in yellow, have a significant level of cross-correlation ( $> 0.06$ ) with the X3TD signal. The yellow dashed line represents the 0.06 threshold. b)  $I_{sat}$  current measured by Langmuir probe 50, corresponding to the maximum level of cross-correlation in a). The negative values of  $I_{sat}$  might be due to fast electrons or insufficient bias voltage. c) Cross-correlation function associated with the probe 50 ( $z = -14$  cm, in yellow in a) and probe 53 ( $z = -20$  cm, in black in a). Their positions are indicated by the matching-color arrows.

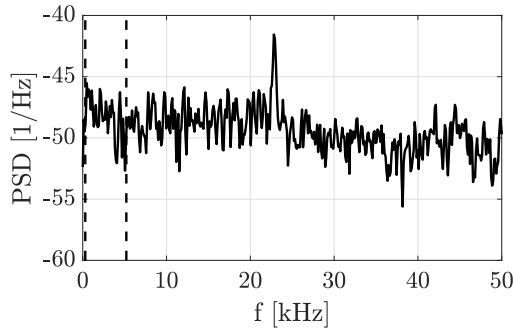


Figure 7.13 – Power spectral density of the  $I_{sat}$  current measured by probe 50 (indicated by the red arrow in fig. 7.12) the TCV discharge 60614. The dashed lines identifies the frequency of the sawtooth oscillation 0.3 kHz and that of the associated mode 5.2 kHz.

is compared to the cross-correlation function for the probe LP 53 (located at  $z = -20$  cm) in fig. 7.13c). The probe LP 53 exhibits no significant level of cross-correlation on the time window 0.95 – 1.05 s. The cross-correlation function corresponding to the probe LP 50 has a negative peak occurring at  $\delta t = -12 \mu s$  and has an amplitude of  $|C_0|_{max} = 0.13$ . This indicates that the

positive spikes detected by LP 50 induce a negative fluctuation of  $P$  and that this fluctuation occurs  $12 \mu\text{s}$  before the spike is detected by the probe.

Figure 7.13 shows the power spectral density of the  $I_{sat}$  measured by the probe LP 50. The spectrum is continuous and shows no characteristic signature at the frequencies corresponding to the sawteeth and the mode oscillations. This indicates that the  $I_{sat}$  measurement from the Langmuir probes is not affected by the sawtooth activity.

As seen in chapter 5, blobs can affect the measured mmw-power when they cross the path of the mmw-beam. Whether or not a blob detected by a Langmuir probe crosses the path of the mmw-beam depends on the location of the intersection between the field line connecting the probe and the plane of the mmw-beam (see fig.7.15). This intersection can be controlled by changing the plasma current  $I_p$  in a discharge. When  $I_p$  is chosen such that the field line connecting the probe and the plane of the mmw-beam intersects the mmw-beam, a blob lying on this field line affects the detected power. We show below that when  $I_p$  is such that the field line associated with same blob does not intersect the mmw-beam, the blob has no effect on the detected mmw-power.

We investigate the influence of  $I_p$  on the maximum of the correlation function associated with LP 50  $|C_0|_{max}$  and the corresponding time lag  $\delta t_{max}$  in fig. 7.14. The errorbars are given by the uncertainty in the estimate of  $|C_0|_{max}$  and are equal to  $\frac{1-|C_0|_{max}^2}{\sqrt{N}}$ , where  $N \sim 2000$  [99]. Figure 7.14a) shows that  $|C_0|_{max}$  increases for  $I_p$  ramping from  $-280$  kA to  $-271$  kA, where it reaches its maximum value and then decreases for  $I_p$  ramping up from  $-271$  kA to  $-260$  kA. For  $I_p > -260$  kA, the  $I_{sat}$  signal from the probe is no longer correlated to  $P$ .

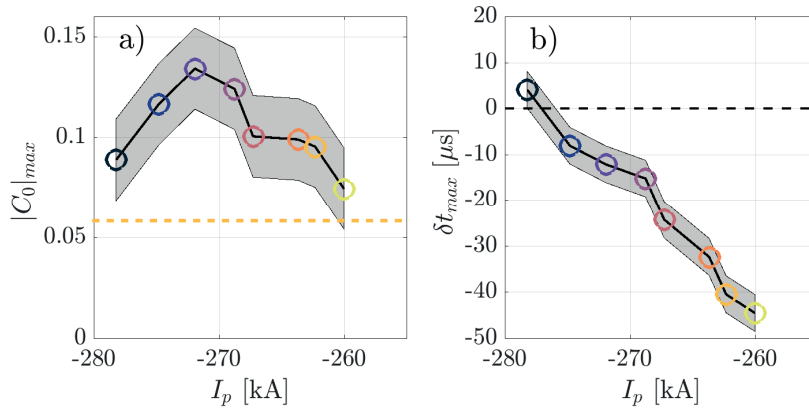


Figure 7.14 – a) Maximum of the cross-correlation function between  $P$  and  $I_{sat}$  measured by Langmuir probe 50 as a function of the plasma current. The level  $|C_0|_{max} > 0.06$  above which the correlation is considered significant is indicated by the yellow dashed line. b) Time lag at which the maximum level of cross-correlation given in a) occurs. The colors of the circles are used to identify the value of  $I_p$  used in fig. 7.16 and fig. 7.20. The errorbars (gray area) in a) are given by the statistical uncertainty in the estimate of  $|C_0|_{max}$  and in b) by the sampling period of the signals.

### 7.3. Experimental evidence of mmw-scattering from turbulence in the scrape-off layer

We will see later that the two signals are significantly correlated ( $|C_0|_{max} > 0.06$ , indicated by the yellow dashed line in fig. 7.14) when the field line terminating on the Langmuir probe intersects the path of the mmw-beam at the location of the upper part of the scrape-off layer.

Figure 7.14b) shows that the time lag  $\delta t_{max}$  decreases linearly, from  $\delta t_{max} = +4 \mu s$  to  $\delta t_{max} = -44 \mu s$ , when  $I_p$  increases from  $-278 \text{ kA}$  to  $-260 \text{ kA}$ . When  $\delta t_{max}$  is negative (positive), the blob affects the mmw-propagation before (after) being detected by the Langmuir probe. Below, we interpret these results by explaining how the magnetic field geometry varies as a function of the plasma current.

Figure 7.15 shows two field lines connecting the LP 50 to the plane of the mmw-beam for two values of plasma current:  $I_p = -271 \text{ kA}$  in blue, where  $|C_0|_{max}$  is maximum, and  $I_p = -250 \text{ kA}$ , when  $I_{sat}$  and  $P$  are no longer correlated. For  $I_p = -271 \text{ kA}$ , when  $I_{sat}$  and  $P$  are correlated, the field line intersects the path of the mmw-beam at the entrance of the SOL. For  $I_p = -250 \text{ kA}$ , the field line intersects the plane of the mmw-beam further to the low-field side, away from the beam. Figure 7.16 shows the location of the intersection of the field line with the plane of the mmw-beam identified in fig.7.15 for the values of  $I_p$  from fig.7.14 and for  $I_p = -250 \text{ kA}$ . We find that for values of  $I_p$  associated with  $I_{sat}$  being correlated to  $P$ , in blue and green (following the colormap of fig.7.14), the field line intersects the beam path. For  $I_p = -250 \text{ kA}$ , the field line passes further away from the beam and does not intersect its path (red cross).

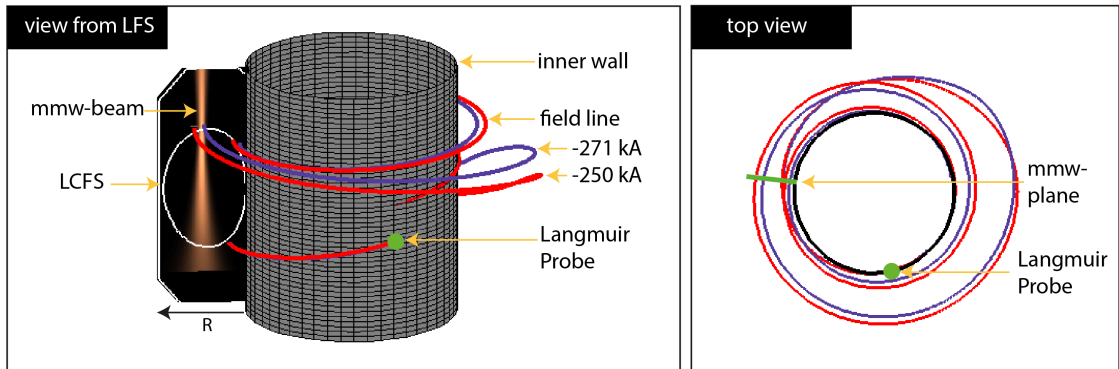


Figure 7.15 – Field lines connecting the LP 50 to the plane of mmw-beam for two values of plasma current:  $I_p = -271 \text{ kA}$  in blue, where  $|C_0|_{max}$  is maximum and the field line connects the probe to the beam; and  $I_p = -250 \text{ kA}$ , when  $I_{sat}$  and  $P$  are no longer correlated and the field line does not cross the beam. Note that both field lines terminate on the LP; on the part between the LP and the mmw-beam plane, the purple field line is hidden behind the red one. The copper-colored surface represents  $|E|$  of the mmw-beam as calculated by the full-wave model. The white solid line represents the last closed flux surface computed from LIUQE.

From the values of  $\delta t_{max}(I_p)$  and the knowledge of the position of the intersection between the corresponding field line and the path of the beam, we can deduce a quasi-poloidal speed  $v = \frac{d_{1,2}}{\Delta t_{1,2}}$  associated with the motion of the blobs, defined by the ratio of the distance between the intersection points  $d_{1,2}$  on the poloidal plane of the mmw-beam, and the time

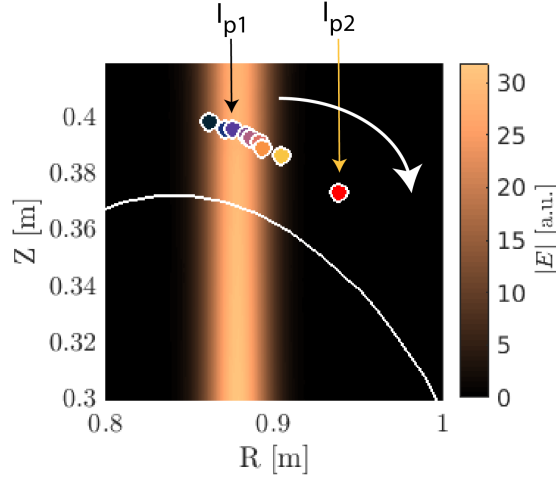


Figure 7.16 – The circles represent the intersection of the field line connecting LP 50 to the plane of the mmw-beam for the values of  $I_p$  indicated in fig.7.14. The red circle corresponds to  $I_p = -250$  kA, where  $I_{sat}$  shows no statistically significant correlation to  $P$ . The copper-colored surface is the norm of the electric field as computed by the full-wave model and the solid white line is the last-closed flux surface. The white arrow indicate the direction of the poloidal rotation of the blobs.  $I_{p1} = -271$  kA and  $I_{p2} = -250$  kA.

delay  $\Delta t_{1,2} = \delta t_{max}(I_{p1}) - \delta t_{max}(I_{p2})$ . By choosing  $I_{p1} = -260$  kA and  $I_{p2} = -278$  kA, we find  $|\nu| \approx 0.9 \text{ km}\cdot\text{s}^{-1}$ . Given that when the field line intersect the plane of the mmw-beam more to the LFS when  $I_p$  increases,  $|\delta t_{max}|$  increases (and  $\delta t_{max} < 0$ ), we deduce that the associated poloidal motion is directed clockwise (the direction of motion is indicated by the white arrow in fig. 7.16).

From the measurements of the fast-reciprocating probe (FRP) on discharge 55394 (a discharge similar to the one studied here), we can deduce the expected poloidal velocity  $v_{pol}$  using the single-ion force-balance equation [100, 53] :

$$\mathbf{v}_{pol} = \frac{\mathbf{E} \times \mathbf{B}}{B^2} - \frac{\nabla p_i \times \mathbf{B}}{q_i n_i B^2}. \quad (7.2)$$

We assume that blobs have the same poloidal velocity as the background plasma. Following the procedure detailed in [53],  $v_{pol}$  is calculated from the measurement of  $T_e$ ,  $n_e$  and the floating potential  $V_p$  of the fast-reciprocating probe. The ion temperature and density are taken to be equal to the electron temperature ( $T_i = T_e$  and  $n_i = n_e$ ) and the plasma potential  $V_p$  is given by  $V_p = V_{fl} + 2.5 k_B T_e$  [53].  $\mathbf{E}$  is computed from the simultaneous measurement of  $V_{fl}$  by two pins of the fast reciprocating probe (FRP) (see chapter 2 for more details) and  $p_i = n_i k_B T_i = n_e k_B T_e$ . The result is shown in fig.7.17. As a convention, the sign of  $v_{pol}$  is chosen such that a positive  $v_{pol}$  is directed upwards at the equatorial plane on the low-



## 7.4. Investigating the effect of a single ‘average’ blobs on the mmw-transmission

field side (counter-clockwise rotation), and a negative  $v_{pol}$  is directed downwards (clockwise rotation).

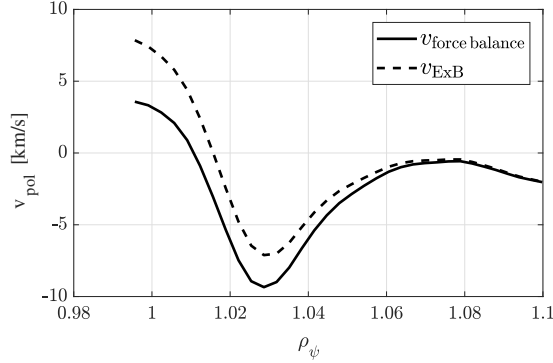


Figure 7.17 – Poloidal rotation velocity as a function of  $\rho_\psi$  using the force balance equation. The dotted line shows the  $\mathbf{E} \times \mathbf{B}$  contribution

At  $I_p = -271$  kA, the field line intersects the mmw-beam at  $\rho_\psi \approx 1.013 \pm 0.001$  which corresponds to  $v_{pol} \in [-2, -1]$  km·s<sup>-1</sup>. We can therefore conclude that the value of  $v_{pol}$  and its direction are in qualitative agreement with those computed using a phase delay technique and geometrical considerations of field line geometry. This further comforts the interpretation of the effects of blobs on the mmw-beam.

## 7.4 Investigating the effect of a single ‘average’ blobs on the mmw-transmission

In this section, we use the conditional sampling (CS) method detailed in chapter 3 and 5, to investigate the effect of a single blob structure upon the mmw-transmission in TCV.

Blobs are detected as bursts in  $I_{sat}$  satisfying the following condition:  $I_{sat} > \langle I_{sat} \rangle + m\sigma$ , where  $\langle I_{sat} \rangle$  is the time-average of  $I_{sat}$  performed over the time trace,  $\sigma$  the standard deviation of  $I_{sat}$  and  $m = 1, 1.5, 2, 2.5, \dots$ . We first take  $m = 2$  and we perform the CS of  $P$  using LP 50 as the conditioning signal, located at  $z = -14.7$  cm, and LP 52 located at  $z = -18.2$  cm on the HFS. We find  $N \approx 300$  events in discharge 61330, between  $t = 0.95$  s and  $t = 1.05$  s ( $I_p = 271$  kA).

The results of the CS analysis are shown in fig. 7.18. The ‘average’ blob detected by LP 50 induces a decrease of the detected mmw-power of  $\approx 8\%$  at  $\tau = -14 \mu\text{s}$  (earlier than the moment of the detection). The blob detected by LP 52 has an opposite effect and induces an increase of the detected mmw-power of 7% (at  $\tau = -30 \mu\text{s}$ ). The position of field line connecting the blob at  $\tau = 0 \mu\text{s}$  is shown in fig. 7.18b). As on TORPEX [35], the results show that depending on their spatial location, blobs can either increase or decrease the locally detected mmw-power.

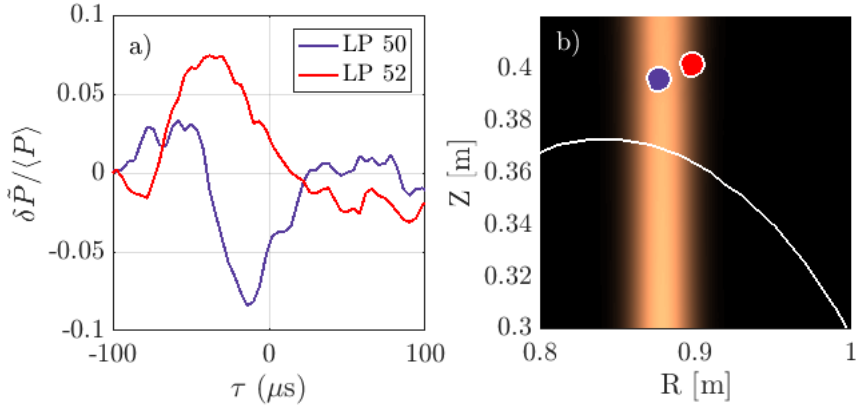


Figure 7.18 – a) CS of the X3TD signal using LP 50 (blue) and 52 (red) as a reference for  $I_p = -270$  k. b) Intersection of the field line terminating on the respective probe and the mmw-beam.

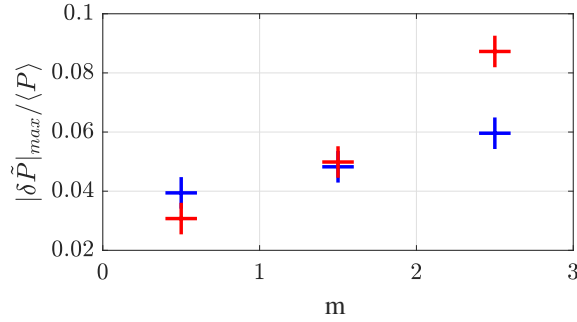


Figure 7.19 – Maximum fluctuation level on the CS of the X3TD signal as a function of the threshold  $m$  using LP 50 (blue) and LP 52 (red) as a reference.

The dependence of the two extrema of fig. 7.18a) on the threshold level  $m$  is shown in fig. 7.19. Several classes of blobs are defined by the condition  $\langle I_{sat} \rangle + (m + 0.5)\sigma > I_{sat} > \langle I_{sat} \rangle + m\sigma$ , with  $m = 0.5, 1.5, 2.5$ . Larger values of  $m$  correspond to blobs with larger electron density compared to the background electron density. Thus, fig. 7.19 shows that the maximum level of the conditionally-sampled fluctuation  $|\delta\tilde{P}|_{max}/\langle P \rangle$  depends on the electron density and increases with blobs of larger electron density. Extrema of up to  $\sim 10\%$  can be measured.

The dependence of the CS profile upon  $I_p$  is shown in fig. 7.20a). Here, the reference probe used in the CS is LP 50 and the threshold is set to  $m = 2$ . In agreement with the evolution of  $\delta t(I_p)$ , we find that the decrease in the detected mmw-power becomes more significant with when  $I_p$  is ramped from  $-262$  kA to  $-278$  kA; similarly,  $\tau$  decreases.

#### 7.4. Investigating the effect of a single ‘average’ blobs on the mmw-transmission

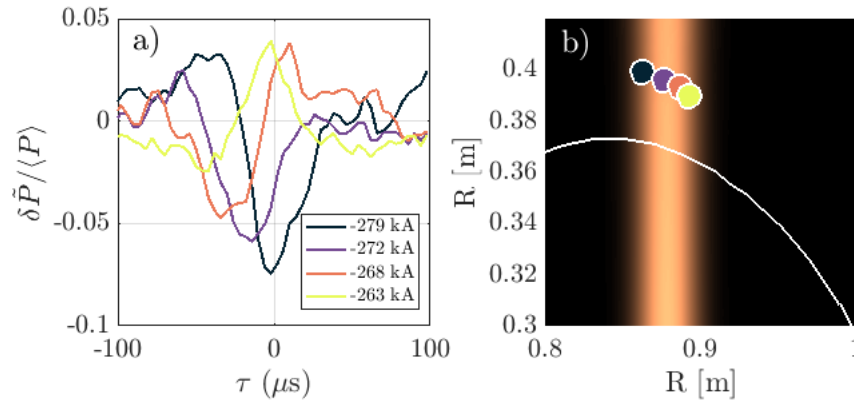


Figure 7.20 – a) CS of the X3TD signal using LP 50 as a reference for different values of  $I_p$ . b) Intersection of the field line terminating on the probe 50 and the mmw-beam for the values of  $I_p$  in a).

#### Conclusions from the experimental measurements

We have shown evidence of high-power mmw-beam scattering by the blobs in the SOL in a TCV L-mode limited plasma. Using Langmuir probes measurements, we have seen that when blobs located in the upper-part of the SOL intersects the paths of the mmw-beam, they induce changes in the mmw-power measured at the floor of the tokamak. The changes can be positive, resulting in a increase of the measured power, or negative, resulting in a decrease of the measured power, depending on the position of the blob. When many blobs pass through the beam during the acquisition period, these changes appear as fluctuations of the measured power. The level of fluctuation is larger for blobs of larger electron density. The results found in this section are very similar to those observed in TORPEX (presented in chapter 5).

In the last part of this chapter, using turbulence simulations from the GBS code and mmw simulations based on a full-wave model and the WKBeam code, the effect of the SOL turbulence on the mmw-beam propagation is investigated numerically.

## 7.5 Numerical investigation of the effect of the edge turbulence on the mmw-beam

In this section, the effects of blobs present in the SOL on the fluctuations of the mmw-beam power and its time-averaged profile are investigated numerically. In section 7.5.1, similarly to the investigations carried out on TORPEX described in chapter 5, the effect of a conditionally-sampled ‘single blob’ on the mmw-transmission is investigated numerically. Here, the CS is performed on the GBS simulations data (instead of HEX TIP data on TORPEX) to identify fluctuations of the electron density  $\delta \tilde{n}_e$  associated with single blobs. The numerical results are found in good agreement with the experimental results presented in section 7.4. Similarly to TORPEX, a single blob is found to defocus the mmw-beam in its wake, resulting in a drop of the measured mmw-power. In section 7.5.2, the effect of the edge turbulence on the time-averaged mmw-beam is investigated numerically using the full-wave model and the WKBeam code and the GBS turbulence data. Although no significant average beam broadening is observed when only considering the turbulence present in the SOL, an average beam broadening of 50% is found to be caused by the edge turbulence, this latter result is in good agreement with the width of the experimental  $P(\theta_m)$  profile, which cannot be explained by only considering the equilibrium plasma, thus confirming the effect of edge turbulence on mmw-propagation .

### 7.5.1 Effect of a single blob on the mmw-beam power

Full-wave simulations are used to interpret the normalized fluctuations  $\delta \tilde{P}/\langle P \rangle$  in the measured power  $P$  caused by a single blob passing through the mmw-beam as shown in fig. 7.18. As in the TCV experiments, the numerical beam is launched vertically. The equilibrium  $\langle n_e(\mathbf{x}) \rangle$  is taken from the TS data and  $\mathbf{B}(\mathbf{x})$  from the equilibrium code LIUQE.  $\delta n_e(\mathbf{x}, t)$  associated with the turbulence in the SOL is obtained from GBS data (see chapter 4 for more details on the GBS). Similarly to the technique used on TORPEX to reconstruct the 2D evolution of  $\delta \tilde{n}_e(\mathbf{x}, t)$  associated with the blob propagation by applying CS on HEX TIP data, CS is applied to  $\delta n_e(\mathbf{x}, t)$  from the GBS simulations presented in chapter 4. The reference signal  $\delta n_e(\mathbf{x}_0, t)$  is used, where  $\mathbf{x}_0$  is the location of the GBS grid point in the poloidal plane corresponding to the intersection between the field-line and the mmw-beam shown in purple in fig. 7.18. The threshold for the blob selection is  $m\sigma = 1.5\sigma$ . Three snapshots of  $\delta \tilde{n}_e$  associated with the propagation of the blob are shown by the contours in fig. 7.21. The conditionally-sampled blob has a typical perpendicular size  $L_\perp \approx 1$  cm a quasi-poloidal rotation motion with a velocity of  $|\nu| \approx 0.92 \text{ km} \cdot \text{s}^{-1}$ . Both the value the velocity and the direction of motion are in agreement with the velocity ( $|\nu| \approx 0.9 \text{ km} \cdot \text{s}^{-1}$ ) estimated experimentally (see fig. 7.16 and 7.17).

Full-wave simulations are performed at 15 times  $\tau_i$ , with  $\delta\tau = \tau_{i+1} - \tau_i = 10 \mu$ . Here, only the first pass through the SOL is taken into account ( $\delta n_e = 0$  in the lower SOL). Figure 7.21 shows the fluctuations of the conditionally-sampled  $\delta|\tilde{E}| = |E| - \langle |E| \rangle$  of the mmw-beam caused by the propagation of the blob. In fig. 7.21a), the negative  $\delta \tilde{n}_e$  preceding the blob is responsible for the focusing of the mmw-beam, resulting in an increase of mmw-power at the location of

## 7.5. Numerical investigation of the effect of the edge turbulence on the mmw-beam

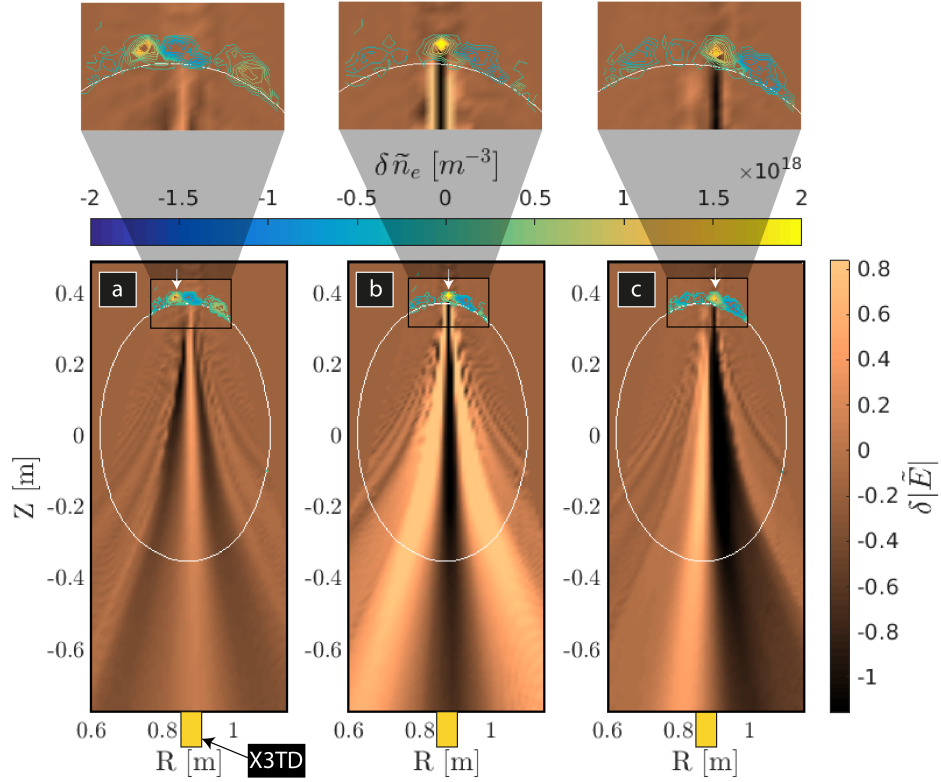


Figure 7.21 – Snapshots of the fluctuation of the electric field norm resulting from the propagation of the blob at the times indicated in fig. 7.22. The colored contours represent fluctuations of the conditionally-sampled electron density associated with the blob from GBS simulations. The LCFS is represented by the white contour. a) A structure with  $\delta \tilde{n}_e < 0$  preceding the blob focuses the mmw-beam. b) The blob is at the center of the mmw-beam and has a defocusing effect on the mmw-beam. c) The defocusing of the beam still occurs in the wake of the blob (which is now off-axis of the beam) and is responsible for the deviation of mmw-power to X3TD.

the X3TD diagnostic. Later, (fig. 7.21b), the blob with  $\delta \tilde{n}_e > 0$  is responsible for a defocusing of the mmw-beam in the wake<sup>1</sup> of the blob, resulting in a decrease in the mmw-power at the location of X3TD. Finally, in fig. 7.21c), the blob (slightly off the mmw-axis) causes a small deflexion to one side of the mmw-beam, increasing the mmw-power at the location of the X3TD detector. These observations are similar to those made in TORPEX in chapter 5.

The normalized fluctuations in the simulated detected power  $\delta \tilde{P} / \langle P \rangle$  are compared with the experimental measurements (purple curve in fig. 7.18a) in fig. 7.22.  $\delta \tilde{P} / \langle P \rangle$  is obtained numerically by computing the power  $\tilde{P}$  coupled to the X3TD detector for each snapshot using the synthetic diagnostic defined in chapter 2. The experimental measurements are obtained by performing CS using the LP connecting the field line intersecting the mmw-

<sup>1</sup>i.e. behind the blob, on the receiver side.

beam at the location  $\mathbf{x}_0$  ( $\approx$  center of the mmw-beam) as a reference. The mmw-beam is injected experimentally at  $R = 0.88$  m and with an angle of the poloidal mirror  $\theta_m = 45.2^\circ$ . The comparison shows a good agreement between the simulations and the experiments.

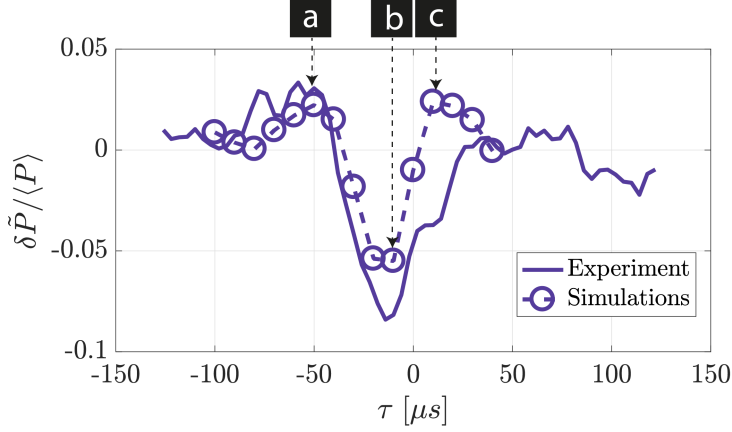


Figure 7.22 – The CS time evolution of the detected mmw-power (solid line) is obtained using LP 50 from fig. 7.18, which lines up with the center of the mmw-beam. Experimental results (solid line) are compared to numerical simulations (dashed line).

### 7.5.2 Effect of edge turbulence on the time-averaged mmw-beam power

The effect of the edge turbulence on the time-averaged mmw-beam profile is studied in this section using both full-wave and WKB simulations. In the following, we will often refer to the “quiet plasma” and the “turbulent plasma” case. In the first case, simulations are performed considering a wave-propagation in the equilibrium plasma, with no turbulence in the edge. In the second case, simulations are run considering a propagation in a quiet core plasma ( $0 < \rho_\psi \leq 0.6$  or  $0 < \rho_\psi \leq 1$  for the SOL only case), taken to be the same as in the previous case, and a turbulent edge ( $\rho_\psi > 0.6$  or  $\rho_\psi > 1$  for the SOL only case).

#### Full-wave simulations

Full-wave simulations are performed for mmw-beam propagation in both quiet and turbulent plasmas. In both cases, the mmw-beam is injected vertically at  $R = 0.88$  m. In the case of the quiet plasma, the equilibrium electron density profile  $\langle n_e(\mathbf{x}) \rangle$  is taken from the TS data and  $\mathbf{B}(\mathbf{x})$  from the magnetic equilibrium code LIUQE. In the case of the turbulent plasma,  $\langle n_e(\mathbf{x}) \rangle$  and  $\mathbf{B}(\mathbf{x})$  are obtained as previously. The fluctuating part of the electron density,  $\delta n_e(\mathbf{x})_i = n_e(\mathbf{x})_i - \langle n_e(\mathbf{x}) \rangle$ , associated with the turbulence in the SOL is obtained from snapshots of GBS simulations ( $\rho_\psi > 1$ ). The snapshots are statistically independent from each other. They are selected to be either separated by a time  $\Delta t$  larger than the autocorrelation time of  $\delta n_e(\mathbf{x}_0, t)$ , where  $\mathbf{x}_0$  is along the path of the mmw-beam, or taken in two poloidal planes such that a field line intersecting the first plane at  $\mathbf{x}_1$  intersects the second plane at  $\mathbf{x}_2$  with  $\|\mathbf{x}_2 - \mathbf{x}_1\| > L_\perp$  (i.e not in the same flux tube from the point of view of the turbulent structures).

## 7.5. Numerical investigation of the effect of the edge turbulence on the mmw-beam

The simulations are performed using  $N = 200$  GBS snapshots.

The time-averaged  $|E|^2$  profile at  $z = -0.77$  m ( $z$ -location of X3TD) after propagation through the turbulent plasma is computed using  $N = 200$  instantaneous beam profiles and is shown in fig. 7.23. The convergence of the mean and standard deviation estimator is verified in fig. 7.24. Figure 7.24 shows  $\langle P \rangle$  and  $\sigma(P)/\langle P \rangle$ , computed using the synthetic diagnostic, as a function of the number of snapshots  $N$  used in the simulations and shows that the estimators are converged for  $N = 200$ .

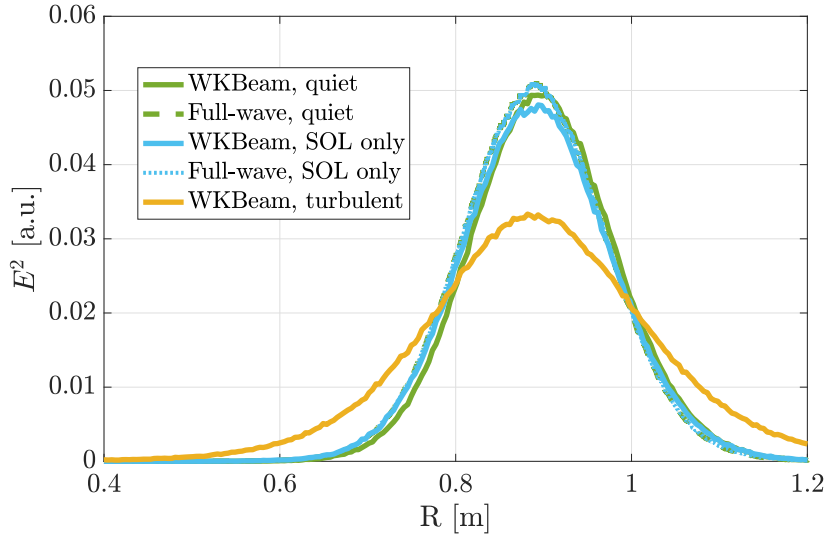


Figure 7.23 –  $|E|^2$  radial profile from numerical simulations at the position of X3TD ( $z = -0.77$  m). The green dashed (solid) line is the  $|E|^2$  profile from full wave (WKBeam) simulations after propagation in the quiet plasma. The blue dashed (solid) line is the average  $|E|^2$  profile after propagation through the plasma with the turbulent SOL only ( $\rho_\psi > 1$ ) from full-wave (WKBeam) simulations. The yellow line is the average  $|E|^2$  profile after propagation through the plasma with the turbulent edge ( $\rho_\psi > 0.8$ ) from WKBeam.

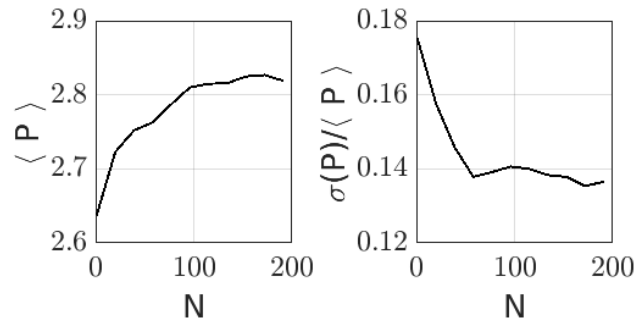


Figure 7.24 – Convergence study: First two moments of the distribution of the beam power computed from the synthetic diagnostic at  $R_{det} = 0.88$  m as a function of the number of turbulence snapshot  $N$ ; for  $N \geq 100$ , the simulations are well converged. Experimentally, this is equivalent to computing these moments around  $P_{max}$

The time-averaged beam profile after propagation through the turbulent plasma is compared to the beam profile after propagation through the quiet plasma in fig.7.23. Except for a small variation in  $|E|_{max}^2$ , the full-wave simulations show no broadening of the mmw-beam caused by its propagation through the SOL.

### WKBeam simulations

WKBeam simulations are also performed for the quiet and turbulent plasma cases. Similarly to the full-wave simulations,  $\langle n_e(\mathbf{x}) \rangle$  and  $\mathbf{B}(\mathbf{x})$  are taken from the TS data and the magnetic equilibrium code LIUQE, respectively. In WKBeam, the plasma turbulence is modeled by the in the Wigner function of the density correlation  $\Gamma$  (see eq. 4.15 in chapter 4). Here,  $\Gamma$  is computed from the GBS simulations. The GBS simulations are characterized by a r.m.s fluctuation level of the electron density associated with the turbulence  $\delta n_e / n_e \sim 0.3$  at the LCFS and the presence of turbulent structures with a correlation length of  $L_\perp \approx 0.5$  cm (HWHF).  $L_\perp$  is estimated from the half-width at half-maximum of a conditionally sampled blob (in GBS) located at  $R = 0.88$  m and  $Z = 0.39$  m, in the path of the mmw-beam. The r.m.s electron density fluctuation function  $F(\rho_\psi, \theta)$  is computed from the GBS data in the domain corresponding to the radial interval

$$\rho_\psi \in [\rho_1, \rho_2],$$

with  $\rho_1 = 1.0$  and  $\rho_2 = 1.1$ . In the region  $\rho_\psi \geq \rho_2$ , we set  $F(\rho, \theta) = F(\rho_2, \theta)$ . In this region, the choice of the extrapolation function is not critical since the background electron density is only residual. In the region  $\rho_\psi < \rho_1$ , we use two definitions of  $F(\rho_\psi, \theta)$ . In the case of a turbulent plasma with the turbulence localized only in the SOL region,  $F(\rho_\psi, \theta) = 0$  for  $\rho_\psi < 1$ . In the case of a turbulent plasma with turbulence localized at the edge, the r.m.s function is extrapolated as follows:

$$F(\rho_\psi, \theta) = F_c + \frac{b(\theta)}{(a(\theta) - \rho_\psi)^\alpha} - \frac{b(\theta)}{(a(\theta) - \rho_c)^\alpha}.$$

$F_c$  is the fluctuation level in the core plasma  $\rho_\psi < \rho_c$ . Based on previous studies [101], we chose  $F_c = 0.02$  and  $\rho_c = 0.6$ . The functions  $a(\theta)$  and  $b(\theta)$  are given by the fact that two continuity conditions are met uniformly for  $\theta \in [-\pi, \pi]$ . The first one is the continuity of  $F$  at  $\rho_1$ , i.e.  $F(\rho_1^-, \theta) = F(\rho_1^+, \theta)$ , and the second one that the estimate of the first derivative given by the finite difference is matched at  $\rho_1$ , namely

$$F_1(\rho_1, \theta) = \frac{1}{\Delta\rho} (F(\rho_1 + \Delta\rho, \theta) - F(\rho_1, \theta)),$$

with  $\Delta\rho = \beta(\rho_2 - \rho_1)$  and  $\beta$  is a free parameter. The free parameters  $\alpha$  and  $\beta$  are set to  $\alpha = 2$  and  $\beta = 0.5$ ; this corresponds to using the midpoint in  $[\rho_1, \rho_2]$  for the computation of the



## 7.5. Numerical investigation of the effect of the edge turbulence on the mmw-beam

approximate derivative.

The  $|E|^2$  profiles at  $z = -0.77$  m (location of X3TD) obtained from WKBeam, after propagation in the quiet and turbulent plasmas, are shown in fig. 7.23 and are compared to profiles obtained from the full-wave simulations described previously. In the case of a quiet plasma, the width of the beam<sup>2</sup> is similar in the two cases ( $w_{0,C} = 0.163$  m for the COMSOL based full-wave simulations and  $w_{0,W} = 0.162$  m for the WKBeam simulations). The two profiles show a good agreement between the two codes.

The full-wave code and WKBeam predict no significant broadening ( $w_{0,W} = 0.167$  m) of the mmw-beam (in blue in fig. 7.23) due to the presence of the SOL turbulence.

However, the WKBeam code predicts a  $\approx 50\%$  broadening ( $w_{0,W} = 0.243$  m) of the waist of the beam (cyan curve in fig. 7.23) in the case of a turbulent plasma with turbulence localized at the edge. We will see later that the broadening of the mmw-beam computed by WKBeam is in good agreement with the experimental measurements.

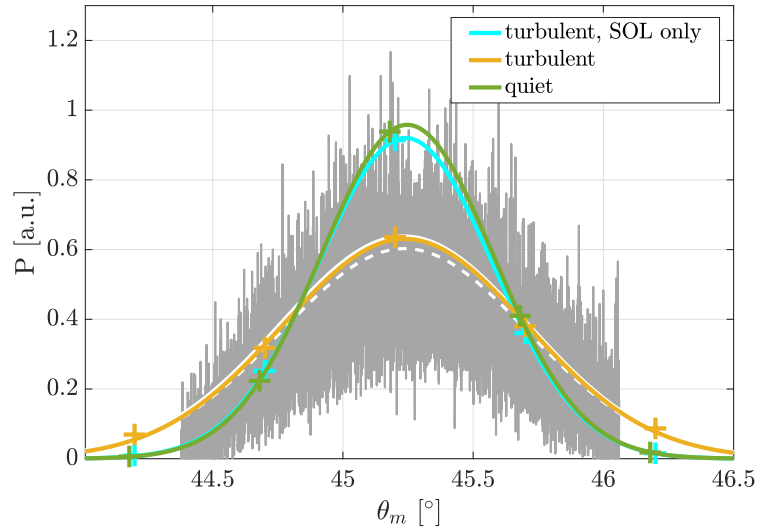


Figure 7.25 – Measured mmw-power as a function of the poloidal angle  $\theta_m$  of the injection mirror in discharge 60612. The experimental measurement (gray) is compared to the WKBeam simulations corresponding to the propagation through a quiet plasma (in green) and a turbulent plasma (blue for the SOL only case and yellow for the turbulent edge). The white lines are gaussian fits to the experimental measurements considering post sawtooth crash (solid) and pre sawtooth crash time windows (dotted). The green, yellow and cyan curves are Gaussian fits to the simulations. The amplitude of the simulated Gaussian  $A_{0,turb}$  in the turbulent case is normalized to match  $A_{0,exp}$ .

<sup>2</sup>computed at  $1/e$  in electric field

### Comparison between WKBeam and the experiments

WKBeam simulations are performed for five angles (see fig. 7.25) to reconstruct the  $P(\theta_m)$  profile and compare it to the experimental one. In WKBeam,  $P$  is computed as the power entering the aperture of X3TD. A comparison between the experimental  $P(\theta_m)$  (corresponding to the measured mmw-power during a scan of the poloidal angle of the injection mirror, shown in fig. 7.4, section 7.2) and the numerically obtained  $P(\theta_m)$  profile after propagation in both a quiet and turbulent plasmas (SOL only and full edge) is shown in fig. 7.25. A Gaussian fit to the data of the form  $A_0 e^{-2 \frac{(\theta_m - \theta_0)^2}{w_\theta^2}}$  is also shown. In fig. 7.25, the WKBeam profiles are normalized such that the amplitude of the scan after propagation through the turbulence matches the experimental one ( $A_{0,turb} = A_{0,exp}$ ). The WKBeam profiles are shown shifted by  $+0.2^\circ$ . We find that the width of the WKBeam profile computed with turbulence ( $w_{\theta,turb} = 0.94^\circ$ ) is in good agreement with the experimental one ( $w_{\theta,exp} = 0.94^\circ$ ). The WKBeam profile obtained without taking into account the turbulence is 42% narrower ( $w_{\theta,turb} = 0.66^\circ$ ) and is not in agreement with the experiment. Using the synthetic diagnostic in the full-wave mode, the width of  $P(\theta_m)$  was also computed in the case of a quiet plasma and has a width of  $0.61^\circ$ , which is consistent with the quiet plasma WKBeam case. WKBeam simulations predict a 50% broadening of the mmw-beam measured in TCV due to presence of edge turbulence.

### Conclusion from the numerical study

Using conditional sampling of blobs present in the SOL applied to GBS data, the time-resolved effect of conditionally-sampled blobs on the mmw-beam propagation is investigated using full-wave simulations. The simulations are found to be in good agreement with the experiments (fig. 7.22). Structures associated with negative fluctuations of the electron density preceding a single blob focus the mmw-beam whereas the blob itself defocuses the mmw-beam (fig. 7.21). This interaction of the blobs with the mmw-beam results in time-dependent fluctuations of the detected power between 3 – 10% of the time-averaged value, depending on the blob density.

WKBeam simulations predict the 50% broadening of the mmw-beam measured in TCV due to presence of edge turbulence (fig. 7.25). This observed mmw-beam broadening in TCV supports the concerns on the upper-launcher beam broadening in ITER, although the precise value of the broadening in ITER will depend on the precise characterization of the turbulence characteristics.

## 8 Summary & Conclusions

In this thesis, the effect of plasma turbulence on the propagation of millimeter-wave (mmw) beams is investigated both experimentally and numerically. The investigation was initiated by the urgent need to quantify the effect of the edge-turbulence on the profile of the mmw-beam launched by the upper launcher in ITER to ensure a design allowing the stabilization of neo-classical tearing mode with the planned power and/or to provide advise on the need for power modulation. A summary of the main results presented of this thesis is given below.

The effect of plasma turbulence on mmw-beam propagation is first investigated in the simple magnetized toroidal configuration, which exhibits turbulence with properties similar to those observed in the scrape-off layer of tokamaks. A low-power mmw-injection/detection system is installed on the simple magnetized toroidal device TORPEX. A mmw-beam is launched from the top of the vessel using a pyramidal antenna and detected at the bottom of the vessel using a similar antenna. The time-evolution of the absolutely calibrated electron density in the entire poloidal cross-section is measured using the HEXTIP-U 2D hexagonal array of Langmuir probes. Although the measured time-averaged mmw-beam profile is not affected by the presence of the plasma, the plasma is responsible for time-dependent fluctuations of the measured mmw-power. Using a conditional sampling technique, the effect of single blobs on the fluctuations of the detected mmw-power are identified. Blobs associated with fluctuations of the electron density as small as  $10^{-3} n_c$ ,  $n_c$  being the cut-off density, and a size  $\lambda/L_{\perp} \sim 0.4$ ,  $\lambda$  being the wavelength of the beam and  $L_{\perp}$  the typical size of the blobs in the direction transverse to the magnetic field, are responsible for fluctuations of the measured power of  $\sim 1\%$ . The amplitude of the fluctuations increases with the electron density of the blobs.

A full-wave model based on the finite element solver COMSOL is implemented in the frequency domain to investigate numerically the mmw-scattering process. The conditionally-sampled 2D electron density profiles from HEXTIP-U are used to compute the dielectric permittivity of the plasma, obtained from the cold plasma model. The use of the frequency domain by the smaller timescale of the turbulence than that of the beam propagation through the plasma. The full-wave model is found in agreement with the experiments and reveals that blobs have a

defocusing effect on the mmw-beam in the wake of the blob structure, leading to local changes in the mmw-power.

Leveraging TORPEX experiments, a transmission diagnostic was installed on TCV in the frame of this thesis to measure the mmw-power from the high-power third harmonic beam reaching the floor of the vessel after propagation through plasma. We observed that MHD activity (i.e. MHD mode  $m=1, n=1$  and sawteeth) in the core region of the L-mode plasmas can strongly affect the mmw-propagation. The particular case of the MHD kink mode  $m=1, n=1$ , which consists of a periodic rigid rotation of the plasma column around the plasma axis, is studied. Periodic drops (up to  $\approx 100\%$ ) in the measured mmw-power are observed and are synchronized with the frequency of the mode rotation. Using spatio-temporal imaging of the electron density, obtained using the soft X-ray tomographic inversion, the time-evolution of the mmw-beam propagation through the plasma during one oscillation of the kink mode is solved numerically using both the full-wave model and the WKBeam code. Results from the two codes are found in good agreement and reveal that a deflection of the mmw-beam is caused by changes in the electron density associated with the rotation of the mode and is responsible for the drop in the measured power. The sawtooth activity is also found to be responsible for periodic deflections of the mmw-beam, generating changes in the measured mmw-power.

A particular care is given in this thesis to differentiate the contribution of the core plasma and the edge turbulence to the variations in the detected mmw-power. A set of wall-embedded Langmuir probes located in the inner-wall of the TCV vessel is used to perform conditional sampling on the detected mmw-power signal and identify the effect of blobs present in the scrape-off layer on the mmw-transmission. As in TORPEX, blobs are detected as spikes in the ion saturation current measured by the probes. Blobs located in the upper-part of the scrape-off layer intersecting the path of the mmw-beam are responsible for changes in the transmitted power ( $\sim 10\%$ ), which can result in either an increase or a decrease in the measured power depending on the position of the blob. The position of the intersection between the detected blob (detected by a given probe) and the mmw-beam is varied by changing the pitch of the magnetic field lines. The largest amplitude of the variation in the detected mmw-power is found when the blob is aligned with the mmw-beam. A full-wave model is implemented for the third harmonic beam propagation in TCV plasmas using the equilibrium quantities (magnetic field and electron density profile) from the experiments. The fluctuating part of the electron density associated with the turbulence is obtained from the turbulence code GBS. Conditional sampling is performed on the turbulence data from GBS to reconstruct the time-resolved two-dimensional evolution of the electron density in the scrape-off layer associated with the propagation of a blob in TCV. The typical size of the blobs satisfies  $\lambda/L_{\perp} \approx 0.5$ . The time-evolution of the detected mmw-power associated with the blob propagation is successfully compared to the experiment. The numerical simulations show that negative fluctuations of the electron density preceding the blob focus the mmw-beam and the blobs themselves defocus the mmw-beam, resulting in variations of the mmw-power.

---

The effect of the edge turbulence on the time-averaged mmw-beam is computed numerically using the full-wave model, by averaging the mmw-beam profile over  $N = 200$  realizations of the turbulence from GBS, and the WKBeam code. Although both codes predict no significant broadening of the time-averaged mmw-beam profile due to the presence of the SOL turbulence only, a combination of the WKBeam simulations considering a turbulent edge, and the corresponding experimental measurements of the transmitted mmw-power demonstrate that the mmw-beam is both predicted and measured to be  $\approx 50\%$  broader in TCV due to the edge turbulence than the predicted mmw-beam after propagation in a non-turbulent plasma.

The mmw-broadening measured in TCV supports the previous prediction of a broadening of the upper-launcher beam in ITER [25] caused by the presence of the edge turbulence in the path of the beam. This broadening is expected to have a detrimental effect on neo-classical tearing mode stabilization. Current predictions estimate that the mmw-beam of the upper-launcher in ITER will also be broadened by the edge-plasma turbulence. The numerical tools presented in this thesis will be able to make reliable estimations of the broadening of the beam. However, only a precise characterization of the turbulence –level of the electron density fluctuations, size of the turbulent structures and width of the scrape-off layer– will enable an accurate prediction of the upper-launcher beam size at the expected location of the neo-classical tearing modes. This will require either numerical simulations of turbulence in ITER or theory-based predictions of turbulence features such as those produced by GBS for TCV plasmas.



# A Notations

## A.1 List of frequently used symbols

$\parallel$	Component of a vector parallel to the magnetic field
$\perp$	Component of a vector perpendicular to the magnetic field
$\langle \cdot \rangle$	Time-average value of a quantity
$\sigma(\cdot)$	Standard deviation of a quantity
$a$	Minor radius
$A$	Effective surface of a Langmuir probe
$\mathbf{B}$	Magnetic field
$B_0$	Magnetic field norm on axis
$c$	Speed of light
$e$	Elementary charge
$f$	Frequency
$f_{EC}$	Electron-cyclotron frequency
$I_p$	Plasma current
$j_{bs}$	Bootstrap current density
$j_{CD}$	Density of the driven current
$j_{sat}$	Ion-saturation current density
$\mathbf{k}$	Wave vector

## Appendix A. Notations

---

$L_{\perp}$	Size of the turbulent structures
$m_e$	Mass of an electron
$m_i$	Ion mass
$n, N$	Refractive index
$n_c$	Cut-off density
$n_e$	Electron density
$P$	Millimeter-wave power
$q$	Plasma safety factor
$R_0$	Major radius
$R_m$	Radial position of the launching mirror
$t$	Time
$T_e$	Electron temperature
$w, w_0$	Waist
$\delta$	Plasma triangularity
$\Delta l$	Width of the scrape-off layer
$\epsilon_0$	Permittivity of vacuum
$\epsilon_r$	Relative permittivity
$\theta_m$	Poloidal angle of the launching mirror
$\kappa$	Plasma elongation
$\lambda$	Wavelength of the wave
$\tau$	Time of the conditional sampling
$\omega$	Pulsation of the wave
$\Omega_e$	Electron cyclotron frequency
$\omega_p$	Plasma frequency



**A.2 List of acronyms**

CS	Conditional sampling
EC	Electron cyclotron
ECCD	Electron-cyclotron current drive
ECRH	Electron-cyclotron resonant heating
EL	Equatorial launcher
fft	Fast Fourier transform
GBS	Global Braginskii solver
H& CD	Heating and current drive
HWHM	Half-width half-maximum
LP	Langmuir probe
LSM	Lower steering mirror
mmw	Millimeter-wave
NTM	Neoclassical tearing mode
O-mode	Ordinary mode
OIMD	Optically-isolated millimeter-wave detector
RF	Radio-frequency
RFCU	Radio-frequency conditioning unit
r.m.s	Root mean square
SOL	Scrape-off layer
SPC	Swiss Plasma Center
TCV	Tokamak à Configuration variable
TORPEX	Toroidal plasma experiment
TC	Toroidal conductor
TL	Transmission line
UL	Upper launcher

## Appendix A. Notations

---

USM Upper steering mirror

X-mode Extraordinary mode

X3TD X3 transmission diagnostic

USM Upper steering mirror

## B Gaussian beams

This annexe is a reminder of the theory of Gaussian beams [102] which are often mentioned in this thesis.

In the frequency domain, the wave equation can be written in the form proposed by Helmholtz:

$$(\nabla^2 + k^2)E(x, y, z). \quad (\text{B.1})$$

Here,  $E(x, y, z)$  is the complex electric field for any polarization. If we suppose a propagation along the  $z$ -axis,  $E(x, y, z)$  can be written as:

$$E(x, y, z) = \psi(x, y, z)e^{-ikz}, \quad (\text{B.2})$$

where  $\psi(x, y, z)$  is the transverse electric field profile. Under the paraxial approximation (also known as the slow varying envelope)

$$\left| \frac{\partial^2 \psi}{\partial z^2} \right| \ll 2k \left| \frac{\partial \psi}{\partial z} \right| \quad \text{and} \quad \left| \frac{\partial^2 \psi}{\partial z^2} \right| \ll \left| \frac{\partial^2 \psi}{\partial x^2} \right|, \left| \frac{\partial^2 \psi}{\partial y^2} \right|, \quad (\text{B.3})$$

equation B.1 can be written in terms of  $\psi$  as:

$$\Delta_T \psi - 2ik \frac{\partial \psi}{\partial z} = 0, \quad (\text{B.4})$$

where  $\Delta_T = \partial^2 / \partial x^2 + \partial^2 / \partial y^2$ . In cylindrical coordinates, equation B.4 is

$$\frac{1}{r} \frac{\partial}{\partial r} \left( r \frac{\partial \psi}{\partial r} \right) - 2ik \frac{\partial \psi}{\partial z} = 0. \quad (\text{B.5})$$

Assuming a cylindrically symmetric solution of the form  $\psi_0(z)\alpha e^{-i(P(z) + \frac{kr^2}{2q(z)})}$ , we find

## Appendix B. Gaussian beams

---

the (lowest order TEM<sub>00</sub>) Gaussian solution (referred to as Gaussian beam)

$$E(x, y, z) = E_0 \frac{w_0}{w(z)} e^{-\frac{r^2}{w^2(z)}} e^{-i \frac{kr^2}{2R(z)}} e^{-i[kz - \phi(z)]}. \quad (\text{B.6})$$

$w(z)$  is the beam spot size,  $R(z)$  is the curvature radius of the phase fronts and  $\phi(z)$  is the phase shift. They can be written as

$$w(z) = w_0 \sqrt{1 + (z/z_R)^2}$$

$$R(z) = z[1 + (z_R/z)^2]$$

$$\phi(z) = \tan^{-1}(z/z_R).$$

$w_0$  is the waist of the beam,  $z_R = \frac{\pi n w_0^2}{\lambda}$  ( $n$  being the refractive index of the medium) is the Rayleigh length. It characterizes the distance over which the beam can be considered collimated. A beam spreading angle  $\theta$  can be defined as  $\theta = w/z = \frac{\lambda}{\pi n w_0}$ . The above relations are summarized in the figure below:

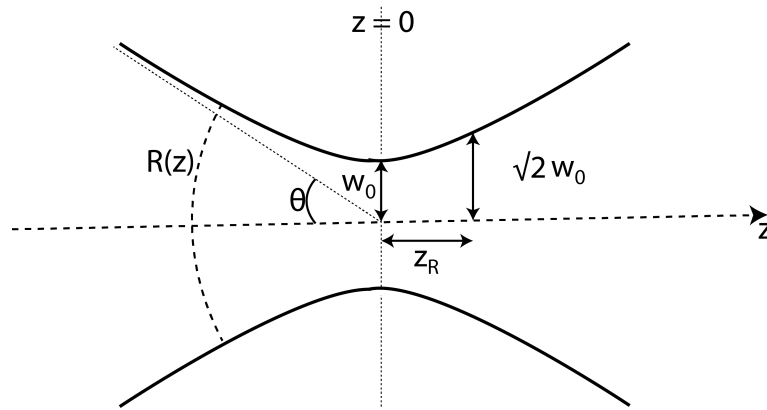


Figure B.1 – Gaussian beam propagation: beam size and curvature radius over the propagation distance

## C X3 mirror

This document was written by S. Coda in an internal report of the Swiss Plasma Center in 2012 and details the calculation of the focal length in the toroidal and poloidal directions of the X3 injection mirror.

### C.1 Mirror surface parametrization

We'll model/construct the X3 mirror as a torus section with two radii of curvature,  $R_R$  in the  $(\xi, \zeta)$  plane and  $R_t$  in the  $(\xi, \eta)$  plane. The surface is parametrized by two angles,

$$\begin{cases} \xi &= R_t - (R_t - R_R + R_R \cos \mu) \cos \nu \\ \eta &= (R_t - R_R + R_R \cos \mu) \sin \nu \\ \zeta &= R_R \sin \mu \end{cases} \quad (1)$$

i.e.,

$$\xi = R_t - \left[ (R_t - R_R + \sqrt{R_R^2 - \zeta^2})^2 - \eta^2 \right]^{1/2}. \quad (2)$$

In the special case  $R_t = \infty$ , the equation becomes

$$\xi = R_R - \sqrt{R_R^2 - \zeta^2}. \quad (3)$$

In the frame of reference of the mirror, as the radii approach infinity the mirror lies in the  $(\eta, \zeta)$  plane with the reflecting surface on the positive  $\xi$  side.

We now equate the initial  $(\xi, \eta, \zeta)$  coordinates with  $(x, y, z)$  in the lab frame, where  $x$  corresponds to the major radius of the torus (outwards),  $y$  is the toroidal direction (positive

## Appendix C. X3 mirror

counterclockwise from the top), and  $z$  is the vertical direction. The origin is taken to be the impact point of the center ray of beam 8 on the mirror. At this point the mirror is to be visualized as being in a vertical orientation. We shall now move it while keeping the origin fixed, and we will use the mirror-frame coordinates  $\eta$  and  $\zeta$  to parametrize the surface.

We rotate the mirror in the lab frame, first by an angle  $\alpha$  (counterclockwise or clockwise, we shall use  $\alpha > 0$  when counterclockwise) around  $z$ , and then by an angle  $\theta$  *counterclockwise* around  $y$ . The angle  $\theta$  is generally close to  $45^\circ$ . The angle  $\alpha$  is to give the beams a tilt away from sector 1;  $\alpha > 0$  moves the beams towards sector 2, so in general we'll choose  $\alpha < 0$ .

The rotation matrix is

$$M = \begin{pmatrix} \cos\theta & 0 & \sin\theta \\ 0 & 1 & 0 \\ -\sin\theta & 0 & \cos\theta \end{pmatrix} \times \begin{pmatrix} \cos\alpha & -\sin\alpha & 0 \\ \sin\alpha & \cos\alpha & 0 \\ 0 & 0 & 1 \end{pmatrix} = \begin{pmatrix} \cos\alpha \cos\theta & -\sin\alpha \cos\theta & \sin\theta \\ \sin\alpha & \cos\alpha & 0 \\ -\cos\alpha \sin\theta & \sin\alpha \sin\theta & \cos\theta \end{pmatrix}. \quad (4)$$

So

$$\begin{pmatrix} x \\ y \\ z \end{pmatrix} = M \begin{pmatrix} \xi \\ \eta \\ \zeta \end{pmatrix} = \begin{pmatrix} \left\{ R_t - \left[ (R_t - R_R + \sqrt{R_R^2 - \zeta^2})^2 - \eta^2 \right]^{1/2} \right\} \cos\alpha \cos\theta - \eta \sin\alpha \cos\theta + \zeta \sin\theta \\ \left\{ R_t - \left[ (R_t - R_R + \sqrt{R_R^2 - \zeta^2})^2 - \eta^2 \right]^{1/2} \right\} \sin\alpha + \eta \cos\alpha \\ - \left\{ R_t - \left[ (R_t - R_R + \sqrt{R_R^2 - \zeta^2})^2 - \eta^2 \right]^{1/2} \right\} \cos\alpha \sin\theta + \eta \sin\alpha \sin\theta + \zeta \cos\theta \end{pmatrix}. \quad (5)$$

In the case  $R_t = \infty$ ,

$$\begin{pmatrix} x \\ y \\ z \end{pmatrix} = \begin{pmatrix} \left[ R_R - \sqrt{R_R^2 - \zeta^2} \right] \cos\alpha \cos\theta - \eta \sin\alpha \cos\theta + \zeta \sin\theta \\ \left[ R_R - \sqrt{R_R^2 - \zeta^2} \right] \sin\alpha + \eta \cos\alpha \\ - \left[ R_R - \sqrt{R_R^2 - \zeta^2} \right] \cos\alpha \sin\theta + \eta \sin\alpha \sin\theta + \zeta \cos\theta \end{pmatrix}. \quad (6)$$

### C.2 Intersection of incoming beams with mirror

For  $(\eta, \zeta) \ll (R_t, R_R)$ , if we linearize Eqs. (5) and (6), both reduce to

$$\begin{pmatrix} x \\ y \\ z \end{pmatrix} \simeq \begin{pmatrix} -\eta \sin\alpha \cos\theta + \zeta \sin\theta \\ \eta \cos\alpha \\ \eta \sin\alpha \sin\theta + \zeta \cos\theta \end{pmatrix}. \quad (7)$$

the first perturbation terms are second-order. We use this approximation to locate the intersection of the beams with the mirror. The beams are defined by the equations

$$\begin{cases} y = -(x + R + l_0) \tan \phi \\ z = 0 \end{cases}, \quad (8)$$

where  $R$  is the major radius of the impact point of the center of beam 8,  $l_0 = 12.45$  cm, and  $\phi = -4^\circ$  for beam 7,  $\phi = 0$  for beam 8, and  $\phi = +4^\circ$  for beam 9.

By substituting Eq. (8) into Eq. (7), the intersection is easily found to have the coordinates

$$\begin{cases} \eta \simeq \frac{-(R+l_0) \cos \theta \tan \phi}{\cos \alpha \cos \theta - \sin \alpha \tan \phi} \\ \zeta \simeq \frac{(R+l_0) \sin \theta \sin \alpha \tan \phi}{\cos \alpha \cos \theta - \sin \alpha \tan \phi} \end{cases} \quad (9)$$

in the mirror frame, and

$$\begin{cases} x \simeq \frac{(R+l_0) \sin \alpha \tan \phi}{\cos \alpha \cos \theta - \sin \alpha \tan \phi} \\ y \simeq \frac{-(R+l_0) \cos \alpha \cos \theta \tan \phi}{\cos \alpha \cos \theta - \sin \alpha \tan \phi} \\ z = 0 \end{cases} \quad (10)$$

in the lab frame.

The major radius of the impact point is given by  $[(R+x)^2 + y^2]^{1/2}$ . In the limit  $\alpha \ll 1$ ,  $\phi \ll 1$ , the major radius for the three beams is the same up to first order in these two parameters, and a difference appears only at second order, equal to

$$\Delta R \simeq (R + l_0) \frac{\alpha \phi}{\cos \theta} + \frac{(R + l_0)^2 \phi^2}{R} \frac{1}{2}. \quad (11)$$

### C.3 Orientations of outgoing beams

To calculate the change in direction of the surface normal when moving away from the origin, we need to take the calculation to second order in  $\eta/R_t$  and  $\zeta/R_R$ . Expanding Eq. (3) to second order, we find

$$\xi \simeq \frac{\eta^2}{2R_t} + \frac{\zeta^2}{2R_R}. \quad (12)$$

$\partial \mathbf{r} / \partial \zeta \times \partial \mathbf{r} / \partial \eta$ , where  $\mathbf{r} = (\xi, \eta, \zeta)$ . Thus

$$\hat{\mathbf{n}}' \simeq [-1, \eta/R_t, \zeta/R_R] \times (1 + \eta^2/R_t^2 + \zeta^2/R_R^2)^{-1/2}. \quad (13)$$

## Appendix C. X3 mirror

---

Upon rotation,

$$\begin{aligned}\hat{\mathbf{n}} = M\hat{\mathbf{n}}' \simeq & -\cos\alpha\cos\theta - \sin\alpha\cos\theta\eta/R_t + \sin\theta\zeta/R_R, \\ & -\sin\alpha + \cos\alpha\eta/R_t, \\ & \{\cos\alpha\sin\theta + \sin\alpha\sin\theta\eta/R_t + \cos\theta\zeta/R_R\} \\ & \times (1 + \eta^2/R_t^2 + \zeta^2/R_R^2)^{-1/2}.\end{aligned}\quad (14) \quad (C.1)$$

We can now substitute Eq. (9) into Eq. (14) and find

$$N\hat{n}_x \simeq -\cos\alpha\cos\theta + \frac{(R+l_0)\sin\alpha\tan\phi}{\cos\alpha\cos\theta - \sin\alpha\tan\phi} \left( \frac{\cos^2\theta}{R_t} + \frac{\sin^2\theta}{R_R} \right), \quad (15a)$$

$$N\hat{n}_y \simeq -\sin\alpha - \frac{(R+l_0)\cos\alpha\cos\theta\tan\phi}{R_t(\cos\alpha\cos\theta - \sin\alpha\tan\phi)}, \quad (15b)$$

$$N\hat{n}_z \simeq \cos\alpha\sin\theta + \frac{(R+l_0)\sin\alpha\cos\theta\sin\theta\tan\phi}{\cos\alpha\cos\theta - \sin\alpha\tan\phi} \left( \frac{1}{R_R} - \frac{1}{R_t} \right), \quad (15c)$$

with

$$N = \left[ 1 + \frac{(R+l_0)^2\tan^2\phi}{(\cos\alpha\cos\theta - \sin\alpha\tan\phi)^2} \left( \frac{\cos^2\theta}{R_t^2} + \frac{\sin^2\theta\sin^2\alpha}{R_R^2} \right) \right]^{1/2}. \quad (16)$$

The incoming beam is defined by the unit direction vector

$$\hat{\mathbf{i}} = [-\cos\phi, \sin\phi, 0] \quad (17)$$

The reflected beam has direction vector

$$\hat{\mathbf{r}} = \hat{\mathbf{i}} - 2(\hat{\mathbf{i}} \cdot \hat{\mathbf{n}})\hat{\mathbf{n}}. \quad (18)$$

This can readily be calculated from the above formulas but there is little to be gained in spelling out the components here. The formulas will be used, to this level of approximation, for the launching parameters in Toray.

Here we can explore in detail the common limit  $\phi \ll 1$  and  $\alpha \ll 1$  to second order in these two parameters. In this case, Eqs. (15)–(17) give

$$N \simeq 1 + \frac{(R+l_0)^2\phi^2}{2R_t^2}, \quad (19)$$



$$\hat{n}_x \simeq -\cos\theta \left( 1 - \frac{\alpha^2}{2} - \frac{(R+l_0)^2\phi^2}{2R_t^2} \right) + \frac{(R+l_0)\alpha\phi}{\cos\theta} \left[ \frac{\cos^2\theta}{R_t} + \frac{\sin^2\theta}{R_R} \right], \quad (20a)$$

$$\hat{n}_y \simeq -\alpha - \frac{(R+l_0)\phi}{R_t}, \quad (20b)$$

$$\hat{n}_z \simeq \sin\theta \left( 1 - \frac{\alpha^2}{2} - \frac{(R+l_0)^2\phi^2}{2R_t^2} \right) + \frac{(R+l_0)(R_t-R_R)\alpha\phi\sin\theta}{R_R R_t}, \quad (20c)$$

$$\hat{\mathbf{i}} \simeq [-1 + \phi^2/2, \phi, 0]. \quad (21)$$

The  $\hat{r}_y$  component, which is the tangent of what is generally called the “toroidal angle”, is first-order only and thus easier to express; from Eq. (18),

$$\hat{r}_y \simeq \phi + 2 \left[ \alpha + \frac{(R+l_0)\phi}{R_t} \right] \cos\theta. \quad (22)$$

In the case  $\theta = 45^\circ$ , this becomes simply

$$\hat{r}_y \simeq \phi + \sqrt{2} \left[ \alpha + \frac{(R+l_0)\phi}{R_t} \right]. \quad (23)$$

It is of interest also to calculate  $\hat{r}_x$  and  $\hat{r}_z$  but for this we will specialize our remarks to the case  $R_t = \infty$  and  $\theta = 45^\circ$ . In this case there is no zeroth- nor first-order component to  $\hat{r}_x$ .

Substituting Eqs. (20) and (21) into Eq. (18), we find

$$\hat{r}_x \simeq -\alpha^2 - [\sqrt{2} + 2(R+l_0)/R_R] \alpha\phi, \quad (24a)$$

$$\hat{r}_y \simeq \phi + \sqrt{2}\alpha, \quad (24b)$$

$$\hat{r}_z \simeq -1 + (\alpha + \phi/\sqrt{2})^2. \quad (24c)$$

We notice that, for  $\alpha < 0$ ,  $\hat{r}_x < 0$  for beams 7 and 8 ( $\phi \leq 0$ ) whereas for beam 9  $\hat{r}_x$  can take either sign. In all cases, however,  $\hat{r}_{x7} < \hat{r}_{x8} < \hat{r}_{x9}$ .

We can now list the following effects of a mirror tilt in the direction of sector 16 ( $\alpha < 0$ ).

## Appendix C. X3 mirror

---

(1) The impact points of beams 7 and 9 shift radially as per Eq. (11):  $\Delta R_7 > 0$  and  $\Delta R_7 > \Delta R_9$ . For the case  $\alpha = -4.5^\circ$ ,  $\theta = 45^\circ$ , and  $R = 93$  cm, we obtain  $\Delta R_7 = +1.1$  cm,  $\Delta R_9 = -0.5$  cm.

(2) The direction of propagation of the reflected beams shifts radially as per Eq. (24a). For the same parameters and  $R_R = 1.3435$  m we get  $\arctan \hat{r}_{x7} = -1.3^\circ$ ,  $\arctan \hat{r}_{x8} = -0.4^\circ$ , and  $\arctan \hat{r}_{x9} = +0.6^\circ$ .

(3) The toroidal component  $\hat{r}_y$  causes a precession that tends to move the beams to larger major radii. For our parameters, from Eq. (24b) we find  $\arctan \hat{r}_{y7} = -10.3^\circ$ ,  $\arctan \hat{r}_{y8} = -6.3^\circ$ , and  $\arctan \hat{r}_{y9} = -2.4^\circ$ .

The effects of (1) and (2) go in the opposite sense and roughly compensate each other. The relative effect of (3), in terms of separating the three beams, is approximately independent of  $\alpha$ .

### C.4 Focal lengths

We now proceed to calculate the focal lengths of the mirror in the  $(x, z)$  (radial) and  $(y, z)$  (toroidal) planes. For the former, we modify Eq. (8) to construct an incoming ray with  $\phi = 0$  but with a small shift along  $z$ , i.e.,

$$\begin{cases} y = 0 \\ z = \Delta \end{cases}, \quad (25)$$

which, using Eq. (7), yields

$$\begin{cases} \eta = 0 \\ \zeta = \Delta / \cos \theta \\ x = \Delta \tan \theta \end{cases}. \quad (26)$$

$$\hat{n}_x = \left( -\cos \alpha \cos \theta + \frac{\Delta \tan \theta}{R_R} \right) \left( 1 + \frac{\Delta^2}{R_R^2 \cos^2 \theta} \right)^{-1/2}. \quad (27)$$

The  $\hat{x}$  component of Eq. (18) then yields

$$\hat{r}_x = -1 + 2\hat{n}_x^2 = -1 + 2 \left( -\cos \alpha \cos \theta + \frac{\Delta \tan \theta}{R_R} \right)^2 \left( 1 + \frac{\Delta^2}{R_R^2 \cos^2 \theta} \right)^{-1}. \quad (28)$$

We now consider two rays with  $\Delta_{1,2} = \pm \epsilon$  and calculate the radial focal length  $F_R$  as the distance over which the two rays converge in the  $(x, z)$  plane, i.e., using the ordering  $|\hat{r}_z| \gg |\hat{r}_x|$ ,

$$F_R = \left| \frac{x_2 - x_1}{\hat{r}_{x2} - \hat{r}_{x1}} \right| = \frac{R_R \tan \theta \left( 1 + \frac{\epsilon^2}{R_R^2 \cos^2 \theta} \right)}{4 \sin \theta \cos \alpha}. \quad (29)$$

In the limit  $\epsilon \rightarrow 0$ , this reduces to

$$F_R = \frac{R_R}{4 \cos \theta \cos \alpha}. \quad (30)$$

In a similar vein, we calculate the toroidal focal length by considering two rays at  $z = 0$  with  $\phi = 0$ , but shifted by  $\Delta = \pm \epsilon$  in the  $y$  direction. Equation (8) is then replaced by

$$\begin{cases} y = \Delta \\ z = 0 \end{cases}, \quad (31)$$

which, using Eq. (7), yields

$$\begin{cases} \eta = \Delta / \cos \alpha \\ \zeta = -\Delta \tan \theta \tan \alpha \end{cases}. \quad (32)$$

Substituting Eq. (32) into Eq. (14), we obtain

$$\hat{n}_x = \left( -\cos \alpha \cos \theta - \tan \alpha \cos \theta \frac{\Delta}{R_t} - \frac{\sin^2 \theta \tan \alpha}{\cos \theta} \frac{\Delta}{R_R} \right) \left( 1 + \frac{\Delta^2}{R_t^2 \cos^2 \alpha} + \frac{\Delta^2 \tan^2 \theta \tan^2 \alpha}{R_R^2} \right)^{-1/2}, \quad (33a)$$

$$\hat{n}_y = \left( -\sin \alpha + \frac{\Delta}{R_t} \right) \left( 1 + \frac{\Delta^2}{R_t^2 \cos^2 \alpha} + \frac{\Delta^2 \tan^2 \theta \tan^2 \alpha}{R_R^2} \right)^{-1/2}. \quad (33b)$$

The  $\hat{y}$  component of Eq. (18) then yields

$$\hat{r}_y = 2 \hat{n}_x \hat{n}_y, \quad (34)$$

and, by analogy with Eq. (29), we may write

$$F_t = \left| \frac{y_2 - y_1}{\hat{r}_{y2} - \hat{r}_{y1}} \right| = \frac{\left( 1 + \frac{\epsilon^2}{R_t^2 \cos^2 \alpha} + \frac{\epsilon^2 \tan^2 \theta \tan^2 \alpha}{R_R^2} \right)}{2 (\cos \theta \cos \alpha / R_t - \sin \alpha \tan \alpha \cos \theta / R_t - \sin \alpha \tan \alpha \sin \theta \tan \theta / R_R)}, \quad (35)$$

### Appendix C. X3 mirror

---

and, for  $\epsilon \rightarrow 0$ ,

$$F_t = \frac{1}{2(\cos\theta \cos\alpha/R_t - \sin\alpha \tan\alpha \cos\theta/R_t - \sin\alpha \tan\alpha \sin\theta \tan\theta/R_R)}. \quad (36)$$

For  $\alpha \ll 1$ , the first term in the denominator dominates and one has

$$F_t \simeq \frac{R_t}{2\cos\theta \cos\alpha}. \quad (37)$$

## D Estimation of uncertainty in $n_e$ measured by HEXTIP

In chapter 2, we have seen that the current measured by a Langmuir probe is:

$$I = I_{sat}(1 - \alpha(V - V_{float})) \quad (D.1)$$

with:

$$I_{sat} = \frac{n_e}{2} A \sqrt{T_e} \quad (D.2)$$

from which we get:

$$n_e = \frac{2I}{A\sqrt{T_e}(1 - \alpha(V - V_{float}))}$$

Taking into account the errors in the estimation of  $A, T_e$  and  $V - V_{float}$  [87], we find a lower boundary  $n_{e,min}$  for  $n_e$ :

$$n_{e,min} = \frac{2}{(A + \delta A)\sqrt{T_e + \delta T_e}(1 - \alpha(V - V_{float} + \delta(V - V_{float})))} \quad (D.3)$$

$$= \frac{2I}{A(1 + \frac{\delta A}{A})\sqrt{T_e}\sqrt{1 + \frac{\delta T_e}{T_e}}(1 - \alpha(V - V_{float}))(1 + \frac{\delta(V - V_{float})}{V - V_{float}})} \quad (D.4)$$

$$= n_e \frac{1}{(1 + \frac{\delta A}{A})\sqrt{1 + \frac{\delta T_e}{T_e}}(1 + \frac{\delta(V - V_{float})}{V - V_{float}})} \quad (D.5)$$



# Bibliography

- [1] IGJ Classen, E Westerhof, CW Domier, AJH Donné, RJE Jaspers, NC Luhmann Jr, HK Park, MJ van de Pol, GW Spakman, MW Jakubowski, et al. Effect of heating on the suppression of tearing modes in tokamaks. *Physical review letters*, 98(3):035001, 2007.
- [2] G Gantenbein, H Zohm, G Giruzzi, S Günter, F Leuterer, M Maraschek, J Meskat, Q Yu, ASDEX Upgrade Team, et al. Complete suppression of neoclassical tearing modes with current drive at the electron-cyclotron-resonance frequency in asdex upgrade tokamak. *Physical Review Letters*, 85(6):1242, 2000.
- [3] E Poli, C Angioni, FJ Casson, D Farina, L Figini, TP Goodman, O Maj, O Sauter, H Weber, H Zohm, et al. On recent results in the modelling of neoclassical-tearing-mode stabilization via electron cyclotron current drive and their impact on the design of the upper ecr launcher for iter. *Nuclear Fusion*, 55(1):013023, 2015.
- [4] R Prater. Heating and current drive by electron cyclotron waves. *Physics of Plasmas*, 11(5):2349–2376, 2004.
- [5] K Takahashi, CP Moeller, K Sakamoto, K Hayashi, and T Imai. High power experiments of remote steering launcher for electron cyclotron heating and current drive. *Fusion engineering and design*, 65(4):589–598, 2003.
- [6] TH Stix. The theory of plasma waves. *The Theory of Plasma Waves*, New York: McGraw-Hill, 1962.
- [7] A Mueck, L Curchod, Y Camenen, Stefano Coda, TP Goodman, HP Laqua, A Pochelon, L Porte, and F Volpe. Demonstration of electron-bernstein-wave heating in a tokamak via o- x- b double-mode conversion. *Physical review letters*, 98(17):175004, 2007.
- [8] S Alberti, G Arnoux, L Porte, J-P Hogge, B Marletaz, P Marmillod, Y Martin, S Nowak, TCV Team, et al. Third-harmonic, top-launch, ecrh experiments on tcv tokamak. *Nuclear fusion*, 45(11):1224, 2005.
- [9] J-L Segui, Y Michelot, G Giruzzi, TP Goodman, AH Kritz, A Pochelon, O Sauter, GR Smith, and MQ Tran. Measurement of the optical depth at the third electron cyclotron harmonic in tore supra. *Nuclear fusion*, 36(2):237, 1996.

## Bibliography

---

- [10] M Bornatici. Theory of electron cyclotron absorption of magnetized plasmas. *Plasma Physics*, 24(6):629, 1982.
- [11] M Henderson, G Saibene, C Darbos, D Farina, L Figini, M Gagliardi, F Gandini, T Gassmann, G Hanson, A Loarte, et al. The targeted heating and current drive applications for the iter electron cyclotron system. *Physics of plasmas*, 22(2):021808, 2015.
- [12] S Günter, A Gude, M Maraschek, S Sesnic, H Zohm, ASDEX Upgrade Team, and DF Howell. High-confinement regime at high  $\beta$  n values due to a changed behavior of the neoclassical tearing modes. *Physical review letters*, 87(27):275001, 2001.
- [13] RJ La Haye, R Prater, RJ Buttery, N Hayashi, A Isayama, ME Maraschek, L Urso, and H Zohm. Cross-machine benchmarking for iter of neoclassical tearing mode stabilization by electron cyclotron current drive. *Nuclear Fusion*, 46(4):451, 2006.
- [14] O Sauter, MA Henderson, G Ramponi, H Zohm, and C Zucca. On the requirements to control neoclassical tearing modes in burning plasmas. *Plasma Physics and Controlled Fusion*, 52(2):025002, 2010.
- [15] Z Chang and JD Callen. Global energy confinement degradation due to macroscopic phenomena in tokamaks. *Nuclear Fusion*, 30(2):219, 1990.
- [16] O Sauter. The physics of iter. *DPG Advanced Physics School*, 2014.
- [17] H Zohm, G Gantenbein, F Leuterer, M Maraschek, E Poli, L Urso, et al. Control of ntms by eccd on asdex upgrade in view of iter application. *Plasma Physics and Controlled Fusion*, 49(12B):B341, 2007.
- [18] E Poli, C Angioni, FJ Casson, D Farina, L Figini, TP Goodman, O Maj, O Sauter, H Weber, H Zohm, et al. On the criteria guiding the design of the upper electron-cyclotron launcher for iter. In *EPJ Web of Conferences*, volume 87, page 01008. EDP Sciences, 2015.
- [19] MA Henderson, R Heidinger, D Strauss, R Bertizzolo, A Bruschi, R Chavan, E Ciattaglia, S Cirant, A Collazos, I Danilov, et al. Overview of the iter ec upper launcher. *Nuclear fusion*, 48(5):054013, 2008.
- [20] D Strauss, G Aiello, R Bertizzolo, A Bruschi, N Casal, R Chavan, D Farina, L Figini, M Gagliardi, TP Goodman, et al. Nearing final design of the iter ec h&cd upper launcher. *Fusion Engineering and Design*, 2018.
- [21] D Strauss, G Aiello, A Bruschi, N Casal, R Chavan, D Farina, L Figini, M Gagliardi, TP Goodman, G Grossetti, et al. Approaching final design of the iter ec h&cd upper launcher. In *30th Symposium on Fusion Technology (SOFT 2018)*, 2018.
- [22] FR Hansen, Jens-Peter Lynov, P Michelsen, and HL Pécseli. Ordinary wave propagation in a tokamak with random density fluctuations. *Nuclear fusion*, 28(5):769, 1988.



- 
- [23] B Hui, E Ott, PT Bonoli, and PN Guzdar. Scattering of electron cyclotron resonance heating waves by density fluctuations in tokamak plasmas. *Nuclear Fusion*, 21(3):339, 1981.
- [24] C Tsironis, AG Peeters, H Isliker, D Strintzi, I Chatziantonaki, and L Vlahos. Electron-cyclotron wave scattering by edge density fluctuations in iter. *Physics of Plasmas*, 16(11):112510, 2009.
- [25] A Snicker, E Poli, O Maj, L Guidi, A Köhn, H Weber, G Conway, M Henderson, and G Saibene. The effect of density fluctuations on electron cyclotron beam broadening and implications for iter. *Nuclear Fusion*, 58(1):016002, 2017.
- [26] A Köhn, E Holzhauer, J Leddy, MB Thomas, and RGL Vann. Influence of plasma turbulence on microwave propagation. *Plasma Physics and Controlled Fusion*, 58(10):105008, 2016.
- [27] A Köhn, E Holzhauer, J Leddy, MB Thomas, and RGL Vann. Influence of plasma turbulence on microwave propagation. *Plasma Physics and Controlled Fusion*, 58(10):105008, 2016.
- [28] Y Peysson, J Decker, L Morini, and S Coda. Rf current drive and plasma fluctuations. *Plasma Physics and Controlled Fusion*, 53(12):124028, 2011.
- [29] AK Ram and K Hizanidis. Scattering of radio frequency waves by cylindrical density filaments in tokamak plasmas. *Physics of Plasmas*, 23(2):022504, 2016.
- [30] ZC Ioannidis, AK Ram, K Hizanidis, and IG Tigelis. Computational studies on scattering of radio frequency waves by density filaments in fusion plasmas. *Physics of Plasmas*, 24(10):102115, 2017.
- [31] ZC Ioannidis, AK Ram, K Hizanidis, and IG Tigelis. Computational studies on scattering of radio frequency waves by density filaments in fusion plasmas. *Physics of Plasmas*, 24(10):102115, 2017.
- [32] M W Brookman, M E Austin, K W Gentle, C C Petty, D E Ernst, Y Peysson, J Decker, and K Barada. *EPJ Web of Conferences*, 147:03001, 2017.
- [33] M Baquero-Ruiz, S Alberti, O Chellaï, I Furno, T Goodman, F Manke, P Micheletti, G Plyushchev, and AK Skrivervik. Optically isolated millimeter-wave detector for the toroidal plasma experiment. *Review of Scientific Instruments*, 89(12):124702, 2018.
- [34] O Chellai, S Alberti, I Furno, T Goodman, A Koehn, L Figini, D Ricci, L Hizanidis, P Papiannidis, and C Tsironis. Experimental study of high power mm-waves scattering by plasma turbulence in tcv plasmas. In *EPJ Web of Conferences*, volume 157, page 03008. EDP Sciences, 2017.

## Bibliography

---

- [35] O Chellaï, S Alberti, M Baquero-Ruiz, I Furno, T Goodman, F Manke, G Plyushchev, L Guidi, A Koehn, O Maj, et al. Millimeter-wave beam scattering by field-aligned blobs in simple magnetized toroidal plasmas. *Physical review letters*, 120(10):105001, 2018.
- [36] O Chellaï, S Alberti, M Baquero-Ruiz, I Furno, T Goodman, B Labit, O Maj, P Ricci, F Riva, L Guidi, et al. Millimeter-wave beam scattering by edge-plasma density fluctuations in tcv. *Plasma Physics and Controlled Fusion*, 61(1):014001, 2018.
- [37] TP Goodman, SM Ahmed, S Alberti, Y Andrebe, C Angioni, K Appert, G Arnoux, R Behn, P Blanchard, P Bosshard, et al. An overview of results from the tcv tokamak. *Nuclear fusion*, 43(12):1619, 2003.
- [38] A Fasoli. Overview of physics research on the tcv tokamak. *Nuclear Fusion*, 49(10):104005, 2009.
- [39] S Coda, J Ahn, R Albanese, S Alberti, E Alessi, S Allan, H Anand, G Anastassiou, Y Andrèbe, C Angioni, et al. Overview of the tcv tokamak program: scientific progress and facility upgrades. *Nuclear Fusion*, 57(10):102011, 2017.
- [40] Annual work plan. *Eurofusion*, (issue 3), 2015.
- [41] F Hofmann, JB Lister, W Anton, S Barry, R Behn, S Bernel, G Besson, F Buhlmann, R Chavan, M Corboz, et al. Creation and control of variably shaped plasmas in tcv. *Plasma Physics and Controlled Fusion*, 36(12B):B277, 1994.
- [42] G Arnoux. Chauffage de plasma par ondes électromagnétiques à la troisième harmonique de la fréquence cyclotron des électrons dans le tokamak tcv. *EPFL PhD thesis*, page 196, 2005.
- [43] J-P Hogge, S Alberti, L Porte, and G Arnoux. Preliminary results of top launch third harmonic x-mode electron cyclotron heating in the tcv tokamak. *Nuclear fusion*, 43(11):1353, 2003.
- [44] J Hawke, Y Andrebe, R Bertizzolo, P Blanchard, R Chavan, J Decker, B Duval, P Lavanchy, X Llobet, B Marlétaz, et al. Improving spatial and spectral resolution of tcv thomson scattering. *Journal of Instrumentation*, 12(12):C12005, 2017.
- [45] A Pitzschke. Pedestal characteristics and mhd stability of h-mode plasmas in tcv. *EPFL PhD thesis*, page 247, 2011.
- [46] I Furno. Fast transient transport phenomena measured by soft x-ray emission in tcv tokamak plasmas. *EPFL PhD thesis*, page 193, 2001.
- [47] M Anton, H Weisen, MJ Dutch, W Von der Linden, F Buhlmann, R Chavan, B Marletaz, Ph Marmillod, and P Paris. X-ray tomography on the tcv tokamak. *Plasma physics and controlled fusion*, 38(11):1849, 1996.

- 
- [48] A Sushkov, V Andreev, Y Camenen, A Pochelon, I Klimanov, A Scarabosio, and H Weisen. High-resolution multiwire proportional soft x-ray diagnostic measurements on tcv. *Review of Scientific Instruments*, 79(2):023506, 2008.
- [49] L Curchod. High density plasma heating in the tokamak à configuration variable. *EPFL PhD thesis*, page 324, 2011.
- [50] JD Swift and MJR Schwar. Electrical probes for plasma diagnostics. 1970.
- [51] O Février, C Theiler, H De Oliveira, B Labit, N Fedorczak, and A Baillo. Analysis of wall-embedded langmuir probe signals in different conditions on the tokamak à configuration variable. *Review of Scientific Instruments*, 89(5):053502, 2018.
- [52] JA Boedo, N Crocker, L Chousal, R Hernandez, J Chalfant, H Kugel, P Roney, J Wertebaker, and NSTX Team. Fast scanning probe for the nstx spherical tokamak. *Review of Scientific Instruments*, 80(12):123506, 2009.
- [53] CK Tsui, JA Boedo, JR Myra, B Duval, B Labit, C Theiler, N Vianello, WAJ Vijvers, H Reimerdes, S Coda, et al. Filamentary velocity scaling validation in the tcv tokamak. *Physics of Plasmas*, 25(7):072506, 2018.
- [54] B Labit, I Furno, A Fasoli, A Diallo, SH Müller, G Plyushchev, M Podestà, and FM Poli. Universal statistical properties of drift-interchange turbulence in torpex plasmas. *Physical review letters*, 98(25):255002, 2007.
- [55] Dtacq aquisition cards. <http://d-tacq.com/>. Accessed: 2018-12-07.
- [56] Mdsplus database description. <http://www.mdsplus.org/index.php/Introduction>. Accessed: 2018-12-07.
- [57] F Avino, A Fasoli, and I Furno. The new torpex in-vessel toroidal conductor for the generation of a poloidal magnetic field. *Review of Scientific Instruments*, 85(3):033506, 2014.
- [58] F Avino, A Fasoli, I Furno, S Jolliet, and P Ricci. Basic characterization of torpex electrostatic modes in closed field line configurations. *Physics of Plasmas*, 21(12):122115, 2014.
- [59] F Avino, A Fasoli, I Furno, P Ricci, and C Theiler. X-point effect on plasma blob dynamics. *Physical review letters*, 116(10):105001, 2016.
- [60] M Baquero-Ruiz, O Avino, Fand Chellai, A Fasoli, I Furno, R Jacquier, F Manke, and S Patrick. Dual langmuir-probe array for 3d plasma studies in torpex. *Review of Scientific Instruments*, 87(11):113504, 2016.
- [61] RJ Adrian. On the role of conditional averages in turbulence theory. 1975.

## Bibliography

---

- [62] RA Antonia. Conditional sampling in turbulence measurement. *Annual review of fluid mechanics*, 13(1):131–156, 1981.
- [63] I Furno, B Labit, A Fasoli, FM Poli, Paolo Ricci, Christian Theiler, S Brunner, A Diallo, JP Graves, M Podestà, et al. Mechanism for blob generation in the torpex toroidal plasma. *Physics of Plasmas*, 15(5):055903, 2008.
- [64] F Nespoli, I Furno, B Labit, P Ricci, F Avino, FD Halpern, F Musil, and F Riva. Blob properties in full-turbulence simulations of the tcv scrape-off layer. *Plasma Physics and Controlled Fusion*, 59(5):055009, 2017.
- [65] F Riva, N Vianello, M Spolaore, P Ricci, R Cavazzana, L Marrelli, and S Spagnolo. Three-dimensional simulations of plasma turbulence in the rfx-mod scrape-off layer and comparison with experimental measurements. *Physics of Plasmas*, 25(2):022305, 2018.
- [66] P Ricci, C Theiler, A Fasoli, I Furno, K Gustafson, D Iraji, and J Loizu. Methodology for turbulence code validation: Quantification of simulation-experiment agreement and application to the torpex experiment. *Physics of Plasmas*, 18(3):032109, 2011.
- [67] OE Garcia, J Horacek, RA Pitts, AH Nielsen, W Fundamenski, JP Graves, V Naulin, and J Juul Rasmussen. Interchange turbulence in the tcv scrape-off layer. *Plasma physics and controlled fusion*, 48(1):L1, 2005.
- [68] SI Braginskii. Transport processes in a plasma. *Reviews of plasma physics*, 1, 1965.
- [69] F Riva. Verification and validation procedures with applications to plasma-edge turbulence simulations. *EPFL PhD thesis*, page 132, 2017.
- [70] IH Hutchinson. *Principles of Plasma Diagnostics*. Cambridge University Press, 2005.
- [71] R Prater, D Farina, Yu Gribov, RW Harvey, AK Ram, Y-R Lin-Liu, E Poli, AP Smirnov, F Volpe, E Westerhof, et al. Benchmarking of codes for electron cyclotron heating and electron cyclotron current drive under iter conditions. *Nuclear Fusion*, 48(3):035006, 2008.
- [72] E Poli, AG Peeters, and GV Pereverzev. Torbeam, a beam tracing code for electron-cyclotron waves in tokamak plasmas. *Computer Physics Communications*, 136(1-2):90–104, 2001.
- [73] D Farina. A quasi-optical beam-tracing code for electron cyclotron absorption and current drive: Gray. *Fusion Science and Technology*, 52(2):154–160, 2007.
- [74] SW McDonald. Wave kinetic equation in a fluctuating medium. *Physical Review A*, 43(8):4484, 1991.
- [75] H Weber, O Maj, and E Poli. Scattering of diffracting beams of electron cyclotron waves by random density fluctuations in inhomogeneous plasmas. In *EPJ Web of Conferences*, volume 87, page 01002. EDP Sciences, 2015.

- 
- [76] COMSOL RF Module User's Guide v5.2a.
- [77] A Köhn, L' Guidi, E' Holzhauer, O' Maj, E' Poli, A Snicker, and H Weber. Microwave beam broadening due to turbulent plasma density fluctuations within the limit of the born approximation and beyond. *Plasma Physics and Controlled Fusion*, 60(7):075006, 2018.
- [78] W Frei. Using perfectly matched layers and scattering boundary conditions for wave electromagnetics problems, 2015.
- [79] J-P Berenger. A perfectly matched layer for the absorption of electromagnetic waves. *Journal of computational physics*, 114(2):185–200, 1994.
- [80] I Furno, M Spolaore, C Theiler, N Vianello, R Cavazzana, and A Fasoli. Direct two-dimensional measurements of the field-aligned current associated with plasma blobs. *Physical review letters*, 106(24):245001, 2011.
- [81] M Podesta, A Fasoli, B Labit, I Furno, P Ricci, FM Poli, A Diallo, SH Müller, and C Theiler. Cross-field transport by instabilities and blobs in a magnetized toroidal plasma. *Physical review letters*, 101(4):045001, 2008.
- [82] C Theiler, I Furno, P Ricci, A Fasoli, B Labit, SH Müller, and G Plyushchev. Cross-field motion of plasma blobs in an open magnetic field line configuration. *Physical review letters*, 103(6):065001, 2009.
- [83] D Douai, T Goodman, A Isayama, M Fukumoto, T Wauters, C Sozzi, S Coda, P Blanchard, L Figini, S Garavaglia, et al. Development of helium electron cyclotron wall conditioning on tcv. *Nuclear Fusion*, 58(2):026018, 2017.
- [84] A Sangtae and JA Fessler. *EECS Department, The University of Michigan*, pages 1–2, 2003.
- [85] JS Bendat and AG Piersol. Random data analysis and measurement procedures. *Measurement Science and Technology*, 11(12):1825, 2000.
- [86] M Podesta, A Fasoli, B Labit, M McGrath, SH Müller, and FM Poli. Plasma production by low-field side injection of electron cyclotron waves in a simple magnetized torus. *Plasma physics and controlled fusion*, 47(11):1989, 2005.
- [87] C Theiler, I Furno, A Kuenlin, Ph Marmillod, and A Fasoli. Practical solutions for reliable triple probe measurements in magnetized plasmas. *Review of scientific instruments*, 82(1):013504, 2011.
- [88] P Ricci and BN Rogers. Turbulence phase space in simple magnetized toroidal plasmas. *Physical review letters*, 104(14):145001, 2010.
- [89] FM Poli, P Ricci, A Fasoli, and M Podestà. Transition from drift to interchange instabilities in an open magnetic field line configuration. *Physics of Plasmas*, 15(3):032104, 2008.

## Bibliography

---

- [90] C Theiler, I Furno, J Loizu, and A Fasoli. Convective cells and blob control in a simple magnetized plasma. *Physical review letters*, 108(6):065005, 2012.
- [91] AK Ram, K Hizanidis, and Y Kominis. Scattering of radio frequency waves by blobs in tokamak plasmas. *Physics of Plasmas*, 20(5):056110, 2013.
- [92] JA Wesson. Hydromagnetic stability of tokamaks. *Nuclear Fusion*, 18(1):87, 1978.
- [93] H Reimerdes. Mhd stability limits in the tcv tokamak. *EPFL PhD thesis*, page 177, 2001.
- [94] J-M Moret, F Buhlmann, D Fasel, F Hofmann, and G. Tonetti. Magnetic measurements on the TCV Tokamak. *Review of Scientific Instruments*, 69(6):2333–2348, 1998.
- [95] C Galperti, S Coda, BP Duval, X Llobet, P Milne, O Sauter, JM Moret, and D Testa. Integration of a real-time node for magnetic perturbations signal analysis in the distributed digital control system of the tcv tokamak. *IEEE Transactions on Nuclear Science*, 64(6):1446–1454, 2017.
- [96] H Reimerdes, Antoine Pochelon, and W Suttrop. Toroidally asymmetric elm precursors in tcv. *Nuclear fusion*, 38(3):319, 1998.
- [97] M Anton, M Dutch, W Von der Linden, J-Ma Moret, Y Peysson, and S Sagbo. The tcvxti software package in matlab. Technical report, 1996.
- [98] F Nespoli. Scrape-off layer physics in limited plasmas in tcv. page 151, 2017.
- [99] RA Fisher et al. *Metron*, 1921.
- [100] RJ Groebner, KH Burrell, and RP Seraydarian. Role of edge electric field and poloidal rotation in the l-h transition. *Physical review letters*, 64(25):3015, 1990.
- [101] A Medvedeva, C Bottereau, F Clairet, P Hennequin, U Stroth, G Birkenmeier, M Cavedon, GD Conway, T Happel, S Heuraux, et al. Density profile and turbulence evolution during lh transition studied with the ultra-fast swept reflectometer on asdex upgrade. *Plasma Physics and Controlled Fusion*, 59(12):125014, 2017.
- [102] PF Goldsmith et al. *Quasioptical systems*. Chapman & Hall, 1998.

# Oulfa Chellaï

## Curriculum Vitae

### Education

- 2015–present **Doctoral student**, *Swiss Plasma Center*, Ecole Polytechnique Fédérale de Lausanne, Switzerland.  
**Millimeter-wave beam scattering by edge-turbulence in fusion plasmas.**
- 2011–2014 **Master of Engineering**, *Ecole Nationale Supérieure d'Electricité (Supélec)*, France.  
Photonic Systems and Communication
- 2014 **Master of Science**, *Université de Lorraine*, France.  
Photonics and Quantum Optics
- 2013 **Internship**, *Observatorio Astronómico Nacional de Chile*, Santiago, Chile.
- 2013 **Exchange semester**, *Ecole Polytechnique Fédérale de Lausanne*, Switzerland.
- 2009–2011 **Ecole Préparatoire**, *Lycée Montaigne de Bordeaux*, France.
- 2009 **French Scientific Baccalauréat**, *High Honours*, Lycée Victor Hugo, Morocco.

### Awards

- 2017 **Best student poster award**, *22<sup>nd</sup> Topical conference on Radio Frequency Power in Plasmas*, Aix-en-Provence, France.
- 2009–2014 **Excellence Major Scholarship**, France.

### Conferences

- 2018 **Invited 44<sup>th</sup> European Physical Society Conference on Plasma Physics**, Prague, Czech Republic.
- 2017 **22<sup>nd</sup> Topical conference on Radio Frequency Power in Plasmas**, Aix-en-Provence, France.
- 2016 **19<sup>th</sup> Joint Workshop on Electron Cyclotron Emission and Electron Cyclotron Resonance Heating**, Gandhinagar, India.
- 2015 **Joint Annual Meeting of ÖPG, SPG, ÖGAA und SGAA**, Vienna, Austria.
- 2015 **COMSOL Conference**, Grenoble, France.

### Publications

- [1] O Chellaï, S Alberti, M Baquero-Ruiz, I Furno, T Goodman, B Labit, O Maj, P Ricci, F Riva, L Guidi, et al. Millimeter-wave beam scattering by edge-plasma density fluctuations in tcv. *Plasma Physics and Controlled Fusion*, 61(1):014001, 2018.

- [2] O. Chellaï et al. Millimeter-wave beam scattering by field-aligned blobs in simple magnetized toroidal plasmas. *Physical Review Letters*, 120(10):105001, 2018.
- [3] O Chellaï, S Alberti, I Furno, T Goodman, A Koehn, L Figini, D Ricci, K Hizanidis, P Papagiannis, C Tsironis, and the TCV team. Experimental study of high power mm-waves scattering by plasma turbulence in tcv plasmas. *EPJ Web Conf.*, page 03008, 2017.
- [4] M Baquero-Ruiz, S Alberti, O Chellaï, I Furno, T Goodman, F Manke, P Micheletti, G Plyushchev, and AK Skrivervik. Optically isolated millimeter-wave detector for the toroidal plasma experiment. *Review of Scientific Instruments*, 89(12):124702, 2018.
- [5] M Baquero-Ruiz, F Avino, O Chellaï, A Fasoli, I Furno, R Jacquier, F Manke, and S Patrick. Dual langmuir-probe array for 3d plasma studies in torpex. *Review of Scientific Instruments*, 87(11):113504, 2016.

---

## Teaching

- 2015-2017 **Physique Générale I.**
- 2015-2018 **Physique Générale II, pour mathématiciens.**
- 2016 **EuroTech PhD summer school, Integrated Approach to Energy Systems.**

---

## Languages

- French**, *Mother tongue.*
- Arabic**, *Mother tongue.*
- English**, *Fluent.*
- Spanish**, *Fluent.*
- German**, *Basic knowledge.*





